

# Sheffield Hallam University

*Microstructure and cutting performance of V-C based coatings deposited by HIPIMS/UBM*

ONISZCZUK, Anna Wiktoria

Available from the Sheffield Hallam University Research Archive (SHURA) at:

<http://shura.shu.ac.uk/20896/>

## A Sheffield Hallam University thesis

This thesis is protected by copyright which belongs to the author.

The content must not be changed in any way or sold commercially in any format or medium without the formal permission of the author.

When referring to this work, full bibliographic details including the author, title, awarding institution and date of the thesis must be given.

Please visit <http://shura.shu.ac.uk/20896/> and <http://shura.shu.ac.uk/information.html> for further details about copyright and re-use permissions.

---

# Microstructure and Cutting Performance of V-C based coatings deposited by HIPIMS/UBM

---

Anna Wiktorja Oniszczyk

A thesis submitted in partial fulfilment of the requirements of  
Sheffield Hallam University  
for the degree of Doctor of Philosophy

In collaboration with The National HIPIMS technology Centre UK at Sheffield Hallam  
University and Sandvik Coromant

December 2016

# Content

<b>ANNA WIKTORIA ONISZCZUK</b> .....	<b>1</b>
<b>A THESIS SUBMITTED IN PARTIAL FULFILMENT OF THE REQUIREMENTS OF</b> .....	<b>1</b>
<b>SHEFFIELD HALLAM UNIVERSITY</b> .....	<b>1</b>
<b>FOR THE DEGREE OF DOCTOR OF PHILOSOPHY</b> .....	<b>1</b>
<b>DECEMBER 2016</b> .....	<b>1</b>
<b>CONTENT</b> .....	<b>2</b>
<b>LIST OF FIGURES AND TABLES</b> .....	<b>5</b>
<b>ABSTRACT</b> .....	<b>I</b>
<b>1 INTRODUCTION</b> .....	<b>4</b>
1.1 MOTIVATION.....	4
1.2 AIMS .....	7
<b>2 LITERATURE REVIEW</b> .....	<b>8</b>
2.1 PHYSICAL VAPOUR DEPOSITION BASICS.....	9
2.1.1 <i>Sputtering</i> .....	10
2.1.2 <i>Deposition with substrate bias</i> .....	12
2.1.3 <i>DC Magnetron Sputtering</i> .....	13
2.1.4 <i>High Power Impulse Magnetron Sputtering</i> .....	17
2.2 REACTIVE SPUTTERING.....	18
2.2.1 <i>Target Poisoning</i> .....	19
2.2.2 <i>Target poisoning using two reactive gases</i> .....	23
2.2.3 <i>Reactive Sputtering Control Systems</i> .....	26
2.3 SOLID LUBRICANTS .....	27
2.3.1 <i>Carbon based coatings</i> .....	28
2.3.2 <i>Vanadium Magnéli phases</i> .....	32
2.4 THIN FILM GROWTH .....	34
2.5 MULTILAYERS .....	38
<b>3 EXPERIMENTAL SETUP</b> .....	<b>43</b>
3.1 SAMPLE PREPARATION AND COATING DEPOSITION .....	43
3.1.1 <i>Specimen Preparation before Coating</i> .....	43
3.1.2 <i>Coating Unit</i> .....	44
3.1.3 <i>Deposition Process Sequence</i> .....	46
3.2 GAS FLOW CONTROL .....	49
3.3 CURRENT AND VOLTAGE MEASUREMENT .....	51
3.4 PLASMA DIAGNOSTIC TECHNIQUES .....	53
3.4.1 <i>Plasma Sampling Mass-Spectroscopy</i> .....	53
3.4.2 <i>Optical Emission Spectroscopy</i> .....	55
3.4.3 <i>Quartz crystal micro balance</i> .....	57
3.4.4 <i>Flat Electrostatic Probe</i> .....	58
3.5 SAMPLE CHARACTERIZATION TECHNIQUES .....	60
3.5.1 <i>Optical Microscopy</i> .....	60
3.5.2 <i>Scanning Electron Microscopy</i> .....	61
3.5.3 <i>Atomic Force Microscopy</i> .....	64
3.5.4 <i>X-ray Diffraction</i> .....	65
3.5.5 <i>Raman spectroscopy</i> .....	70

3.5.6 Film Thickness.....	71
3.5.7 Pin on disc test .....	72
3.5.8 Adhesion test.....	74
3.5.9 Hardness.....	77
3.5.10 Dry High Speed Milling.....	80
<b>4 EFFECT OF PULSE ENERGY ON THE ION ETCHING .....</b>	<b>83</b>
4.1 METHODOLOGY.....	84
4.2 PLASMA ANALYSIS RESULTS .....	86
4.3 MICROSTRUCTURE AND ION ETCHING ANALYSIS RESULTS .....	99
4.4 CONCLUSIONS.....	105
<b>5 DEVELOPMENT OF THE SYSTEM .....</b>	<b>105</b>
<b>6 EFFECT OF TARGET POISONING IN MIXED AR, N<sub>2</sub> AND CH<sub>4</sub> REACTIVE ATMOSPHERE .....</b>	<b>109</b>
6.1 OVERVIEW OF THE EXPERIMENT .....	109
6.2 EFFECT OF THE DISCHARGE MODE, REACTIVE ATMOSPHERE AND TARGET MATERIAL ON THE PLASMA CONTENT.....	111
<i>Nitrogen Reactive Atmosphere</i> .....	111
<i>Methane Reactive Atmosphere</i> .....	112
<i>Mixed Reactive Atmosphere</i> .....	114
<i>Discussion</i> .....	115
6.3 HYSTERESIS BEHAVIOUR OF THE TARGET AND THE TOTAL GAS .....	116
6.3.1 V Target.....	116
6.3.2 TiAl Target .....	126
6.4 EFFECT OF REACTIVE GAS FLOW ON THE PLASMA STIOCHIMETRY .....	135
6.4.1 V Target.....	135
6.4.2 TiAl Target .....	144
6.5. DISCUSSION .....	153
6.6. CONCLUSION .....	156
<b>7 SINGLE NANOSCALE MULTILAYER COATINGS DEPOSITED AT CONSTANT OES SIGNAL .....</b>	<b>158</b>
7.1 OVERVIEW OF THE EXPERIMENTS .....	158
7.2 DEPOSITION PROCESS .....	159
7.3 COMPOSITION OF SINGLE NANOSCALE MULTILAYER COATINGS.....	162
7.4 CRYSTALLOGRAPHIC STRUCTURE OF SNMC INVESTIGATED BY XRD ANALYSIS AND SEM.....	164
<i>Coating 45% OES signal</i> .....	164
<i>Coating 37% OES signal</i> .....	168
<i>Coating 30% OES signal</i> .....	171
<i>Coating 25% OES signal</i> .....	174
<i>Coating 20% OES signal</i> .....	177
7.5 ADHESION.....	180
<i>Rockwell C test</i> .....	180
<i>Scratch Test</i> .....	181
7.6 WEAR RESISTANCE – PIN ON DISK .....	183
<i>Coating 45% OES</i> .....	185
<i>Coating 37% OES</i> .....	187
<i>Coating 30% OES</i> .....	189
<i>Coating 25% OES</i> .....	191
<i>Coating 20% OES</i> .....	193
7.7 DISCUSSION .....	196
7.8 CONCLUSIONS.....	201

<b>8 ADVANCED NANOSCALE MULTILAYER COATINGS DEPOSITED AT GRADIENT PRESSURE.....</b>	<b>202</b>
8.1 OVERVIEW OF THE EXPERIMENTS .....	202
8.2 DEPOSITION PROCESS .....	203
8.3 COMPOSITION OF ANMC.....	205
8.4 CRYSTALLOGRAPHIC STRUCTURE OF ANMC INVESTIGATED BY XRD ANALYSIS AND SEM .....	206
<i>Coating 25% OES (B)</i> .....	206
<i>Coating 37/25% OES</i> .....	209
<i>Coating 45:20% OES</i> .....	212
8.5 STRUCTURE EVOLUTION OF ADVANCED TiALCN/VCN NANOSCALE COATING.....	215
8.5.1 <i>Coating 37/25% OES</i> .....	215
8.5.2 <i>Coating 45:20% OES</i> .....	217
8.6 ADHESION.....	221
<i>Rockwell B test</i> .....	221
<i>Scratch Test</i> .....	222
8.7 WEAR RESISTANCE – PIN ON DISK .....	223
<i>25% OES B</i> .....	225
<i>37/25% OES</i> .....	227
<i>45:20% OES</i> .....	229
8.8 DISCUSSION .....	230
8.9 CONCLUSION .....	232
<b>9 EFFECT OF TARGET POISONING LEVEL ON THE TRIBIOLOGICAL PROPERTIES....</b>	<b>234</b>
9.1 OVERVIEW OF THE EXPERIMENTS .....	234
9.2 FLANK WEAR OF INSERTS .....	235
9.3 POST MORTEM ANALYSIS .....	237
<i>Standard Coating</i> .....	237
<i>Coating 25% OES B</i> .....	239
<i>Coating 25% OES</i> .....	240
<i>Coating 20% OES</i> .....	243
<i>Coating 37% OES</i> .....	246
<i>Coating 45:20% OES</i> .....	249
<i>Coating 30% OES</i> .....	251
<i>Coating 37/25% OES</i> .....	254
9.4 DRILLING TEST OF COATING DEPOSITED AT 45:20% .....	257
9.5 DISCUSSION .....	258
9.5 CONCLUSION .....	259
<b>SUMMARY .....</b>	<b>259</b>

## List of figures and tables

Figure 1.1 BF TEM cross-section of TiAlCN/VCN nanoscale coating deposited by reactive HIPIMS deposition with highlighted various architecture regions [1].

Figure 2.1: PVD family tree with expanded sputtering branch).

Figure 2.2: Schematic presentation of the surface a) before ion bombardment and b) during ion bombardment.

Figure 2.3 Applied fields and electron motion in a planar magnetron

Figure 2.4: Different magnetron configurations a) balanced magnetron, b) unbalance magnetron with stronger inner pole and c) unbalance magnetron with stronger outer pole.

Figure 2.5: Multi - cathode systems with two and four cathodes.

Figure 2.6: Schematic diagram of: a) Magnetron DC sputtering and b) HIPIMS. During HIPIMS deposition the plasma is high ionised. This leads to dense coating structure.

Figure 2.7: The hysteresis behaviour of reactive magnetron sputtering.

Figure 2.8: (a) Diagram of atomic orbitals of carbon and  $sp^3$  hybridization, (b) hybridized orbitals of carbon atom.

Figure 2.9: The crystal structure of graphite.

Figure 2.10: The crystal structure of diamond.

Figure 2.11: Carbon phase diagram.

Figure 2.12: Phase diagram of the binary system V-O.

Figure 2.13: The phase diagram of V<sub>2</sub>O<sub>5</sub>.

Figure 2.14 Structure Zone Model according to Movchan and Demchishin for evaporated films, showing the 3 zones in relation to the ratio of substrate temperature (T) and melting temperature of the material ( $T_m$ ).

Figure 2.15 Structure Zone Model according to Thornton for sputtered films showing the added zone T and the influence of argon pressure.

Figure 2.16 Structure model according to Messier showing the effect of substrate bias voltage.

Figure 2.17 Structure Zone Model according to Kelly and Arnell showing the effect of the ion to neutral ratio on the morphology.

Figure 2.18: Simplified illustration of multilayers coatings with only few layers for different bilayer thickness: a) multilayers, b) nanoscale multilayers, c) superlattice.

Figure 2.19: Change in properties of nanoscale multilayer coatings as a function of the interface volume (schematically, disregarding superlattice structures).

Figure 2.20: Toughening and strengthening mechanisms in ceramic multilayer coatings (schematically) according to Holleck and Schier.

Figure 2.21: Hardness as a function of Superlattice period.

Figure 3.1: Examples of samples used for deposition. 1: polished HSS disk, 2: polished SS disk, 3: Si wafer 4: polished plain WC

Figure 3.2 Hauzer 1000/4 PVD coater

Figure 3.3: Schematic cross section of chamber of Hauzer HTC 1000-4 unit.

Figure 3.4 PID control loop applied into the system. Light is passing via a feedthrough (1) to a spectrometer (2). A selected spectra line passes to a control unit (3), where the light intensity is compared with the set value.

Figure 3.5 Schematic of the quadrupole mass analyzer showing resonant ion passing the analyzer and reaching the detector and nonresonant ion scattered in the analyzer.

Figure 3.6: Spectrum of HIPIMS with TiAl and V targets in Ar, N<sub>2</sub> and CH<sub>4</sub> atmosphere.

Figure 3.7: Typical shapes of Langmuir probes.

Figure 3.8: I – V Characteristic of a Langmuir probe for different electrode shapes

Figure 3.9: Schematic drawing of a scanning electron beam incident on a solid sample.

Figure 3.10 Schematic view of the basic working principle of the atomic force microscope.

Figure 3.11 Diffraction of X-rays by planes of atoms

Figure 3.12 Bragg-Brentano geometry configuration.

Figure 3.13: Example of spectrum of TiAlCN/VCN coated on M2 HSS substrate, collected by using Bragg- Brentano geometry.

Figure 3.14: Example of Low-angle X-ray diffraction spectrum.

Figure 3.15: Glancing angle geometry configuration

Figure 3.16: schematic diagram of stylus profilometer.

Figure 3.17: Determination of adhesion according to BS ISO 26443:2008 standards

Figure 3.18: Scratch test for the determination of the adhesive strength: a) principle of scratch test, b) progressive damage along scratch track.

Figure 3.19: Schematics of: a) an indenter applied for microhardness measurement by Knoop method, b) an indentation of an indenter in the material;  $\alpha=172^\circ$  ,  $\beta=130^\circ$  , d- longer diagonal of the indentation (PN ISO 4545:1996standard )

Figure 3.20: Loading and unloading curve of nanoindentation test.

Figure 3.21 Dry High Speed Milling test; a) face milling using the R390-11-T3 08M-PM cutting insert with indicated the cutting depth. b) The roll entry of the milling head.

Figure 3.22 Optical microscopy analysis of the cutting edge. Presented insert has 0.133 mm wide wear along the edge.

Figure 4.1: Sheath edge curves around a square corner.

Figure 4.2: Chamber equipment with plasma diagnostic devices: Quartz crystal microbalance, flat probe and optical fibre attached to Optical Emission Spectrometer.

Figure 4.3: Temporal evolution of cathode current during pulse for different charge values.

Figure 4.4: Temporal evolution of ion flux current during pulse for different charge values.

Figure 4.5: Deposition rate increases with increasing cathode current width.

Figure 4.6: Ion flux density vs. cathode charge.

Figure 4.7: Temporal evolution of PMT current during pulse for different charge values. a) Argon(I), b) Vanadium(I), c) Vanadium(II).

Figure 4.8: Normalized PMT current for different species, for charge 0 and 16.

Figure 4.9: With increase of cathode current the intensity of all species increases. Slopes for trend lines are Ar:0.73, V(I):1.22, V(II):1.57.

Figure 4.10: Plasma composition obtained with mass spectroscopy

Figure 4.11: The ion flux composition in respect to cathode current

Figure 4.12: Relationship between different species as function of cathode current.

Figure 4.13: Insert surface depth profile plots of the DYNAMIC TRIM simulations; this shows how the chemical composition changes with increased depth into the substrate.

Figure 4.14: Vanadium content depth profile at different times.

Figure 4.15: Ion etching rate as a function of ramping and hold time for polished HSS, SS and Inserts.

Figure 4.16: SEM image of a) unpolished and b) polished Insert at the border between masked and exposed surface. a) Loosely bonded small grains are removed from exposed area. Thus roughness of the sample increases. b) Sample roughness increased on after etching.

Figure 4.17: Surface of a) untreated sample and b) structure inside sample.

Figure 4.18: SEM image of polished Insert cutting edge. Etching parameters: a)

10 min ramping and 10 min of holding time, b) 20 min ramping and 20 min of holding time.

Figure 4.19: SEM image of unpolished Insert cutting edge. Etching parameters:

a) 10 min ramping and 10 min of holding time, b) untreated.

Figure 4.20: AFM image of polished Inserts for masked a) and etched b) areas.

Figure 4.21: AFM image of unpolished Inserts for masked a) and etched b) areas.

Figure 4.22: Waviness as function of ramping time and holding time for a) unpolished and b) polished surface.

Figure 4.23: Roughness as function of ramping time and holding time for a) unpolished and b) polished surface.

Figure 5.2 Left: The light is collected from the entire chamber including reflection from substrate table. Right: After angling the collimator, light is collected only from the target area

Figure 6.1 V target discharge resistance and total gas pressure vs. argon flow rate curves: 4 targets operating in DCMS discharge.

Figure 6.2 V target discharge resistance and total gas pressure vs. total reactive flow rate curves: 4 targets operating in DCMS discharge; Nitrogen reactive atmosphere.

Figure 6.3 V target discharge resistance and total gas pressure Vs total reactive flow rate curves: 4 targets operating in DCMS discharge; Methane reactive atmosphere

Figure 6.4 V target discharge resistance and total gas pressure Vs total reactive flow rate curves: 4 targets operating in DCMS discharge; mixed nitrogen and methane reactive atmosphere

Figure 6.5 V target discharge resistance and total gas pressure Vs total reactive flow rate curves: mixed DCMS/HIPIMS discharge; Argon atmosphere

Figure 6.6 V target discharge resistance and total gas pressure Vs total reactive flow rate curves: mixed DCMS/HIPIMS discharge; Nitrogen reactive atmosphere

Figure 6.7 V target discharge resistance and total gas pressure Vs total reactive flow rate curves: mixed DCMS/HIPIMS discharge; Methane reactive atmosphere.

Figure 6.8 V target discharge resistance and total gas pressure Vs total reactive flow rate curves: mixed DCMS/HIPIMS discharge; mixed nitrogen and methane reactive atmosphere

Figure 6.9 The total pressure hysteresis for HIPIMS and DCMS sputtering for the  $N_2CH_4$  process

Figure 6.10 TiAl target discharge resistance and total gas pressure vs. argon flow rate curves: 4 targets operating in DCMS discharge.

Figure 6.11 TiAl target discharge resistance and total gas pressure vs. total reactive flow rate curves: 4 targets operating in DCMS discharge; Nitrogen reactive atmosphere.

Figure 6.12 TiAl target discharge resistance and total gas pressure vs. total reactive flow rate curves: 4 targets operating in DCMS discharge; Methane reactive atmosphere

Figure 6.13 TiAl TiAl target discharge resistance and total gas pressure vs. total reactive flow rate curves: 4 targets operating in DCMS discharge; mixed nitrogen and methane reactive atmosphere

Figure 6.14 TiAl target discharge resistance and total gas pressure vs. total reactive flow rate curves: mixed DCMS/HIPIMS discharge; Argon atmosphere

Figure 6.15 TiAl target discharge resistance and total gas pressure vs. total reactive flow rate curves: mixed DCMS/HIPIMS discharge; Nitrogen reactive atmosphere

Figure 6.16 TiAl target discharge resistance and total gas pressure vs. total reactive flow rate curves: mixed DCMS/HIPIMS discharge; Methane reactive atmosphere.

Figure 6.17 TiAl target discharge resistance and total gas pressure vs. total reactive flow rate curves: mixed DCMS/HIPIMS discharge; mixed nitrogen and methane reactive atmosphere

Figure 6.18 Discharge resistance, total gas pressure and mass-spectrometer data evolution in the DCMS of V discharge in an inert gas (Ar) atmosphere

Figure 6.19 Discharge resistance, total gas pressure and mass-spectrometer data evolution in the DCMS of V discharge in a reactive gas (Ar+N<sub>2</sub>) atmosphere

Figure 6.20 Discharge resistance, total gas pressure and mass-spectrometer data evolution in the DCMS of V discharge in a reactive gas (Ar+CH<sub>4</sub>) atmosphere

Figure 6.21 Discharge resistance, total gas pressure and mass-spectrometer data evolution in the DCMS of V discharge in a reactive gas (Ar+N<sub>2</sub>+CH<sub>4</sub>) atmosphere

Figure 6.22 Discharge resistance, total gas pressure and mass-spectrometer data evolution in the HIPIMS of V discharge in an inert gas (Ar) atmosphere

Figure 6.23 Discharge resistance, total gas pressure and mass-spectrometer data evolution in the HIPIMS of V discharge in a reactive gas (Ar+N<sub>2</sub>) atmosphere

Figure 6.24 Discharge resistance, total gas pressure and mass-spectrometer data evolution in the HIPIMS of V discharge in a reactive gas (Ar+CH<sub>4</sub>) atmosphere

Figure 6.25 Discharge resistance, total gas pressure and mass-spectrometer data evolution in the HIPIMS of V discharge in a reactive gas (Ar+N<sub>2</sub>+CH<sub>4</sub>) atmosphere

Figure 6.26 Discharge resistance, total gas pressure and mass-spectrometer data evolution in the DCMS of TiAl discharge in an inert gas (Ar) atmosphere

Figure 6.27 Discharge resistance, total gas pressure and mass-spectrometer data evolution in the DCMS of TiAl discharge in a reactive gas (Ar+N<sub>2</sub>+CH<sub>4</sub>) atmosphere

Figure 6.28 Discharge resistance, total gas pressure and mass-spectrometer data evolution in the DCMS of TiAl discharge in a reactive gas (Ar+CH<sub>4</sub>) atmosphere

Figure 6.29 Discharge resistance, total gas pressure and mass-spectrometer data evolution in the DCMS of TiAl discharge in a reactive gas (Ar+N<sub>2</sub>+CH<sub>4</sub>) atmosphere

Figure 6.30 Discharge resistance, total gas pressure and mass-spectrometer data evolution in the HIPIMS of TiAl discharge in an inert (Ar) atmosphere

Figure 6.31 Discharge resistance, total gas pressure and mass-spectrometer data evolution in the HIPIMS of TiAl discharge in a reactive gas (Ar+N<sub>2</sub>) atmosphere

Figure 6.32 Discharge resistance, total gas pressure and mass-spectrometer data evolution in the HIPIMS of TiAl discharge in a reactive gas (Ar+CH<sub>4</sub>) atmosphere

Figure 6.33 Discharge resistance, total gas pressure and mass-spectrometer data evolution in the HIPIMS of TiAl discharge in a reactive gas (Ar+CH<sub>4</sub>) atmosphere

Figure 7.1 The process average total flows of the reactive gases for SNMC (black points) overlapped with the OES signal hysteresis of the Vanadium line for the DCMS (red line) and the HIPIMS (black line) discharges.

Figure 7.2 Composition of SNMC: a) metal to gas content ratio, b) atomic % of elements.

Figure 7.3 The Bragg-Brentano and Glancing Angle XRD patterns of the 45% OES coating

Figure 7.1 SEM image of the surface structure for coating 45% OES. The coating consists of glassy amorphous structure and porous islands with globular structure.

Figure 7.5 The EDX analysis of V, Ti, Al, N and C elements for coating 45% OES. The glassy structure have uniform distribution of all metal elements, whereas porous island consists mainly of Al, C and N.

Figure 7.6 SEM cross-section of the 45% OES coating. The glassy structure is up to about 2  $\mu\text{m}$ , then coating become structured and porous structures become to growth over the whole coating.

Figure 7.7 RAMAN Spectra of carbon peaks of the coating 45% OES.

Figure 7.8 The Bragg-Brentano and Glancing Angle XRD patterns of the 37% OES coating

Figure 7.9 SEM image of the surface structure for coating 37% OES

Figure 7.10 SEM cross-section of the 37% OES coating.

Figure 7.11 RAMAN Spectra of carbon peaks of the coating 37% OES

Figure 7.2 The Bragg-Brentano and Glancing Angle XRD patterns of the 45% OES coating

Figure 7.13 SEM image of the surface structure for coating 30% OES

Figure 7.3 SEM cross-section of the 30% OES coating

Figure 7.4 RAMAN Spectra of carbon peaks of the coating 30% OES

Figure 7.16 The Bragg-Brentano and Glancing Angle XRD patterns of the 25% OES coating

Figure 7.5: SEM cross-section of the 25% OES coating.

Figure 7.6 SEM image of the surface structure for coating 25% OES

Figure 7.7 RAMAN Spectra of carbon peaks of the coating 25% OES

Figure 7.8 The Bragg-Brentano and Glancing Angle XRD patterns of the 20% OES coating

Figure 7.21 SEM cross-section of the 25% OES coating

Figure 7.9 SEM image of the surface structure for coating 20% OES

Figure 7.23 RAMAN Spectra of carbon peaks of the coating 20% OES

Figure 7.24 Coefficient of friction as a function of number of laps for room temperature of SNMC

Figure 7.25 SEM image of the wear track created by room temperature pin on disk testing.

Figure 7.26 The EDX analysis of V, Ti, Al, N, C, Fe, and O elements within the wear track created by room temperature pin on disk testing

Figure 7.27 SEM image of the wear track created by room temperature pin on disk testing

Figure 7.28 The EDX analysis of V, Ti, Al, N, C, Fe, and O elements within the wear track created by room temperature pin on disk testing

Figure 7.29 SEM image of the wear track created by room temperature pin on disk testing

Figure 7.30 The EDX analysis of V, Ti, Al, N, C, Fe, and O elements within the wear track created by room temperature pin on disk testing

Figure 7.31 SEM image of the wear track created by room temperature pin on disk testing

Figure 7.32 The EDX analysis of V, Ti, Al, N, C, Fe, and O elements within the wear track created by room temperature pin on disk testing

Figure 7.33 SEM image of the wear track created by room temperature pin on disk testing

Figure 7.34 The EDX analysis of V, Ti, Al, N, C, Fe, and O elements within the wear track created by room temperature pin on disk testing

Figure 7.35 A shift to lower  $2\theta$  values has been observed

Figure 8.1 The Bragg-Brentano and Glancing Angle XRD patterns of the 25% OES (B) coating.

Figure 8.2 SEM cross-section of the 25% OES (B) coating

Figure 8.3 SEM image of the surface structure for coating 25% OES (B).

Figure 8.4 RAMAN Spectra of carbon peaks of the coating 25% OES (B).

Figure 8.5. The Bragg-Brentano and Glancing Angle XRD patterns of the 45:20% OES coating

Figure 8.6 SEM cross-section of the 37/25% OES coating

Figure 8.7 SEM image of the surface structure for coating 37/25% OES.

Figure 8.8 RAMAN Spectra of carbon peaks of the coating 37/25% OES

Figure 8.9 The Bragg-Brentano and Glancing Angle XRD patterns of the 45:20% OES coating

Figure 8.10 SEM of the surface structure for coating 45:20% OES

Figure 8.11 cross-section of the 45:20% OES coating

Figure 8.12 RAMAN Spectra of carbon peaks of the coating 45:20% OES (B).

Figure 8.13 The evolution of coating stoichiometric along the coating thickness.

Figure 8.14 The BS SEM analysis of the FIB cross section on the Insert. Colours indicates various regions of the coating: yellow – the high metal content region; blue – the low metal content region; red – the low nitrogen and high carbon content region.

Figure 8.15 The high magnification cross section SEM image of the 45:20% OES coating. Borders between the VN base layer and 45% layer of the TiAlCN/VCN coating and between 45% and 37% layers are rapid and easily distinguished.

Figure 8.16 The evolution of coating stoichiometric along the coating thickness.

Figure 8.17 The BS SEM analysis of the FIB cross section on the Insert. Two regions can be observed – bright at the bottom of the coating is metal rich and dark, where metal content is reduced.

Figure 8.18 Coefficient of friction as a function of number of laps for room temperature of ANMC

Figure 8.19 SEM image of the wear track created by room temperature pin on disk testing.

Figure 8.20 The EDX analysis of V, Ti, Al, N, C, Fe, and O elements within the wear track created by room temperature pin on disk testing

Figure 8.21 SEM image of the wear track created by room temperature pin on disk testing.

Figure 8.22 The EDX analysis of V, Ti, Al, N, C, Fe, and O elements within the wear track created by room temperature pin on disk testing

Figure 8.23 SEM image of the wear track created by room temperature pin on disk testing.

Figure 8.24 The EDX analysis of V, Ti, Al, N, C, Fe, and O elements within the wear track created by room temperature pin on disk testing

Figure 9.1 Flank wear of coated Inserts plotted against number of passes (1 pas = 33 mm) in milling P20 steel.

Figure 9.2 SE (top) and BS (bottom) SEM image of insert flank coated with the standard coating after 19 passes on the P20 steel bar

Figure 9.3 The EDX analysis of V, Ti, Al, N, C, O, Fe, and W elements within the wear Scar created by milling in P20 steel bar. The presence of the FE indicates BUE creation; presence of the W – exposure of the substrate.

Figure 9.4 SE (top) and BS (bottom) SEM image of insert rake coated with the standard coating after 19 passes on the P20 steel bar

Figure 9.5 The EDX analysis of V, Ti, Al, N, C, O, Fe, and W elements within the wear Scar created by milling in P20 steel bar. The presence of the FE indicates BUE creation; presence of the W – exposure of the substrate.

Figure 9.6 SE (top) and BS (bottom) SEM image of insert flank coated with the 25% OES (B) coating after 1 pass on the P20 steel bar

Figure 9.7 SE (top) and BS (bottom) SEM image of insert rake coated with the 25% OES (B) coating after 1 pass on the P20 steel bar

Figure 9.8 SE (top) and BS (bottom) SEM image of insert flank coated with the 25% OES coating after 2 passes on the P20 steel bar

Figure 9.9 The EDX analysis of V, Ti, Al, N, C, O, Fe, and W elements within the wear Scar created by milling in P20 steel bar. The presence of the FE indicates BUE creation; presence of the W – exposure of the substrate.

Figure 9.10 SE (top) and BS (bottom) SEM image of insert rake coated with the 25% OES coating after 2 passes on the P20 steel bar

Figure 9.11 SE (top) and BS (bottom) SEM image of insert flank coated with the 20% OES coating after 4 passes on the P20 steel bar

Figure 9.12 The EDX analysis of V, Ti, Al, N, C, O, Fe, and W elements within the wear Scar created by milling in P20 steel bar. The presence of the FE indicates BUE creation; presence of the W – exposure of the substrate.

Figure 9.13 SE (top) and BS (bottom) SEM image of insert rake coated with the 20% OES coating after 4 passes on the P20 steel bar

Figure 9.14 The EDX analysis of V, Ti, Al, N, C, O, Fe, and W elements within the wear Scar created by milling in P20 steel bar. The presence of the FE indicates BUE creation; presence of the W – exposure of the substrate.

Figure 9.19 SE (top) and BS (bottom) SEM image of insert flank coated with the 37% OES coating after 9 passes on the P20 steel bar

Figure 9.20 The EDX analysis of V, Ti, Al, N, C, O, Fe, and W elements within the wear Scar created by milling in P20 steel bar. The presence of the FE indicates BUE creation; presence of the W – exposure of the substrate.

Figure 9.21 SE (top) and BS (bottom) SEM image of insert rake coated with the 37% OES coating after 9 passes on the P20 steel bar

Figure 9.22 SE (top) and BS (bottom) SEM image of insert rake coated with the 37% OES coating after 9 passes on the P20 steel bar

Figure 9.23 SE (top) and BS (bottom) SEM image of insert flank coated with the 45:20% OES coating after 12 passes on the P20 steel bar

Figure 9.24 The EDX analysis of V, Ti, Al, N, C, O, Fe, and W elements within the wear Scar created by milling in P20 steel bar. The presence of the FE indicates BUE creation; presence of the W – exposure of the substrate.

Figure 9.25 SE (top) and BS (bottom) SEM image of insert rake coated with the 45:20% OES coating after 12 passes on the P20 steel bar

Figure 9.15 SE (top) and BS (bottom) SEM image of insert flank coated with the 30% OES coating after 15 passes on the P20 steel bar

Figure 9.16 The EDX analysis of V, Ti, Al, N, C, O, Fe, and W elements within the wear Scar created by milling in P20 steel bar. The presence of the FE indicates BUE creation; presence of the W – exposure of the substrate.

Figure 9.17 SE (top) and BS (bottom) SEM image of insert rake coated with the 30% OES coating after 15 passes on the P20 steel bar

Figure 9.18 The EDX analysis of V, Ti, Al, N, C, O, Fe, and W elements within the wear Scar created by milling in P20 steel bar. The presence of the FE indicates BUE creation; presence of the W – exposure of the substrate.

Figure 9.26 SE (top) and BS (bottom) SEM image of insert flank coated with the 37/25% OES coating after 19 passes on the P20 steel bar

Figure 9.27 The EDX analysis of V, Ti, Al, N, C, O, Fe, and W elements within the wear Scar created by milling in P20 steel bar. The presence of the FE indicates BUE creation; presence of the W – exposure of the substrate.

Figure 9.28 SE (top) and BS (bottom) SEM image of insert rake coated with the 37/25% OES coating after 19 passes on the P20 steel bar

Figure 9.29 The EDX analysis of V, Ti, Al, N, C, O, Fe, and W elements within the wear Scar created by milling in P20 steel bar. The presence of the FE indicates BUE creation; presence of the W – exposure of the substrate.

Figure 8.30 Top view of coated drill after drilling 290 holes in aluminium. The BUE is visible at the cutting edges.

Table 2.1 Kinetics of the radicals created from CH<sub>4</sub> dissociation and ionization as well as of the species created in reactions with active nitrogen

Table 3.1: Dimensions and materials used for various tests and analytical methods

Table 3.2 List of electrical properties of target materials and the compounds on the target

Table 3.3 List of observed gas and metal ions

Table 3.4 Elementary tribological process

Table 4.1 Properties of chosen optical emission lines for different species

Table 4.2: Data input used for dynamic TRIM simulation.

Table 6.1 Varies process gas mixtures with specified gas flows

Table 6.2 Plasma composition measured at nitrogen flow of 300 sccm for DC and HIPIMS processes. The MS signal is normalized to all measured species. Colour scales indicate low (red) and high (green) mass signal level within the process.

Table 6.3. Plasma composition measured at methane flow of 150 sccm for DC and HIPIMS processes. The MS signal is normalized to all measured species. Colours scales indicate low (red) and high (green) mass signal level within the process.

Table 6.4 Plasma composition measured at nitrogen flow of 300 sccm and methane of 150 sccm flow for DC processes. The MS signal is normalized to all measured species. Colour scales indicate low (red) and high (green) mass signal level within the process.

Table 6.5. Plasma composition measured at nitrogen flow of 300 sccm and methane of 150 sccm flow for HIPIMS processes. The MS signal is normalized to all measured species. Colour scales indicate low (red) and high (green) mass signal level within the process.

Table 7.1 Deposition of the final SNMC TiAlCN/VCN coatings

Table 7.2 Process parameters during deposition of SNMC

Table 7.3 The Mechanical Properties and Chemical Composition of the SNMC

Table 7.4: Rockwell indentation marks of SNMC

Table 7.5 Results of the scratch test on HSS and plain inserts

Table 7.6 of the Tribiological properties of TiAlCN/VCN deposited at different OES levels

Table 8.1 Deposition of the ANMC TiAlCN/VCN coatings

Table 8.2 Process parameters during deposition of ANMC

Table 8.3 Mechanical properties of ANMC

Table 8.4 Composition of ANMC

Table 8.5 Thickness of the individual layer calculated using deposition rate of the SNMC

Table 8.6 Rockwell indentation marks of ANMC

Table 8.7 Maximum load during the scratch test on HSS and plain inserts

Table 8.8 Wear behaviour of ANMC

Table 9.1 Summary of failure mechanisms of the SNMC and ANMC TiAlCN/VCN coating, during cutting tests in P20 steel bar

## List of Abbreviations

Al	Aluminium
ANMC	Advanced nanoscale multilayer coating
Ar	Argon
BE	Backscattered electrons
BUE	Build Up Edge
C	Carbon
CCD	Charge-coupled device
CoF	Friction coefficient
DC	Direct Current Magnetron Sputtering
DCMS	Direct Current Magnetron Sputtering
EDX	energy dispersive x-ray spectroscopy
Fe	Iron
HIPIMS	high power impulse magnetron sputtering
HSS	High speed steel
MS	Mass spectrometer
N	Nitrogen
O	Oxygen
OES	Optical emission spectroscopy
PEM	Plasma emission monitoring
PVD	Physical vapour deposition
PWC	Polished tungsten carbide
RF	Radio frequency
SE	Secondary electrons

SEM	scanning electron microscope
SNMC	Single nanoscale multilayer coating
Ti	Titanium
UBM	Unbalanced magnetron
UWC	Unpolished tungsten carbide
V	Vanadium
XRD	X-ray diffraction

# Declaration

---

I hereby declare that this thesis is my own work and effort and that it has not been submitted anywhere for any award apart from that of Doctor of Philosophy at Sheffield Hallam University.

Where other sources of information have been used, they have been acknowledged.



Anna Wiktoria Oniszczyk

22.12.2016

Date

## Abstract

The poisoning of different target materials under Direct Current Magnetron Sputtering (DCMS) and DCMS/ High Power Impulse Magnetron Sputtering (HIPIMS) discharges, using two reactive gases, were analysed.

For both discharges, in mixed Ar+CH<sub>4</sub>+N<sub>2</sub> atmosphere, low flow processes were influenced by methane; conversely, at high flow they were dominated by nitrogen.

In DC discharges, vanadium targets were poisoned at 55% of reactive gas flow.

Poisoning resulted in a 2-fold increase in total pressure and a 50 % increase in discharge voltage/current ratio. TiAl targets poisoned at lower reactive gas flows exhibited narrower hysteresis than V targets.

For DCMS/HIPIMS discharges, both targets poisoned earlier and the hysteresis was narrower than in DC discharge. It is confirmed by trends in the partial pressure, the voltage/current ratio and ion fluxes of metals and reactive gasses. These effects are due to higher reactivity of the plasma; this is evidenced by higher fluxes of N<sup>+</sup> and N<sub>2</sub><sup>+</sup> and radicals containing H, C and N. The voltage/current ratio reduced by 50% as the target is poisoned; this is a contrast to operation in DC mode where it increased. This could be attributed to efficient ionization and drop in plasma impedance.

The effect of target poisoning using two reactive gases was utilised to deposit a series of TiAlCN/VCN coatings.

As the target was more poisoned, the coating thickness decreases. The microstructure of coatings changed from glassy amorphous to a NaCl-type cubic crystalline phase with columnar structure. The column density decreases with increased flow. Coatings showed an increase in nitrogen and carbon content.

Coatings with a high nitrogen and carbon content, show low adhesion to the base layer, and therefore poor wear resistance. Introducing a gas flow ramping between a VN base layer and the TiAlCN/VCN multilayer coating, as well as introducing a metallic layer, improves wear resistance of the coatings. The wear resistance was confirmed during cutting test on the P20 metal bar.

## Acknowledgements

I would like to thank everyone who directly or indirectly has been involved during the four years leading to this Thesis, but the space here is limited...

Foremost I would like to thank my supervisor, Professor Arutiun P. Ehiasarian for giving me the opportunity to carry out this research. For his patience and understanding during discussion of the tough parts of the research; for allowing me working in my own way. His expertise, guidance, and kindness kept me going, until the end.

I am grateful also to Professor Papken E. Hovsepien for all the knowledge he has passed on to me and for the all advices.

I would like to thank the sponsoring company - Sandvik especially Dr. Mats Ahlgren, Dr. Carl-Fredrick Carlström, Dr. Johan Böhlmarm and the rest of team based in Stockholm, whereby this project could be realized.

The special thanks for support at so many levels to my co-workers, who become my friends Daniel and Tom. Thank you for being there for me, always. Without you guys, it would not be possible.

Acknowledgements to all co-workers in the National HIPIMS Institute: Yash, Arun, Barnali and Paranjayee for support, advices and especially for common lunches at 3rd floor and discussions over the meal.

I am also grateful to Gary Robinson for the technical support and assistance he has given me over the past few years. And mostly for each “no” that meant “yes”

I would like to acknowledge everyone from the MERI, both past and present, who have made the past few years a pleasant, enjoyable and fun experience. Corrie, Trinh, Chinh, Ronak, Sampan, Vincenzo, Steve, Itai, and to everyone else who has kept me company in the Tap, River Side, OQH and others after work.

My most sincere gratitude is extended to my fiancé, Marcin for supporting me from far away and while being next to me. For letting me go, knowing how hard the separation would be. BILY!

Finally, I would like to thank to my mother Alicja and my father Adam Andrzej, who have given me their utmost support to all that I have tried to do and encouraged me to be myself and to follow my dreams.

# 1 Introduction

## 1.1 Motivation

Constant development of metallurgical industries demands new solutions for faster and more precise production of elements. One of today's problems in metallurgy is creation of the Build Up Edge (BUE) during high-speed cutting (HSC). Creation of the BUE reduces longevity of cutting tools and finishing quality, resulting in an increase of production costs. BUE forms especially whilst machining soft and metallurgically aggressive alloys like Ti-, Al- and N-based alloys. Due to properties of these alloys such as toughness and lightness, they are often used in automotive and aerospace industries. In order to reduce the probability of BUE formation, cutting tools are coated. These coatings need to combine features such as:[2]

- High wear resistance (high hardness)
- Low affinity to machined surface
- Low friction
- Smooth and dense microstructure
- Good thermal conductivity
- High adhesion
- Good oxidation resistance

Recent research at Sheffield Hallam University considered use of coatings based on nanoscale multilayers technology consisting of Ti, Al, N, V and carbon. These coatings were aimed at applications of Ti-based alloys used in turning of acetabular cups and high strength Al - 7010 alloys used in aerospace applications [3, 4].

TiAlN coatings are well-known for their hardness and they are often used for cutting tool protection. The addition of vanadium and carbon enhances the wear resistance and attenuates the friction[5]. These coatings were deposited with the HIPIMS technology in a multilayer structure of TiAlCN/VCN. This research revealed a new process of segregation of carbon, whereby the structure can transform from multilayer to nanocomposite in the course of the deposition process as presented in fig. 1.1 [6].

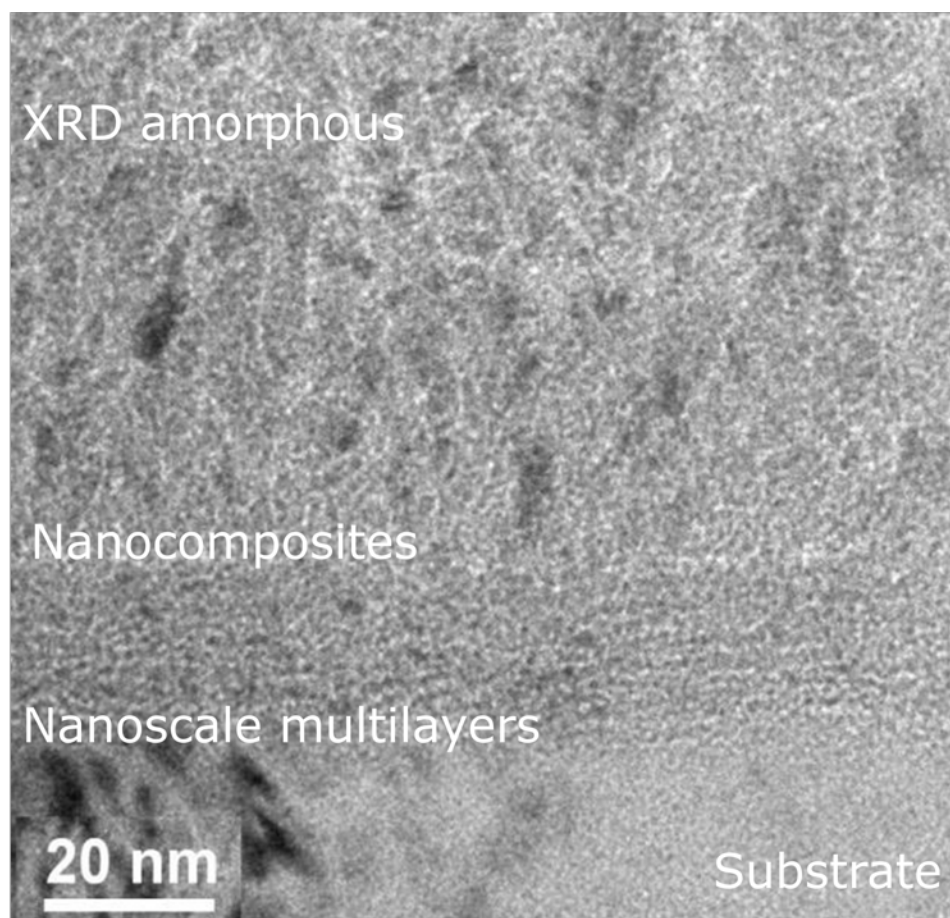


*Figure 1.1 BF TEM cross-section of TiAlCN/VCN nanoscale coating deposited by reactive HIPIMS deposition with highlighted various architecture regions [1]*

This can provide a graded coating with a high load bearing capacity and excellent adhesion at the base; the coating surface is chemically inert with low friction and low wear. However, obtained thickness of the multilayer structure was very low (about 20 nm). In order to achieve

good mechanical properties of the coating, the thickness of the individual regions must be controlled. The main subject of this thesis is to utilize the target poisoning effect and plasma emission monitoring system to control the architecture and properties of the TiAlCN/VCN coatings.

## 1.2 Aims

The aim of this research project is to improve TiAlCN/VCN coatings properties by optimizing the coating architecture and process. From the considerations given in the previous section, the objectives of the present work are as follows:

1. To exploit HIPIMS Technology to improve TiAlCN/VCN coating density, roughness and adhesion
2. To exploit the effect of nanoscale-multilayer and nanocomposite structures
3. To exploit synergy effect from the use of V and C
4. To understand the target poisoning in complex system with different target materials and two reactive gasses.
5. To exploit the target poisoning effect to control the coating properties
6. To better understand BUE formation on the TiAlCN/VCN coating
7. To develop HIPIMS based technology on a large scale.

This thesis is divided into 9 chapters. In chapter 2 a basic review of magnetron sputtering concepts, film properties and an overview of the V- C based coatings are provided for understanding the function of the system. An overview of the deposition unit design and deposition procedures is presented in Chapter 3. This is followed by the range of experimental techniques for characterisation of samples.

Chapter 4 describes the effect of the plasma sample pre-treatment on the material removal of the substrate and the metal ion implantation. An upgrade of the hardware is presented in chapter 5.

In chapter 6 the influence of reactive gases on concentrations of the most populated species in the discharge is determined; furthermore, a brief overview of the main dissociation mechanisms in a  $N_2$ -  $CH_4$  glow discharge is given. Following a hysterical behaviour of target electrical properties, total pressure in the chamber and plasma composition as function of nitrogen and methane flow and the discharge mode is investigated. Chapter 7 describes the effect of different poisoning level of the target on the deposited coatings. Coating microstructure, composition and mechanical properties are defined. Next, using results from chapter 7, in chapter 8 advanced coatings with graduate transformation of structure are deposited and characterized. Finally, in chapter 9 the lifetime of tools coated with coatings is tested, the wear mechanism is analysed and compared with the standard used coatings.

At the end of the thesis the conclusions drawn from our results are discussed.

## 2 Literature Review

### 2.1 Physical Vapour Deposition Basics

Physical vapour deposition (PVD) is one of the coating deposition methods used in surface engineering. PVD encompasses an extensive group of different deposition processes in which the deposited material is vaporised by physical processes from the source material. The deposition of vaporized material causes film growth on the substrate. In order to avoid impurities and increase source to substrate distance, PVD processes are usually performed in a vacuum or low-pressure environment. A source can consist of one or more elements; depending on desired composition of the thin film, there can also be a number of sources. Certain elements cannot be used as a source, and they are introduced into the system as a reactive gas (see section 2.2.2).

PVD processes can generally be divided into two main groups regarding vaporisation processes: evaporation and sputtering.

For evaporation, the source is heated to its melting point and particles from the source are removed by thermal energy. The advantage of this method is the possibility of obtaining a high deposition rate; however, this process is hard to control. It is also limited by the melting point of the materials used. In systems with different sources, it is impossible to use materials with very different melting points. Moreover, for materials with a high melting point, it is difficult to attain the melting temperature without harming the substrate.

In sputtering, the source is called a target and is eroded due to collisions with high energetic particles, otherwise known as ion bombardment. Due to ion bombardment, the removed material is highly energetic which leads to a dense microstructure of the coatings. However, with this method, the deposition rate is much lower than when using evaporation. Thereby evaporation, which is cheaper, is usually used for simple coatings;

sputtering is used for specialized coatings where the microstructure of coatings plays a key role in its properties. Fig.2.1 shows the family tree of PVD processes and the structure of sputtering processes. Blue highlighted fields will be described in following sections.

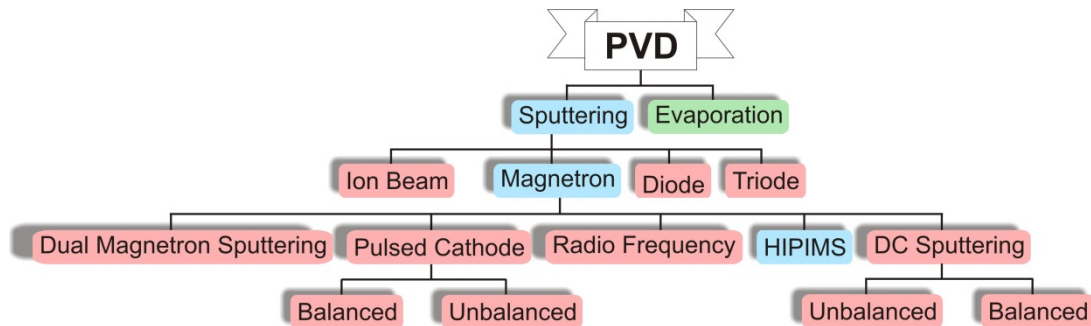


Figure 2.1: PVD family tree with expanded sputtering branch (after [2]).

### 2.1.1 Sputtering

Sputtering is related to the momentum transfer from ions to the surface atoms of the target due to elastic collisions. Commonly, ions are generated in the plasma discharge. The simplest way to ignite gas is to apply a potential between two electrodes placed in a vacuum. The ionization process initially requires electrons. The electric field accelerates the electron towards the anode, and gas ion towards the cathode (placed behind target). Accelerated particles will collide with other atoms and an avalanche process of ionization will commence. The ionization by accelerated electrons can be described as:

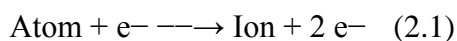
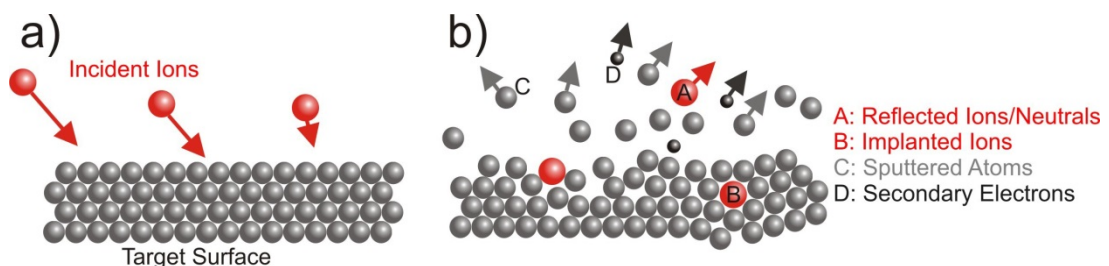


Fig.2.2 shows the schematic process of sputtering and its effect on the near surface area.



*Figure 2.2: Schematic presentation of the surface a) before ion bombardment and b) during ion bombardment.*

When ions hit the target surface, the kinetic energy is transferred to atoms in the surface. A binary collision is characterised by the energy transfer function ( $\epsilon$ )[7]:

$$\epsilon = \frac{4m_i m_t}{(m_i + m_t)^2} \quad (2.3)$$

where  $m_i$ , and  $m_t$  are the masses of the colliding ion and target atoms.

If the energy of incoming ions is sufficient, the atomic bonds are broken and atoms are ejected from the surface. Sometimes, to sputter, multi-collisions are necessary. However, lower energy ions also influence the surface; it causes lattice vibrations and displacement of lattice atoms, which leads to defects. Due to collisions, secondary electrons are also emitted. The ion after collision can be backscattered, or, if it has high energy, can be implanted into the solid. In order to eject atoms, the incident particle should be massive enough to transfer sufficient momentum to the target. For this purpose, a working gas is allowed into the vacuum chamber during sputtering and is ionized in order to create plasma. Typically, an inert gas such as argon is used as a working gas in order to prevent chemical reactions with the growing film.

One fundamental parameter for characterising sputtering is the sputtering yield  $S$ ; this is the number of atoms or molecules ejected from a target surface per incident ion. The Sputtering Rate quantifies the efficiency of sputtering. Equation 2.3 gives sputtering yield based on Sigmund's [7] early theory that assumes perpendicular ion incidence onto a polycrystalline monoatomic target.

$$Y(E) = 0,042\alpha\left(\frac{m_t}{m_i}\right)\frac{S_n(E)}{U} \quad (2.3)$$

where  $S_n(E)$  is the nuclear stopping power of the target,  $U$  is the binding energy of the target atoms,  $E$  is the incident atom energy and  $\alpha(m_t/m_i)$  is a correction function to account deviations from a single –event hard shape collisions behaviour[8].

### 2.1.2 Deposition with substrate bias

In order to enhance flux of charged particles, an electric field near the substrate is applied. Substrate is usually biased by either a negative DC (direct current) or RF (radio frequency). The plasma potential  $V_p$  remains unaffected because it tends to remain positive with respect to everything in the chamber. If the applied bias  $V_b$  is negative, a sheath of potential difference  $V_p - V_b$  is established in front of the substrate. Positive ions are accelerated across the sheath towards the substrate surface. By changing bias voltage, parameters such as the following can be controlled:

- Resistivity
- Hardness
- Residual stress
- Dielectric properties
- Etch rate
- Optical reflectivity
- Step coverage
- Film morphology
- Density
- Adhesion.

Typically, bias voltages of -50 to -3000 V are used [9].

### 2.1.3 DC Magnetron Sputtering

DC Magnetron sputtering (DCMS) is currently the most widely practiced commercial sputtering method. The main reason for its success is the high deposition rates achieved. These are typically an order of magnitude higher than the rates attained by conventional sputtering techniques [10]. DCMS utilizes the Lorentz force to confine the electrons in front of the target, not allowing electrons to reach the anode and recombine. For this purpose, permanent magnets are placed behind the cathode. The magnetic field lines first emanate normal to the target; they then bend with a component parallel to the target surface and finally return, completing the magnetic circuit as presented in fig 2.3.

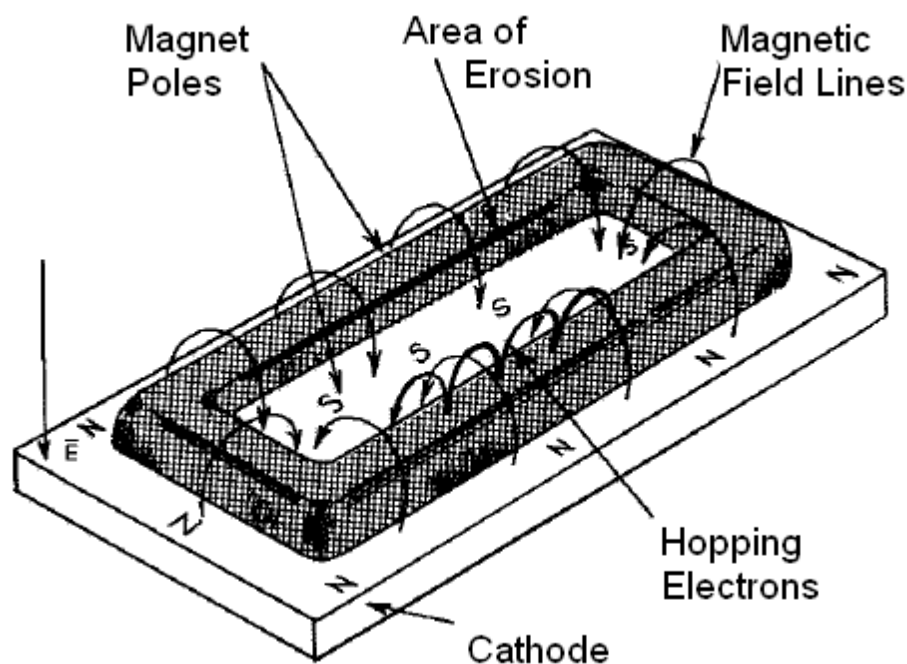


Figure 2.3 Applied fields and electron motion in a planar magnetron

Electrons emitted from the cathode are initially accelerated towards the anode. However, charged particles moving in a magnetic field are enforced by the Lorentz Force (eq. 2.5) to a cycloidal motion; they are bent in an orbit back to the target [11]. The radius of the helix

is called the Larmor radius and is given in equation 2.6. [12]. When electrons re-enter, the sheath they are reflected electrostatically from the target.

$$\vec{F} = q(\vec{E} + \vec{v} \times \vec{B}) \quad (2.5)$$

$$r_L = \frac{m_e V_{\perp}}{B} \quad (2.6)$$

Where  $\vec{E}$  is the electric field,  $\vec{B}$  is the magnetic field,  $q$  is the charge and  $v$  is the velocity.  $V_{\perp}$  is the magnitude of the particle's velocity in the plane perpendicular to the magnetic field,  $B$  is the magnetic field strength and  $m_e$  is the electron mass.

Both the magnetic and electric fields force the electrons to 'hop' near the target surface, enhancing the probability of ion collisions and the ionization efficiency. This results in increased bombardment of the target and a greater deposition rate.

However, since high plasma density is confined in the target vicinity, there is a sharp decrease in ion flux and ionization degree with increasing distance from the target. The large substrate-target distances result in low deposition rate and ionisation. An improvement was achieved by Windows and Savvides by introducing the unbalanced magnetron (UBM) concept in 1986 [13]. They described three magnetic configurations, as shown in fig.2.4, by changing the strength of magnetic field in one of the magnetrons.

Figure 2.4a) presents a conventional magnetron configuration where inner and outer poles have the same strength. Image 2.4b) shows a configuration where the inner pole is stronger than the outer. This configuration is called Type I. Type II, with stronger outer poles, is presented in figure (2.4c)). Commercially, in PVD coatings technology, type II is mainly used as it enhances ion bombardment of the substrate.

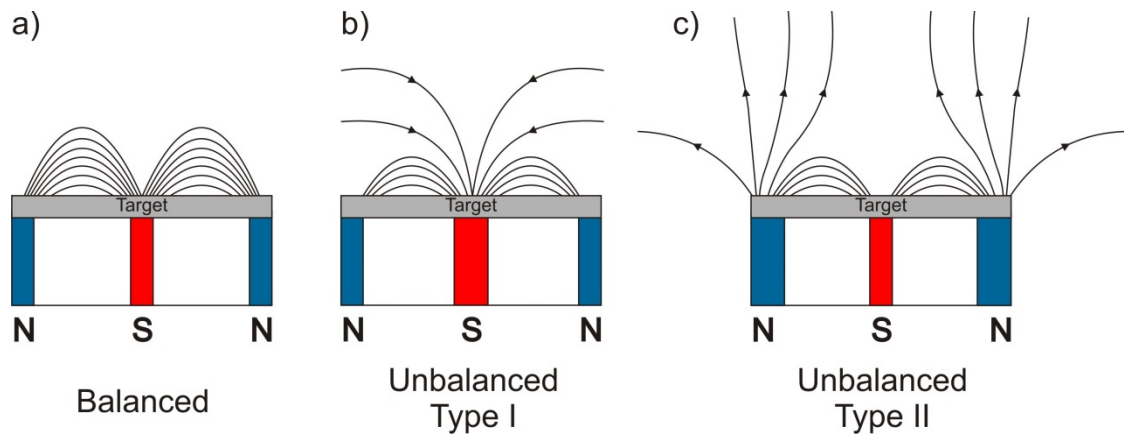


Figure 2.4: Different magnetron configurations a) balanced magnetron, b) unbalance magnetron with stronger inner pole and c) unbalance magnetron with stronger outer pole [14].

Strengthening the outer poles leads to the outer magnetic field lines merging deeper into the space of the chamber, towards the substrate. The plasma is therefore no longer bound in the target vicinity and expands outwards, resulting in increased ion bombardment of the substrate.

This results in an increased expulsion distance of sputtered species, providing a high ion flux at large target-substrate distances. This leads to an increase of the substrate bias current density by approximately two orders of magnitude, compared to conventional magnetron sputtering. The ion to neutral ratio in DCMS is higher when compared to conventional sputtering. By changing magnetic field or unbalancing, the ion energy and ion flux can be controlled almost independently from each other [15].

Additional improvement of plasma confinement is achieved by the Close Field

Unbalanced Magnetron Sputtering (CFUBMS) configuration; in this set-up, two or four magnets of opposite polarity are installed opposed to each other, constituting a closed magnetic field trap between the magnets (fig. 2.5). This implies that few electrons are lost to the chamber walls and dense plasma is maintained in the substrate region, therefore leading to high levels of ion bombardment of the growing film [16].

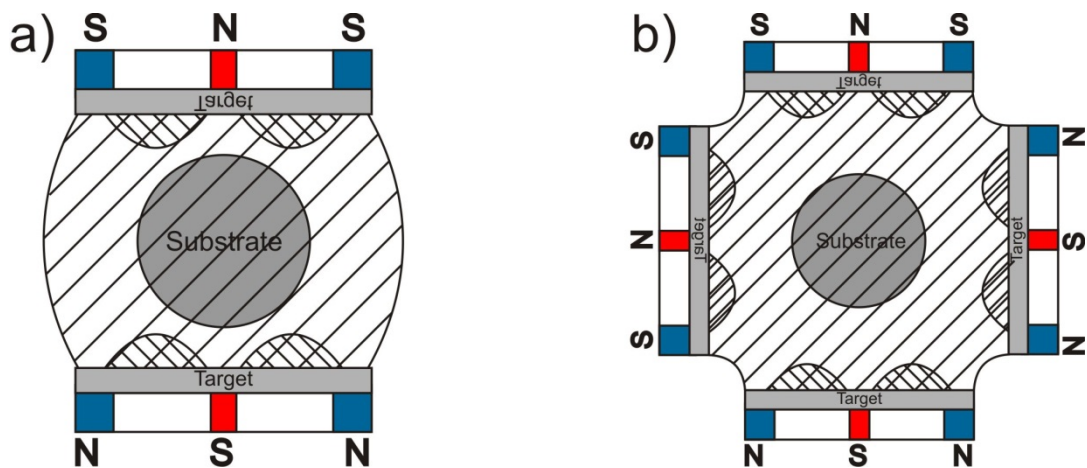


Figure 2.5: Multi - cathode systems with two and four cathodes [16].

This arrangement reduces electron losses due to recombination with the chamber walls; dense plasma is maintained in the substrate region, leading to high levels of ion bombardment of the growing film. Multi cathode systems enable the use of different target materials during one process. This allows deposition of coating with more advanced composition (e.g. TiAlN coating) as well as production of multilayers (e.g. TiN/AlN coating). Multilayers are described in detail in section 2.5.

The DCMS discharges are usually operated at the current density of the order of 10 - 100  $\text{mAcm}^{-2}$  and power densities  $\leq 15 \text{ Wcm}^{-2}$ . This results in typical electron density of  $10^{14}$ - $10^{15} \text{ m}^{-3}$  at pressures about 1Pa [12]. In plasma, mostly the working gas (Ar) atoms are ionized, resulting in ion flux of about 0.1 - 1.0  $\text{mAcm}^{-2}$  towards the substrate. Further increase of discharge current leads to overheating of the magnets; this can result in melting of the target, as well as arcing. DCMS power densities are therefore limited. Densities of above mentioned parameters represent (technical) limits which are hard to exceed in DCMS [17]

Moreover, the trapped electrons are restricted to follow the magnetic lines. This means that only about 30% of the target is utilized [18].

## 2.1.4 High Power Impulse Magnetron Sputtering

A higher electron density can be achieved by pulsing with a low duty-cycle current applied to the cathodes. The peak power can therefore be increased considerably, whilst the average power can be kept at the same level as in DCMS [19 – 21]. High Power Impulse Magnetron Sputtering (HIPIMS) was first reported by Khodachenko and Mozgrin in Moscow and later described in a seminal paper by Kouznetsov et.al. in 1999 [22]. They reported that HIPIMS produces a highly ionized flux of the target material, along with higher electron densities than standard DC magnetron sputtering. The HIPIMS discharges are operated in pulse from 50-500  $\mu\text{s}$  regime, with low repetition frequency from 1 to 100 Hz and the duty cycle  $\leq 1\%$  [23 – 25]. The pulse power density in HIPIMS is typically two orders of magnitude greater than the average power density [26]; the peak power can reach up to 16 MW [27]. This leads to a significant increase in the ion density, very high plasma densities up to nearly  $10^{18} \text{ m}^{-3}$  and a degree of ionization of 30–70% [28]. Highly ionized flux produces denser coatings and improved properties of the coating. HIPIMS is a proven technology in the deposition of CrN [25] and TiN [29] hard thin films, applications include tribological protection of automotive engines and turning. Figure 2.6 shows a comparison of schematic diagrams of DC magnetron sputtering and HIPIMS.

Coatings deposited with this technology show excellent adhesion strength, dense microstructure and good mechanical properties [30 – 32].

Moreover, with HIPIMS, the adhesion of coatings can be improved by implanting highly ionized metal ions in the surface of the substrate [33, 34].

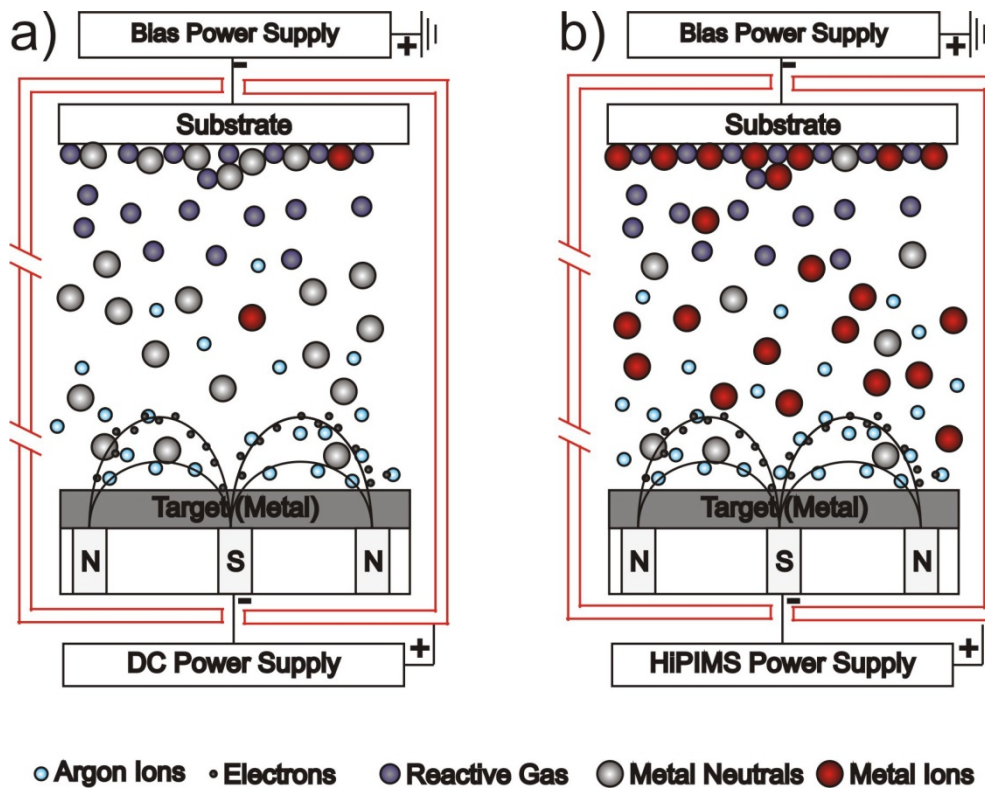


Figure 2.6: Schematic diagram of: a) Magnetron DC sputtering and b) HIPIMS. During HIPIMS deposition the plasma is high ionised. This leads to dense coating structure.

## 2.2 Reactive Sputtering

Reactive sputtering is the sputtering of elemental targets in the presence of chemically reactive gases. It has become a very popular technique for the deposition of a wide range of compounds and alloy thin films including oxides, nitrides, carbides, fluorides or arsenides [35, 36]. The deposited thin film composition is a compound formed from both target material and reactive gases.

Gases are used due to the fact that not all materials can easily be used as a target. The bombardment of a non-conducting target with positive ions would lead to a charging of the surface; this would subsequently cause electrical breakdown [37].

### 2.2.1 Target Poisoning

Target poisoning applies to every reactive process to a lesser or greater extent. When reactive gas flow ( $f_R$ ) is relatively high, the molecules of gas deposit on the target surface and produce a non-conductive layer. This might lead to arcing. Moreover, this layer reduces the sputtering rate of target material; this is due to the fact that now both the target material and reactive gas species are sputtered. Reduced sputter rate results in higher partial pressure of the reactive gas at the same  $f_R$ . This leads to hysteresis behaviour of the sputtering process, therefore, it is hard to control compounds of the deposited thin film.

There are two main approaches explaining hysteresis behaviour of reactive sputtering. In the well-known Berg model [36, 38 – 40], the reactive gas balance is determined by the inlet and outlet flows and by the gas consumption; this is due to layer deposition at the chamber walls, the substrate and the sputtering target. It describes three different target poisoning stages which are dependent on the deposition rate and partial pressure of the gas. Figure 2.7 presents hysteresis behaviours of a) reactive partial pressure and b) sputtering rate during the increase and decrease of reactive gas flow. There are three modes of reactive sputtering: (a) metallic, (b) transition and (c) reactive [41]. In metallic mode, the plasma is dominated by metal ions and neutrals. In reactive mode, the plasma is dominated by reactive gas particles. The transition mode is between these two stages.

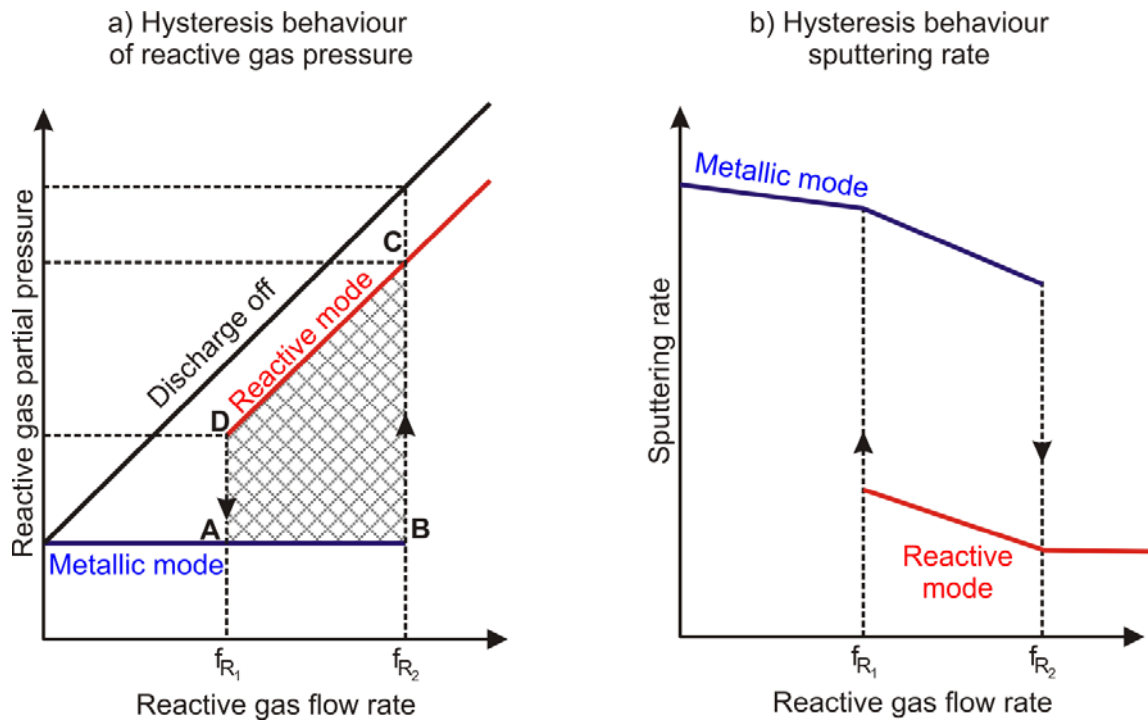


Figure 2.7: The hysteresis behaviour of reactive magnetron sputtering [35].

The metallic mode is characterized by a high deposition rate and, thereby a high consumption of reactive gas. This means that all the reactive gas is gettered by the sputter metal. In this mode, no change in  $P_R$  is observed. When  $f_R$  reaches critical value B, the reactive gas flow exceeds the rate of sputtered metal flux and reactive gas will start to cover the chamber walls and the metal target. At this point, a metal-gas compound will start to grow. At  $f_{R2}$ , the system transfers from metal mode to reactive mode (from point B to point C), as described above. When reactive gas flow is decreasing, the  $f_R$  reduces linearly below point C and the system remains in reactive mode. This is because the target is still poisoned and reactive gas consumption is low. Thereby,  $P_R$  remains high when compared to the metallic mode during increase of the gas flow. When reactive gas flow decreases to  $f_{R1}$  at point D, the  $P_R$  is low enough that the compound layer at the target becomes removed through sputtering, and the system comes back to metallic mode.

The area between reactive gas flows  $f_{R1}$  and  $f_{R2}$  is highly unstable which makes deposition of defined layers impossible. However, it is necessary to work within this area in order to produce coatings with stoichiometric chemistry whilst also maintaining high deposition rates. Therefore, several attempts have been made to stabilize processes within this area [36, 42].

This model considers only the adsorbed layer; however, both Depla [43] and Kubart's [44] models also include implantation of the reactive gas ion into the target material and recoil implantation of adsorbed reactive gas atoms.

Deposition of the compound material on the cathode, as well as implantation of gas atoms into the target surface, leads to a change in properties of the target; the deposition will now depend on reactive gas partial pressure in the vacuum chamber. Additionally, as the reactive gas is added, the composition of the plasma will change. These changes will alter the discharge voltage.

As both plasma and target properties change at the same time, it is difficult to distinguish their influence on discharge energy. Depla et al. [45] shows that three main factors influence discharge voltage behaviour: the gas composition, gas pressure and the target condition. These can be explained by the following equation:

$$V_{\text{discharge}} = W_0 / (\gamma_{\text{ISEE}} \epsilon_e \epsilon_i E_m) \quad [46]$$

with  $W_0$  the effective ionization energy (in eV),  $\epsilon_i$  the ion collection efficiency,  $\epsilon_e$  the fraction of the theoretical amount of ions that the electron effectively generates before it is lost from the discharge,  $\gamma_{\text{ISEE}}$  the ion induced electron emission (ISEE) coefficient, while it gives the number of electrons emitted per incoming ion on the target,  $E$  ionization probability and  $m$  the multiplication factor.

The  $\epsilon_e$  and  $\epsilon_i$  can be considered close to unity because most ionisation takes place close to the target surface, with the vast majority of the ions reaching the cathode [45].  $W_0$  depends

on the gas composition of the discharge and will change with addition of different gases, hence the discharge voltage will change for different gases.  $E$  depends on the magnetic field, pressure and the discharge power. Since both magnetic field and discharge power are unchanged, the  $E$  depends mainly on pressure. The  $\gamma_{\text{ISEE}}$  depends strongly on the target condition.

As the target becomes covered with a compound, the amount of secondary electrons, emitted by ion bombardment of the target surface, changes. This, in turn, changes the ratio between ion and electron current [36, 47]. The  $\gamma_{\text{ISEE}}$  depends on both the target voltage  $U$  and the degree of target poisoning. Pflug et al. [48] suggested the expression (2.1).

$$\gamma_{\text{ISEE}} = (\gamma_m (1 - \theta_t) + \gamma_c \theta_t) \frac{U}{U_0} \quad (2.1)$$

Where  $\gamma_m$  and  $\gamma_c$  are the secondary electron emission coefficients at the metal and compound areas, respectively, at the target surface and  $U_0$  is a reference voltage required for keeping the equation dimensionless. It should be noticed that  $\gamma_m$  can be either smaller or larger than  $\gamma_c$ , consequently, the voltage may either increase or decrease for a large supply of reactive gas. Voltage behaviour depends on target material and the choice of reactive gas [36].

Depla et. al reviewed the influence of both oxygen and nitrogen on secondary electron emission yield (SEY) and discharge voltage [49]. They found that generally, the SEY of nitrides could be directly related to the material's electrical properties. For conducting materials (some oxides and nitrides of metals e.g. TiN), the SEY will reduce when compared to originating metal, increasing discharge voltage. For the materials with a wide

band gap (oxides of Al, Ce, Mg, Li, Pb and Y and the nitrides of Al, Mg, Ce and Y), the SEFY will increase, decreasing discharge voltage.

The poisoning effect of oxides and nitrides has been widely investigated. However, few studies have examined the hysteresis behaviour of hydrocarbons. Electron impact with methane leads to creation of different radicals from the methane and acetylene families [50]. As a result of this, there will be different poisoning mechanisms during one process. Fouad et al. have investigated the effect of target poisoning on the titanium target in Ar/CH<sub>4</sub> gas mixture on cathode current and coating properties [51]. They have observed changes in the cathode current at 1.5% methane concentration and up to 10%; this indicates a transition from metallic to poison sputtering mode. Investigations of plasma content, when using C<sub>2</sub>H<sub>2</sub> as reactive gas, show promoted dissociation of the reactive species and the types of dissociation products created [52, 53]. The plasma density and plasma species present will have an influence on properties of the resulting films.

Recently, there is a focus on the effect of discharge mode on hysteresis behaviour. Research reports that during HIPIMS discharge, hysteresis effect is lower or is not present [54–56]. However, there are some contradicting results neglecting the effect of HIPIMS [57].

### **2.2.2 Target poisoning using two reactive gases**

The hysteresis behaviour of reactive sputtering using one reactive gas is well-established. However, due to an interest in reactive sputtering using one target material and two reactive gasses, there is a need for further understanding of the poisoning processes using multiple reactive gases [58–61].

Sputtering using two reactive gases is more complex and presents unique challenges [60]. Both reactive gases affect the plasma conditions in different ways. Moreover, gases will

not only react with the sputter metal, but also with each other therefore producing different radicals.

Thompson et al. [62] have investigated the dissociation mechanism of  $\text{CH}_4$  in a  $\text{N}_2\text{-xCH}_4$  glow discharge, and interaction between dissociation products. They developed a kinetic model to describe a low-pressure glow-discharge in  $\text{N}_2\text{-CH}_4$  for the most populated neutral and ionic species present in the discharge. Plasma consists of the vibrational levels and the electronically excited states of  $\text{N}_2$ . The N (4S) atoms and the neutral methane species are produced from either dissociation of  $\text{CH}_4$  ( $\text{CH}_3$ ,  $\text{CH}_2$ ,  $\text{H}_2$ , H), or in reactions with  $\text{N}_2$  (HCN,  $\text{H}_2\text{CN}$ , CN, NH). The dominant ionic species ( $\text{N}^{2+}$ ,  $\text{N}^{4+}$ ,  $\text{CH}^{3+}$ ,  $\text{CH}^{4+}$ ,  $\text{CH}^{5+}$ ), along with others, which were included in the model for mathematical convenience only ( $\text{C}_2\text{H}_4$ ,  $\text{C}_2\text{H}_5$ ,  $\text{C}_2\text{H}_6$ ); this was to ensure that the complete system of master equations had a non-zero steady-state solution. The reaction and kinetics of the radicals can be found in table 2.1. In section 6 the effect of using one or two reactive gases in a multiple target system is shown.

Table 2.1 Kinetics of the radicals created from  $CH_4$  dissociation and ionization as well as of the species created in reactions with active nitrogen[62].

$e + CH_4 \longrightarrow e + CH_3 + H$	$f(E/N)$
$e + CH_4 \longrightarrow e + CH_2 + H + H$	$f(E/N)$
$e + CH_4 \longrightarrow e + CH_4^+ + e$	$f(E/N)$
$e + CH_4 \longrightarrow e + CH_3^+ + H + e$	$f(E/N)$
$e + H_2 \longrightarrow e + H + H$	$f(E/N)$
$N_2(X, v) + H_2 \rightleftharpoons N_2(X, v - 1) + H_2$	see text
$N_2(X, v) + H \rightleftharpoons N_2(X, v - 1) + H$	see text
$N_2(A) + CH_4 \longrightarrow N_2(X, v = 0) + CH_4$	$k = 3.2 \times 10^{-15} \text{ cm}^3 \text{ s}^{-1}$
$N_2(B) + CH_4 \longrightarrow N_2(A) + CH_4$	$k = 0.95 \times 3 \times 10^{-10} \text{ cm}^3 \text{ s}^{-1}$
$N_2(B) + CH_4 \longrightarrow N_2(X, v = 0) + CH_4$	$k = 0.05 \times 3 \times 10^{-10} \text{ cm}^3 \text{ s}^{-1}$
$N_2(a') + CH_4 \longrightarrow N_2(X, v = 0) + CH_4$	$k = 3 \times 10^{-10} \text{ cm}^3 \text{ s}^{-1}$
$N_2(a) + CH_4 \longrightarrow N_2(X, v = 0) + CH_4$	$k = 5.2 \times 10^{-10} \text{ cm}^3 \text{ s}^{-1}$
$N_2(A) + H_2 \longrightarrow N_2(X, v = 0) + H + H$	$k = 2.4 \times 10^{-15} \text{ cm}^3 \text{ s}^{-1}$
$N_2(A) + H \longrightarrow N_2(X, v = 0) + H$	$k = 2.1 \times 10^{-10} \text{ cm}^3 \text{ s}^{-1}$
$N_2(B) + H_2 \longrightarrow N_2(A) + H_2$	$k = 2.4 \times 10^{-11} \text{ cm}^3 \text{ s}^{-1}$
$N_2(a') + H_2 \longrightarrow N_2(X, v = 0) + H + H$	$k = 2.6 \times 10^{-11} \text{ cm}^3 \text{ s}^{-1}$
$N_2(a') + H \longrightarrow N_2(X, v = 0) + H$	$k = 2.1 \times 10^{-10} \text{ cm}^3 \text{ s}^{-1}$
$N + CH_3 \longrightarrow HCN + H_2$	$k = 1.4 \times 10^{-11} \text{ cm}^3 \text{ s}^{-1}$
$N + CH_3 \longrightarrow H_2CN + H$	$k = 6.2 \times 10^{-11} + 2.2 \times 10^{-9} \exp(-1250/T_g(K)) \text{ cm}^3 \text{ s}^{-1}$
$N + CH_2 \longrightarrow HCN + H$	$k = 5 \times 10^{-11} \exp(-250/T_g(K)) \text{ cm}^3 \text{ s}^{-1}$
$N + CH_2 \longrightarrow CN + H_2$	$k = 1.6 \times 10^{-11} \text{ cm}^3 \text{ s}^{-1}$
$N + CH_2 \longrightarrow CN + H + H$	$k = 1.6 \times 10^{-11} \text{ cm}^3 \text{ s}^{-1}$
$N + H_2CN \longrightarrow HCN + NH$	$k = 6.7 \times 10^{-11} \text{ cm}^3 \text{ s}^{-1}$
$N + NH \longrightarrow N_2(X, v = 0) + H$	$k = 8.6 \times 10^{-12} \times T_g^{0.5} \text{ cm}^3 \text{ s}^{-1}$
$CH_2 + CH_4 \longrightarrow CH_3 + CH_3$	$k = 2.14 \times 10^{-11} \times T_g^{0.5} \text{ cm}^3 \text{ s}^{-1}$
$CH_4^+ + CH_4 \longrightarrow CH_3 + CH_5^+$	$k = 1.5 \times 10^{-9} \text{ cm}^3 \text{ s}^{-1}$
$C_2H_5 + H \longrightarrow CH_3 + CH_3$	$k = 7.95 \times 10^{-11} \times \exp(-127/T_g(K)) \text{ cm}^3 \text{ s}^{-1}$
$CH_3 + H + N_2 \longrightarrow CH_4 + N_2$	$k = 6 \times 10^{-29} (T_g(K)/300)^{-1.8} \text{ cm}^6 \text{ s}^{-1}$
$CH_3 + CH_3 \longrightarrow C_2H_6$	$k = 4 \times 10^{-10} \times T_g^{-0.4} \text{ cm}^3 \text{ s}^{-1}$
$CH_3 + CH_3 \longrightarrow C_2H_5 + H$	$k = 1.3 \times 10^{-9} \exp(-13\,275/T_g(K)) \text{ cm}^3 \text{ s}^{-1}$
$CH_3 + CH_2 \longrightarrow C_2H_4 + H$	$k = 7 \times 10^{-11} \text{ cm}^3 \text{ s}^{-1}$
$CH_2 + CH_2 \longrightarrow C_2H_4$	$k = 1.7 \times 10^{-12} \text{ cm}^3 \text{ s}^{-1}$
$C_2H_5 + H \longrightarrow C_2H_6$	$k = 6 \times 10^{-11} \text{ cm}^3 \text{ s}^{-1}$
$C_2H_6 + CH_3 \longrightarrow C_2H_5 + CH_4$	$k = 2.5 \times 10^{-31} \times T_g^6 \exp(-3730/T_g(K)) \text{ cm}^3 \text{ s}^{-1}$
$C_2H_4 + H + (M) \longrightarrow C_2H_5 + (M)$	$k_0 = 2.15 \times 10^{-29} \exp(-349/T_g(K)) \text{ cm}^6 \text{ s}^{-1}$ $k_\infty = 4.39 \times 10^{-11} \exp(-1087/T_g(K)) \text{ cm}^3 \text{ s}^{-1}$
$CN + CH_4 \longrightarrow HCN + CH_3$	$k = 10^{-11} \exp(-857/T_g(K)) \text{ cm}^3 \text{ s}^{-1}$
$HCN + H + (M) \longrightarrow H_2CN + (M)$	$k_0 = 6.4 \times 10^{-25} \times T_g^{0.5} \text{ cm}^6 \text{ s}^{-1}$ $k_\infty = 9.2 \times 10^{-12} \exp(-1200/T_g(K)) \text{ cm}^3 \text{ s}^{-1}$
$C_2H_5 + CH_3 \longrightarrow C_2H_4 + CH_4$	$k = 3.3 \times 10^{-11} \times T_g^{0.5} \text{ cm}^3 \text{ s}^{-1}$
$C_2H_5 + C_2H_5 \longrightarrow C_2H_6 + C_2H_4$	$k = 1.2 \times 10^{-11} \exp(-540/T_g(K)) \text{ cm}^3 \text{ s}^{-1}$
$CN + C_2H_6 \longrightarrow HCN + C_2H_5$	$k = 1.8 \times 10^{-11} \times T_g^{0.5} \text{ cm}^3 \text{ s}^{-1}$
$C_2H_6 + H \longrightarrow C_2H_5 + H_2$	$k = 2.4 \times 10^{-15} \times T_g^{1.5} \exp(-3730/T_g(K)) \text{ cm}^3 \text{ s}^{-1}$
$CH_4 + H \longrightarrow H_2 + CH_3$	$k = 2.2 \times 10^{-20} \times T_g^3 \exp(-4045/T_g(K)) \text{ cm}^3 \text{ s}^{-1}$
$CH_4 + CH_3 \longrightarrow C_2H_5 + H_2$	$k = 1.7 \times 10^{-11} \exp(-11\,500/T_g(K)) \text{ cm}^3 \text{ s}^{-1}$
$H + H + N_2 \longrightarrow H_2 + N_2$	$k = 1.5 \times 10^{-29} \times T_g^{-1.3} \text{ cm}^6 \text{ s}^{-1}$
$NH + H \longrightarrow N + H_2$	$k = 1.7 \times 10^{-12} \times T_g^{0.68} \exp(-950/T_g(K)) \text{ cm}^3 \text{ s}^{-1}$
$NH + NH + (M) \longrightarrow H_2 + N_2(X, v = 0) + (M)$	$k = 10^{-33} \text{ cm}^6 \text{ s}^{-1}$
$H_2CN + H \longrightarrow HCN + H_2$	$k = 2.9 \times 10^{-11} \times T_g^{0.5} \text{ cm}^3 \text{ s}^{-1}$
$CH_2 + H_2 \longrightarrow CH_3 + H$	$k = 3.34 \times 10^{-11} \times T_g^{0.5} \text{ cm}^3 \text{ s}^{-1}$
$N_2^+ + CH_4 \longrightarrow N_2 + CH_3^+ + H$	$k = 1.3 \times 10^{-9} \text{ cm}^3 \text{ s}^{-1}$
<b>Ambipolar diffusion of electrons and <math>N_2^+</math>, <math>N_4^+</math>, <math>CH_3^+</math>, <math>CH_4^+</math> and <math>CH_5^+</math> ions</b>	
$H + \text{wall} \longrightarrow \frac{1}{2}H_2$	$\gamma_H = 5 \times 10^{-3}$
$CH_3 + \text{wall} \longrightarrow CH_4 - \eta H - \frac{1}{2}(1 - \eta)H_2$	$\gamma_{CH_3} = 0.003$
$CH_2 + \text{wall} \longrightarrow CH_4 - 2\eta H - (1 - \eta)H_2$	$\gamma_{CH_2} = 0.026$
$HCN + \text{wall} \longrightarrow CH_4 + \frac{1}{2}N_2(X, v = 0) - 3\eta H - \frac{3}{2}(1 - \eta)H_2$	$\nu_{dep.}$
$H_2CN + \text{wall} \longrightarrow CH_4 + \frac{1}{2}N_2(X, v = 0) - 2\eta H - (1 - \eta)H_2$	$\nu_{dep.}$

<sup>a</sup> Three-body reactions:  $k = k_0 k_\infty M / (k_0 + k_\infty M)$ .

<sup>b</sup>  $\eta = ([H]/2)/([H]/2 + [H_2])$  is the fractional concentration of dissociated  $H_2$  in the discharge (see text).

<sup>c</sup>  $\nu_{dep.}$  is given in the text.

### 2.2.3 Reactive Sputtering Control Systems

The coating quality and film stoichiometry are sensitive to reactive gas partial pressure. Control of process parameters is key to producing good quality coatings with reasonable deposition rates. There are a range of ways to control systems, all of which have both advantages and disadvantages:

**Flow control** of the reactive gas is the simplest method. However, reactive sputtering is typically done in the transition or poisoned mode of the target; in this mode, the deposition rate is low compared to the rate from the elemental target. In addition, the film properties produced by flow control reactive sputtering are less than optimal [42].

**Increased pumping speed** reduces the hysteresis effect [63]. At very high pumping speeds, the hysteresis disappears and there is a linear relationship between the reactive gas flow and the partial pressure. However, this technique comes at a high expense. The cost of the extra pumps to achieve this effect is high, as is the cost of operating the pumps. This is particularly problematic in very large deposition systems. For these reasons, the high pumping speed approach is not used very often. In order to achieve a linear relationship, absurdly high pumping speeds are required [42].

**Cathode voltage** changes when the poisoning occurs and the compound is created at the target. Thus, it can be used as a feedback signal for controlling the reactive sputtering processes [64]. However, the relationship between cathode voltage and reactive gas flow is not always linear; therefore, for some materials and gases, it cannot be used. Moreover, when the target is covered with a thick insulating layer, the arcs lead to an unstable signal which becomes difficult to control.

**Partial pressure control** of the reactive gas, similarly to cathode voltage control, requires active feedback control [42]. There are different kinds of signal used as a feedback:

- Optical emission spectrometer (OES) signal of the sputtered material or the reactive gas [65];
- Mass spectrometer signal [66];

Partial pressure control of the reactive gas allows operation of the process in all stages of the poisoning. By operating in this region, higher deposition rates can be achieved compared to flow control resulting, in improved film properties.

In this work we are using a plasma emission monitoring – PEM in order to control partial pressure as a function of OES. The PEM system is described in detail in section 3.2.

## 2.3 Solid Lubricants

Solid lubricants are well-known and widely described in literature (e.g. [67]). They are primarily used to reduce friction and wear where conventional materials and lubricants cannot be used:

- When liquid lubricants interact with reactive materials (e.g. corrosion)
- When the environment can influence liquid lubricants (e.g. rain, snow)
- In dusty environments where particles diffuse into liquid lubricant and increase friction coefficient
- When pressure between two working materials is very high so that liquid lubricants are pushed out.

There are numerous types of solid lubricant, typically including soft metals (silver), lamellar compounds (graphite) or special oxides called Magnéli phases ( $V_nO_{n-1}$ ). These materials reduce friction and wear by interposing a thin adherent layer of material between sliding surfaces that shears easily; this prevents direct contact between the substrate materials. In this work, two types of solid lubricant were used for coating production and are described below.

### 2.3.1 Carbon based coatings

Carbon based coatings are often produced due to their excellent properties, such as high hardness, low friction coefficients and wear resistance [68]. However, pure carbon coatings suffer from poor toughness and brittleness due to high compressive residual stress [69]. Doping the carbon coatings with a small amount of a ductile metal can improve the properties of the coating. Coating properties can be also improved by multilayering of coatings; this allows the selection and combination of materials according to the desired properties [69, 70]. Physical and electrochemical properties of carbon-based materials depend on the bonding configuration of carbon atoms with other atoms. There are three configurations in which carbon can be bound [71]:

- $sp$  where, the carbon atom forms linear strings
- $sp^2$  where, the carbon forms a two-dimensional layer structure
- $sp^3$  where, the carbon forms a three-dimensional tetrahedral lattice

These three configurations refer to the atomic structure of carbon. Each carbon atom has six electrons of which two are strongly bound with the atomic nucleus, and four poorly bound valence electrons. The first two occupy orbital 1s, while four others occupy orbitals 2s and 2p. In the carbon atom, the energy difference between the upper level 2p and lower level of 2s is small compared with the energies of chemical bonds. The wave functions of these four electrons can easily mix with each other. In this way, the filling of orbitals 2s and 2p ( $2p_x$ ,  $2p_y$ ,  $2p_z$ ) can change. The binding energy of the atom with neighbouring atoms is therefore increased. This mixing of orbitals is responsible for different configurations of carbon atom binding. Figure 2.8 shows an orbital filling diagram of carbon and the possible hybridizations.

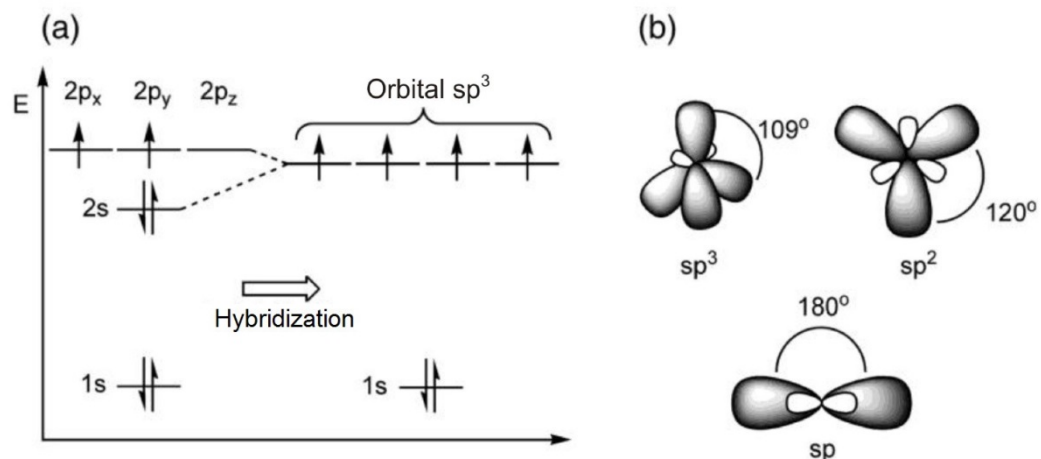


Figure 2.8: (a) Diagram of atomic orbitals of carbon and  $sp^3$  hybridization, (b) hybridized orbitals of carbon atom [72].

Carbon exists in various material forms called polymorphs or allotropes. The most commonly known allotropes of carbon are graphite and diamond. Graphite carbon is black-and-grey in colour and metallic glossy with a very low hardness, while diamond forms colourless, transparent crystals with a high gloss with hardness of 56-102 GPa [73, 74]. Such vastly different properties stem from the different crystal structures.

A perfect graphite crystal structure (see Figure 2.9) consists of layers (graphene) in which the carbon atoms are arranged in a two-dimensional honeycomb lattice, propagating along the xy plane.

These layers are connected by the Van der Waals forces in the z-direction (vertical direction). In each graphene layer, carbon atoms are located at the corners of hexagons which are connected together in a lattice. Each atom has three bindings that run along the edges of hexagons ( $sp^2$  hybridization). The remaining electrons contained in  $p_z$  orbitals produce delocalized electron cloud throughout the entire layer of graphene. The distance between neighbouring atoms in one layer connected by the covalent bonds is 141.5 pm. In

contrast, the distance between atoms in different layers, connected along the Z axis with the Van der Waals forces, is 335.4 pm [75]. As the layers are bound by weak interactions, they can easily be shifted or detached causing deformation of the lattice [72, 76]. This layered-lattice (lamellar) structure [68] allows for easy shearing between contacting surfaces and reduces friction coefficient [77].

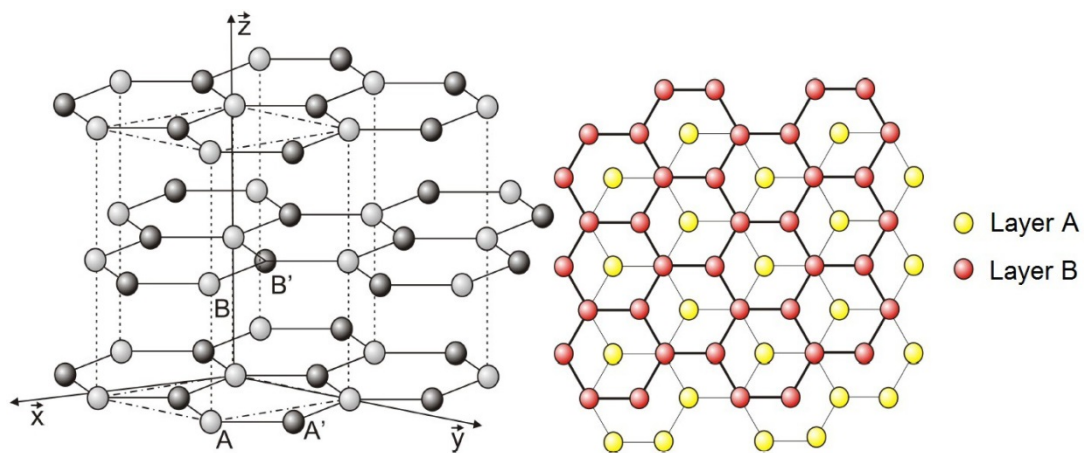


Figure 2.9: The crystal structure of graphite [72].

In diamond, each carbon atom is bound with four other atoms arranged at the corners of a regular tetrahedron with covalent bonds. All carbon atoms are in  $sp^3$  hybridization and the bond length is 154.45 pm [75]. There are two varieties of diamond structure, cubic and hexagonal, of which the first is most commonly found. The crystal lattice of cubic diamond is face-centred with constant  $a = 356.68$  pm (fig.2.10). The unit cell consists of eight atoms [72].

The structure of the diamond is regular, built from an identical network and offset from each other by one quarter of the main diagonal. During heating to temperatures greater than  $3770^\circ\text{C}$ , and a pressure of 1840 psi, the diamond transforms into graphite. Figure 2.11 shows the phase diagram of carbon.

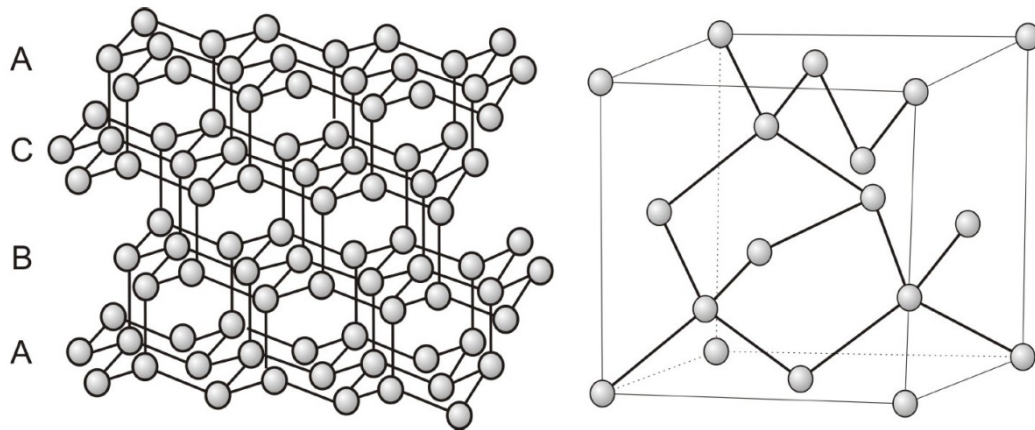


Figure 2.10: The crystal structure of diamond [72].

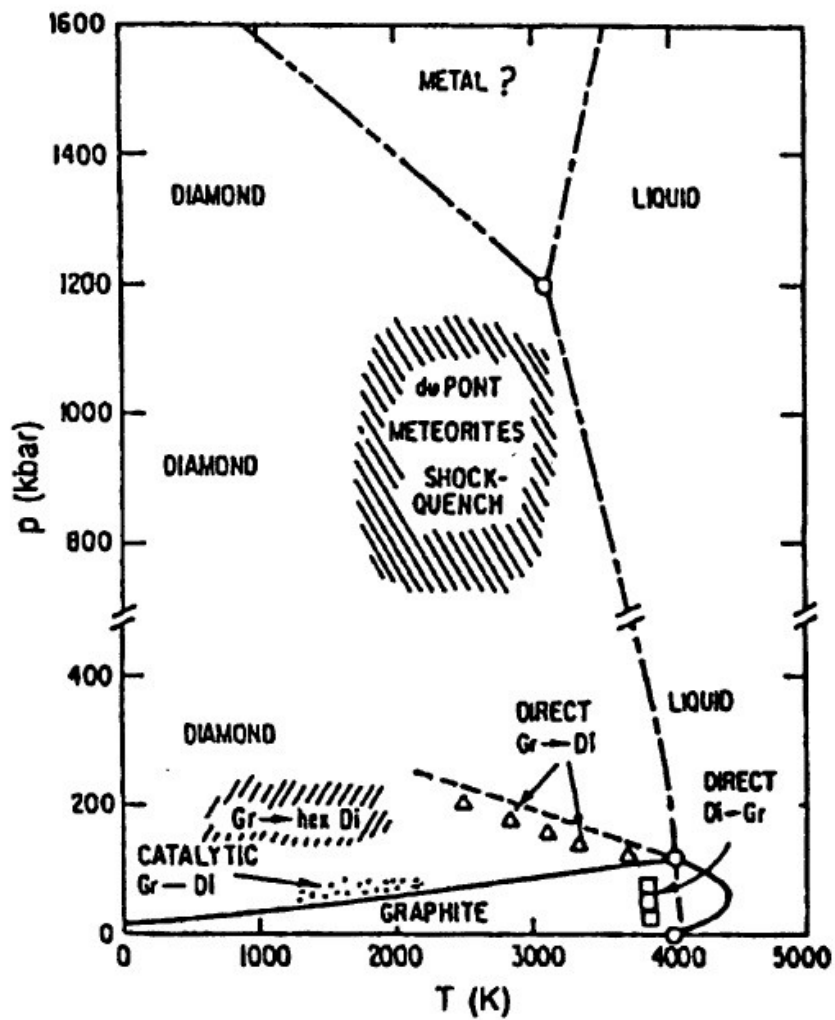


Figure 2.11: Carbon phase diagram [73].

### 2.3.2 Vanadium Magnéli phases

Some oxides of certain metals and metalloids are used as solid lubricants due to their ability to form oxygen deficient Magnéli phases at elevated temperatures. Magnéli phases, named after the main investigator [78], show good oxidization stability and low adhesion [79]. There are different metals which can form Magnéli phases such as Ti, W and V. Since vanadium is used as a component of the coatings in this research, only vanadium oxides are described in detail here. The chemical formula for Magnéli phases for vanadium can be written as  $V_nO_{2n-1}$  which are intermediate compounds between  $V_2O_3$  and  $VO_2$  [80]. Vanadium oxide exists in a numerous phases. Figure 2.12 shows the complex phase diagram of binary V-O system.

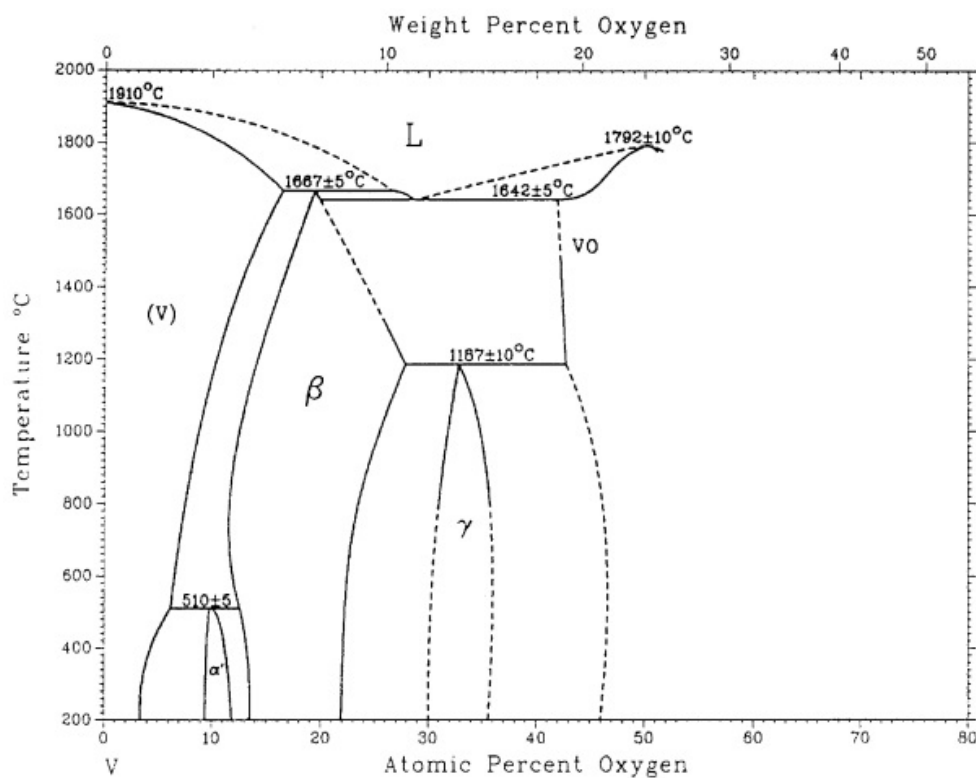


Figure 2.12: Phase diagram of the binary system V-O [81].

The tribological behaviour of Magnéli phases strongly depends on the temperature. This dependence is a result of different crystal lattice structures forming at different temperatures. Balog et al. [82] summarized and analysed the phase diagram of  $V_2O_5$ . The resulting diagram is presented in fig.2.13. Erdemir [83] described a crystal-chemical model that enables one to predict the shear rheology or lubricity of an oxide or oxide mixture at elevated temperatures. According to this model, the shear strength, which is correlated with the friction coefficient, is strongly related to the crystal chemistry of the oxides and their ionic potential. With higher ionic potential, the friction coefficient reduces and the extent of cation screening in an oxide by surrounding anions is increased. As a result of this, isolated cations have little or no chemical interactions with other cations in the system. The anions groups are weakly bound with each other, and they easily dislocate; this is the same for lamellar compounds.

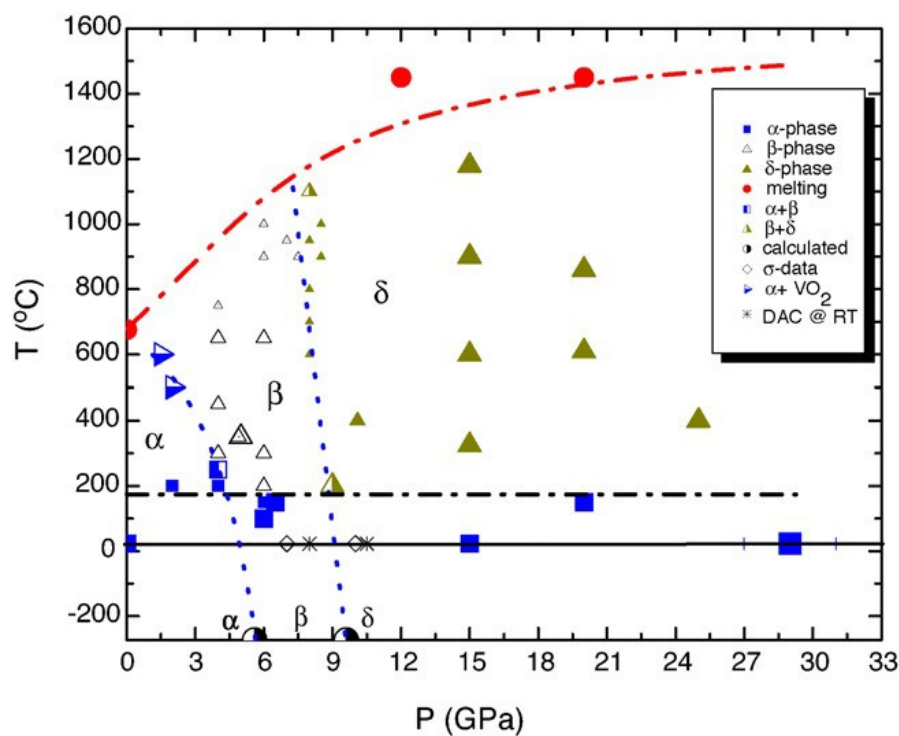


Figure 2.13: The phase diagram of  $V_2O_5$  [82].

## 2.4 Thin Film Growth

One of the most attractive features of sputtering deposition is the control of film properties that one can have by choosing the suitable deposition parameters. The mechanical properties of coatings greatly depend on the microstructure. An example is the change in coating colour which depends on applied bias voltage to the substrate [84]. The microstructure of thin film is affected by many parameters, such as:

- System pressure
- Substrate temperature
- Target power
- Substrate bias
- Substrate material and orientation
- The ion bombardment energy resulting from variations in deposition parameters.

In a conventional magnetron sputtering system, the plasma confinement and the increased plasma ionisation result in greater ion bombardment during film growth; this largely affects the final microstructure of the films (denser coatings, increased gas incorporation). When low energetic particles are incident, high points on the growing surface receive more coating flux than valleys, leading to voids in coatings. This effect is called the atomic shadowing [85]. The atomic shadowing effect causes a columnar structure of the coating with low-density boundaries between columns.

Different models have been developed to help predict the microstructure according to the external process parameters. The first model describing the influence of substrate temperature on the morphology was presented by Movchan and Demchishin [86]. They introduced a representation of thin film microstructures as a function of  $T/T_m$  (where  $T$  is the temperature of the substrate surface and  $T_m$  is the melting temperature of the material).

The model involves the formation of the three zones with their own characteristic structure as shown in fig 2.14.

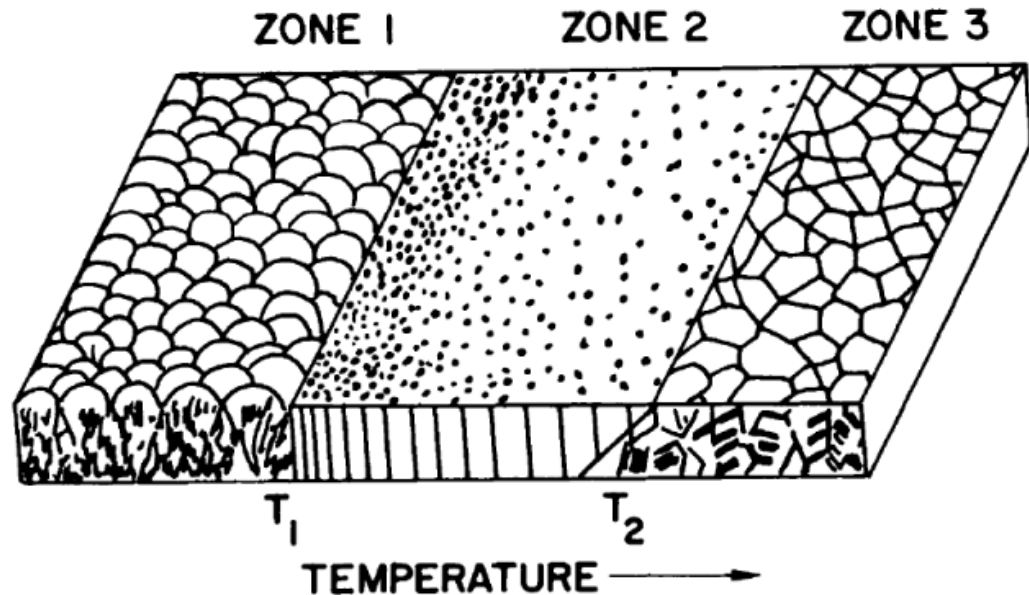


Figure 2.14 Structure Zone Model according to Movchan and Demchishin for evaporated films, showing the 3 zones in relation to the ratio of substrate temperature ( $T$ ) and melting temperature of the material ( $T_m$ ).

Zone 1 has a  $T/T_m$  ratio up to 0.3 and exhibits a porous, tapered columnar structure with unclear boundaries. This is a result of low adatom diffusion due to low temperatures.

Higher temperatures increase adatom mobility leading to formation of well-defined columnar structures. This characterizes zone 2 and is valid for  $T_s$  to be between 0.3 and 0.5  $T_m$ . Zone 3 is characterised by equiaxed grains, this is due to recrystallization effects at very high temperatures [87]. Additionally, there are narrow transitions between each zone where microstructures have characteristics of both bordering zones.

Later work by Thornton [87] expanded the theory by adding the influence of argon pressure on the morphology. In Thornton's model, the zone T between zone I and II was expanded for low argon flow and it narrows with increasing Ar pressure. Zone T consists

of densely packed fibrous grains.

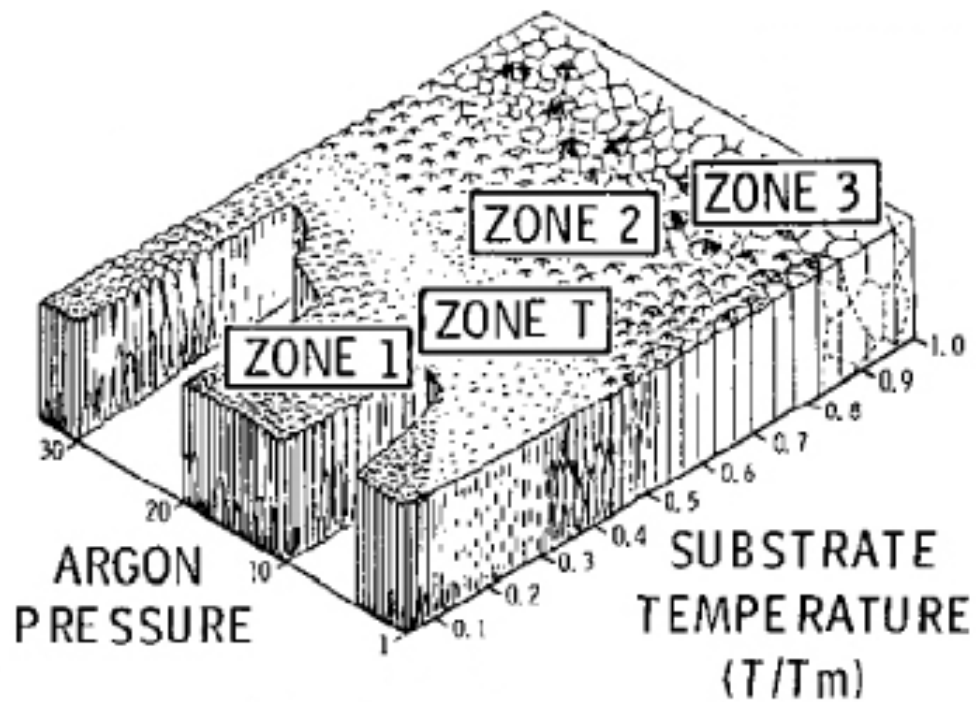


Figure 2.15 Structure Zone Model according to Thornton for sputtered films showing the added zone T and the influence of argon pressure.

Messier et al. [88] further expand this model by adding the effect of bias voltage onto the structure zones (fig 2.16). They found that for increasing bias on the substrate, the transition from zone 1 to zone T started at a lower homologous temperature. This was due to increased ion energy of the bombarding ions.

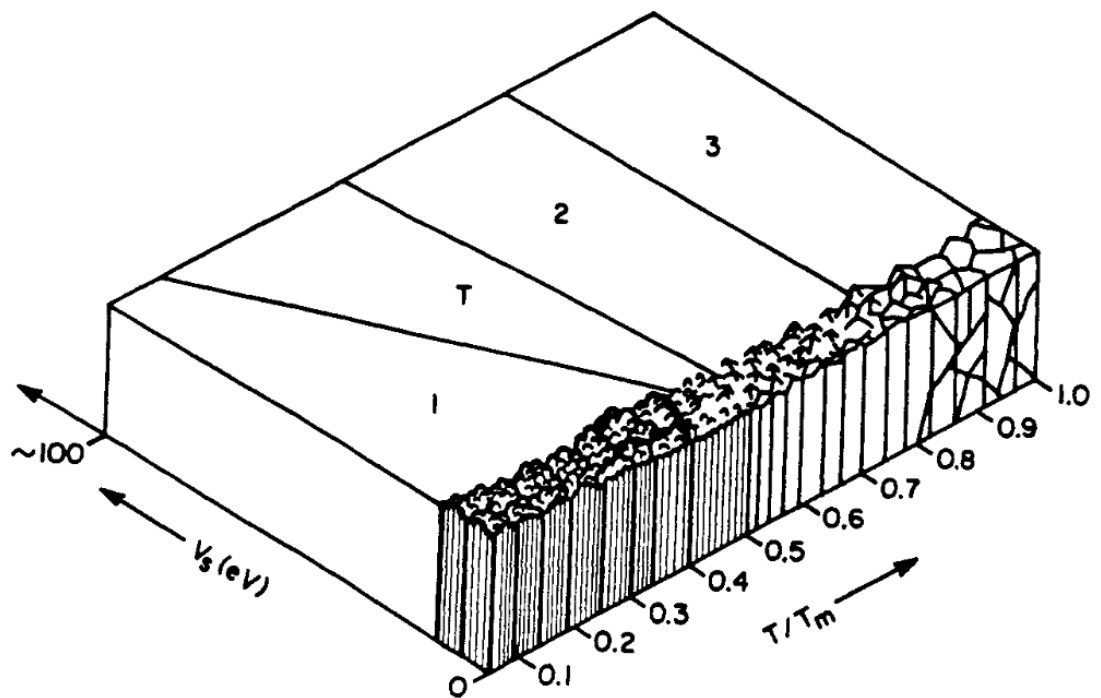


Figure 2.16 Structure model according to Messier showing the effect of substrate bias voltage.

Another model presented by Kelly and Arnell [89] relates to closed-field unbalanced magnetron sputtering systems. It refines previous models and adds the influence of ion to neutral ratio ( $J_i/J_n$ ). This model includes the homologous temperature, the substrate bias voltage and the ion to neutral ratio in three dimensions as presented in fig. 2.17. The zone boundaries are displayed as a spherical segment indicating the boundary. Zone 0 is the lowest boundary for normal operating conditions and not the transition from zone 1 to 2 as in the earlier model.

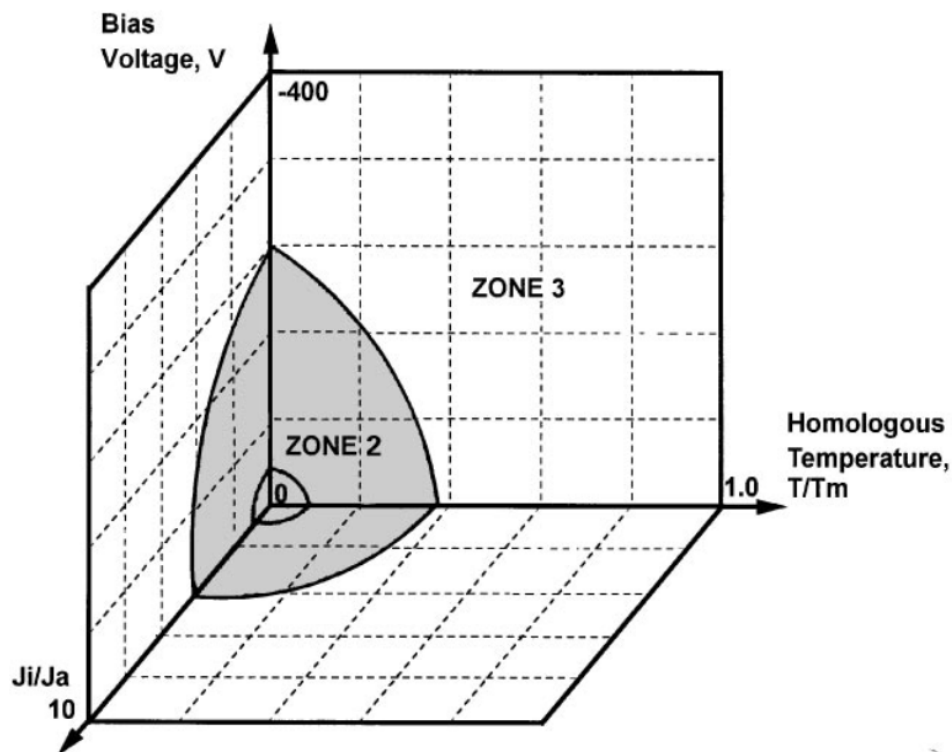


Figure 2.17 Structure Zone Model according to Kelly and Arnell showing the effect of the ion to neutral ratio on the morphology.

## 2.5 Multilayers

Multilayers have been widely investigated since the 1980s. They are successfully used to improve the surface mechanical properties, such as hardness and wear resistance, of materials. The concept of multilayers is that coatings have a repeated structure of two different materials [90]. Such structures allow one to utilize and combine advantages of different materials. Multilayers can either be isostructural (each layer material has the same crystal structure) or non-isostructural (layer materials have different crystal structures [91]. Holleck et al. [92] classify multilayers as a function of a number of layers in the same coating thickness (see fig.2.18). This refers to the bilayer thickness ( $\Lambda$ ). A multilayer material in which the individual layer thickness is in nanometre range is called nanoscale multilayer; when this is comparable to the lattice constant, it is called a superlattice.

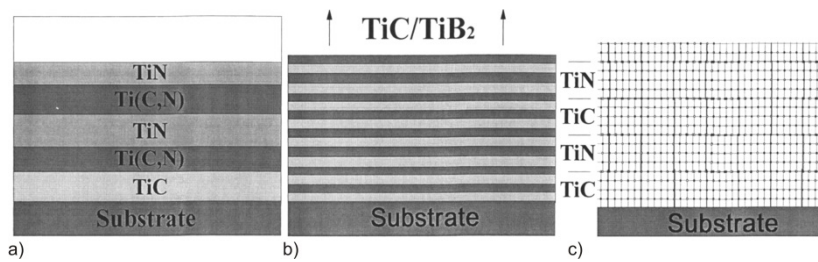


Figure 2.18: Simplified illustration of multilayers coatings with only few layers for different bilayer thickness: a) multilayers, b) nanoscale multilayers, c) superlattice [92].

It has been shown that the reduction of an individual layer thickness, and the crystalline size of the layered material, dramatically enhances the thin layer properties [93]. Fig.2.19 shows different properties of nanoscale multilayer coatings as a function of interface volume (which refers to numbers of layers). Different properties have different maximum interface volume numbers, however, it is possible to indicate the range of optimum values for protective coatings.

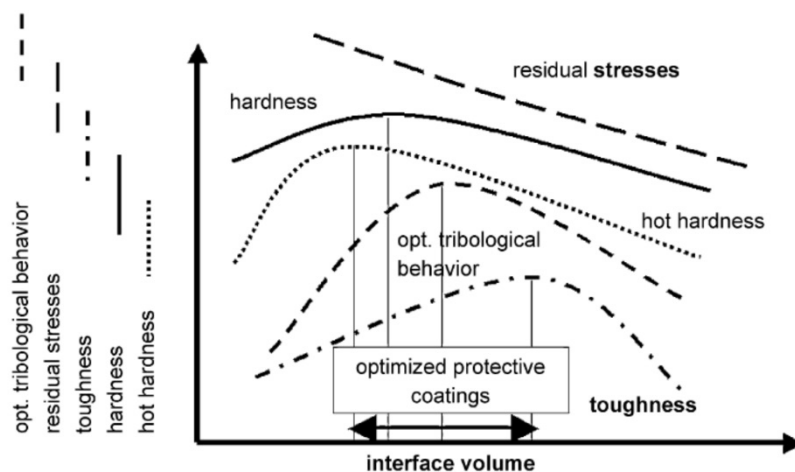


Figure 2.19: Change in properties of nanoscale multilayer coatings as a function of the interface volume (schematically, disregarding superlattice structures)[93].

Special role in enhancement of hardness and tribological behaviour are due to interfaces between individual layers [90]. Cracks that are formed due to forces are deflected at the

interfaces. Fig.2.20 schematically describes different mechanisms for toughening (i.e. deflection of the crack).

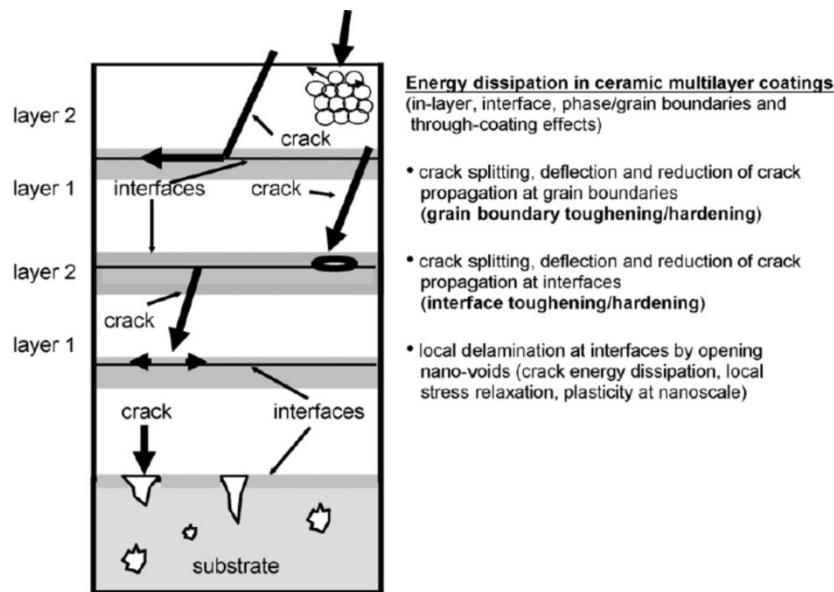


Figure 2.20: Toughening and strengthening mechanisms in ceramic multilayer coatings (schematically) according to Holleck and Schier [92].

Helmerson et al. investigated hardness as a function of the bilayer thickness ( $\Lambda$ ) (fig.2.21) of TiN/VN coating [94]. They found that at very low  $\Lambda$ , hardness is low (approximately 2000 kg/mm<sup>2</sup>) and increases linearly with  $\Lambda$  reaching superhard values of approximately 5500 kg/mm<sup>2</sup>. Further increase of  $\Lambda$  causes a logarithmic drop of hardness. When the  $\Lambda$  is very small (1-2 nm), layers almost interdiffuse and the modulus of each layer becomes the same, thus causing no hardness enhancement. Moreover, very close interfaces can exert opposing forces on a dislocation at the interface, thus lowering the stress needed to move the dislocation [95]. When  $\Lambda$  is large, hardness decreases due to dislocations moving within individual layers, since they are not able to cross the interferences; it has been shown that multilayer coatings have higher hardness than single layer coatings with similar thickness [94, 96].

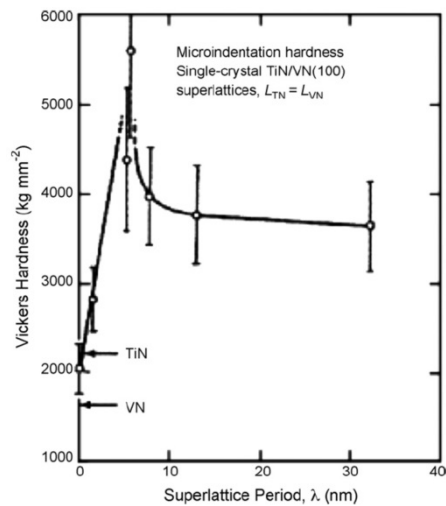


Figure 2.21: Hardness as a function of Superlattice period [93].

The multilayer concept is well-established and widely used for wear and tribological protective applications [93]. However, for specific engineering applications there is need to find the optimum conditions for the individual component multilayers and deposition parameters such as reactive gas partial pressure, ion current density and relative thickness of multilayers.

Previously, Sheffield Hallam University has developed TiAlN/VN and TiAlCN/VCN nanoscale multilayer coatings deposited by conventional magnetron sputtering. TiAlN coatings are well-known and widely used for machining tools due to their high hardness. VN coatings show good tribological behaviour due to Magnéli phases. During the early 2000s, P. Eh. Hovsepian at el. successfully combined these two coatings in TiAlN/VN multilayered coating with a low coefficient of friction and a low wear rate coefficient [97]. Coolant free, high-speed milling tests on aluminium alloys revealed significantly reduced build up edge (BUE) formation when compared with other TiAlN-based coated and non-coated tools [98].

Since carbon-based coatings show a good performance in machining aluminium alloys due to their high shear, carbon was added during the coating deposition process. The new

coating family shows very low affinity to aluminium and titanium alloys; these are well-known for BUE formation on tools.

In our work, we are investigating TiAlCN/VCN multilayer coatings which utilize the hardness of TiAlN layers, wear resistance of Magnéli phases in VN and the presence of carbon in both layers for good shear behaviour. This coating was developed by Kamath et al. at Sheffield Hallam University [5].

## 3 Experimental Setup

### 3.1 Sample preparation and coating deposition

In this section, the sample preparation, coating deposition sequence, plasma analysis and coating characterisation techniques are described. During the deposition process, five kinds of samples were used for the purposes of coating characterization. Samples and the test which they were used for are listed in table 3.1

Table 3.1: Dimensions and materials used for various tests and analytical methods

Substrate	Dimension	Tests
M2 high speed steel disks (HSS) (mirror polished)	$\phi 30 \times 6$ mm	Rockwell C indentation, scratch test, Pin on disc, nanohardness, Knoop Hardness, Raman, SEM, XRD
Stainless Steel disks (SS) (mirror polished)	$\phi 30 \times 6$ mm	SEM, XRD
Si Wafer	$\phi 6 \times 3$ mm	SEM, Profilometry
Stainless steel square plates for TEM (mirror polished)	$25 \times 25 \times 0.8$ mm	TEM
Plain Inserts (mirror polished and unpolished)	$\phi 10 \times 10 \times 5$ mm	Rockwell C indentation, nanohardness, Knoop Hardness
Cutting inserts		Milling test
Drill		Drilling test

#### 3.1.1 Specimen Preparation before Coating

All high-speed steel disks, stainless steel disks and part of the tungsten carbide inserts were ground with grit paper and then polished to a mirror finish using 1  $\mu$ m diamond paste. The stainless steel square plates were polished before delivery to Sheffield Hallam University. Prior to the deposition process, all samples were cleaned in an industrial -

size, automated ultrasonic cleaning line to remove oil and oxide contaminations. This line consisted of a series of heated tanks filled with ionic and non-ionic surfactants, de-ionized water and a vacuum dryer. After drying, samples were loaded into the PVD unit chamber immediately. Examples of polished HSS, SS disks, plain insert and Si wafer substrate are presented in fig 3.1.

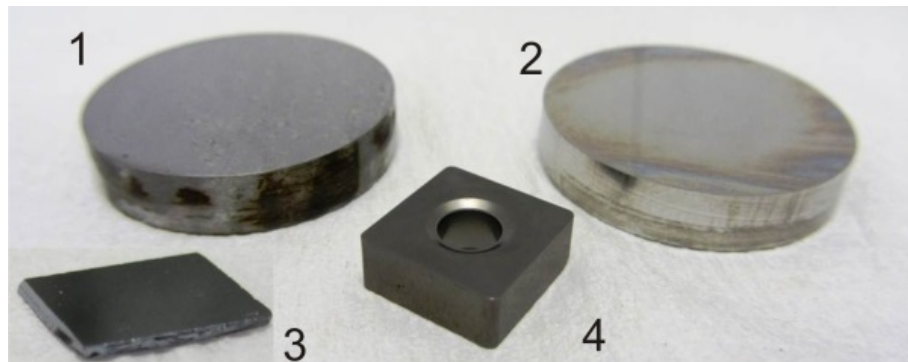


*Figure 3.1: Examples of samples used for deposition. 1: polished HSS disk, 2: polished SS disk, 3: Si wafer  
4: polished plain INSERT*

### **3.1.2 Coating Unit**

All samples were coated in a Hauzer Techno Coating (HTC) 1000-4 HIPIMS enabled unit (Hauzer Techno Coatings, Europe B.V., Venlo, Netherlands) at Sheffield Hallam University.

The Coater is presented in fig 3.2.



Figure 3.2 Hauzer 1000/4 PVD coater

This is an industrial sized, four-target system, with an octagonal cross-section and a volume of  $1 \text{ m}^3$ . This machine is equipped with two HIPIMS power supplies (Hüttinger Electronic Sp. z o.o., Warsaw, Poland) which enable it to operate in either HIPIMS or Unbalanced Magnetron Sputtering (UBM) mode. Samples were mounted to a turntable, which is located in the centre of the chamber. It is possible to have a one-, two- or three-fold planetary rotation of samples. The chamber is evacuated by a system of pumps which will be described later. The machine is heated using two heaters positioned on its doors and one under the turntable. The system's doors and cathodes are water cooled during operation.

Each cathode can be operated in unbalanced magnetron mode (UBM); additionally, two of them can be connected to a HIPIMS power supply. In all experiments two cathodes

were operated in the UBM mode and two in the HIPIMS mode. Cathodes were furnished with 4 targets (200×600 mm). Two of them were titanium-aluminium alloys (50/50 %) and two were vanadium. A cross-section of the deposition chamber, indicating the target configuration is illustrated in fig.3.3. The basic deposition process sequence and short descriptions of them are listed below.

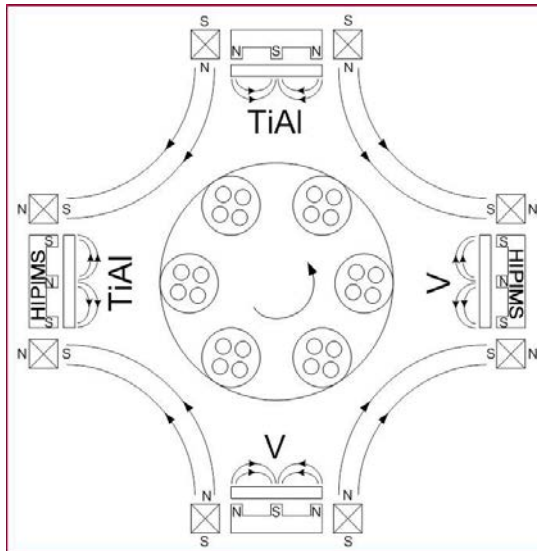


Figure 3.3: Schematic cross section of chamber of Hauzer HTC 1000-4 unit.

### 3.1.3 Deposition Process Sequence

#### I Pumping down

In order to deposit coatings with a low level of impurities it is necessary to evacuate the chamber to a relatively low pressure. The pumping process is divided into two stages. Initially, the pressure is reduced to  $8 \cdot 10^{-2}$  mbar by 250 m<sup>3</sup>/h roots and 500 m<sup>3</sup>/h rotary vane pumps. The final pressure is obtained by a system of two Balzers TPH 2200 turbo molecular pumps. When the pressure reaches  $7.5 \cdot 10^{-5}$  mbar, the heating process can begin.

#### II Heating

The chamber and substrates are heated to the desired temperature by three heaters. For coating deposition processes, the chamber was heated to 450°C. Due to operational

temperature limits of the optical fibre and mass spectrometer during etching and reactive sputtering processes the chamber was only heated to 100 and 200 °C, respectively. Additionally, heating enhances outgassing of moisture and contamination from chamber walls. For these reasons, the chamber is heated up for a few hours before the deposition process commences. When the required temperature and pressure are obtained, the next step is initiated.

### **III Target cleaning**

Target cleaning steps are implemented in order to remove surface contaminations avoiding arcing on the target. To protect substrates from impurities during this step, shutters are placed in front of the target. Targets are cleaned in a plasma discharge through ion bombardment. This step is performed in an Ar atmosphere with constant flow of 200 sccm. There are two target cleaning steps with differing voltages. During target cleaning steps the applied voltage is set to 700 and 1200 V, the voltage in both settings is greater than that used for step IV. Each target cleaning step proceeds for 5-10 min.

### **IV Metal Ion etching**

During this step the substrate surface is cleaned prior to the deposition by ion bombardment. Highly ionized  $V^+$  ions are generated by a HIPIMS discharge in an Ar atmosphere, and accelerated towards the substrates by a bias voltage of 1050 V, applied to the substrate. Highly energized ions hit the substrate surface causing sputtering, thus impurities which could not be removed during the sample cleaning process (e.g. oxidization) are etched. The advantage of this is that during this step some metal ions are implanted into the substrate. Both surface cleaning and implantation positively influence the adhesive strength of the subsequent coating. However, if etching proceeds for an extended period it may result in removal of surface material and can cause changes to the

substrate shape (especially cutting edge of used inserts). This problem will be discussed and investigated in one of the experiments (chapter 4).

During this step only one cathode was in operation, with a voltage of 1100 V in HIPIMS discharge with frequency of 104 Hz and pulse duration of 200  $\mu$ s.

### **V Base layer Deposition**

Plasma coating adhesion depends on thickness, due to internal stresses accumulating with increasing thickness (residual stress) [99]. The base layer provides a gradient in hardness and stress between the substrate and the coating. This results in a better adhesive strength and resistance to coating failure caused by residual stresses. The base layer deposition is carried out in a reactive atmosphere of Ar and N<sub>2</sub> at flow 200 and 160 sccm respectively. The plasma is generated from a HIPIMS (600 V) and DCMS (8 kW) discharge, sustained on the vanadium target. The TiAl target operated at 1 kW in order to avoid unwanted deposition of sputtered material onto the target.

### **VI Coating deposition**

Coating deposition was carried out in a mixed reactive atmosphere of Ar, N<sub>2</sub> and CH<sub>4</sub> with a N<sub>2</sub>:CH<sub>4</sub> ratio of 2:1. The argon flow is constant during this step and all targets were in use. Two cathodes operated in a HIPIMS discharge (one for each kind of target) at average power of 8kW with frequency of 400 Hz and pulse duration of 200  $\mu$ s, and two in a DCMS discharge at power of 8 kW. The deposition step duration is 4 hours.

### **VII Cooling down of the chamber**

Because high temperature difference leads to high air currents, which may damage the samples, the chamber is cooled down to 150 °C or below before venting. During venting, and whilst the chamber is open, warm water flows in chamber walls in order to minimize moisture condensation inside the chamber.

## 3.2 Gas Flow Control

The incorporation of the target poisoning controlling system, involved installing a control unit based on proportional–integral–derivative (PID) control loop into the PVD deposition system (fig. 3.4). In this loop the light passes via feed-through with attached 10 cm long collimator to the spectrometer (Jobin Yvon, Horriba) connected with a 20 cm long  $\text{\O}600\ \mu\text{m}$  fibre. The desired spectra line is collected (438.5 nm for V(I) and 521nm for Ti(I)), which is then transferred to the control unit by a 2.5 m optical  $\text{\O}600\ \mu\text{m}$  fibre. The control unit compares the actual value of the light intensity with the set value and calculates a new value of the reactive gas flow. The feedback is sent to an actuator (mass flow controller (MFC), brooks Brooks SLA 5850). The signal from the Speedflo is sent to the MFC's via electrical signal in range of 0 to 4.999 V, where 0 V means closed gas flow and 4.999 V fully opened. The maximum gas flow depends on the MFC which was 2000 sccm for  $\text{N}_2$  and Ar, and 1000 sccm for  $\text{CH}_4$ . In the system it is possible to set the Lower Actuator Limit (LAL) and the Upper Actuator Limit (UAL) of the gas flow to a desired value. This helps to avoid radically low or high flows. For both gases (LAL) was 0.01 and, UAL 2 and 5 for  $\text{N}_2$  and  $\text{CH}_4$  respectively.



Figure 3.4 PID control loop applied into the system. Light is passing via a feedthrough (1) to a spectrometer (2). A selected spectra line passes to a control unit (3), where the light intensity is compared with the set value.

Algorithm parameters (for PDF+) define how dynamic the feedback response is.  $K_1$  is related to the step of change required on the actuator,  $k_2$  is related to the time constant and  $k_3$  is the initial opening actuator condition. For all process algorithm parameters were  $k_1$ : 0.001  $k_2$ : 5E-05,  $k_3$ : 1000.

With this system,  $N_2$  and  $CH_4$  flow were controlled. When both gases were used, the methane was operated in slave mode of the nitrogen, which means that its flow was calculated depending on the Nitrogen flow in 1:1, 2:1 or 4:1 ratio. For some experiments Speedflo was also used to control the argon flow.

### 3.3 Current and Voltage Measurement

The peak pulse current and voltage during HIPIMS discharge were measured at the target and monitored using a Tektronix DPO7000 oscilloscope. The average voltage of DCMS was measured with Hauzer software. Each value was recorded every 10 seconds during the ramping process.

In order to compare target conditions during the DCMS and the HIPIMS discharge the discharge resistance  $R_D$  was calculated. Equations (3.1) and (3.2) are calculations for DCMS and HIPIMS discharges respectively.

$$U = I * R \rightarrow R = \frac{U}{I} \quad (3.1) \quad I * R \rightarrow R = \frac{P}{I^2} \quad (3.2)$$

Similar to discharge voltage, the  $R_D$  depends on: pressure, target material and plasma composition. The influence of the target material will be called Target Resistivity ( $R_T$ ).  $R_T$  depends on the resistivity of the bulk material, any compounds formed and  $\gamma_{ISEE}$ . Table 3.2 shows the resistivity of target materials and of the possible compounds on the target.

Bulk Material	Ti	Al	TiAl	V		
$\mu\Omega \cdot \text{cm}$	43 [100]	$10^{-4}$ [101]	0.1-0.9 [102]	24- 26[100]		
Bulk Material	TiN	TiC	TiAlN	AlN	VN	VC
$\mu\Omega \cdot \text{cm}$	20- 25 [100]	68 [100]	200 - 400 [103],[104]	2.3-8.1	85 [100]	60 [100]

Table 3.2 List of electrical properties of target materials and the compounds on the target

For vanadium alloys, the addition of carbon or nitrogen causes an increase in the resistivity. The increase for VN is approximately twice as high as VC. For titanium alloys, the resistivity of TiN is approximately twice lower than pure Ti alloy, whereas TiC is 1.5 times higher. The resistivity of AlN alloy is four orders of magnitude higher than pure aluminium. In the complex TiAlN alloy, resistivity is three orders of magnitude higher than in TiAl alloy. The values are given for bulk material and can differ from thin compound values. Additionally, given values are accurate for room temperature and can differ from ones during process. However, they give a good estimation of the general trend. The influence of plasma composition mainly depends on Plasma Impedance ( $R_P$ ), which is dependent on the Ionization level.

The  $R_D$  can be described as (3.3):

$$R_D \propto R_T(\gamma_{\text{ISEE}}) + R_P \quad (3.3)$$

## 3.4 Plasma diagnostic techniques

### 3.4.1 Plasma Sampling Mass-Spectroscopy

Plasma composition was investigated using Mass spectroscopy (MS). In MS the sample of the plasma is filtered by its energy and mass/charge ratio. As the individual monitored species have different masses and charges, it is possible to filter out species which do not have the required mass or charge. In doing so, the MS detects desired species. This can be used to investigate plasma composition as well as to compare the intensity of different species.

Ions extracted from the plasma are focused by applying a constant voltage of -10 V and -80 V on the electrode and on the ion lens electrode respectively. Negative voltage on the extractor is used to repel electrons and accelerate positive ions. Analysis of negative ions is also possible by secondary ionization inside the MS by electron impact ionisation before entering the ion lenses. This measurement is also called residual gas analysis (RGA). In modern MS it is also possible to investigate negative ions.

Positive ions pass from the extraction electrodes and are then filtered by their energy in the Bessel box. Ions with less energy will be retarded and hit an axial blocker. Ions with excessive energy will not pass through the Bessel box exit aperture. Next remaining ions pass through a quadrupole filter where they are further filtered by their mass-to-charge ratio. Mass analysers are based on the dynamics of charged particles in electric and magnetic fields. The basics operation of the quadrupole is presented in fig. 3.5. It consists of two sets of oppositely connected rods with applied alternating DC and RF potentials. This creates an alternating electric field along the z-axis. The alternating electric field deflects ions which start to move in a cycloid path with a specific radius ( $r$ ). This radius depends on the individual mass-to-charge ratio. Only ions that move along specific radii

pass the filter, any other radii will result in the ions colliding with the rods [105].

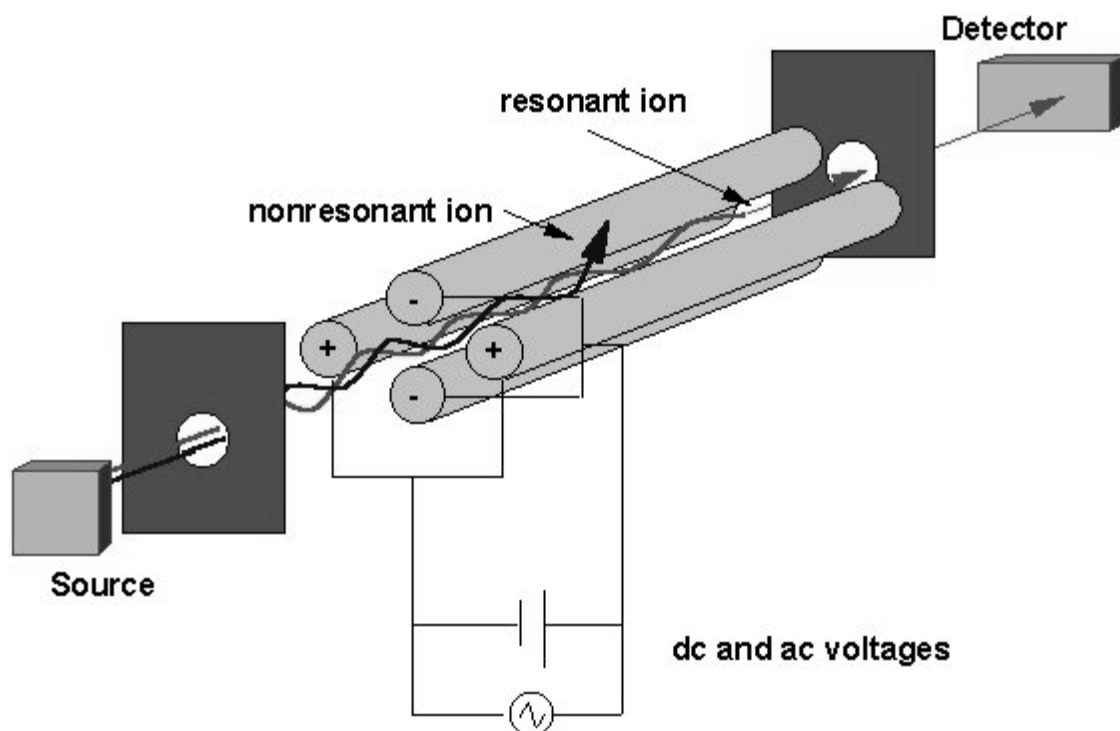


Figure 3.5 Schematic of the quadrupole mass analyzer showing resonant ion passing the analyzer and reaching the detector and nonresonant ion scattered in the analyzer.

Ions with the selected mass-to-charge ratio are accelerated towards a secondary electron multiplier, which consists of a series of electrodes called dynodes.

For plasma analysis in chapter 6, a plasma-sampling time-resolved mass spectrometer (Mass Spectrometer 301 PSM from Hiden Analytical Ltd.) was used.

The MS was mounted at the viewport between two targets of the same material. Ions were extracted through a 200  $\mu\text{m}$  diameter, grounded orifice, oriented at an angle of  $45^\circ$  with respect to the normal of the target. Since the acceptance angle of the instrument was  $1^\circ$ , the current configuration did not detect ions incoming directly from the targets. Before reaching the MS, ions had collided at least once leading to deviation of the trajectory, loss of energy and loss of charge. Thus the possibility of highly ionized ions is low. According to the kinetic theory of gasses, the mean free path,  $L$ , is given by equation 3.4:

$$L = \frac{kT}{\sqrt{2}p\sigma} \quad (3.4)$$

Where  $k$  is the Boltzman constant,  $T$  is the temperature,  $p$  is the pressure and  $\sigma$  is the cross section [106]. This gives the mean free path of 0.06 m for argon atom in a typical deposition process.

The time resolved measurement was conduct for ions listed in table 3.2 each of the following ions:  $\text{Ar}^{1+}$ ,  $\text{Ar}^{2+}$ ,  $\text{Ti}^{1+}$ , and  $\text{Ti}^{2+}$ . Measurements were performed in the vicinity of both target materials. The MS was switched on at the same time as the experiment began, thus there was no possibility to extract background noise.

Mass (u)	13	14	16	17	24	25	27	28	40	48	51
Molecule	$\text{Al}^{2+}$	$\text{N}_2^{1+}$	$\text{CH}_4^{1+}$	$\text{V}^{3+}$	$\text{Ti}_{2+}$	$\text{V}^{2+}$	$\text{Al}^{1+}$	$\text{N}^{1+}$	$\text{Ar}^{1+}$	$\text{Ti}^{1+}$	$\text{V}^{1+}$
Possible Molecule	$\text{CH}^{1+}$	$\text{CH}_2^{1+}$	$\text{O}^{1+}$	$\text{NH}_3^{1+}$ , $\text{OH}^{1+}$	$\text{C}_2^{1+}$	$\text{C}_2\text{H}^{1+}$	$\text{HCN}^{1+}$ , $\text{C}_2\text{H}_3^{1+}$	$\text{C}_2\text{H}_4^{1+}$ , $\text{CO}^{1+}$			

Table 3.3 List of observed gas and metal ions

### 3.4.2 Optical Emission Spectroscopy

Optical emission spectroscopy (OES) is the basic technique to determine the composition of plasma. An example of the OES spectrum is presented in figure 3.6.

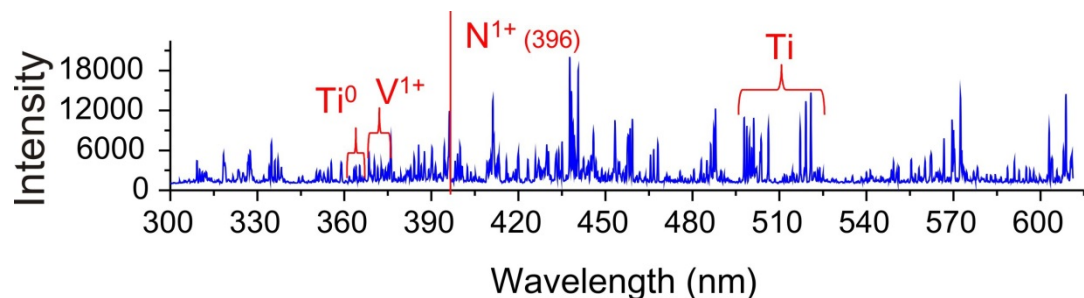


Figure 3.6: Spectrum of HIPIMS with TiAl and V targets in Ar,  $\text{N}_2$  and  $\text{CH}_4$  atmosphere.

OES uses the excitation process to identify the elements. An atom is in an excited state when one of its electrons is transmitted from the ground state to a higher energetic level. In order to move an electron to any higher energy state, the absorption of a specific amount of energy is required. This energy must be equal to the difference between the final and initial energy levels. An atom can retrieve energy from radiation of the appropriate frequency, thermal effect, atomic collision etc. An electron can last in the excited state for a very short time and then returns to a state of lower energy. During relaxation, an atom emits light ( $h\nu$ ) with a characteristic wavelength. The frequency of the emitted light is proportional to the energy difference between two energy levels.

$$h\nu = E_2 - E_1 \quad (3.5)$$

Where  $h$  is the Plank constant. The frequency and wavelength are related by:

$$\lambda = \frac{c}{\nu} \quad (3.6)$$

Where  $c$  is the velocity of the light. The probability of absorption or emission of electromagnetic radiation in transitions between energy levels of an atom or molecule is called the oscillator strength.

There are many allowed transitions between the energy levels of atoms possible, however they are limited by selection rules [107].

In OES, the spectrum of light emitted from the plasma (or other materials) is collected and investigated.

Light from the plasma is collected by optical fibre and transferred to a collimator mirror through an entrance slit. The light is then diffracted by a pair of diffraction gratings (or prism). Diffracted light is focused by a mirror, passes through the exit slit and incident CCD detector. Next, the electrical signals from different parts of the CCD detector are analysed by a computer program. In this work, the Jobin Yvon Triax 320 spectrometer from Horiba was used for the plasma spectrum analysis.

OES was used in two parts:

- To investigate plasma composition. The OES settings were: exposure time: 2 s, accumulations: 5, the front entrance slit: 0.02-0.08 mm and CCD range: 200-850 nm and 400-850 nm when using UV wavelength filter.
- To investigate the selected line for a chosen species change in time by using Photomultiplier Tube (PMT) systems

### 3.4.3 Quartz crystal micro balance

A quartz crystal microbalance (QCM) was used to analyse the deposition rate. The QCM measures a mass per unit area by measuring the change in frequency of a quartz crystal resonator. Since the quartz crystal is a piezoelectric, by applying an alternating electric field a mechanical oscillation of the characteristic frequency,  $f_0$ , is produced in the crystal. An electric field is applied by attaching electrodes to the upper and lower surfaces of the crystal. Changes in mass on the quartz surface are related to changes in the frequency of the oscillating crystal through the Sauerbrey relationship [108]:

$$\Delta f = -2 \frac{\Delta m f^2}{A(\mu \rho_q)^2} = -C_f \Delta m \quad (3.6)$$

Where  $\Delta f$  is the measured resonant frequency decrease (Hz),  $f$  is the intrinsic crystal frequency,  $\Delta m$  is the elastic mass change (g),  $A$  is the electrode area ( $\text{cm}^2$ ),  $\rho_q$  is the density of quartz ( $2.65 \text{ g/cm}^3$ ), and  $\mu$  is the shear modulus ( $2.95 \times 10^{11} \text{ dyn/cm}^2$ ),  $C_f$  is the integrated QCM sensitivity. The Sauerbray relationship is valid only for small elastic masses added to the crystal surface, not greater than about 2% of the crystal mass.

The quartz-crystal settings were adjusted to density =  $4.5 \text{ g/cm}^{-3}$ , tooling = 100, z factor = 1. Thickness measurement was taken after 10 minutes. The probe was biased to a voltage of -100 V.

### 3.4.4 Flat Electrostatic Probe

A Langmuir probe was used to investigate plasma properties such as electron and ion densities, electron temperature or plasma potential. The classical Langmuir probe consists of an electrode connected to the power supply, it is then inserted into the plasma and the current is measured for a ramp voltage. The electrode usually has a simple geometric shape: spherical, cylindrical or planar (flat). All three kinds of electrodes are presented in fig.3.7. In this research a planar electrode was used for plasma analysis. The method of taking Langmuir probe measurements is based on the estimation of the current-voltage characteristics. Voltage,  $V$ , is the potential difference between probe surface,  $V_p$ , and plasma space potentials,  $V_s$ . The probe current depends on the potential imposed on the probe.

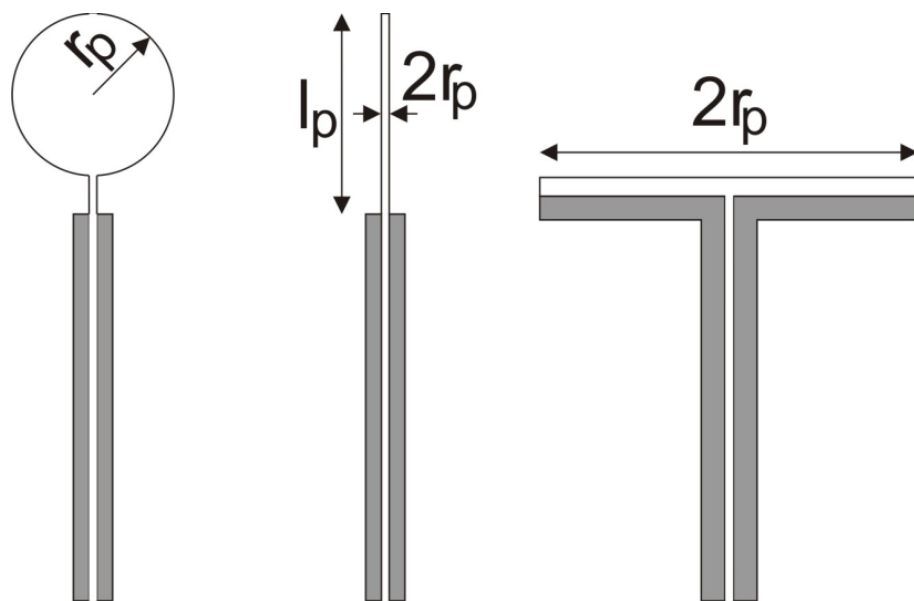


Figure 3.7: Typical shapes of Langmuir probes [109].

A typical current-voltage plot is shown in Fig.3.8. This characteristic is normally determined by the plasma properties in the immediate vicinity of the probe.

The general shape of the I–V characteristic can be divided into three parts. When the probe is disconnected, the probe current is zero. The mean velocity of the electrons in the plasma surrounding the probe exceeds the velocity of ions by a factor of  $(m_+/m_e)$  where  $m$  is the mass of a particle. For this reason, negative charge accumulates on the probe surface. Ions are accelerated to this negative charge but because of their mass, the effect is small [109]. This results in a space-charge sheath around the probe, which acts to shield the plasma from the electric field of the probe.

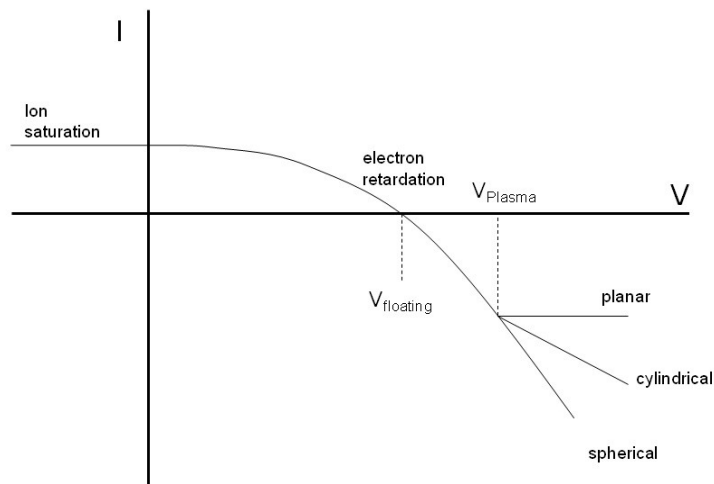


Figure 3.8: *I – V Characteristic of a Langmuir probe for different electrode shapes*[110]

The thickness of the sheath is determined by formula 3.7 [109].

$$\lambda_D = \sqrt{\frac{\epsilon_0 k_B T_e}{q_0^2 n_e}} \quad (3.7)$$

Where  $T_e$  is the electron temperature,  $n_e$  the concentration of the electrons.  $\epsilon_0$  the permittivity of the vacuum,  $k_B$  the Boltzmann constant, and  $q_0$  the elementary charge.

The potential on the probe surface when it is isolated is called floating potential. The region on the I-V characteristic is called the electron retarding region. When the probe is biased positively with respect to the local plasma potential  $V_p \gg V_s$ , the flux of particles reaching the probe will consist of negative charge carriers (mostly electrons). Electrons are collected from a region called the sheath, which is the region close to the probe surface. In this region the potential exerted by the probe is not shielded by the plasma.

When the probe is biased negatively with respect to the plasma potential  $V_p \ll V_s$ , only positive ions will reach the probe. This region is called the ion saturation region.

## 3.5 Sample Characterization Techniques

### 3.5.1 Optical Microscopy

Optical microscopy is the primary tool for scientists and engineers for morphological characterization. Due to metal samples not being transparent, reflective microscopy must be used, and as a result, only surfaces can be analysed [111]. The optical principles of the microscopes are well-known. Light from an observed object passes through a converging lens and is focused, forming a magnified inverted image. Next, the light passes through another converging lens and a final magnified image of the object is created.

The microscope consists of two magnifying elements: the objective and the eyepiece. Microscope magnification is the product of the lens magnification and of the eyepiece magnification. The magnification of a light microscope is limited by its resolution. The resolution of a microscope is a function of its parameters and can be stated as:

$$R = \frac{\lambda}{2NA} \quad (3.8)$$

Where  $NA = \mu \sin \alpha$  is called the numerical aperture with  $\mu$  - index of refraction and  $\alpha$  - s the half-angle of the maximum cone of light that can enter or exit the lens. Optical microscopy is very useful for fast analysis of micro-structures and the influence of the destructive tests on the coating.

### 3.5.2 Scanning Electron Microscopy

Scanning electron microscopy (SEM) is widely used to obtain high-resolution images of micrometer range areas. A highly energetic electron beam scans the specimen of the sample line by line. When an electron beam penetrates the surface of the sample, electrons are scattered due to inelastic and elastic collisions. Due to interactions at atomic level the sample emits different kinds of radiation. The schematic drawing of a scanning electron beam incident on a solid sample is shown in fig.3.9. These signals are collected by a corresponding detector, amplified and then converted into an image of the sample and the spectrum of radiation.

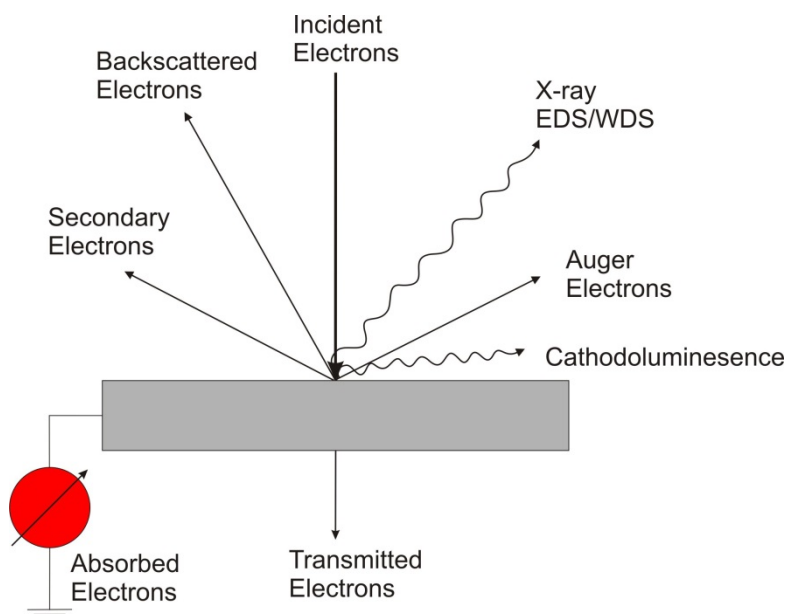


Figure 3.9: Schematic drawing of a scanning electron beam incident on a solid sample [111].

In SEM, the electron beam is produced by an electron gun situated at the top of the column of the microscope. There are several types of electron guns but all of them are designed to produce an electron beam with a stable and sufficient current at the smallest possible size. The electrostatic field in the electron gun directs the emitted electrons from a small area of the cathode, into the electron-optical iris. The electrons are then accelerated in the microscope column toward the sample. The typical energy of an electron beam is in range of 1-40 kV (material characterization). The emitted electron beams diverges, therefore, a set of condenser lenses and apertures are used. Two sets of scanning coils at the bottom of the column are responsible for the movement of the beam in the scanning area. The objective lens focuses the beam to a spot as small as possible on the surface of the sample. The electron signals are collected by detectors, which are allocated with respect to the character of the signal.

For SEM investigation a Nova<sup>TM</sup> NanoSEM 50 series microscope was used. It is equipped with a high-resolution field-emission SEM column and high stability Schottky field emission gun. The incident beam voltage is in range of 5-20 kV.

**Back scattered electrons (BSE)** are produced due to the elastic collisions of primary electrons with the sample. They have energies in the same range as electrons in the electron beam [112]. The fraction of backscattered electrons from the incident beam depends on the atomic number,  $Z$ , of the specimen. The fraction increases with increasing  $Z$  [111]. Through this, contrast between different materials is seen in the image. Materials with higher  $Z$  will appear brighter. Regions of the specimen surface facing towards a backscattered detector will give an enhanced signal, additional to the compositional effect. Therefore, surface topography can also affect the scatter behaviour of BSE [111].

**Secondary electrons (SE)** result from inelastic collisions. An incoming electron hits the atom; this leads to the emission of an electron. The energies of the electrons emitted in this way are significantly lower than those of BSEs, usually 3-5 eV [112]. Due to their low energies they are not able to travel long distances in a solid material. Only electrons from the specimen surface area of 5-50 nm depth are able to escape. Therefore, only SE electrons which are generated near the surface can reach the detector. The SEs are commonly collected by a positive biased detector [113]. The detector is usually placed on the side of the sample. The topographic image is produced due to fact that electrons from specimen surfaces that are facing the detector will give a stronger signal than from surfaces not facing the detector [112]. It is important that there is another possibility for the generation of SEs. They can be generated by high energetic BSEs that collide with atoms, within the near surface area of the sample. These SE deteriorate the quality of the image; they lead to a disturbed signal, which is relatively constant. The constant nature of the signal means it can be subtracted easily [113].

**Characteristic X-rays** are produced due to electron transitions from a higher to a lower shell. This occurs when an incident electron, with sufficient energy, knocks out an electron from the lower electron shell. The transition is accompanied by photon emission (x-rays) with a specific energy and wavelength. Due to this, each atom has its own characteristic radiation, characteristic x-rays and can be used to identify the material composition. In general there are two kinds of detectors used to collect signal from x-rays:

- X-ray Wavelength Dispersive Spectroscopy (WDS) - uses single crystal deflection for detection characteristic x-ray wavelength [112]
- X-ray Energy Dispersive Spectroscopy (EDS or EDX) - uses a photon detector to separate the characteristic X-ray photons according to their energy [112].

### 3.5.3 Atomic Force Microscopy

Atomic Force Microscopy (AFM) is a scanning technique used to provide topographic information of the scanned sample surface. AFM uses a very fine sensor tip, mounted to the end of a small cantilever, which deflects when it is in contact with the sample surface. The recorded deviation of the cantilever is the result of forces existing between the tip and the atoms present at the surface of the sample. Van der Waals forces play a crucial role in these interactions attracting the tip and Short-Range forces which are repulsive. The nature (attractive or repulsive) and sum of the forces depends on the sample-tip distance, which is called the Lennard-Jones potential. In addition, there are other forces interacting between the tip and sample, which have to be taken into account.

- Capillary forces
- Electrostatic interactions
- Adhesion
- Strength of the bilayer.

Accordingly to the nature of the interaction there are two operating modes for atomic force microscope:

- Contact mode - repulsive forces dominate.
- Non-contact modes - attractive forces dominate.

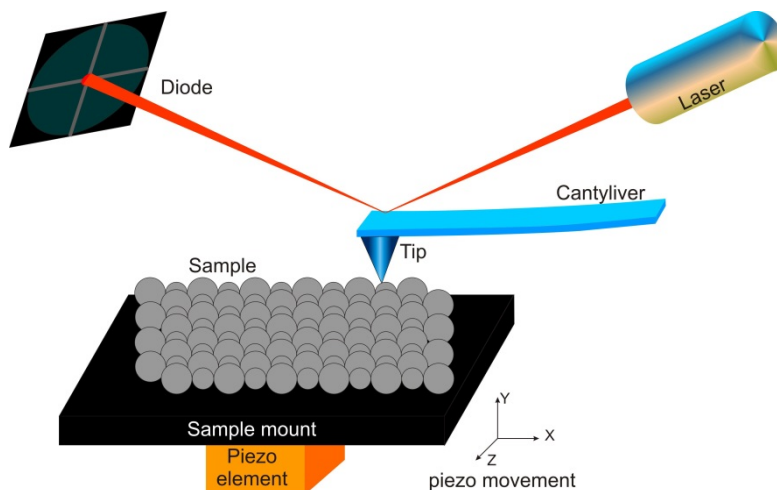


Figure 3.10 Schematic view of the basic working principle of the atomic force microscope.

The cantilever deflection is detected by a laser beam, which is reflected from the rear side of the cantilever (fig.3.10). The reflection is measured by an array of photodiodes. In order to produce a three-dimensional image of the surface, the sensor tip scans the surface plane in two dimensions. The position of the probe and the feedback signal are electronically recorded to produce a three dimensional map of the sample. This technique is especially useful for imaging nanoscale surface features as well as accurately measuring their dimensions, measuring roughness and waviness of the sample.

### 3.5.4 X-ray Diffraction

X-rays are electromagnetic waves produced by high-speed electrons colliding with a metal target. Wavelengths of x-rays are approximately in the same range as the atomic structure and thus can be used to determinate the crystal structure, lattice parameter and texture, lattice strains and to identify superlattice wavelengths [112, 114]. When x-rays pass through a crystal, they are scattered by atoms of the sample (fig. 3.11).

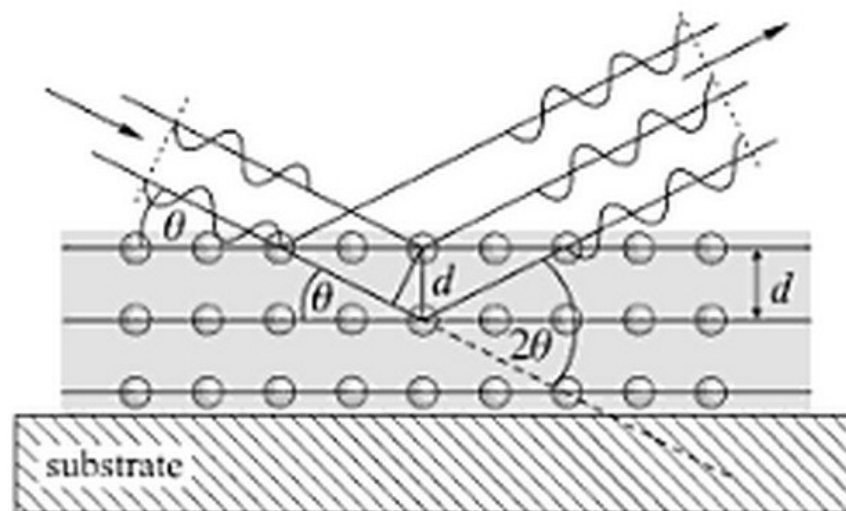


Figure 3.11 Diffraction of X-rays by planes of atoms [113]

The scattered waves interact with each other. This may result in constructive or destructive interference. The resulting intensity of the scattered x-rays shows a pattern that is a result of the interference of the individual waves scattered by each atom. If the sample is a single crystal or polycrystalline, the x-rays will be scattered from successive planes of atoms. In order to get maximum intensity, the interference must be constructive and the x-rays have to be in phase. This means that the x-rays must have a path length difference equal to a wavelength  $\lambda$  or an integer number of wavelengths. These conditions are summarized in Bragg diffraction law [113].

$$n\lambda = 2d \sin \theta \quad (3.9)$$

Where  $\theta$  is the beam incident angle,  $n$  is the order of reflection,  $\lambda$  is the wavelength and  $d$  is the interplanar spacing.

Bragg- Brentano ( $\theta/2\theta$ ) geometry is the simplest arrangement of x-ray tube, sample and detector as shown in fig.3.12.

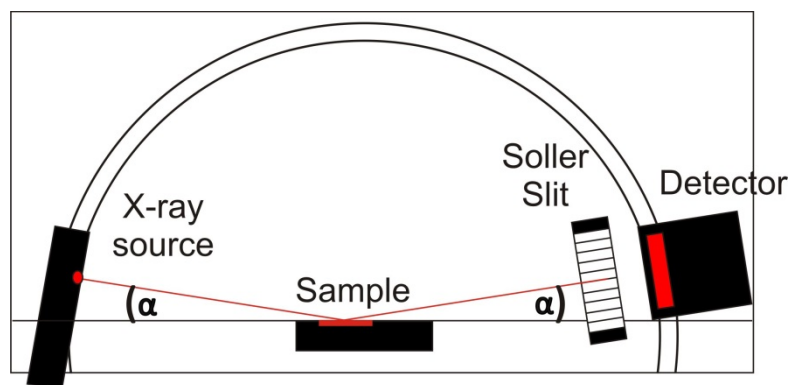


Figure 3.12 Bragg-Brentano geometry configuration.

It is most widely used for XRD analysis. The x-ray source and the detector are placed on two arms of the goniometer. The sample is placed in the centre of a goniometer rotation axis. The x-rays hit the sample at an angle  $\theta$  with respect to the sample surface, and they are diffracted towards the detector situated at an angle  $2\theta$  from the direction of the incident beam. Incident rays at angles that fulfil the Bragg law will reach the detector. By

varying the angle, the sample can be scanned for different plane orientations, and crystal structure can be recognized from the intensity peaks. Usually, a database with a list of peaks is used to determine the sample composition. Example of the Bragg- Brentano spectrum is presented in fig.3.13.

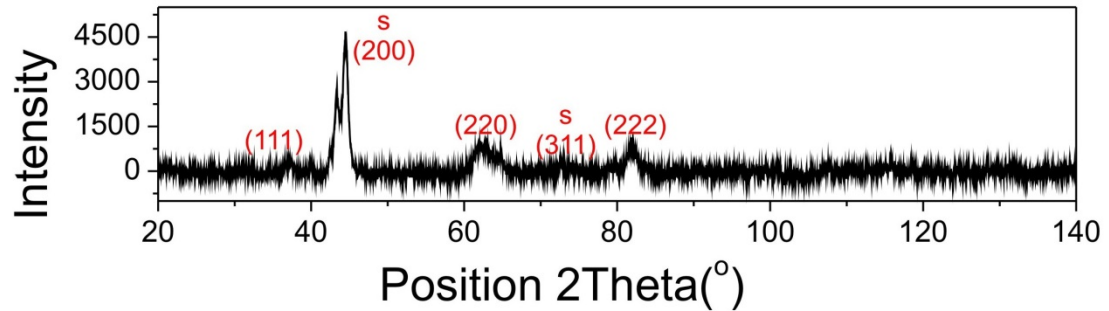


Figure 3.13: Example of spectrum of TiAlCN/VCN coated on M2 HSS substrate, collected by using Bragg-Brentano geometry.

Low-angle X-ray diffraction profiles can provide detailed information about the multilayer periodicity and thickness of the individual layers that make up a multilayer. The principle works with Bragg-Brentano geometry but the calculations are different. The distance of the lattice can be calculated from modified Brag's law:

$$\sin^2(\theta) = \left(\frac{m\lambda}{2\Lambda}\right)^2 + 2\delta \quad (3.10)$$

Where,  $2\theta$  is the angular position of the Bragg peak,  $m$  is the order of the reflection,  $\lambda$  is the X-ray wavelength,  $\Lambda$  is the bilayer period, and  $\delta$  is the deviation of the real part of the refractive index of the film from unity [115].

For low angles ( $0.3^\circ$ - $0.6^\circ$ ),  $\delta$  is about  $10^{-5}$  and it can be neglected. By transforming equation 3.7, the bilayer thickness can be obtained:

$$\Lambda = \left( \frac{m\lambda}{2\sin(\theta)} \right) \quad (3.11)$$

For all measurements the angle  $\theta$  has been varied between 1 and 10 degree. Figure 3.14 shows an example of a Low-angle X-ray diffraction spectrum for the same sample as in fig.3.14.

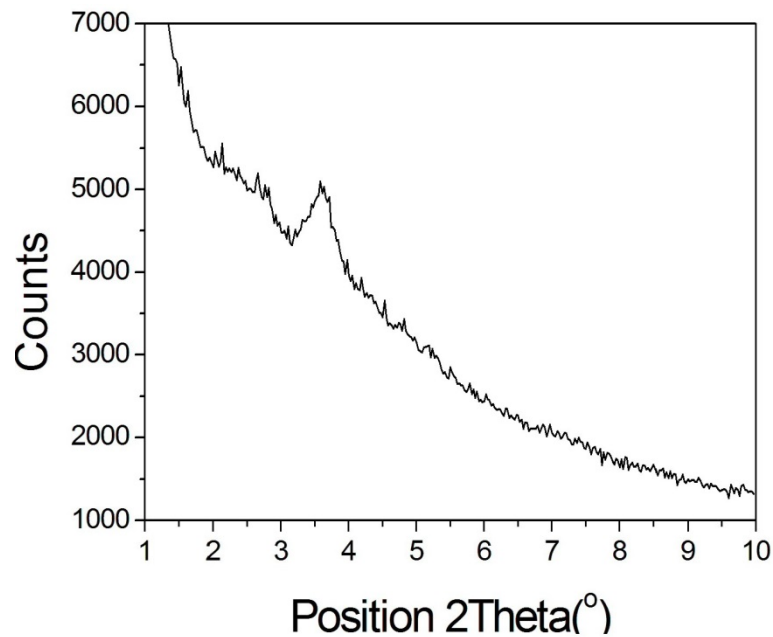


Figure 3.14: Example of Low-angle X-ray diffraction spectrum.

Glancing angle geometry, also called Grazing Incidence Configurations (GIXRD), is used to measure structure and phase of the near surface region of the sample. Moreover, this technique allows one to obtain depth-resolved structural information by measuring diffraction patterns under different angles of incidence. Compared to Bragg- Brentano geometry, the incident beam penetration depth,  $\tau$ , is much smaller (penetration depth reduced from micrometre to nanometre range). Thus, the signal produced from the substrate is weak and the signal from the coating is intense. This geometry is a

modification of the Bragg-Brentano geometry, where the x-ray source is fixed at a low angle,  $\alpha$ , and the detector is moved [116].

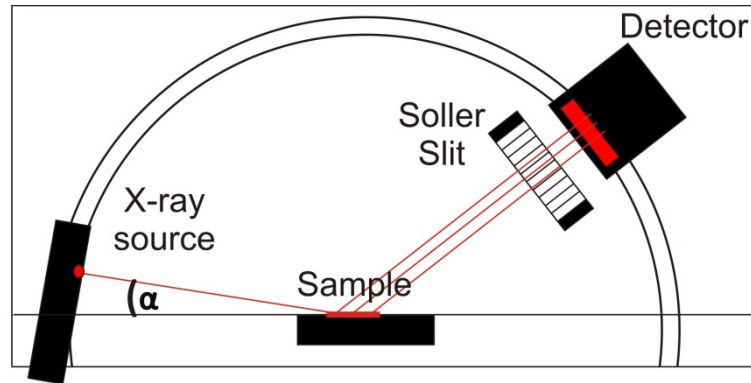


Figure 3.15: Glancing angle geometry configuration

Fig.3.15 shows a typical GAD system. X-rays pass through a suitable slit system and hit the sample while the detector scans the XRD pattern. The diffracted beam optics is modified to parallel beam optics and the Soller slit is incorporated in the diffracted beam. The penetration depth is function of incident beam angle  $\alpha$ , diffracted beam angle,  $2\theta$ , and linear absorption coefficient,  $\mu$ :

$$\tau = \frac{\sin\alpha \sin(2\theta - \alpha)}{\mu(\sin\alpha + \sin(2\theta - \alpha))} \quad (3.12)$$

In the experiments, the XRD stage PANanalytical X'pert has been used for crystal structure analysis and residual stress investigation. The x-ray source was Cu-K $\alpha$ 1 radiation with a wavelength of  $\lambda = 1.5406$  nm. The X-ray generation tube voltage was 45 kV and 40 mA.

### 3.5.5 Raman spectroscopy

Raman spectroscopy is based on the measurement of radiation scattered from a sample [117]. For this purpose, a sample is irradiated with light, usually laser sourced. There are two kinds of light that are reflected from the sample: A small fraction of light that does not interact with matter is scattered and exits the sample at a different angle with the same wavelength as the original incident wave. This is called Rayleigh scattering. The interaction of light and a molecule leads to a very short-lived distortion of the electron cloud caused by the oscillating electric field of the light. The electron cloud of the molecule is also perturbed by molecular vibrations; it is possible for the optical and vibrational oscillations to interact, leading to Raman scattering. The resulting wavelengths correspond to certain vibrational and rotational transitions and can be above and below the energy of the incident beam (Stoke and anti-Stoke respectively). A Raman spectrum consists of scattered intensity plotted vs. energy. Each peak corresponds to a given Raman shift from the incident light energy  $h\nu_0$ . The spectra are of use in structural chemistry.

Raman Spectroscopy was used to analyse carbon phases in coatings. Most characteristic carbon bands appear in the wave number range  $1200\text{-}1700\text{ cm}^{-1}$ . Usually, two Raman active modes are observed in this region in carbide films, one at approximately  $1570\text{ cm}^{-1}$  and another at  $\sim 1360\text{ cm}^{-1}$ . These bands are characteristic of graphitic (G) and disordered (D) bonded carbon. The Raman active G and D can help to interpret the nature of carbon bonds in the coating.

Raman spectra were obtained using HORIBAJOBIN YVON HR800 integrated Raman spectrometer fitted with green ( $\lambda = 532\text{ nm}$ ) and UV ( $\lambda = 325\text{ nm}$ ) lasers. A silicon based CCD detector was used to collect the output scattered light. Various intensity filters were

used in order to protect the coating from the high intensity irradiation that may damage the surface.

### 3.5.6 Film Thickness

Profilometry techniques are used to measure the thickness and roughness of a coating. Generally, these techniques can be divided in contact mode and non-contact mode. The stylus instrument is a widely used profilometry tool. The stylus profilometry is based on contact measurement of the sample. A stylus moves across the surface of the sample. A vertical displacement of the stylus is converted to a height value in Z, equivalent to the step height on the examined surface. The mechanical movements of the stylus are converted into an electrical signal by a transducer attached to it, and then amplified and demodulated. Finally, the signal is passed to a computer where, by using software, it can be analysed and stored. In this experiment a profilometer type Dektak 150 (Veeco Instruments) was used to measure coating thickness and the depth of the wear track. In order to measure the thickness of the deposited film, part of sample (usually silicon substrate) is masked with TiO powder. After the deposition process, the powder is wiped off and the height difference between substrate and coating can be measured. The step height represents the coating thickness. Figure 3.16 shows a schematic of the signal transfer from the sample to the computer.

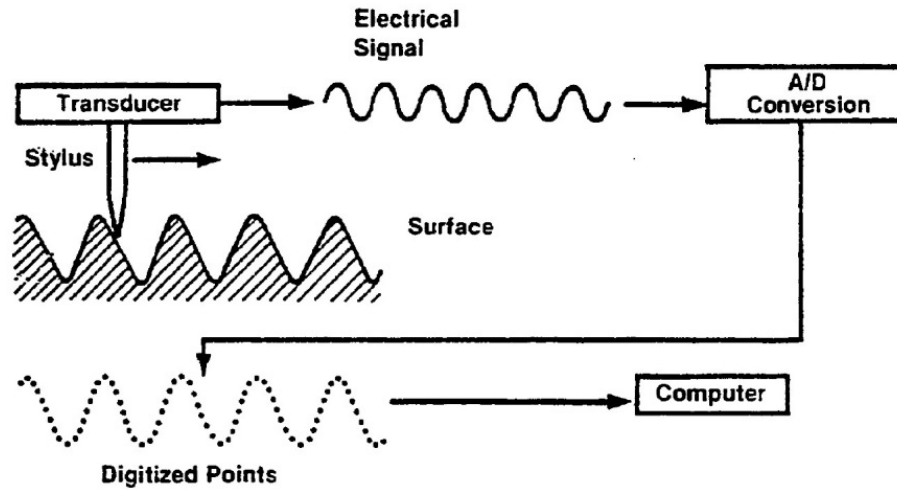


Figure 3.16: schematic diagram of stylus profilometer [118].

### 3.5.7 Pin on disc test

Wear resistance is next to hardness and adhesion as one of the most important properties for cutting tools. Wear of materials occurs during an interaction between two surfaces or during an interaction of the exposed surface with abrasive particles, fluids, active chemicals or heat [119]. Wear is the removal of material due to friction between one or two moving surfaces [120]. Wear is a complex process, which involves different mechanisms. Elementary mechanisms are presented in table 3.3:

Loss of material	Displacement of material	Material discontinuities	Buildups
Microdissection; Peel inequality; Desquamation.	Fissuring; Polishing.	Surface scratches; Vertical cracking;	Antibodies; Oxide film; Settlement.
<b>Changes in geometric structure of the surface</b>		<b>Changes in chemical composition</b>	
Work hardening; Directional shift of the structure; Phase transitions.		New components; Surface oxides.	

Table 3.4 Elementary tribological process [99]

Tribological processes involve different kinds of wear. The several forms of wear[121], [99, 122] are:

- Adhesive wear is associated with the formation of adhesive connections such as bonding or welding between surfaces in contact under an applied load. If the adhesive connection is stronger than a cohesive strength of the material, such bonded parts of surfaces get plucked out during repeated sliding from the softer surface. Surface topography plays an important role in adhesive wear i.e. the more smooth the surface, the fewer interactions between surfaces.
- Abrasive wear is associated with circular or linear sliding motions, usually with an applied load. Particles are removed as a result of microcutting, scratching or fissures. This process occurs at the contact point where there are loose abrasive particles or there is an unevenness of harder materials which act as localized microblades. Wear processes with oxidized products in the contact area behave similarly to that described.
- Corrosive wear is the removal of material associated with electrochemical reactions. Products of these reactions contribute to other wear mechanisms.
- Fretting wear occurs during very small (in range of a mm) mutual movements of bodies in contact. In a broad sense, fretting refers to mechanical, thermal, chemical and electrical effects occurring in the contact zones during low - amplitude rotary or reciprocating movements, as a result of vibration, pulsation loads etc.
- Spalling wear (delamination wear) is associated with the delamination of particles from the substrate material. These particles are formed by the propagation of microcracks initiated inside the surface layer due to cyclic interaction of contact stresses.
- Diffusional wear develops at high temperatures by selective constituent diffusion resulting in weak areas and crater formation.
- Fatigue wear is associated with the formation of fatigue cracks due to repeated elastic and plastic deformations. It is a result of the superposition of internal stresses and stresses from external loads. In areas of stress concentration, fatigue microcracks are formed

which, with time, transform into macro-cracks. The final result is a tearing of the core pieces of metal.

The sliding wear coefficient  $K_c$  is proportional to the volume,  $V$ , of removed material during sliding distance,  $L$ , under load,  $F_n$ , and can be calculated from the formula:

$$K_c = \frac{V}{F_n L} \quad (3.12)$$

The removed volume was calculated by measuring the cross section of the wear track  $A$  multiplied by its perimeter with radius  $R$ . The area was measured with the profilometer.

$$V = A2\pi R \quad (3.13)$$

In this work the deposited coatings were investigated with a CSEM pin on disk tribometer.

The dry sliding friction and wear properties were investigated using a computer-programmed CSM ball-on-disc tribometer with a 6 mm counterpart ball of alumina at conditions: applied load 5 N, sliding speed  $0.1 \text{ ms}^{-1}$ , room temperature in a range of 20–30°C, 10000-200000 laps. The friction coefficient (COF) was measured with software. In order to calculate the wear rate of coatings, after tests, wear tracks were analysed with a profilometer.

### **3.5.8 Adhesion test**

One critical feature of a coating is its adhesion to the substrate. The film-substrate adhesion strongly influences tribological performance of a coated surface. In this work, two different methods are used to measure adhesion; Rockwell C and scratch adhesion tests.

The **Rockwell C** adhesion test is easy and fast to carry out on coated specimens, giving qualitative information about the adhesive characteristics. In a Rockwell C (HRC) test, a diamond brale is used for indentation. The typical load for Rockwell C is 150 kg [123]. In order to eliminate the backlash, a low load (minor load) is applied before a main heavy load. This crushes dust particles on the surface and eliminates the effect of surface roughness, increasing the accuracy of measurement.

This kind of test is strongly dependent on coating thickness and substrate hardness. Loading the Rockwell tip generates damage next to the edge of the indentation mark such as cracking and chip-off at the coating. This technique does not provide a quantitative evaluation of coating adhesion; however, it can be used to establish a classification of the quality of the adhesion. The adhesion of the coating is evaluated using an optical microscope with 100:1 magnification and classified according to the four - grade scale shown on fig.3.21 [124]. The strength adhesion quality varies from class 0 to class 3, where class 2 and 3 indicate poor, unacceptable adhesion.

Acceptable adhesion	Class 0	Class 1
		
Unacceptable adhesion	Class 2	Class 3
		

Figure 3.17: Determination of adhesion according to BS ISO 26443:2008 standards [124]

The **scratch test** is one of the most commonly used, effective, and fast methods to obtain the critical loads that are related to adhesion properties of coatings. It gives quantified

information about coating failures. However, measurements are very sensitive to changes in intrinsic (loading rate, scratching speed) and extrinsic factors (substrate and coating properties, surface roughness) [125].

The technique involves generating a controlled scratch with a diamond tip on the sample surface. A diamond stylus with applied normal, increasing or constant force moves along the sample (fig.3.18a). With increasing load, the stylus produces progressive mechanical damage in the coating and the substrate through the complex combination of elastic and plastic indentation stresses, frictional forces, and residual internal stresses in the coating-substrate system. The progressive damages along scratch track is shown in fig.3.18b).

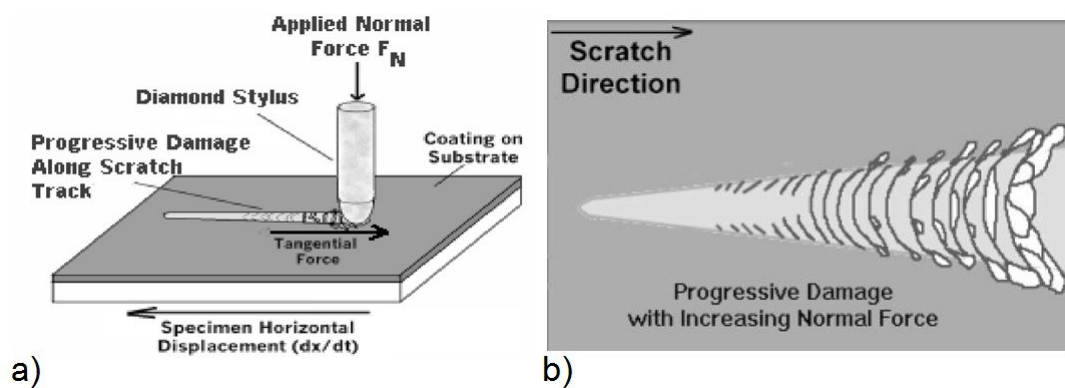


Figure 3.18: Scratch test for the determination of the adhesive strength: a) principle of scratch test, b) progressive damage along scratch track [126].

The coating failure is accompanied by acoustic emission. Resulting elastic waves are detected with acoustic emission equipment and give the first indication of critical load failure. The coating failure post facto observations are performed by reflected optical microscopy and scanning electron microscopy. There are different failure modes but generally they can be split into two kinds [122]:

- Adhesive failure: detachment and separation of a coating from the substrate with cracking and debonding at the coating-substrate interface.

- Cohesive failure: material damage and cracking in the coating or in the substrate, separate and distinct from detachment and adhesive debonding at the coating-substrate interface.

In this work, a CSM REVETEST Automatic Scratch Tester with enabled optical microscopy and emission recorder was used. The standard of this test is written in ASTM G171-03 and BS EN 1071-3:2005.

The Scratch tests were performed on two kinds of substrates: polished HSS discs and unpolished Inserts. The load was applied progressively from 0-10N to 80-100N. Both optical and acoustic failures were detected during the test.

### 3.5.9 Hardness

Hardness is one of the most important properties of a cutting tool. Hardness tests show an ability to resist plastic deformation, fracture toughness and crack propagation [99]. Coatings for the cutting tools have to be strong in order to function without suffering from undue deformation. There are many ways to measure hardness but the principle is the same. An indenter with an applied load penetrates the surface of the coatings and is then removed. In most of the techniques, post-facto examinations are done in order to determine the hardness of the coating. For thin films coatings, unlike the bulk materials, the loads and indenter size must be much smaller. Below, a few techniques are described.

**Knop hardness Tester** of the Mitutoyo (MicroWiZhard) was used to determine the microhardness of thin films and coatings. Due to the relatively small indenter and low load (usually 25 g), the indentation depth is very small, which in thin films eliminates plastic deformation effects of the substrate. A constant load is applied for 10 s. When the load is relieved, the unrecovered area is measured with a microscope. The hardness can be

determined as the ratio of load to area of the permanent indentation in the surface. The indenter in Knoop test is a pyramidal diamond with rectangle base. The ratio between the minor and major axis is 7:1 and respective face angles are  $172^\circ$  for the long edge and  $130^\circ$  for the short edge. The indentation depth is approximately 1/30 of its length (surface wear: analysis, treatment and prevention). The schematic diagram of the indentation tip and shape of the permanent mark is shown in fig.3.19.

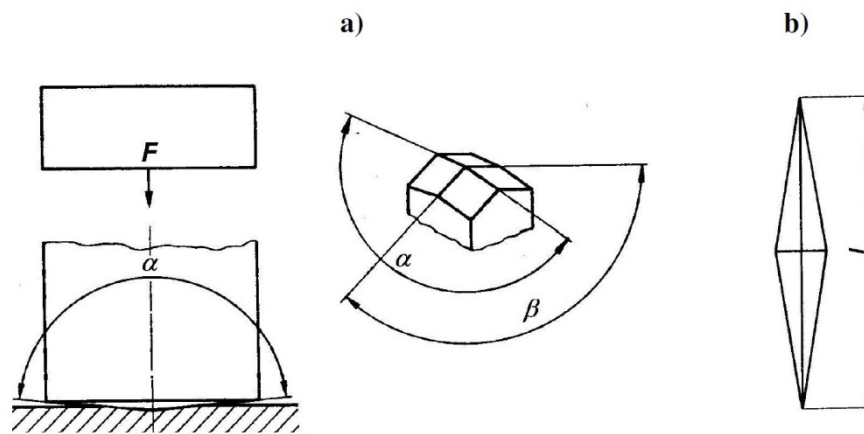


Figure 3.19: Schematics of: a) an indenter applied for microhardness measurement by Knoop method, b) an indentation of an indenter in the material;  $\alpha=172^\circ$ ,  $\beta=130^\circ$ , d-longer diagonal of the indentation (PN ISO 4545:1996standard )

The Knoop hardness HK or KHN is then given by the formula [123]:

$$KHN = \frac{P}{A} = \frac{P}{CL^2} \quad (3.13)$$

Where P = applied load in kg,

A = the permanent indentation area of the indentation in  $\text{mm}^2$

L = measured length of long diagonal of indentation in mm

C = Constant of indenter relating projected area of the indentation to the square of the length of the long diagonal (0.07028).

### Nanohardness test

The nanohardness and elastic modulus ( $E$ ) was measured by CSM nanoindentation tester equipment with Berkovich three-sided pyramidal indenter. Nanoindentation is a dynamic hardness measurement that combines continuous recording of loads and indenter displacements, while regulating rate and velocity [123]. The curve of the indentation force versus the indentation depth is recorded as in fig.3.20.

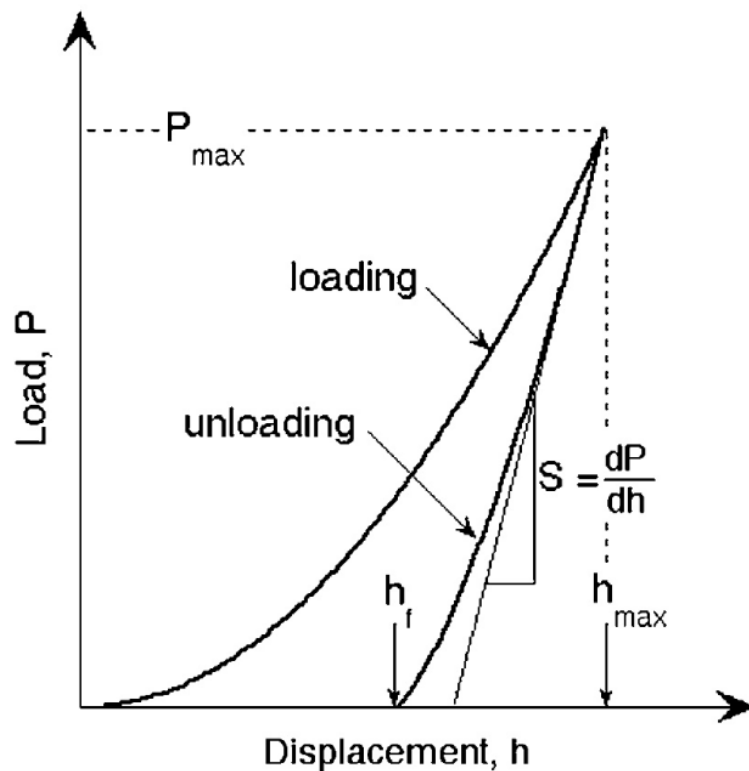


Figure 3.20: Loading and unloading curve of nanoindentation test [127].

The measured indentation curve is a function of the mechanical properties as universal hardness, plastic hardness and the Young's modulus [128, 129]. The Oliver-Pharr method is the most common method used for establishing the projected contact area and predicting the elastic modulus [130].

The formulas 3.14 and 3.15 for calculating hardness and Young's (elastic) modulus are presented below [127].

$$H = \frac{F_{max}}{A} \quad (3.14) \quad \frac{1}{E_{eff}} = \frac{1-\nu^2}{E} + \frac{1-\nu_i^2}{E_i} \quad (3.15)$$

Where:  $F_{max}$  is the maximum load,  $E_{eff}$  the effective elastic modulus,  $E$  is the Young's modulus of the sample,  $\nu$  is the Poisson's ratio of the sample,  $E_i$  is the Young's modulus of the indenter and  $\nu_i$  is the Poisson's ratio of the indenter.

### 3.5.10 Dry High Speed Milling

The cutting performance of the TiAlCN/VCN series coated inserts was tested in comparison with a cemented carbide insert coated with standard TiAlN coating provided by Sandvik. Coatings were deposited on R390-11-T3 08M-PM, 40  $\mu\text{m}$  edge radius inserts presented in fig 3.21a). Milling tests were run on a P20 steel bar with hardness of 48 RC using a high-speed milling machine, MAZAK FJV-25. The bar is hard for the tested coating, which leads to high temperature generation. However, there are good conditions to test mechanical properties of the coatings. The cutting conditions were as follows: cutting speed 100  $\text{m min}^{-1}$ , feed 0.1  $\text{mm/rev}$ , and cutting depth 0.1  $\text{mm}$  and working engagement of 56  $\text{mm}$ . The cutting of the bar was applied with roll entry as shown in fig 3.21b).

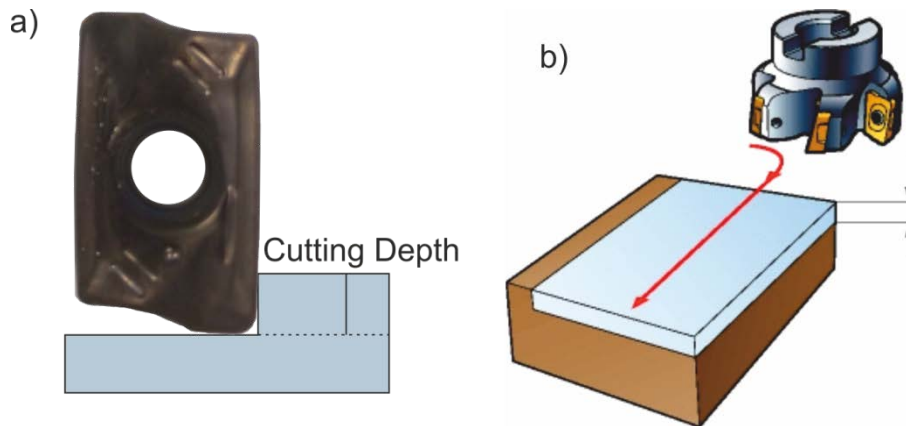


Figure 3.21 Dry High Speed Milling test; a) face milling using the R390-11-T3 08M-PM cutting insert with indicated the cutting depth. b) The roll entry of the milling head.

Each pass over the bar is equivalent of 330 mm of machining distance. The milling head is loaded with only one insert, so each insert has to cut seven times more material than when head is fully loaded with inserts.

The flank wear was measured using an optical image analyser by regularly interrupting the test until reaching pre-defined criteria of 0.13 mm, (as shown in fig 3.22) from which the tool lifetime was obtained or tool tip was damaged.

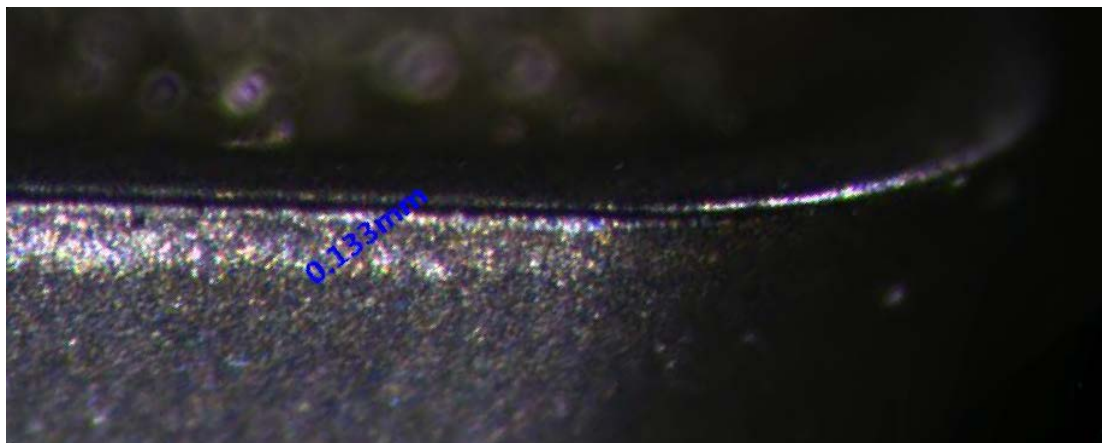


Figure 3.22 Optical microscopy analysis of the cutting edge. Presented insert has 0.133 mm wide wear along the edge.

After reaching critical values, In order to investigate the coating failures, both rake and flank sites of inserts were analysed with EDX spectroscopy and SEM microscopy.

A dry high speed machining is performed using two flute 6 mm diameter drills coated with one of TiAlCN/VCN coating (see section 4.6.4). The end mill was used for dry machining of wrought 2024 grade aluminium, which is a challenge for machining. The experiment was conducted at Sandvik Coromant, Sheffield using their DMU60 milling machine. The spindle speed of 3000 rpm and the feed rate of 0.15 mm/rev were used during machining. No lubricant was used for machining; however air was used through the tool.

## 4 Effect of Pulse Energy on the Ion Etching

Plasma etching is a very important step prior to coating deposition. It cleans specimen surfaces from residual dust and removes oxidation layers. In the case of a highly energetic plasma during etching, highly ionized particles are implanted into the near surface region of the sample. This effect is called Plasma Source Ion Implantation (PSII). Both effects enhance adhesion strength and, thus, the mechanical properties of the coatings. Conrad and Radtke in 1987 described that ion implantation produces material with improved microhardness and wear properties; it dramatically improves the life of manufacturing tools in industrial applications [131]. However, high energetic etching may cause some problems. Firstly, material from the substrate is removed due to the existence of a plasma sheath. In the case of cutting tools, the plasma sheath compresses near sharp edges as shown in fig.4.1. This enhances the electric field at the vicinity of the edge, which causes higher material removal at cutting edges than in the centre of the substrate[132, 133]. This may lead to edge blunting.

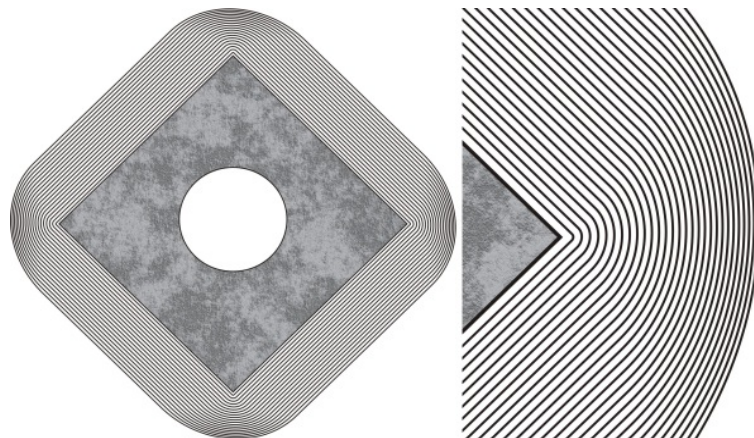


*Figure 4.1: Sheath edge curves around a square corner (after [132] and [133]).*

Secondly, quick changes from low to high pulse energy can cause arcing. For that reason, pulse energy tends to be gradually increased (this process will be called the ramping step). However, this increases etching time, meaning that the cutting edge is exposed for a longer time.

In this experiment, plasma parameters are investigated in order to understand the ramping step. Next, the thickness of removed material and the microstructure of the rake and cutting edge are investigated as a function of ramping and hold time (time after ramping, when pulse energy is constant).

## 4.1 Methodology

In this work, vanadium ion ( $V^+$ ) plasma, produced by HIPIMS technology, was used for etching. Experiments were performed using a Hauzer 1000/4 PVD system furnished with a rectangular vanadium ( $1200 \text{ cm}^2$ ) target; this was powered by a Hüttinger HIPIMS power supply. Two sets of experiments were performed; one was for plasma chemistry analysis and the other for microstructure and erosion analysis.

Plasma analysis:

For plasma analysis, the pulse duration was changed (which is related to pulse energy) while the other process parameters were kept constant. The run was performed without any samples. In order to investigate deposition rate, ion flux and optical emission, diagnostic devices were employed; these included quartz crystal microbalance, flat probe and optical fibre. The optical fibre was attached to an optical emission spectrometer (OES) and all devices were installed into the chamber. Fig.4.2 shows a

schematic of the chamber with the positions of the installed devices. The quartz crystal microbalance was placed in the vicinity of the target

The flat probe and optical fibre were placed on the substrate table. The flat probe was directed towards the target with the aperture of the optical fibre directed downwards; this was in order to measure plasma intensity in the middle of the chamber. The probe and the quartz crystal microbalance were placed at similar distances from the target.

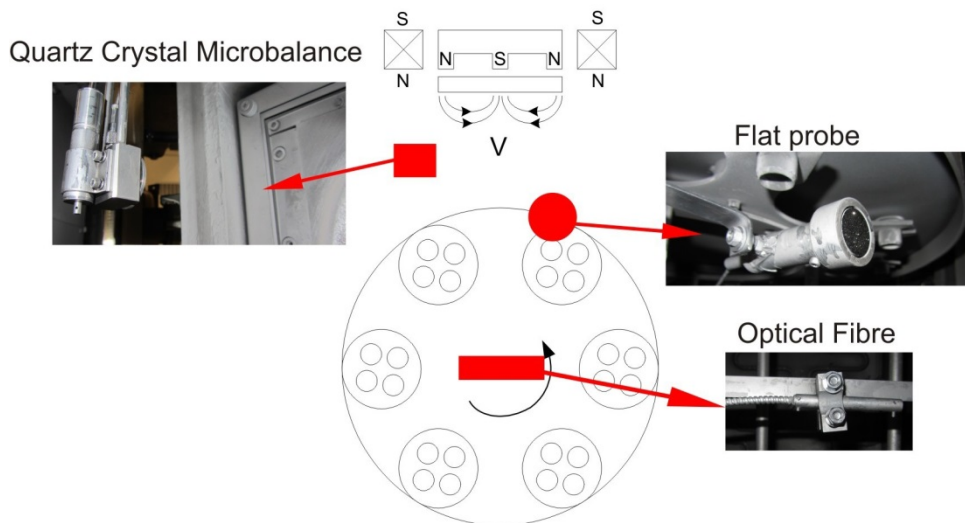


Figure 4.2: Chamber equipment with plasma diagnostic devices: Quartz crystal microbalance, flat probe and optical fibre attached to Optical Emission Spectrometer.

Additionally, using an oscilloscope, cathode current width and cathode voltage amplitude were measured.

Initially, the chamber was pumped down to a pressure of  $9.1 \times 10^{-6}$  mbar and heated up to  $100^\circ$  C. Etching was preceded by two target cleaning steps with target voltages of 800 V and 1300 V respectively. During etching, in order to observe the effect on the plasma conditions, with increasing charge of the cathode, charge was increased from 0 to 16 in twelve steps (0, 1, 2, 3, 4, 5, 6, 8, 10, 12, 14, 16). The target voltage was 1050 V.

For microstructure and erosion analysis, the chamber was loaded with six types of sample:

- Polished tungsten carbide inserts (PWC)
- unpolished tungsten carbide inserts (UWC)
- polished high speed steel disks (HSS)
- stainless steel disks (SS)
- Si wafers
- TEM Stainless Steels.

Areas of the HSS, SS and INSERT samples were masked with TiO<sub>2</sub> powder in order to measure the thickness of material removed.

Initially, the chamber was pumped down to a pressure of  $9.1 \times 10^{-6}$  mbar and heated to 450° C. Etching was preceded by two target cleaning steps. Target voltage for both target cleaning and etching are the same as described in the previous section. There were four runs performed with different ramping and hold times. Initially, the ramping time and the holding time were both 20 minutes. Next, the ramping time was reduced to 10 and 5 minutes whilst the holding time was kept at 20 minutes. The final run lasted 10 minutes for both the ramping and the holding time. Following these processes, the TiO<sub>2</sub> powder was wiped off and the removed thickness was measured using a profilometer. Microstructures of PWC and UPC were investigated by scanning electron microscopy and atomic force microscopy.

## 4.2 Plasma analysis results

In the first part, the cathode charge was set in sequence 0, 1, 2, 3, 4, 5, 6, 8, 10, 12, 14, 16. At each point, measurements of cathode current, cathode voltage, ion flux, deposition rate and OES spectrum were taken.

Cathode current and ion flux during the pulse for different pulse durations are shown in fig.4.3 and fig.4.4 respectively.

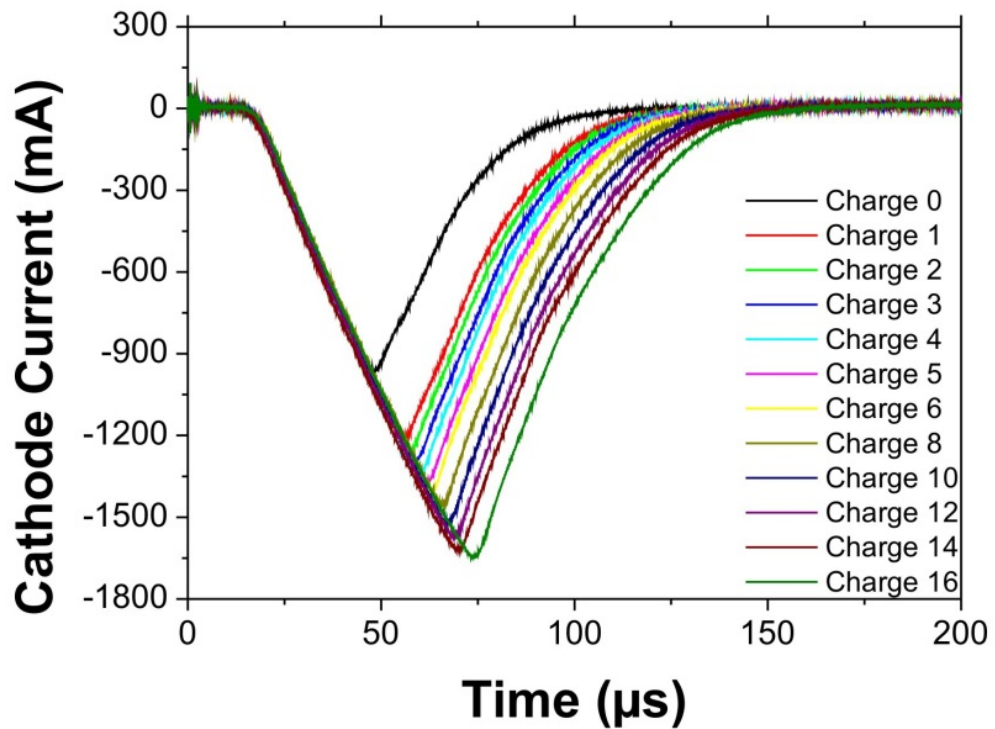


Figure 4.3: Temporal evolution of cathode current during pulse for different charge values.

Increasing the charge increases the peak cathode current from 0.97 A to 1.65 A; it also increases the peak ion flux current from 0.04 A to 0.11 A. For both graphs, the peak maximum shifts to the right. This is because the rate of increase is the same for each charge, therefore the effect is that the peak value occurs at a later time. The same delay can be observed at the end of the pulse. Generally, the overall shapes of the curves do not change significantly.

Ion flux profiles (fig.4.4) indicate that there are two waves of incoming plasma. The secondary plasma wave coincides with the end of the pulse, therefore it can be estimated that this is released from plasma surrounding the target.

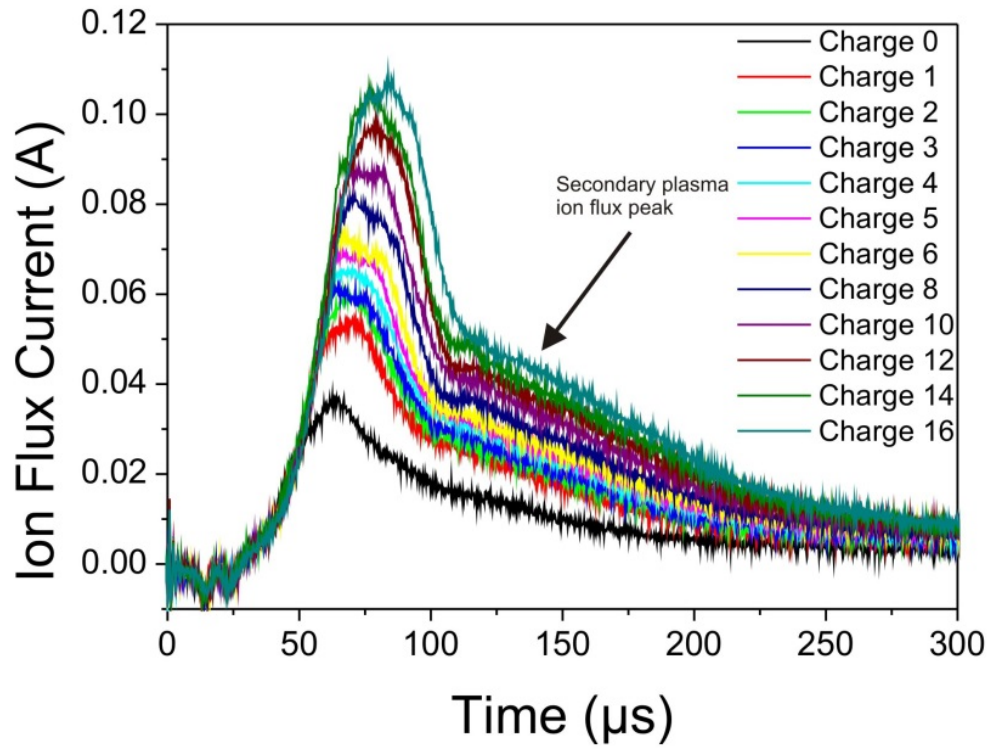


Figure 4.4: Temporal evolution of ion flux current during pulse for different charge values.

The deposition rate measured as a function of cathode current pulse width shows linear growth. This dependence is presented in fig.4.5.

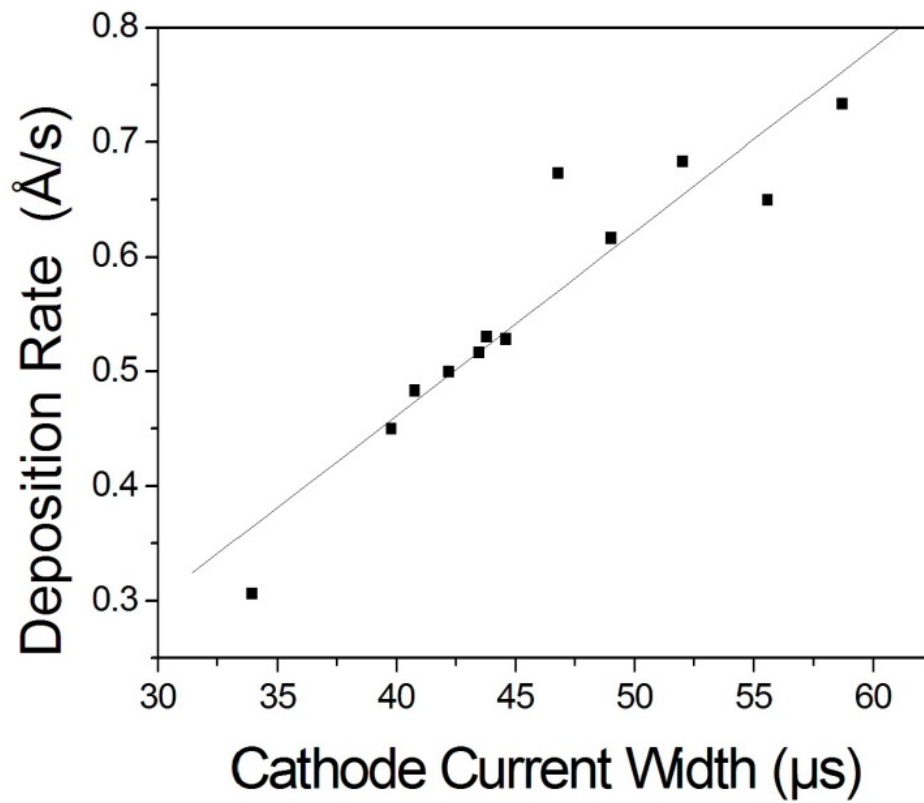


Figure 4.5: Deposition rate increases with increasing cathode current width.

With higher cathode current more particles are produced (ions, neutrals, metal vapour).

Figure 4.6 shows the relationship between ion flux current-time integral per thickness unit and charge, calculated by the time integration of cathode current.

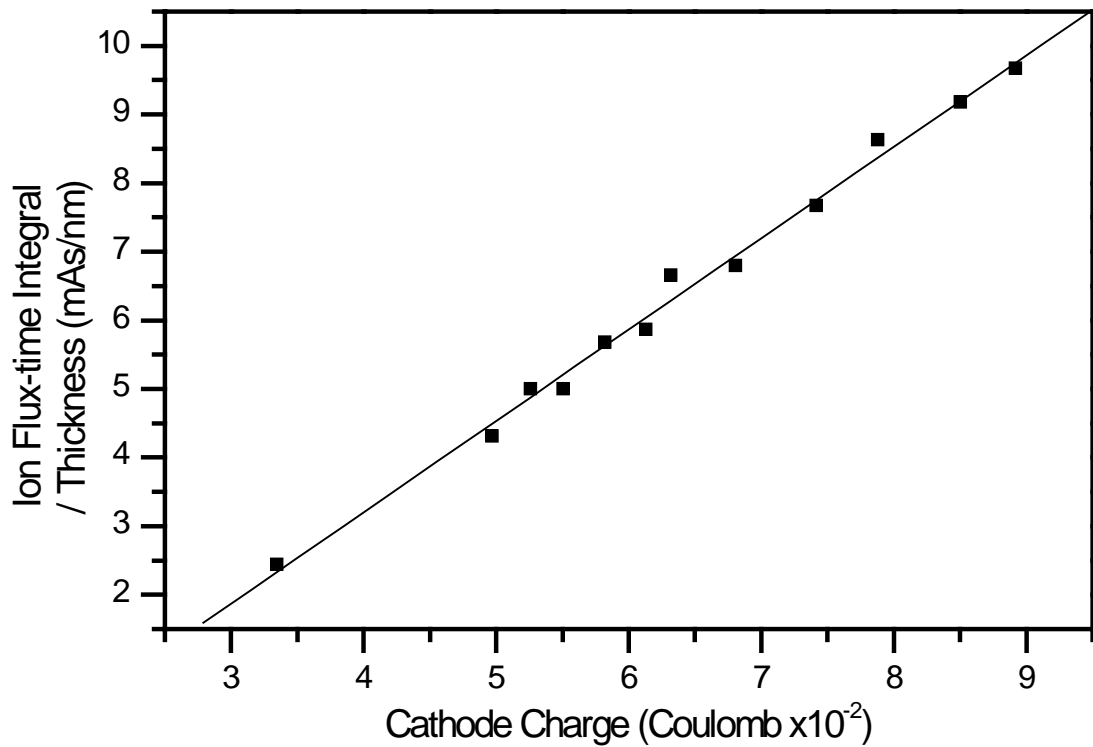


Figure 4.6: Ion flux density vs. cathode charge.

The ion flux current-time integral per thickness unit indicates the neutrals to ions ratio in deposited material. Graph 4.6 shows linear growth of ion flux current-time integral over thickness with increasing charge. It indicates that the charge of the cathode has a direct effect on the ion to neutral ratio.

In the second part, in order to investigate the plasma composition as a function of the charge, the optical emission spectra lines for Ar(I), V(I) and V(II) were chosen and investigated. Table 4.1 gives wavelength, oscillator strength and energy level for the chosen spectral lines.

Table 4.1 Properties of chosen optical emission lines for different species [134]

	Wavelength (nm)	Oscillator Strength	Lower wavenumber (cm <sup>-1</sup> )	Higher wavenumber (cm <sup>-1</sup> )
Argon (ArI)	696.025		137.4	26299
Vanadium (VI)	382.856	0.0781	12706	396313
Vanadium (VII)	371.547	0.032	106237.5718	120600.8905

Figure 4.7 shows how photomultiplier tube current signals respectively for a) Ar(I), b) V(I) and c) V(II) evolve during the pulse time for different charge. For all species, the PMT current increases with charge. The value for argon changed in the range of 1.56 A - 2.2 A, vanadium(I) in the range of 0.68 A - 1.4 A and vanadium(II) in the range of 0.67 A - 1.85 A. The increase developed similarly in all three cases. It is similar to the evolution of cathode current (fig.4.3). Maximum peak shifts to the right and the pulse became broader; this is due to the same rate of increase, however, the overall shape of the curve remained the same.

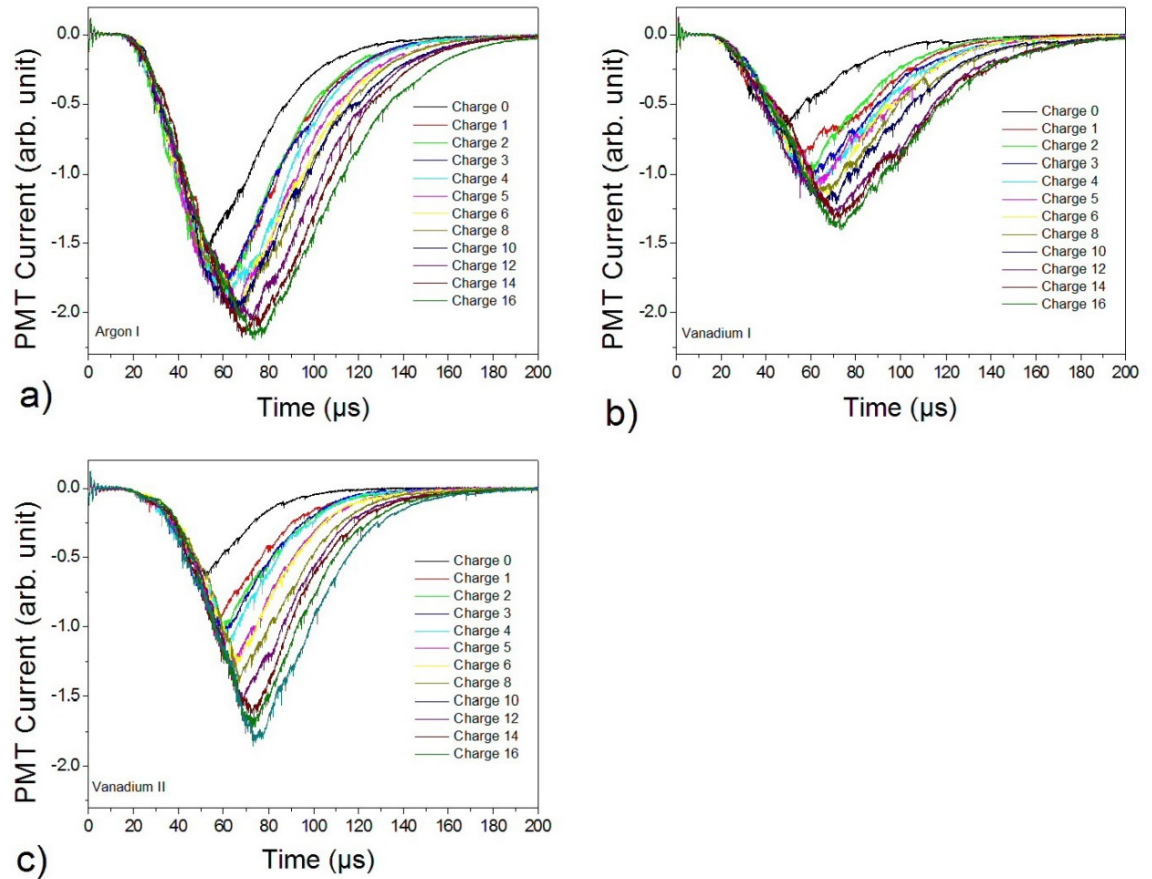


Figure 4.7: Temporal evolution of PMT current during pulse for different charge values. a) Argon(I), b) Vanadium(I), c) Vanadium(II).

In order to observe the difference in PMT peaks for different species for the same charge, normalised time-resolved graphs of the PMT signal were studied for charge 0 and charge 16 (fig. 4).

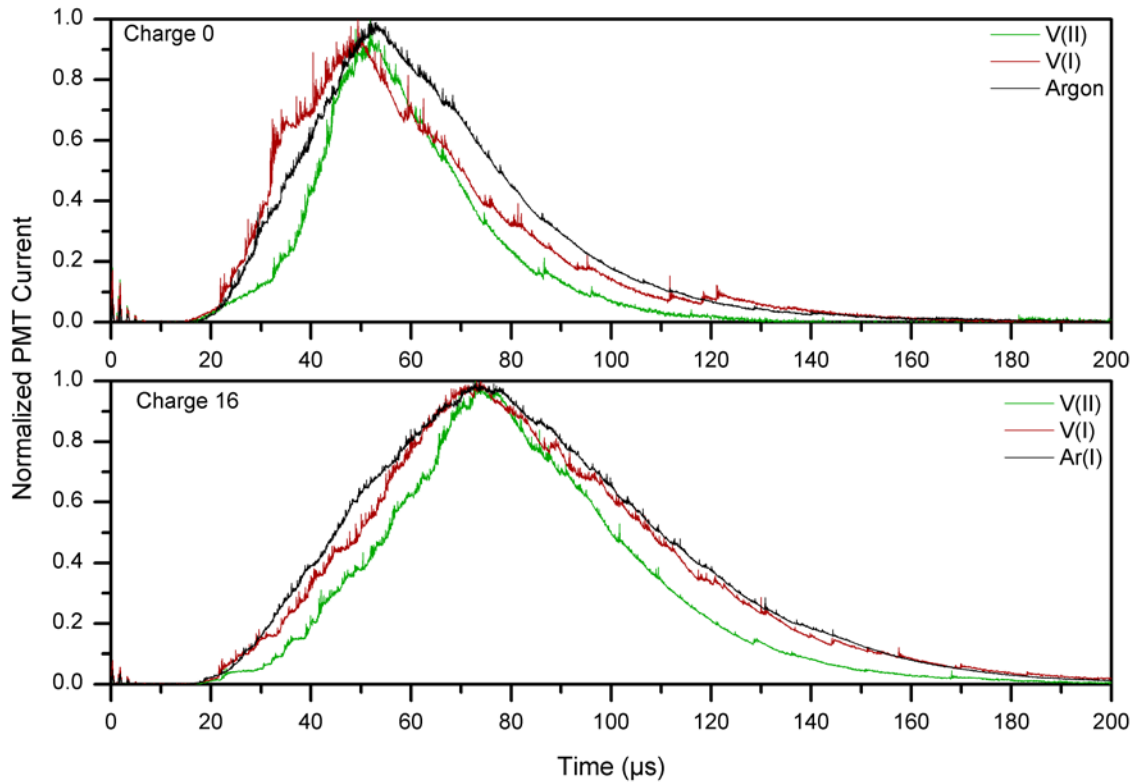


Figure 4.8: Normalized PMT current for different species, for charge 0 and 16.

One can see that argon (I) and vanadium (I) propagate similar, however, vanadium (II) appears after some delay. This could be due to the creation of ions taking more time and it often happens by a multi collisional process. This behaviour is the same for both charges.

By plotting PMT time-integral against cathode current width-time integral on a logarithmic scale for all species (fig.4.9), it allows for the K factor to be determined in the following relationship:

$$I_{\text{emission}} = I_d^K \quad (4.1)$$

Where  $I_d$  is discharge current [135].

Exponent K determines the number of processes involved to create their emission lines. From equation 4.1, the K factor for argon should be 1 (only excitation), for the

neutral metal it should be 2 (sputtering from target and excitation) and the ion should be 3 (sputtering, ionization, excitation) [135].

From image 4.9, the exponent (K) can be found by determining the slopes of each species. The obtained values are: Ar(I): K = 0.73, V(I):K = 1.22, V(II):K =1.57.

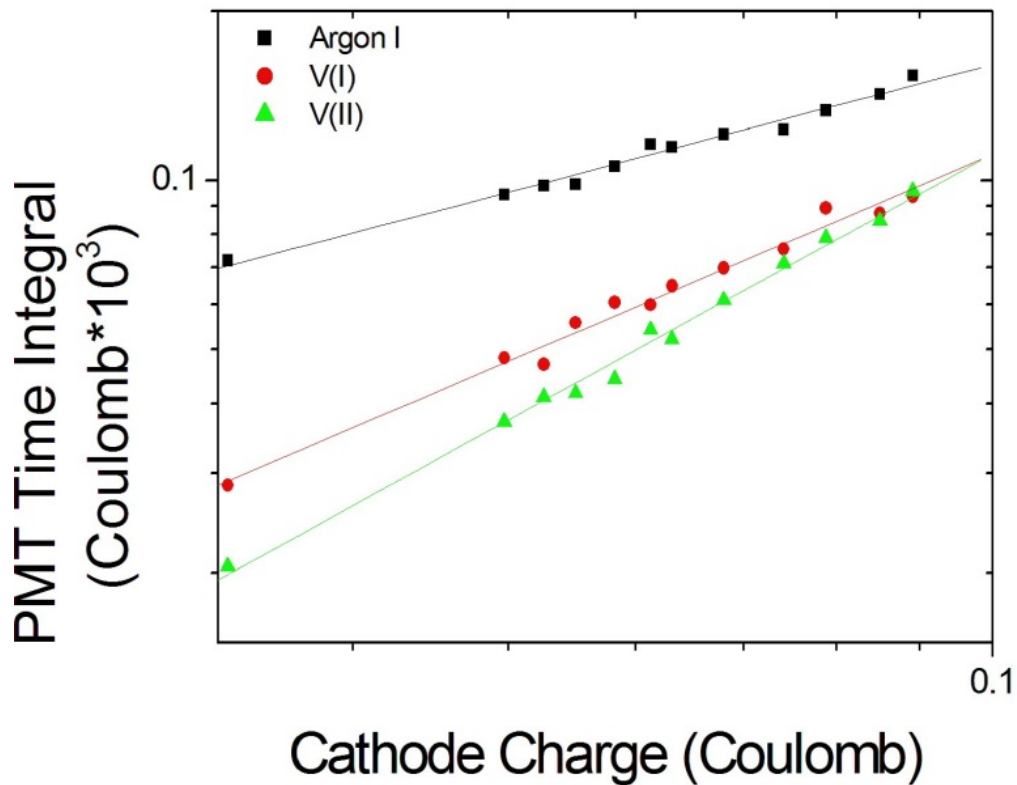


Figure 4.9: With increase of cathode current the intensity of all species increases. Slopes for trend lines are Ar:0.73, V(I):1.22, V(II):1.57.

The determined K factors are smaller than the model predicts. The model also postulates that rarefaction of argon gas may cause the reduction in its K value. It is possible that the K factor is also reduced by rarefaction of metals. Another explanation for lower stray K values for metals may be that there is enough energy in the system to

excite atoms in only one or two steps. If ions are obtained in one step, an atom is ionized during sputtering; if in two steps, an atom is sputtered and ionized without excitation.

Ehiasarian et al. [136] obtained, by the mass spectrometry, the plasma composition for charge 16. Results of their research are presented in fig.4.10.

The intensity of the emission line depends on the number of species. The intensity of excited atoms  $I^*$  is related to the number of excited atoms  $n^*$ ; this is equal to the intensity of ionized atoms  $I^+$  and proportional to the number of ionized atoms  $n^+$ .

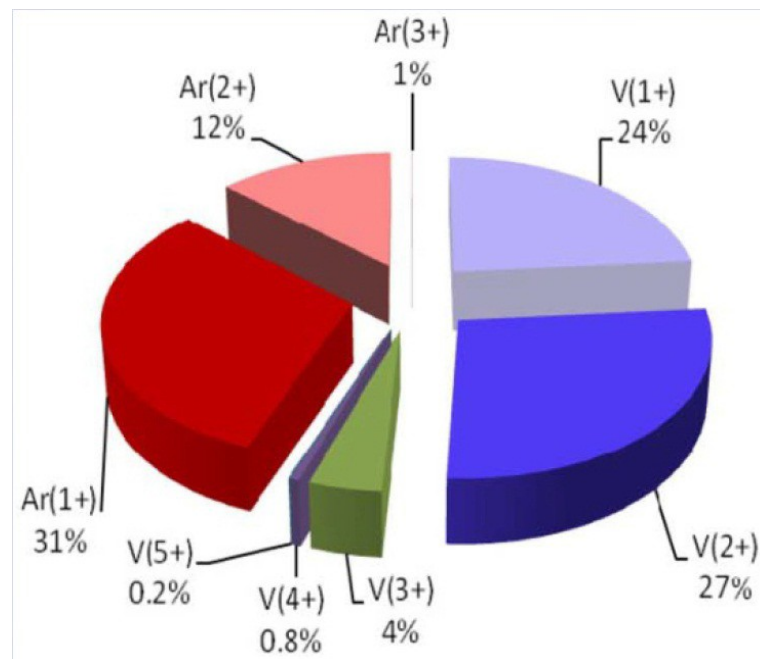


Figure 4.10: Plasma composition obtained with mass spectroscopy

According to Saenger and Rossnagel's model, ionization is the step following the excitation; this means that the number of ionized atoms depends on the number of excited atoms. With these assumptions, we can state that the number of ionized atoms is related to the intensity of excited atoms with some constant  $p$ ,  $n^+ = pI^* \propto I_d^K$ .

By using previous results of plasma composition and intensity values obtained in this research for charge 16, we are able to find a relationship between the number of

ionized atoms and the intensity of excited atoms. By knowing this relationship, we are able to calculate the percentage of ionized atoms in the ion flux for different cathode currents. These calculations have been done for  $\text{Ar}^{1+}$ ,  $\text{V}^{1+}$  and  $\text{V}^{2+}$ . Results are presented in fig.4.11. Ratios of all investigated species are presented in fig.4.12. The ratio of  $\text{V}^{2+} / \text{V}^{1+}$  suggests that at some point there is more  $\text{V}^{2+}$  than  $\text{V}^{1+}$ .  $\text{V}^{2+} / \text{Ar}^{1+}$  increases faster than  $\text{V}^{1+}$ , however, the value of both are smaller than 1.

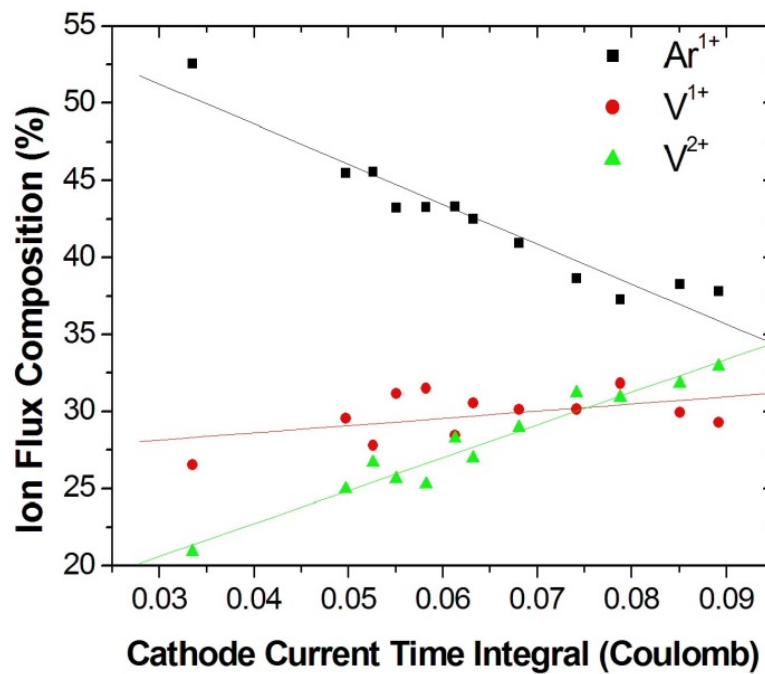


Figure 4.11: The ion flux composition in respect to cathode current

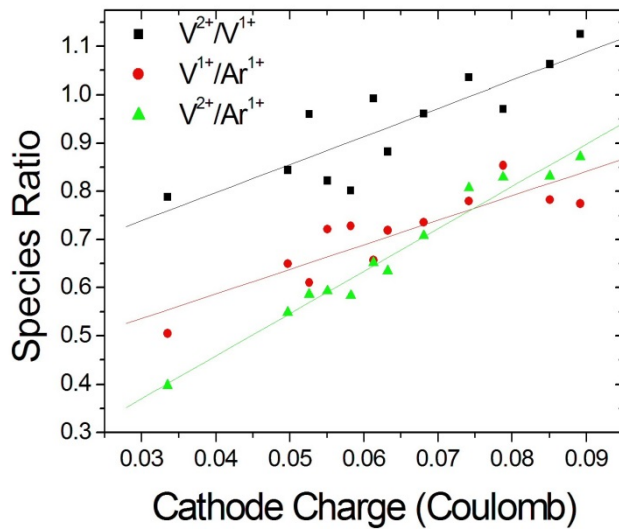


Figure 4.12: Relationship between different species as function of cathode current.

Ion quantities obtained in the previous step enable us to simulate the erosion and implantation within Insert by using dynamic TRIM simulation. Simulations were performed for charge 0 and charge 16. For simulation, it was assumed that the substrate consists of 50 atomic percentage (at. %) tungsten and 50 at. % carbon. The input dose was calculated using formula 4.2:

$$Input\ Dose = \frac{\frac{Ion\ flux}{ion\ charge \times Probe\ area}}{Number\ of\ all\ pulse} \quad (4.2)$$

The ion charge was an average of charges of  $V^{1+}$  and  $V^{2+}$ . The calculated input dose and gas content for charge 0 and 16 are given in table 4.2. Results of simulations are presented in fig.4.13.

Table 4.2: Data input used for dynamic TRIM simulation.

Charge	Ar <sup>1+</sup> (%)	V <sup>1+</sup> (%)	Input dose( $\times 10^{16}$ ions/cm <sup>2</sup> )
0	52.56%	47.44%	590
16	37.80%	62.20%	2327

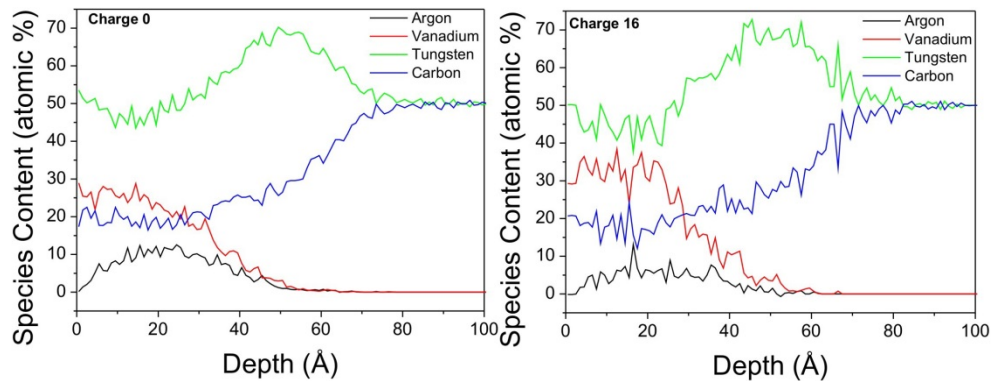


Figure 4.13: Insert surface depth profile plots of the DYNAMIC TRIM simulations; this shows how the chemical composition changes with increased depth into the substrate.

Simulation indicated that, for higher charge, vanadium implantation was more effective with V content, by approximately 10 at. %. Moreover, high vanadium content is observed for greater depth up to 25 Å. Results also show that carbon is removed more easily than tungsten. Material is removed up to approximately 35-40 Å. The increase of tungsten, to more than 50 at. %, is due to the depletion of carbon to a depth greater than the implantation of vanadium. Argon content is reduced significantly as charge is increased and the plasma becomes more metal-ion rich.

Dynamic Trim simulation generates a few output files in which depth profile is calculated at different times. By plotting those profiles for vanadium on one graph, it is possible to estimate temporal evolution of vanadium content at different depths. Fig.4.14 shows 6 plots for vanadium at different times. As the plots overlap, an offset of X: 20 % and Y: 70 % was applied.

The black line represents vanadium content at the beginning of the process where vanadium has not yet been implanted.

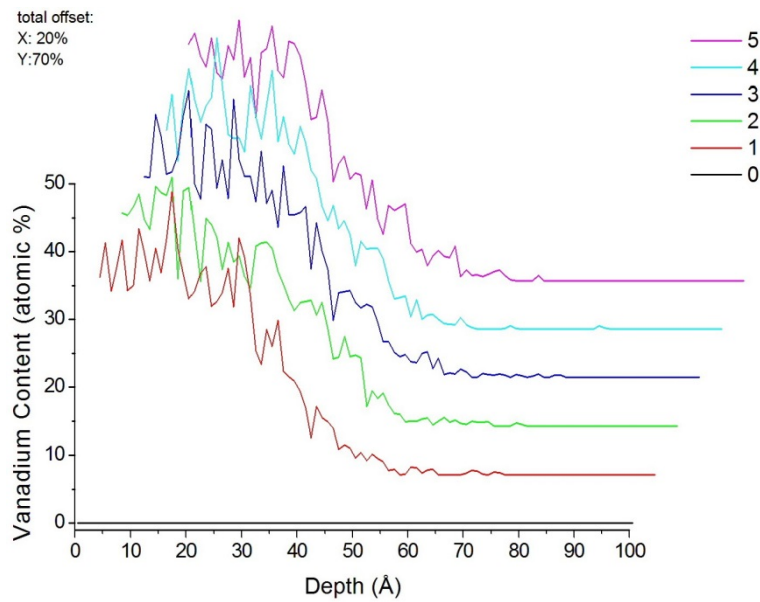


Figure 4.14: Vanadium content depth profile at different times.

There is a large difference between plots 0 and 1 and a small one between 1, 2 and 3. There is no significant difference between plots 3, 4 and 5. It might be that after a certain time, the implantation and etching are in a steady state of equilibrium. This could suggest that for higher vanadium content, the etching rate is higher.

It can be seen that for longer times, except plot 5, the implantation depth is slightly higher: 72.2 Å for plot 1 and 2, 75.5 Å for plot 3 and 79.5 Å for plot 4. For plot 5, the implantation depth is 63.5 Å; this may suggest that in time, between 4 and 5, some more material was removed from the sample surface.

### 4.3 Microstructure and ion etching analysis results

In order to determine the ion etching rate, the height of removed material has been measured by the profilometer. Fig. 4.15 presents results for polished high speed steel

disk (HSS), polished stainless steel disk (SS) and polished tungsten carbide (PWC).

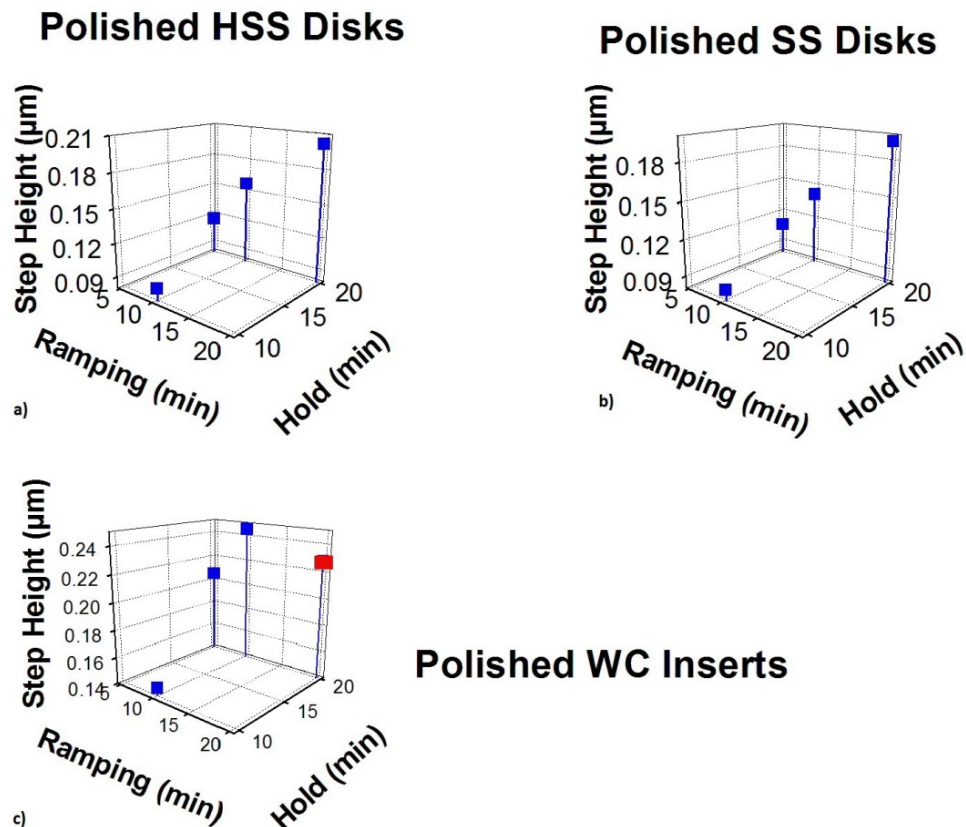


Figure 4.15: Ion etching rate as a function of ramping and hold time for polished HSS, SS and Inserts.

Three-dimensional graphs present different ramp times (X axis) and holding times (Z axis). For HSS and SS, the thickness increases linearly with ramping time. This means that we can easily control the amount of removed material by controlling time. By extrapolating the linear dependence for the data at hold=20, the amount of removed material without ramping was obtained. For HSS this is 90 nm and for SS it is 80 nm. For PWC point 20:20 it is lower; this is due to the fact that the insert was mounted at 90° to the plasma, whereas the others were faced on. However, the rest of the data points have the same trend as SS and HSS. We can see that the removal rate is relatively high; this could be due to the higher sputter rate of tungsten compared to iron.

Three areas of Inserts were investigated with SEM to define the difference in microstructure for different etching conditions: the border between masked and exposed area, the rake and cutting edge. Fig 4.16 shows images of masked area border for a) an unpolished and b) a polished sample.

For both images, an increased surface roughness can be observed in the exposed area (left side of each image).

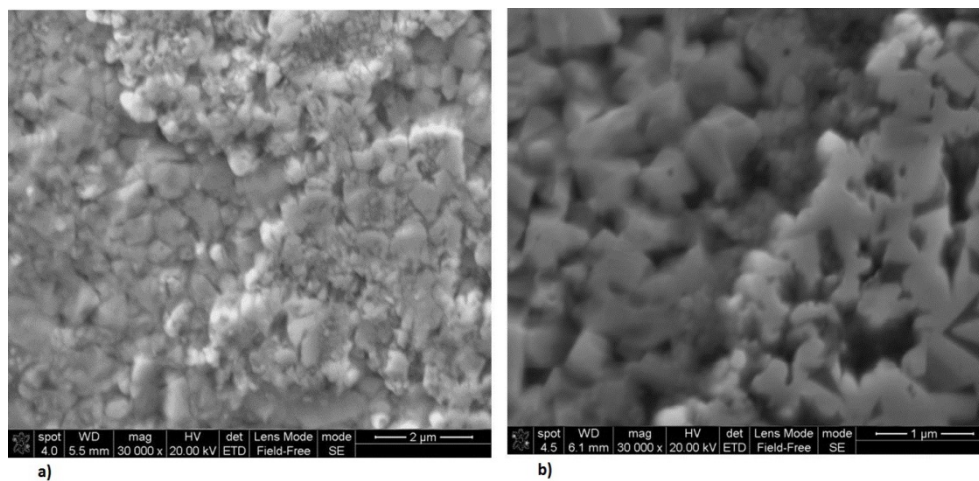


Figure 4.16: SEM image of a) unpolished and b) polished Insert at the border between masked and exposed surface. a) Loosely bonded small grains are removed from exposed area. Thus roughness of the sample increases. b) Sample roughness increased on after etching.

Also, one can see that in the region after etching there are no small grains. Small grains may be weakly bonded which would lead to low adhesive strength. These small grains are only on the surface, and they are produced during sample grinding at the factory. Figure 4.17 a) shows an untreated sample surface (sample was also not cleaned in cleaning line prior to etching) and b) shows the structure inside the sample. In order to image the cutting edge of the sample it was tilted by  $45^\circ$  with respect to observed cutting edge and  $60^\circ$  with respect to the normal edge. Fig.4.18 a) shows the edge of the polished insert after etching with 10 min ramping and 10 min of holding time.

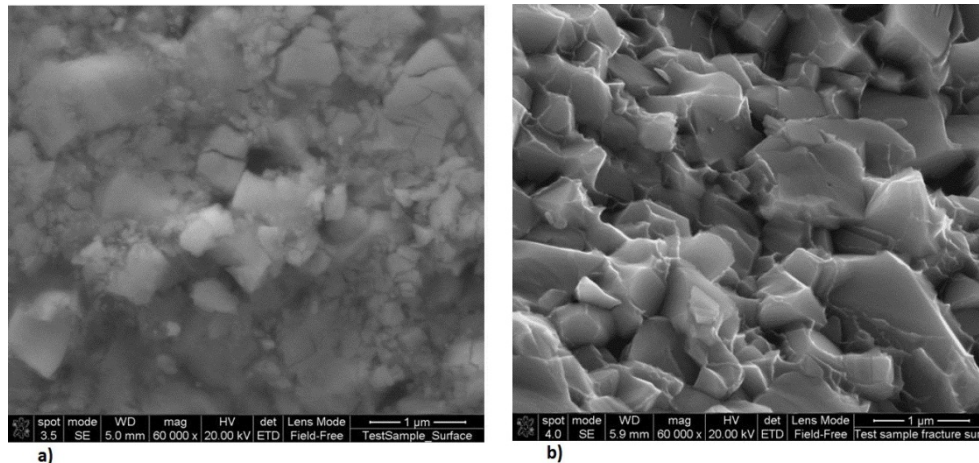


Figure 4.17: Surface of a) untreated sample and b) structure inside sample.

The amount of removed material was measured to be 150 nm on a flat surface. Fig.4.18 b) shows the edge of the SEM of the cutting edge after etching with 20 minutes ramping and 20 minutes of holding time. The amount of removed material was measured to be 230 nm on a flat surface. Observations suggest that for 10:10 the cutting edge is more rounded than for 20:20. However, the difference is not significant.

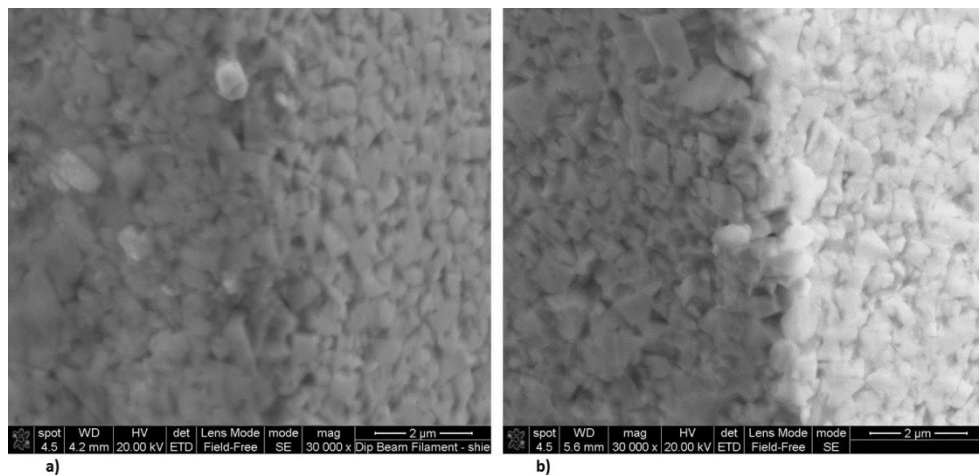


Figure 4.18: SEM image of polished Insert cutting edge. Etching parameters: a) 10 min ramping and 10 min of holding time, b) 20 min ramping and 20 min of holding time.

When the unpolished sample, with 10 minutes of ramping and 10 minutes of holding time, is compared with untreated samples, the difference is visible due to a large roundness of the edge (about 30 micron) (see fig 4.19). On these images we can clearly see that the untreated sample has a lot of small grains.

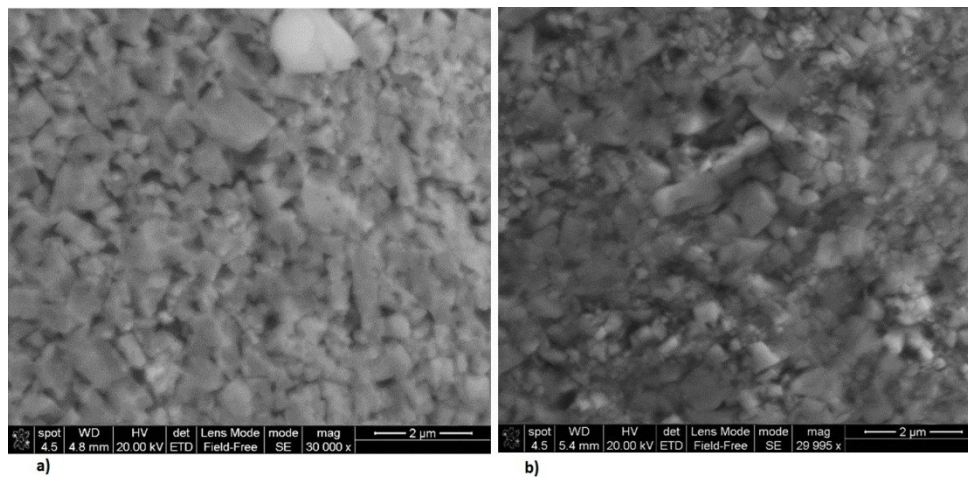


Figure 4.19: SEM images of unpolished Insert cutting edge. Etching parameters: a) 10 min ramping and 10 min of holding time, b) untreated.

Microstructure was also analysed with Atomic Force Microscopy (AFM). On fig.4.20 one can see the microstructure of polished INSERT in the masked (a) and exposed (b) areas. The sample after etching is significantly rougher.

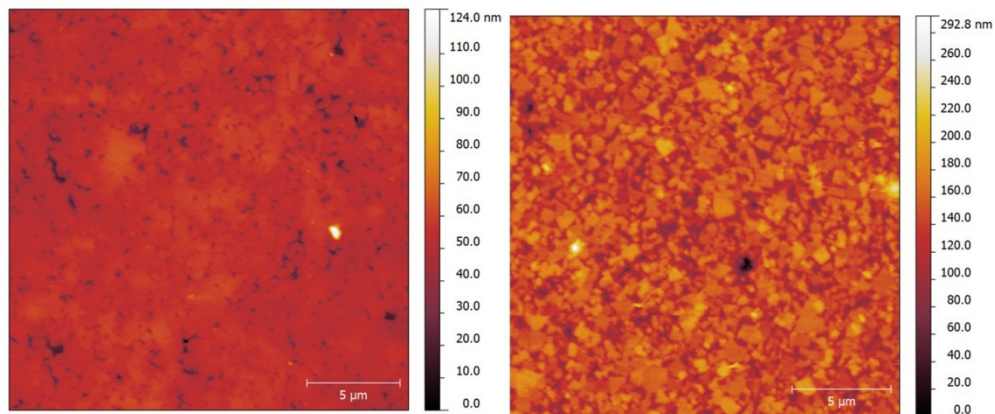


Figure 4.20: AFM image of polished Inserts for masked a) and etched b) areas.

For the unpolished sample the difference is not so obvious (fig.4.21). This is because the topology of sample is very complicated.

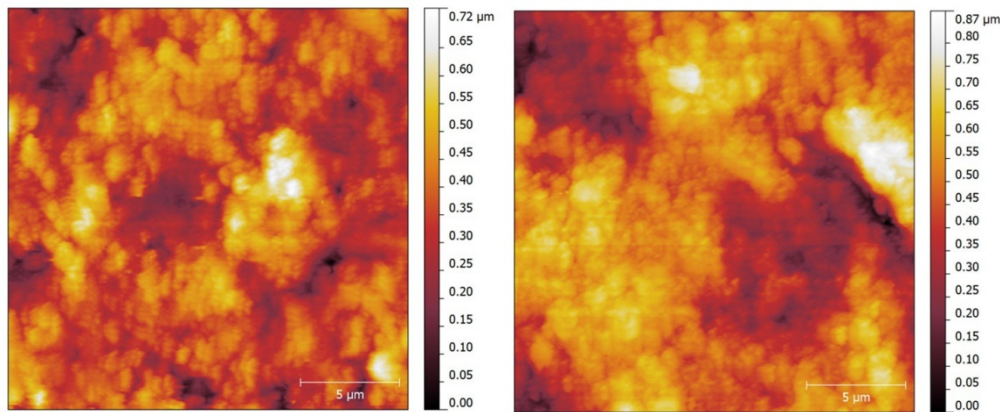


Figure 4.21: AFM image of unpolished Inserts for masked a) and etched b) areas.

In order to have a quantitative comparison, we must introduce two terms: waviness and roughness. Waviness is the low-frequency component corresponding to the grain size range. Roughness is the high-frequency component of atomic size range. Figures 4.22 and 4.23 show the waviness and the roughness as a function of ramping time and holding time respectively.

It can be seen that the waviness of the polished sample is much lower than the unpolished sample. For the unpolished sample, waviness increases with ramping time. A similar trend is observed for different hold times. For the unpolished sample, the change is only for a short period of etching (about 100%); the remaining samples are similar. This behaviour is due to the removal of small grains.

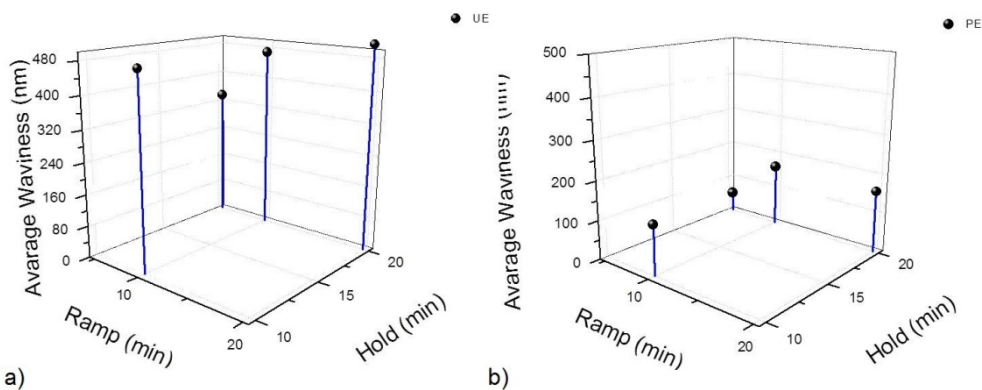


Figure 4.22: Waviness as function of ramping time and holding time for a) unpolished and b) polished surface.

Fig. 4.23 shows that roughness for both unpolished a) and polished b) is in the same range.

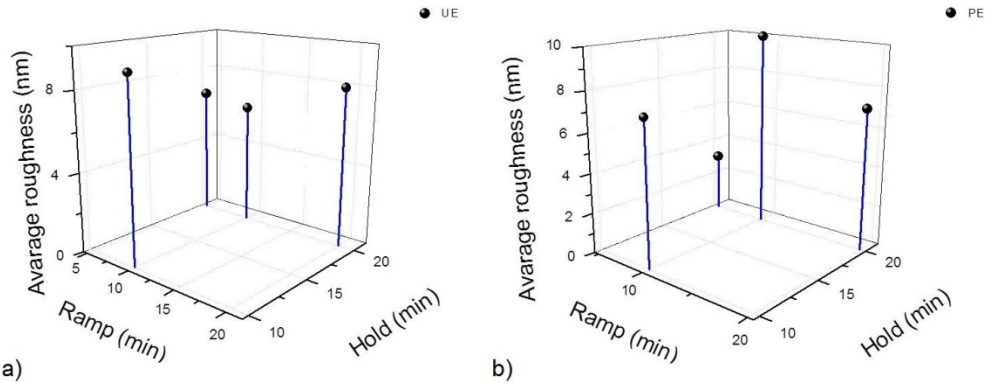


Figure 4.23: Roughness as function of ramping time and holding time for a) unpolished and b) polished surface.

## 4.4 Conclusions

From the results, the following conclusions can be made:

- During ramping with increasing pulse energy peak current, Ion flux current and metal ion content increases
- Etching increases roughness of Inserts due to removal of weak bounded small grains.
- The influence of etching on cutting edge was insignificant.

## 5 Development of the system

In order to control the target poisoning effect, the deposition system had to be upgraded with a plasma monitoring system (PEM), as described in section 3.2. PEM system utilizes a control algorithm capable of extremely fast and accurate feedback for reactive gas inlet control. The instrument is set to detect the optical emission line of a species within the plasma (V in case of this study) as a method of measuring the target

poisoning level. When target become poisoned, the OES signal of the metal species reduces. The speedflo maintains the OES signal by controlling the reactive gas flows; if the signal reduces, the target is becoming more poisoned and the controller reduces the reactive gas flows and vice versa. Change in the reactive gas flow results in change of the OES signal, which is once again analysed by the control unit.

In the PEM system the light was collected via a 150 mm long collimator attached to a feedthrough. The collimator was placed nearby target at the top of the chamber and it was directed downwards.

In early stages of using PEM system a harmonic oscillation of the OES signal during process with stable parameters were observed as shown in fig 5.1. It was found that the rotation of the substrate table causes fluctuations in the plasma that amplifies the signal by reflections. OES signal oscillations could disturb controlling process. To omit the reflection, the feedthrough was directed onto the target, as presented in fig 5.1. Angling the feedthrough gave more stability and a direct signal that could be used to control the process (fig 5.2).

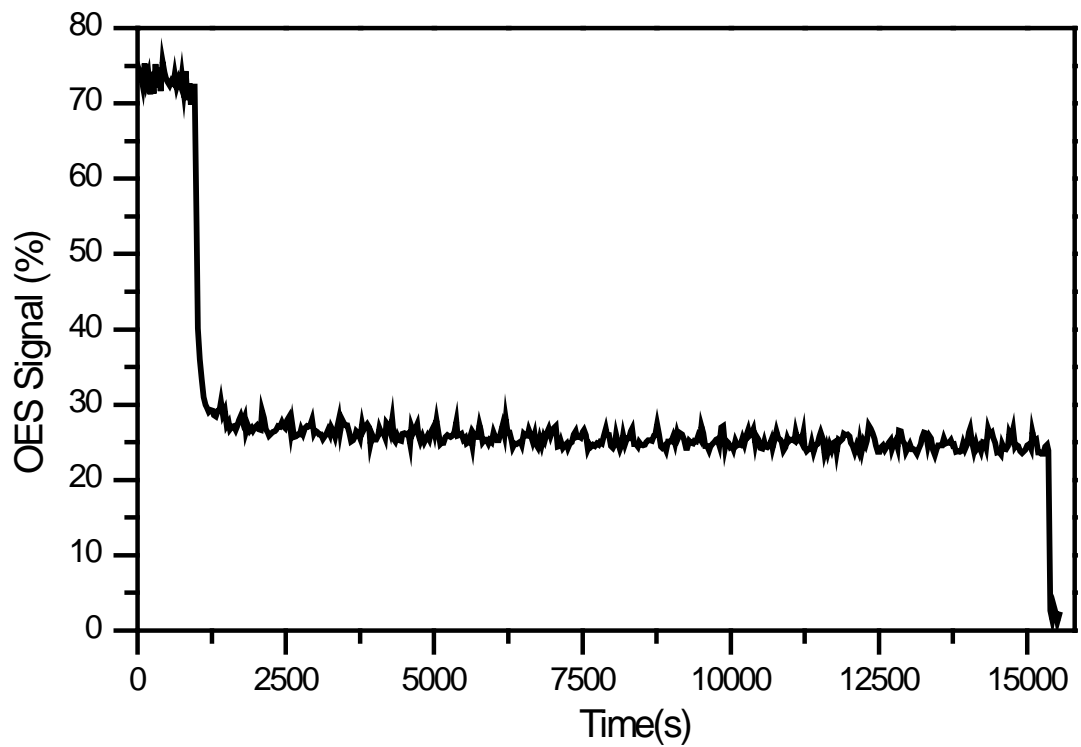


*Figure 5.1 Oscillations observed when the light collimator was directed downwards*

Initially, the feedthrough was positioned using bellows and clamps; this helped in finding the optimal angle with the highest light intensity. It was found that the best position is when collimator is directed at the bottom of the target, so that light from whole target is collected.

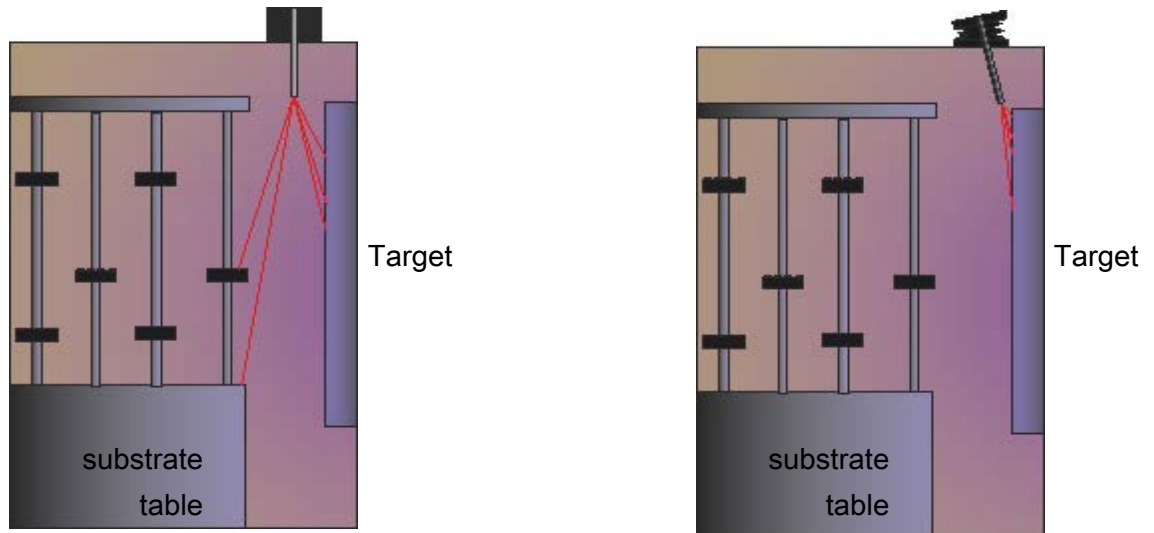


Figure 5.2 Left: The light is collected from the entire chamber including reflection from substrate table. Right: After angling the collimator, light is collected only from the target area.

It was found that the best intensity and most stable signal were obtained at an angle of  $8^\circ$ . For the experiments, a fixed angle feedthrough was used. The bellows could not be used during the poisoning test experiments; the change of the pressure caused the bellows to be compressed / expanded, therefore altering the angle.

## 6 Effect of Target Poisoning in Mixed Ar, N<sub>2</sub> and CH<sub>4</sub> Reactive Atmosphere

The aim of the present work is to determine the concentrations of the most populated species in the discharge; furthermore, it hopes to give an insight into the main dissociation mechanisms in a N<sub>2</sub>-CH<sub>4</sub> glow discharge. The following are observed: hysterical behaviour of target electrical properties, total pressure in the chamber and plasma composition as function of nitrogen and methane flow.

For both investigations, the material target (V, TiAl), atmosphere mixture (Ar+N<sub>2</sub>, Ar+CH<sub>4</sub>, Ar+N<sub>2</sub>+CH<sub>4</sub>) and discharge mode (DCMS, DCMS/HIPIMS) are varied. The individual influences of target and plasma conditions on deposition process properties are discussed.

For this purpose, mass spectrometry diagnostics and oscilloscope have been used to measure the concentrations of metal and gas species and to investigate change in electric properties of the target.

### 6.1 Overview of the experiment

The experiments focused on characterising the plasma discharge and the target electrical properties during increasing reactive gas flows of N<sub>2</sub> and CH<sub>4</sub>. Two different sets of experiments were carried out, here referred to as "DCMS discharge" and "HIPIMS discharge". For the DCMS discharge, all four targets (described in section 3.1) were operating in DCMS discharge mode; conversely, in the HIPIMS discharge, two targets were operating in DCMS discharge and two in HIPIMS discharge mode. The DCMS powered cathodes were set to 8 kW while the HIPIMS cathodes were operated at a voltage of 680 V, with a pulse frequency of 400Hz.

For both sets, the process gas mixture was varied. Here they are referred to as Ar, N<sub>2</sub>, CH<sub>4</sub> and N<sub>2</sub>CH<sub>4</sub> process. Ar processes were conducted in pure argon atmosphere in order to define the effect of pressure for both HIPIMS and DCMS sputtering. The argon flow was increased from 100 to 250 sccm. For all other processes the argon flow was kept constant at 200 sccm. For the N<sub>2</sub> processes the experiment is performed in Ar and N<sub>2</sub> atmosphere, for the CH<sub>4</sub> processes in Ar and CH<sub>4</sub> atmosphere and in N<sub>2</sub>CH<sub>4</sub> processes in Ar, N<sub>2</sub> and CH<sub>4</sub> atmosphere. Details of processes are presented in table 6.1.

Table 6.1 Varies process gas mixtures with specified gas flows

Process	Ar	N <sub>2</sub>	CH <sub>4</sub>	N <sub>2</sub> CH <sub>4</sub>	
Argon flow	Ramped	200 sccm	200 sccm	200 sccm	
Reactive flow	----	N <sub>2</sub>	CH <sub>4</sub>	N <sub>2</sub>	CH <sub>4</sub>
Ramping	0 - 250 sccm	0 - 300 sccm	0-150 sccm	0 -300 sccm	0-150 sccm

The reactive gas flows of nitrogen and methane were controlled via speedFlo mini™ from Gencoa (as described in section 5); this was also used to record total pressure. Argon flow was controlled by Hauzer system software. The gas flows were continuously ramped over an interval of 20 min to the maximum flow; this was then reduced using the same rate.

Despite the precise speedflo control, the mass flow controllers (Brooks SLA 5850) valves open at a minimum flow of 4.5 sccm. Thus, it was not possible to perform detailed experiments in range between 0-5 sccm. Moreover, in the process with N<sub>2</sub>CH<sub>4</sub> atmosphere, the valve for methane opens approximately 6 sccm later than N<sub>2</sub>; this causes formation of nitride compounds prior to carbides.

## 6.2 Effect of the Discharge Mode, Reactive Atmosphere and Target Material on the Plasma Content

In the first part of the experiment, effects of process atmosphere mixture, target material vicinity and discharge mode on the plasma content are studied. The ion signal intensities of different species were measured with the mass spectrometer at maximum flow. Results for reactive processes are given in tables 6.2 to 6.5.

### *Nitrogen Reactive Atmosphere*

Table 6.2 Plasma composition measured at nitrogen flow of 300 sccm for DC and HIPIMS processes. The MS signal is normalized to all measured species. Colour scales indicate low (red) and high (green) mass signal level within the process.

Mass (amu)	Species	Target Material & Sputtering Mode		
		TiAl (DC)	V (DC)	V (HIPIMS)
13	CH	0.00%	0.00%	0.02%
14	N <sup>1+</sup>			
	C <sub>2</sub> H <sub>4</sub> <sup>1+</sup>			
	CO <sup>1+</sup>	4.44%	10.15%	5.64%
16	CH <sub>4</sub> <sup>1+</sup>	0.06%	0.23%	0.28%
	O <sup>1+</sup>			
17	NH <sub>3</sub> <sup>1+</sup>	0.15%	0.44%	0.64%
24	OH <sup>1+</sup>			
	Ti <sup>2+</sup>	0.00%	0.00%	0.00%
25	C <sub>2</sub> <sup>1+</sup>	0.00%	0.00%	0.00%
	V <sup>2+</sup>			
27	C <sub>2</sub> H <sup>1+</sup>	0.00%	0.00%	0.00%
	Al <sup>2+</sup>			
28	HCN <sup>1+</sup>	0.88%	0.30%	0.87%
	N <sub>2</sub> <sup>1+</sup>	93.22%	85.98%	90.67%
48	CH <sub>2</sub> <sup>1+</sup>	0.90%	0.20%	0.41%
51	Ti <sup>1+</sup>	0.34%	2.72%	1.47%

The plasma in the N<sub>2</sub><sup>1+</sup> atmosphere process is dominated by nitrogen molecules and atoms.

For the TiAl target in the HIPIMS discharge, a high amount of carbon/oxygen/hydrogen ion signals can be observed. As only the nitrogen and argon are supplied into the

chamber, this could be attributed to contamination. It may be due to a leakage of atmospheric air into the system or carbon contamination during previous experiments. For this reason, the data was not included in the table.

As the target is fully poisoned and there are low chances for higher ionisation degree of metals such as Al<sup>2+</sup>, it can be assumed that mass 27 amu represents the HCN<sup>1+</sup> signal. It is supported with high signal intensity of mass 27 amu in the vicinity of vanadium target.

A lower gas concentration near the TiAl target than the vanadium target is observed. More vanadium ions are observed near the vanadium target than titanium ions near to the TiAl target.

The gas ion intensities are generally higher for HIPIMS than DCMS whereas metal ion intensities are lower. For the TiAl target, the difference in ion intensities for HIPIMS and DCMC discharges are much higher than for the V target.

### ***Methane Reactive Atmosphere***

For methane sputtering, a high amount of methane ions, as well as its radicals of the acetylene and ethanol groups, are observed. Similarly, as in the nitrogen atmosphere, there is a higher metal signal near to the vanadium target when compared to TiAl target.

*Table 6.3. Plasma composition measured at methane flow of 150 sccm for DC and HIPIMS processes. The MS signal is normalized to all measured species. Colours scales indicate low (red) and high (green) mass signal level within the process.*

Mass (amu)	Species	Target Material & Sputtering Mode			
		TiAl (DC)	TiAl (HIPIMS)	V (DC)	V (HIPIMS)
13	CH	2.00%	2.85%	0.99%	1.43%
14	N <sup>1+</sup>				
	C <sub>2</sub> H <sub>4</sub> <sup>1+</sup>				
	CO <sup>1+</sup>	10.01%	14.17%	15.62%	16.16%
16	CH <sub>4</sub> <sup>1+</sup>	53.83%	51.80%	61.56%	59.43%
	O <sup>1+</sup>				
17	NH <sub>3</sub> <sup>1+</sup>	6.01%	5.82%	2.50%	6.31%
	OH <sup>1+</sup>				

24	Ti <sup>2+</sup> C <sub>2</sub> <sup>1+</sup>	0.12%	0.13%	0.15%	0.08%
25	V <sup>2+</sup> C <sub>2</sub> H <sup>1+</sup>	0.35%	0.82%	0.91%	0.25%
27	Al <sup>2+</sup> HCN <sup>1+</sup>	14.84%	13.28%	2.96%	4.29%
28	N <sub>2</sub> <sup>1+</sup> CH <sub>2</sub> <sup>1+</sup>	10.13%	8.16%	10.08%	9.26%
48	Ti <sup>1+</sup>	1.53%	1.27%	0.23%	0.17%
51	V <sup>1+</sup>	1.18%	1.71%	5.00%	2.61%

For the HIPIMS discharge the radical ion intensities of CH and C<sub>2</sub>H are higher than in DCMS, while CH<sub>4</sub><sup>1+</sup>, N<sub>2</sub><sup>1+</sup>/CH<sub>2</sub><sup>1+</sup> and metal ion intensities are lower. Near vanadium target, the difference in gas ions between DCMS and HIPIMS discharges is less significant.

**Mixed Reactive Atmosphere**

Table 6.4 Plasma composition measured at nitrogen flow of 300 sccm and methane of 150 sccm flow for DC processes. The MS signal is normalized to all measured species. Colour scales indicate low (red) and high (green) mass signal level within the process.

Mass (amu)	Species	Target Material & Sputtering Mode	
		TiAl (DC)	V (DC)
13	CH	0.77%	0.35%
14	N <sup>1+</sup> C <sub>2</sub> H <sub>4</sub> <sup>1+</sup> CO <sup>1+</sup>	5.59%	5.36%
16	CH <sub>4</sub> <sup>1+</sup> O <sup>1+</sup>	20.67%	18.16%
17	NH <sub>3</sub> <sup>1+</sup> OH <sup>1+</sup>	37.58%	23.31%
24	Ti <sup>2+</sup> C <sub>2</sub> <sup>1+</sup>	0.06%	0.14%
25	V <sup>2+</sup> C <sub>2</sub> H <sup>1+</sup>	0.41%	0.14%
27	Al <sup>2+</sup> HCN <sup>1+</sup>	9.58%	11.06%
28	N <sub>2</sub> <sup>1+</sup> CH <sub>2</sub> <sup>1+</sup>	24.81%	40.85%
48	Ti <sup>1+</sup>	0.33%	0.00%
51	V <sup>1+</sup>	0.21%	0.63%

For the DCMS discharge in a mixed atmosphere, the plasma is dominated by N<sub>2</sub>, NH<sub>3</sub> and CH<sub>4</sub> molecules (table 6.4). The metal ion signals are lower than in a single reactive gas atmosphere and NH<sub>3</sub> and HCN signals are higher.

Results for the HIPIMS discharge in a mixed atmosphere with various N:CH<sub>4</sub> ratio, are given in table 6.5. Similarly to the in DCMS discharge, the plasma is dominated by N<sub>2</sub>, NH<sub>3</sub> and CH<sub>4</sub> ions. As in single reactive atmosphere, the metal ion intensities are lower for HIPIMS than for DCMS discharge. CH<sup>1+</sup> and NH<sub>3</sub><sup>1+</sup> intensities are higher than for the DCMS discharge. Lower intensities of CH<sub>4</sub><sup>1+</sup>, V<sup>2+</sup> / C<sub>2</sub>H<sup>1+</sup>, Al<sup>1+</sup> / HNC<sup>1+</sup> and Ti<sup>1+</sup> are observed for HIPIMS discharges near the TiAl target; on the other hand, near the vanadium target, these ion intensities are higher. The N<sub>2</sub><sup>1+</sup> / CH<sub>2</sub><sup>1+</sup>, Ti<sup>2+</sup> / C<sub>2</sub><sup>1+</sup> and N<sup>1+</sup> /

C<sub>2</sub>H<sub>4</sub><sup>1+</sup> / CO<sup>1+</sup> intensities are higher in the HIPIMS discharge near to the TiAl target and lower near the vanadium target .

As the nitrogen to methane ratio increases, the carbon containing radicals ion intensities decreases and nitrogen content increases.

Table 6.5. Plasma composition measured at nitrogen flow of 300 sccm and methane of 150 sccm flow for HIPIMS processes. The MS signal is normalized to all measured species. Colour scales indicate low (red) and high (green) mass signal level within the process.

Mass (amu)	Species	Target Material & Sputtering Mode					
		TiAl (HIPIMS)			V (HIPIMS)		
		1\1	2\1	4\1	1\1	2\1	4\1
13	CH	1.28%	1.18%	0.66%	1.21%	0.95%	0.88%
14	N <sup>1+</sup>						
	C <sub>2</sub> H <sub>4</sub> <sup>1+</sup>						
	CO <sup>1+</sup>	9.83%	5.79%	5.82%	7.77%	5.06%	9.40%
16	CH <sub>4</sub> <sup>1+</sup>						
	O <sup>1+</sup>	22.41%	14.29%	8.72%	21.09%	19.18%	9.87%
17	NH <sub>3</sub> <sup>1+</sup>						
	OH <sup>1+</sup>	29.80%	40.97%	24.97%	39.24%	35.03%	26.21%
24	Ti <sup>2+</sup>						
	C <sub>2</sub> <sup>1+</sup>	0.32%	0.10%	0.00%	0.08%	0.07%	0.05%
25	V <sup>2+</sup>						
	C <sub>2</sub> H <sup>1+</sup>	0.64%	0.21%	0.29%	0.58%	0.37%	0.09%
27	Al <sup>2+</sup>						
	HCN <sup>1+</sup>	9.06%	9.45%	8.27%	4.94%	12.37%	10.57%
28	N <sub>2</sub> <sup>1+</sup>						
	CH <sub>2</sub> <sup>1+</sup>	25.88%	27.63%	51.23%	24.55%	26.53%	42.55%
48	Ti <sup>1+</sup>	0.45%	0.04%	0.00%	0.03%	0.03%	0.09%
51	V <sup>1+</sup>	0.32%	0.34%	0.04%	0.52%	0.41%	0.28%

## Discussion

In all processes there is lower metal signal near to TiAl compared to near the vanadium target; this indicates a higher poisoning level of the TiAl target. The high target poisoning of the TiAl target causes lower plasma density in the target vicinity; this results in lower ionization. As a result of this, less gas ions are observed near the TiAl target.

Tables 6.2-6.5 show that in the mixed atmosphere there is a high content of the radicals. Gas molecules have a larger cross-section which can lead to enhanced ionization of gases than metals[137]. The dissociated N<sub>2</sub> and CH<sub>4</sub> atoms combine together creating new radicals as described in section 2.2.1. A drop in the deposition of gas molecules leads to an increase of the total pressure. Moreover, the compound created on the target is resputtered back to the system, therefore increasing partial pressure of the gases and reducing sputter rate of the metals.

For the HIPIMS discharge, metal ion intensities are generally lower than in DCMS discharge whereas radical ion intensities are higher. Similarly, as in DCMS sputtering, there is a higher possibility to ionize gas due to higher cross section of the molecules. The creation of the radicals is increased in HIPIMS in all atmospheres due to higher energetic plasma.

## **6.3 Hysteresis behaviour of the target and the total gas**

Four sets of experiments were performed; different atmosphere mixtures were studied for two different operational modes in the vicinity of two target materials. The following were calculated and compared: a) the hysteresis behaviour of the total gas pressure, b) the discharge resistance of the target as an effect of changing target condition.

### **6.3.1 V Target**

#### ***6.3.1.1 DCMS Discharge***

##### **Argon Atmosphere**

Figure 6.1 shows that the  $R_D$  decreases almost linearly with argon flow rate while total pressure linearly increases. As argon is an inert gas, it does not react with the target

material. There is no compound creation at the target therefore the  $R_T$  won't change, as there won't be any changes in the  $\gamma_{ISEE}$ .

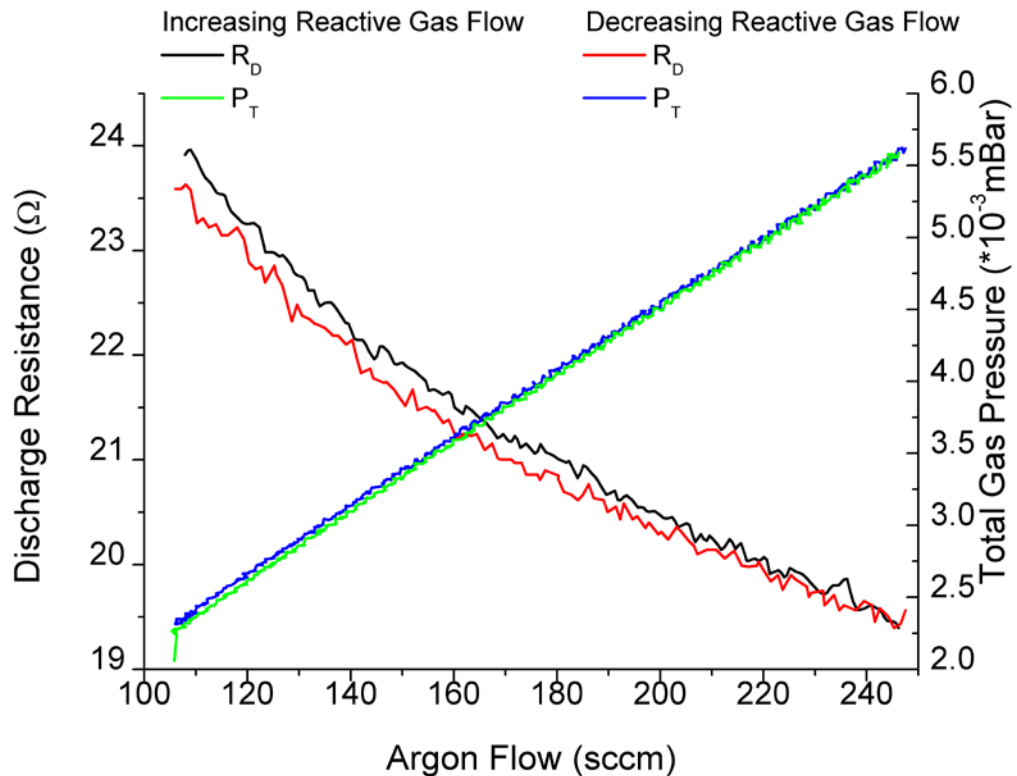


Figure 6.1 V target discharge resistance and total gas pressure vs. argon flow rate curves: 4 targets operating in DCMS discharge.

With increasing argon flow the total pressure increases, leading to more volume ionization. This results in a higher sputter rate which increases the total ionisation of the plasma and thus the plasma impedance  $R_p$  is reduced. As  $R_T$  and  $\gamma$  are unchanged with increasing argon, the  $R_D$  will be influenced only by  $R_p$  and will decrease with increasing argon flow. Both curves show no hysteresis effect and follow closely with the ramping. As the argon flow increase, the  $R_D$  decreases.

**Nitrogen atmosphere**

Figure 6.2 shows the  $R_D$  and total gas pressure vs. reactive gas flow curves when the experiment is performed in a nitrogen reactive atmosphere.

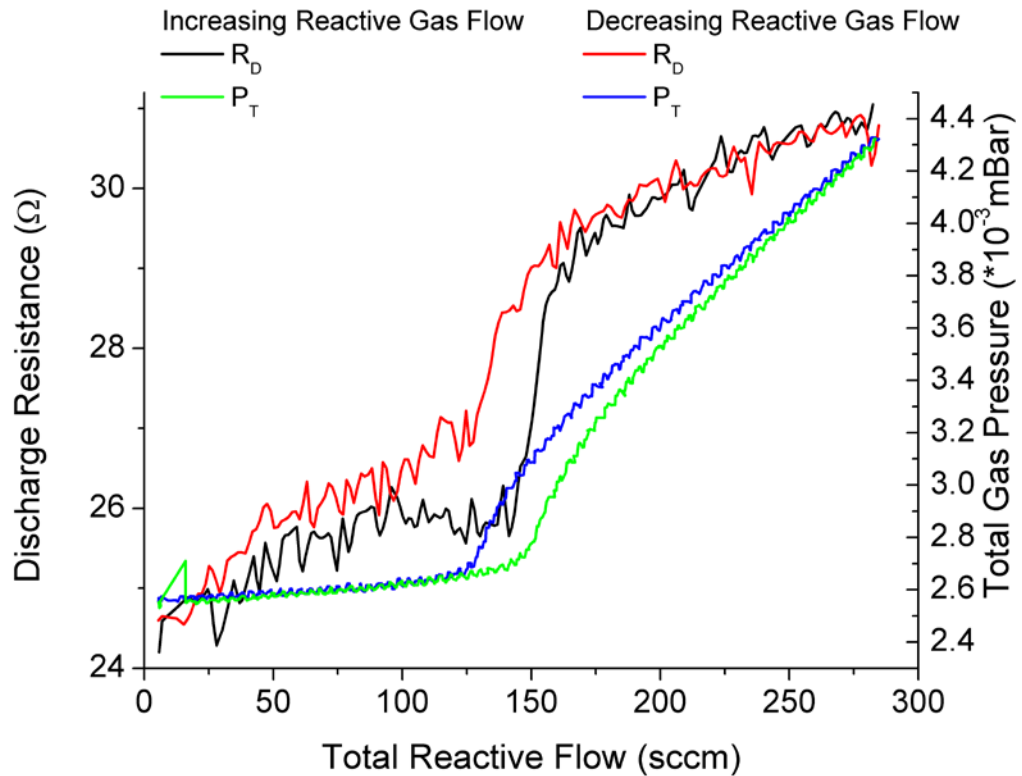


Figure 6.2 V target discharge resistance and total gas pressure vs. total reactive flow rate curves: 4 targets operating in DCMS discharge; Nitrogen reactive atmosphere.

It can be observed that the  $R_D$  increases almost logarithmically with N<sub>2</sub> flow rate until approximately 150 sccm. The slope of the total gas pressure curve is less steep in this flow range when compared with higher flows. At this stage of the poisoning, the target is being covered with nitride compounds, changing the  $R_T$  and  $\gamma_{ISEE}$ . There will also be changes in  $R_P$  due to a change in plasma composition; however, at this stage the target conditions dominate processes in the chamber. For flow rates between 150 and 160 sccm, the  $R_D$  increases at a faster rate (increase from 25.7  $\Omega$  to 29.1  $\Omega$ ). On further increase of the N<sub>2</sub> flow rate, beyond 160 sccm, the  $R_D$  shows a linear increase to values around 31  $\Omega$ . This indicates saturation of nitrides at the target (as well as chamber walls) and release of nitrogen gas into the system. At this stage the compound is

covering a whole target and the thickness of the compound is increasing; the changes in the  $R_D$  can be attributed to changes in plasma parameters as composition and total gas pressure.

On the reverse sweep of flow rates, the poisoning hysteresis is visible between flow rates around 85 to 160 sccm.

### Methane Atmosphere

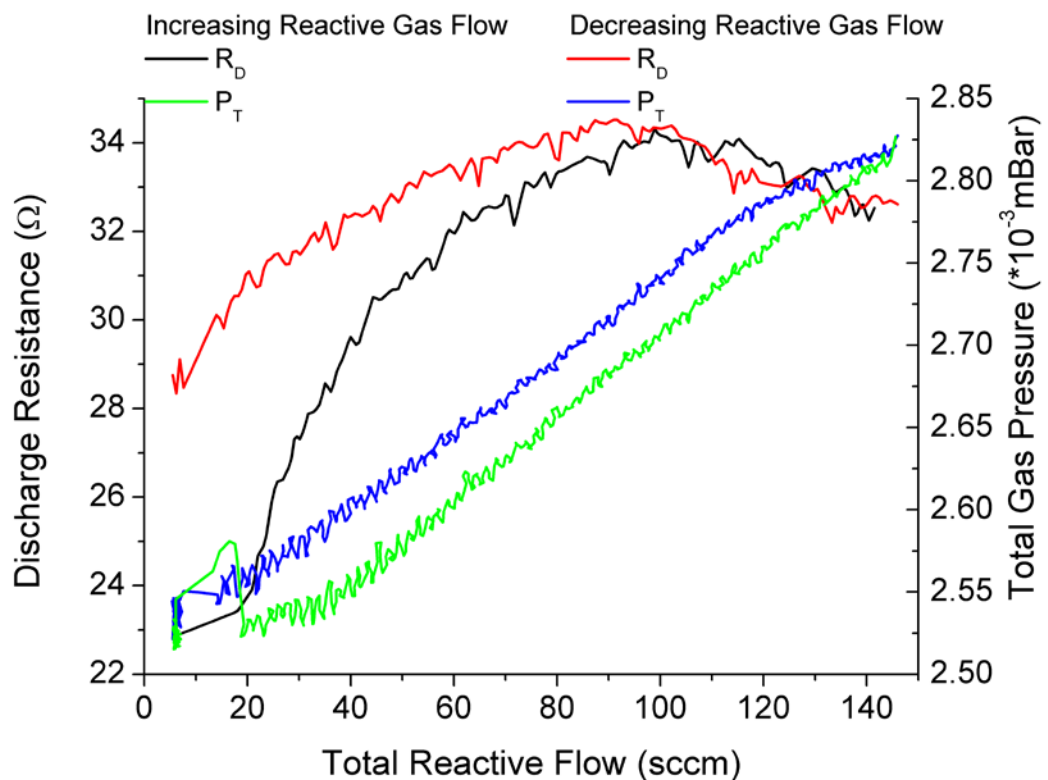


Figure 6.3 V target discharge resistance and total gas pressure Vs total reactive flow rate curves: 4 targets operating in DCMS discharge; Methane reactive atmosphere

Figure 6.3 shows that for the methane atmosphere, at very low flow, up to 15 sccm the  $R_D$  shows slow increase. For flow between 15 to 45 sccm, the  $R_D$  sharply increases from 25 to 31  $\Omega$ , whereas the total gas pressure increase rate is low. This suggests changes at the target surface due to creation of carbides. For flow rates between 45 and 100 sccm, the  $R_D$  drops at a slower rate and reaches a maximum of 35  $\Omega$ . The total gas pressure

curve shows an increase in the slope for this region. At this stage of the process, the target is fully covered by the carbides and the release of methane radicals occurs. Beyond 100 sccm, the  $R_D$  drops and reaches 32  $\Omega$  at a flow rate of 140 sccm. In this region the total pressure increases at slower rate. On the reverse sweep of flow rates, the poisoning hysteresis is visible for all flow rates below 100 sccm. There is a difference of 5.6  $\Omega$  between the beginning and the end of the process. This is a result of high sticking coefficient of carbon atoms.

### Mixed Nitrogen and Methane atmosphere

Figure 6.4 shows the  $R_D$  and the total gas pressure recorded when the experiment was performed in the mixed nitrogen and methane reactive atmosphere.

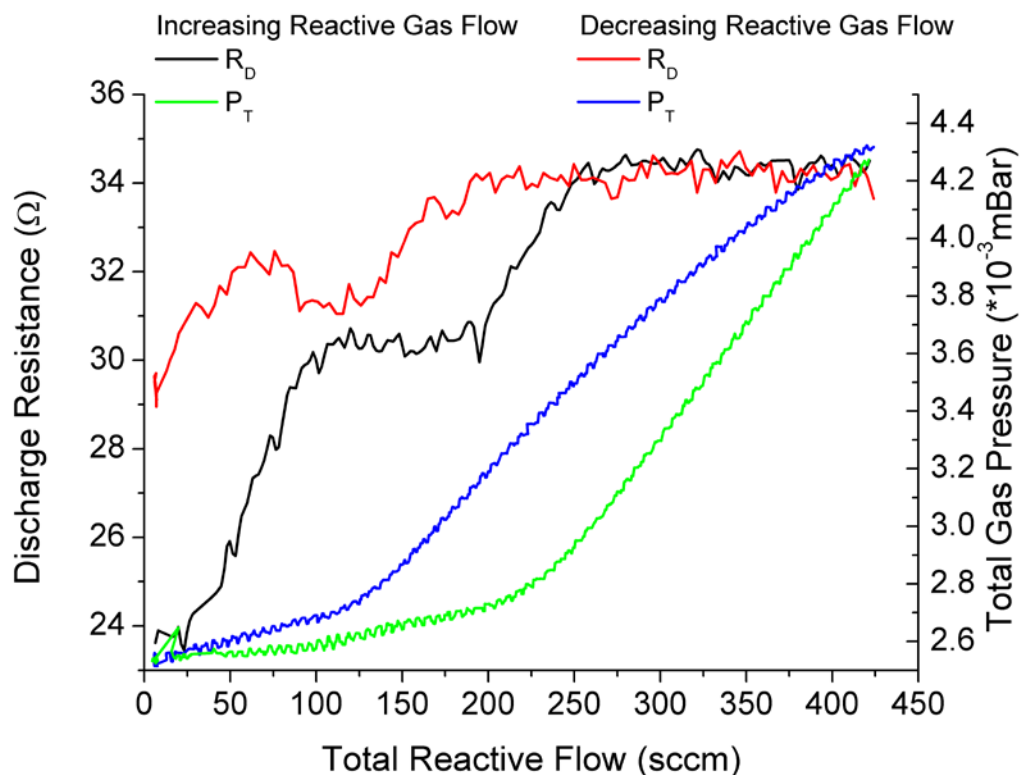


Figure 6.4 V target discharge resistance and total gas pressure Vs total reactive flow rate curves: 4 targets operating in DCMS discharge; mixed nitrogen and methane reactive atmosphere

Initially, up to 25 sccm the  $R_D$  stays at the same level of 25  $\Omega$ . The  $R_D$  then increases in two steps: firstly from 24  $\Omega$  to 30  $\Omega$  between 25 and 100 sccm, and then from 30  $\Omega$  to

35  $\Omega$  between 195 and 150 sccm. Beyond 250 sccm, the  $R_D$  stays at the same level of 35  $\Omega$ . The total gas pressure changes correlates with changes in the  $R_D$  up to 250 sccm. Beyond this flow, the total gas pressure increases linearly. The biggest change in increase rate can be observed at 195 sccm; this relates to the target being fully poisoned. The poisoning hysteresis is prominent compared with the nitrogen and methane reactive atmosphere processes. The hysteresis is very broad and is visible in between flow rates of 0 and 250 sccm. Similarly, as in methane reactive atmosphere, there is resistance at the beginning and at the end of the process which differs by 5.5  $\Omega$ .

#### ***6.3.1.2 DCMS/HIPIMS Discharge***

##### **Argon Atmosphere**

Figure 6.5 shows the  $R_D$  and the total gas pressure recorded when the experiment was performed in the argon atmosphere with mixed DCMS/HIPIMS discharge.

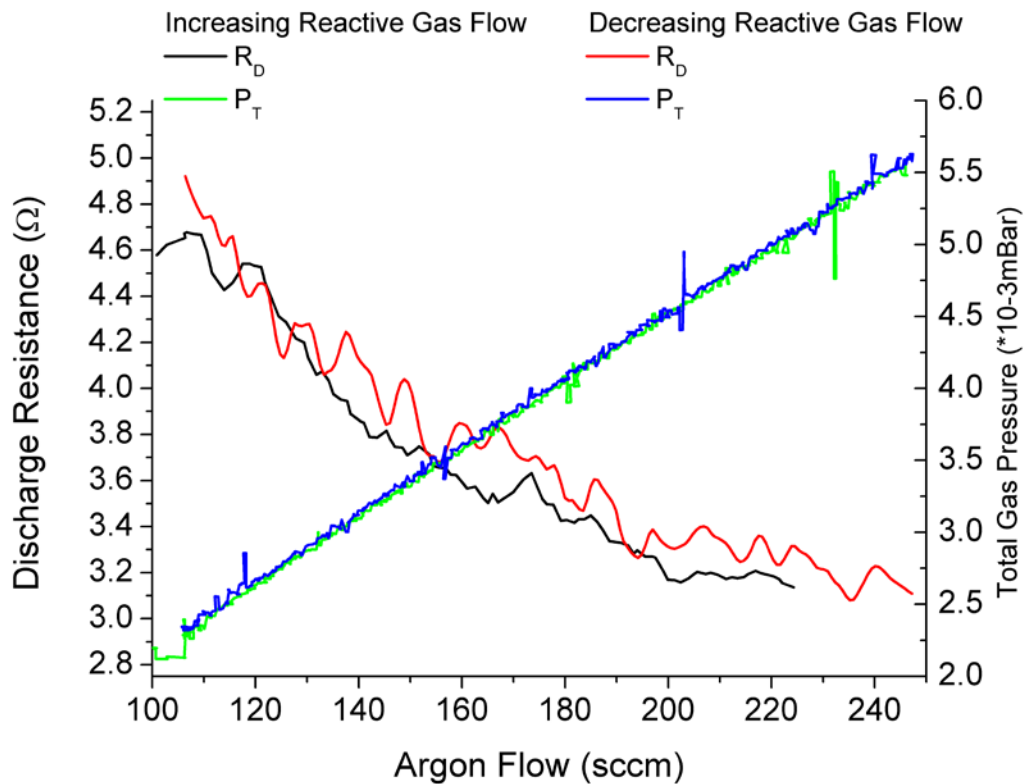


Figure 6.5 6.5 V target discharge resistance and total gas pressure Vs total reactive flow rate curves: mixed DCMS/HIPIMS discharge; Argon atmosphere

The discharge resistance and the total pressure curves are similar as in DCMS discharge. The  $R_D$  decreases almost linearly with argon flow rate; total pressure linearly increases with no hysteresis effect and follow closely with the ramping.

As for the HIPIMS discharge, the power was measured during peak; the discharge resistance is approximately 5 times lower than for the DCMS discharge. The total gas pressure is negligibly higher for the DCMS/HIPIMS cause ( $0.03 \text{ mBar} \cdot 10^{-3}$ ).

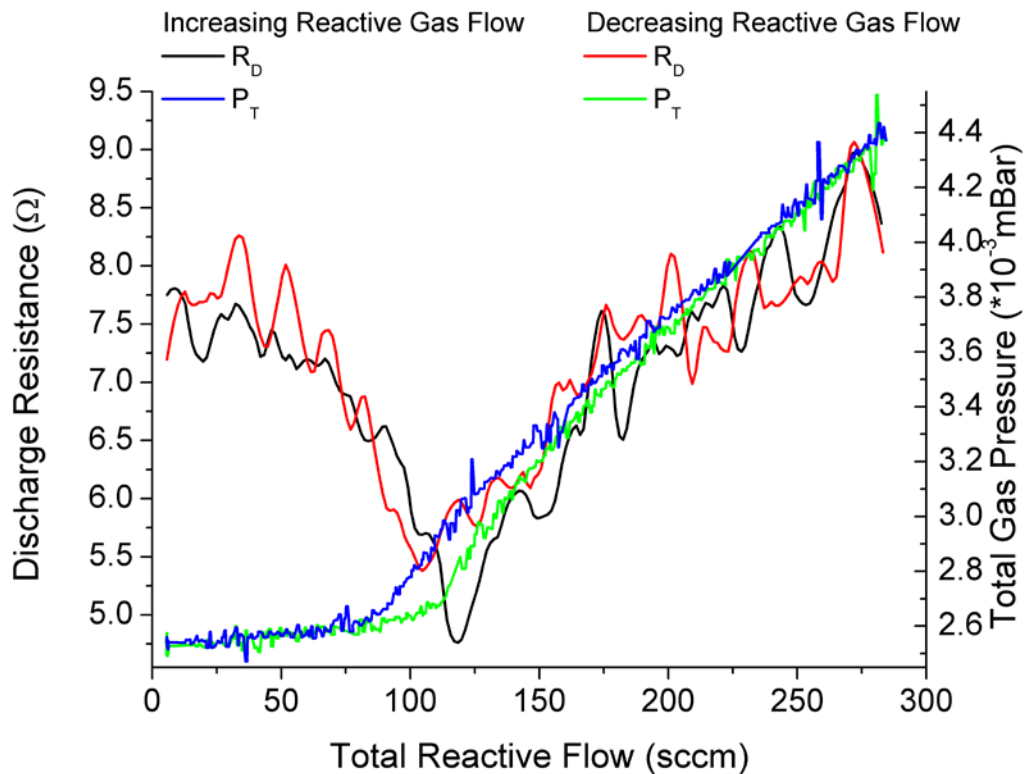
**Nitrogen Atmosphere**

Figure 6.6 V target discharge resistance and total gas pressure Vs total reactive flow rate curves: mixed DCMS/HIPIMS discharge; Nitrogen reactive atmosphere

It can be observed in fig. 6.6 that for the nitrogen atmosphere, the  $R_D$  decrease logarithmically with N<sub>2</sub> flow rate until 115 sccm from 7.8 to 4.8 Ω. At this flow the total gas pressure increases at a faster. On further increase of the N<sub>2</sub> flow rate the  $R_D$  shows an almost linear increase to values around 9 Ω. The total gas pressure reaches 4.41 mBar\*10<sup>-3</sup>, which is 0.08 than in DC case. The hysteresis is very narrow with difference of 20 sccm.

**Methane Atmosphere**

Figure 6.7 shows the  $R_D$  and total gas pressure vs. reactive gas flow curves when the experiment is performed in a methane reactive atmosphere with mixed DCMS/HIPIMS discharge.

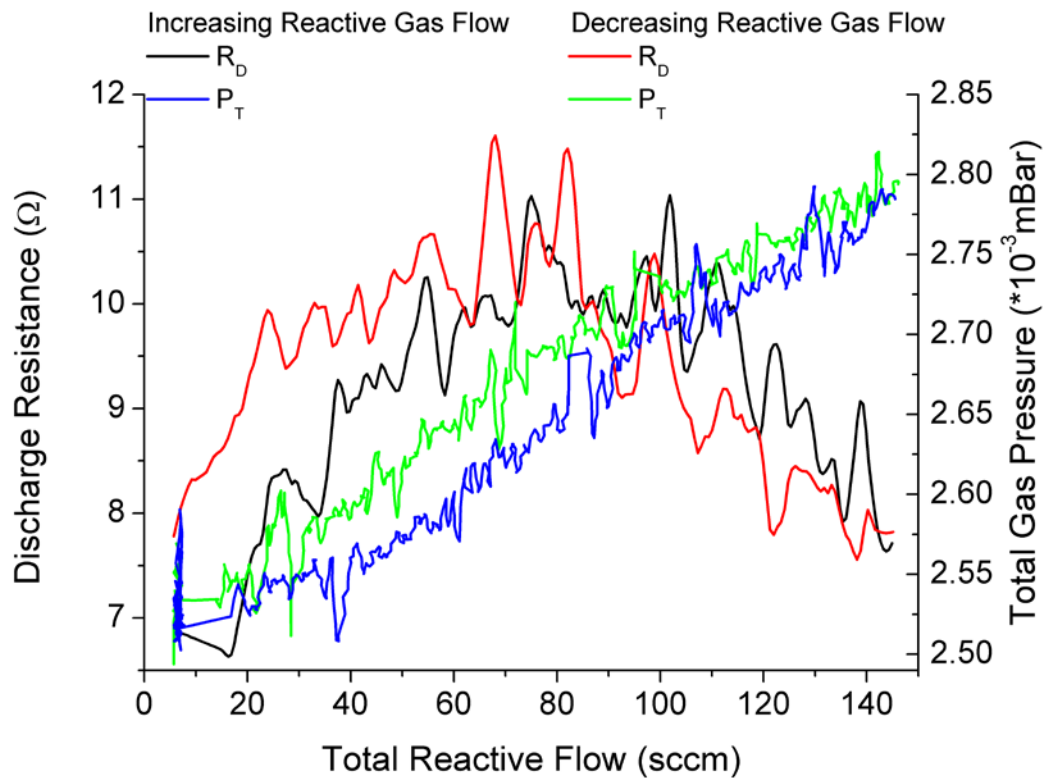


Figure 6.7 V target discharge resistance and total gas pressure Vs total reactive flow rate curves: mixed DCMS/HIPIMS discharge; Methane reactive atmosphere.

In the CH<sub>4</sub> process, the R<sub>D</sub> behaves similarly as in the DCMS process. It initially increases from 6.5 Ω to 10 Ω within 80 sccm before dropping to 7.5Ω at 140 sccm. The hysteresis is very narrow, however, start and end values do not overlap. There is a 1.5 Ω gap between the start and end values, in DCMS this is 5 Ω.

### Mixed Nitrogen and Methane atmosphere

Figure 6.8 shows the R<sub>D</sub> and total gas pressure vs. reactive gas flow curves when the experiment is performed in a mixed nitrogen and methane reactive atmosphere with mixed DCMS/HIPIMS discharge.

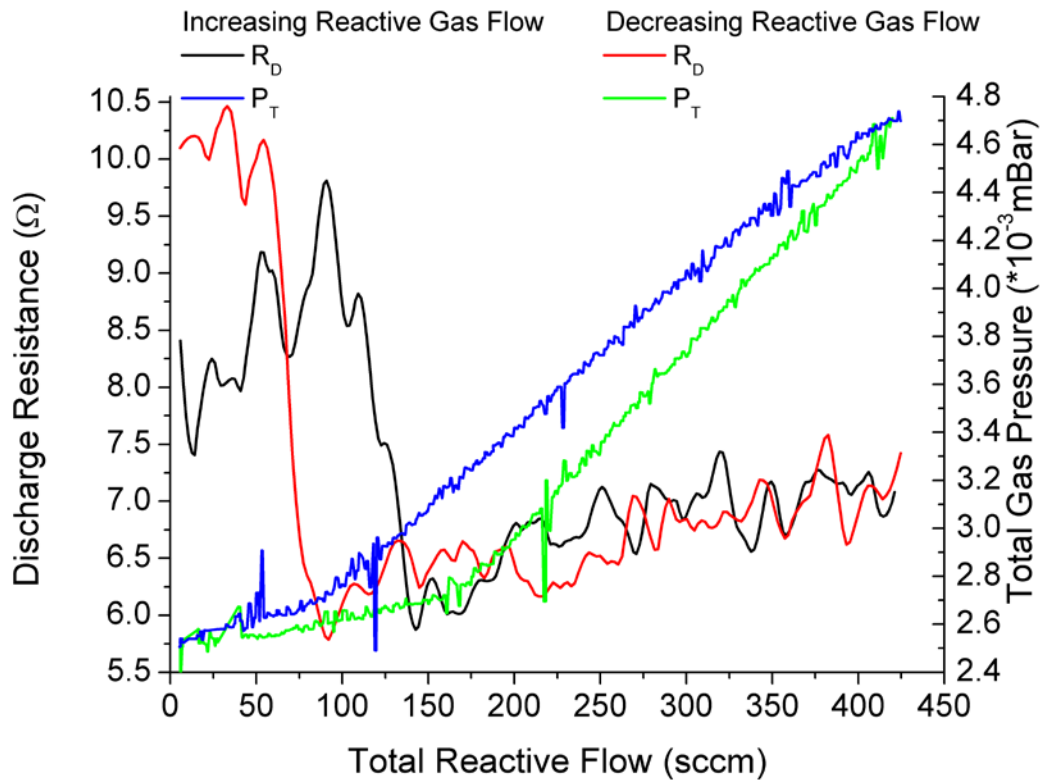


Figure 6.8 V target discharge resistance and total gas pressure Vs total reactive flow rate curves: mixed DCMS/HIPIMS discharge; mixed nitrogen and methane reactive atmosphere

For the HIPIMS N<sub>2</sub>CH<sub>4</sub> process, unlike the DCMS process, after 100 sccm the R<sub>D</sub> drops and after 150 sccm it increases with a lower rate. When the flow is decreased the R<sub>D</sub> drops, overlapping with the increasing profile until 150 sccm. Below 100 sccm, it rapidly increases to maximum level of 10 Ω; this remains until the end of the decreasing flow. In comparison to the DCMS process, the hysteresis is narrow and the difference between the start and end value is small.

The total pressure hysteresis for HIPIMS and DCMS sputtering for the N<sub>2</sub>CH<sub>4</sub> process are compared in fig 6.9. The HIPIMS hysteresis is narrower than DCMS indicating better target cleaning. However, target poisoning in HIPIMS occurs earlier and the total pressure reaches higher values by 0.5 Pa. This means that in HIPIMS, target poisoning has a greater effect than in DCMS.

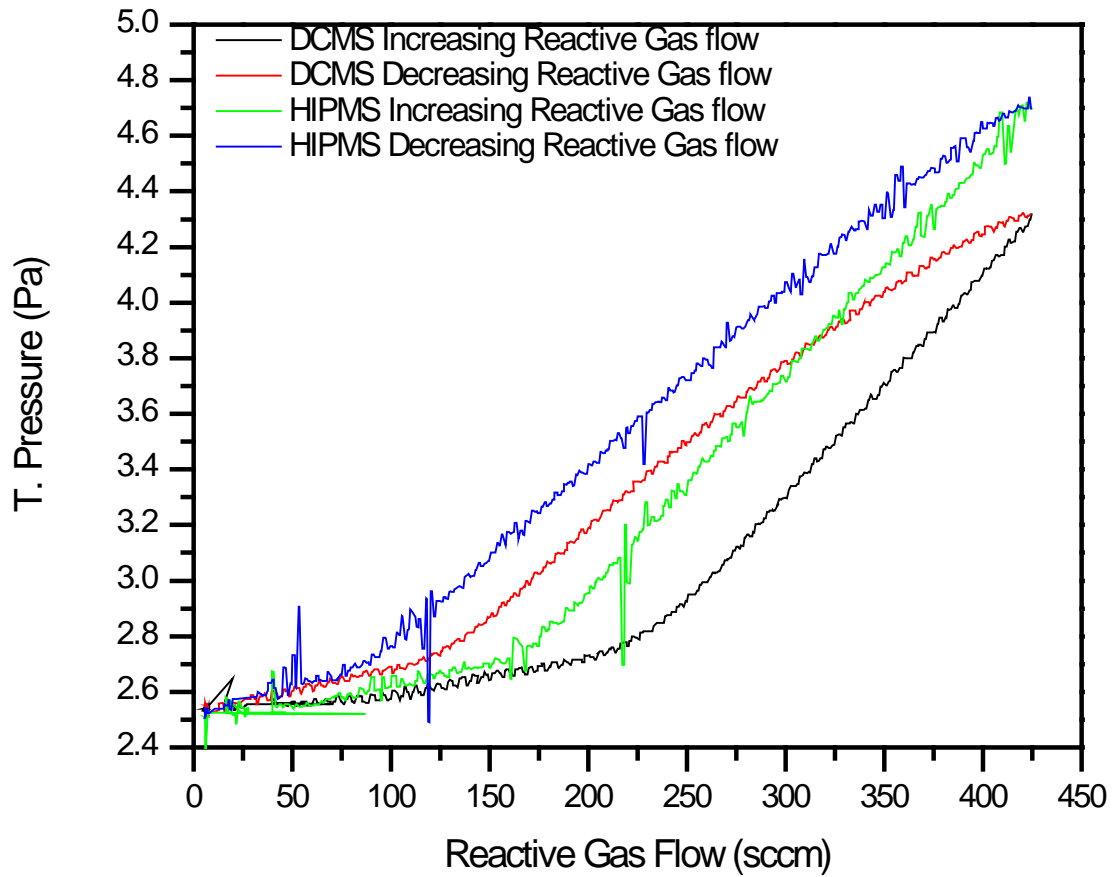


Figure 6.9 The total pressure hysteresis for HIPIMS and DCMS sputtering for the N<sub>2</sub>CH<sub>4</sub> process

## 6.3.2 TiAl Target

### 6.3.21 DCMS Discharge

#### Argon Atmosphere

Figure 6.10 shows the  $R_D$  and the  $P_T$  vs. reactive gas flow curves when the experiment is performed in an argon atmosphere with mixed DCMS/HIPIMS discharge.

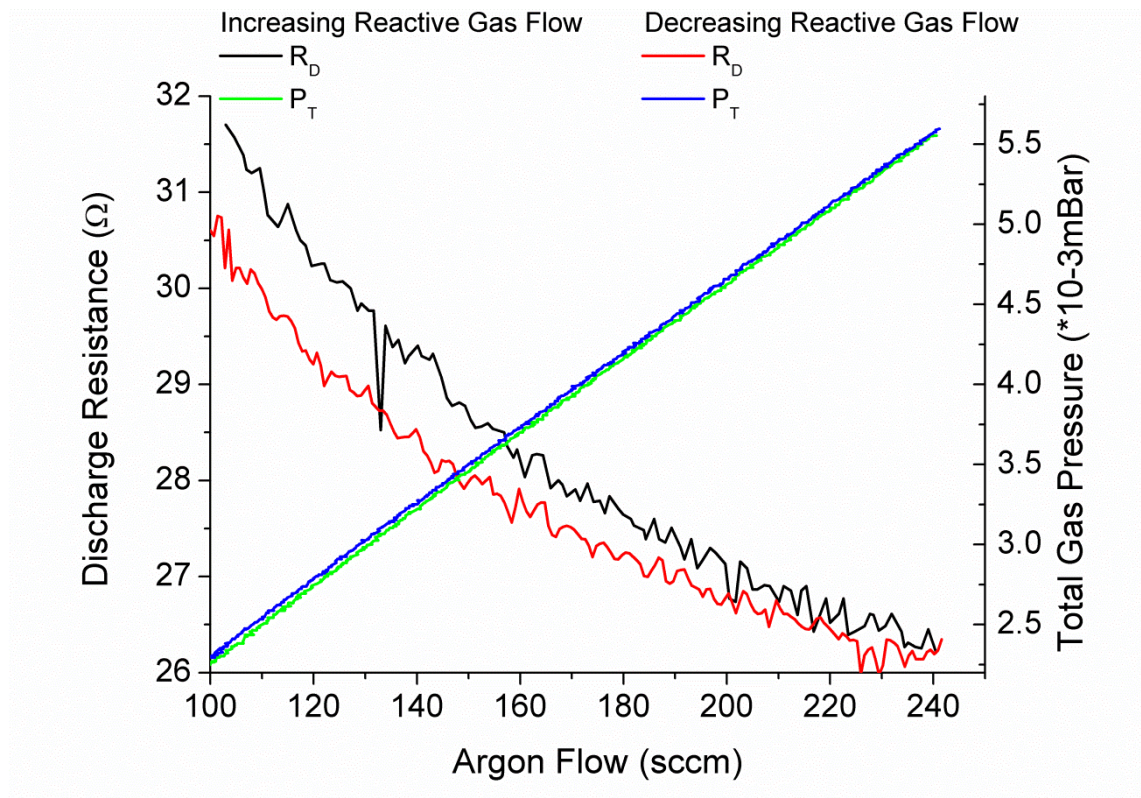


Figure 6.10 TiAl target discharge resistance and total gas pressure vs. argon flow rate curves: 4 targets operating in DCMS discharge.

It can be observed that the  $R_D$  decreases exponentially with argon flow rate, while total pressure increases linearly. The discharge resistance is 6.5  $\Omega$  higher at the beginning and the end of the process than for the vanadium target. There is a difference of 1  $\Omega$  start and end value for the discharge resistance, however the total pressure does not show hysteresis.

**Nitrogen Atmosphere**

Figure 6.11 shows the  $R_D$  and the  $P_T$  evolution for the nitrogen atmosphere.

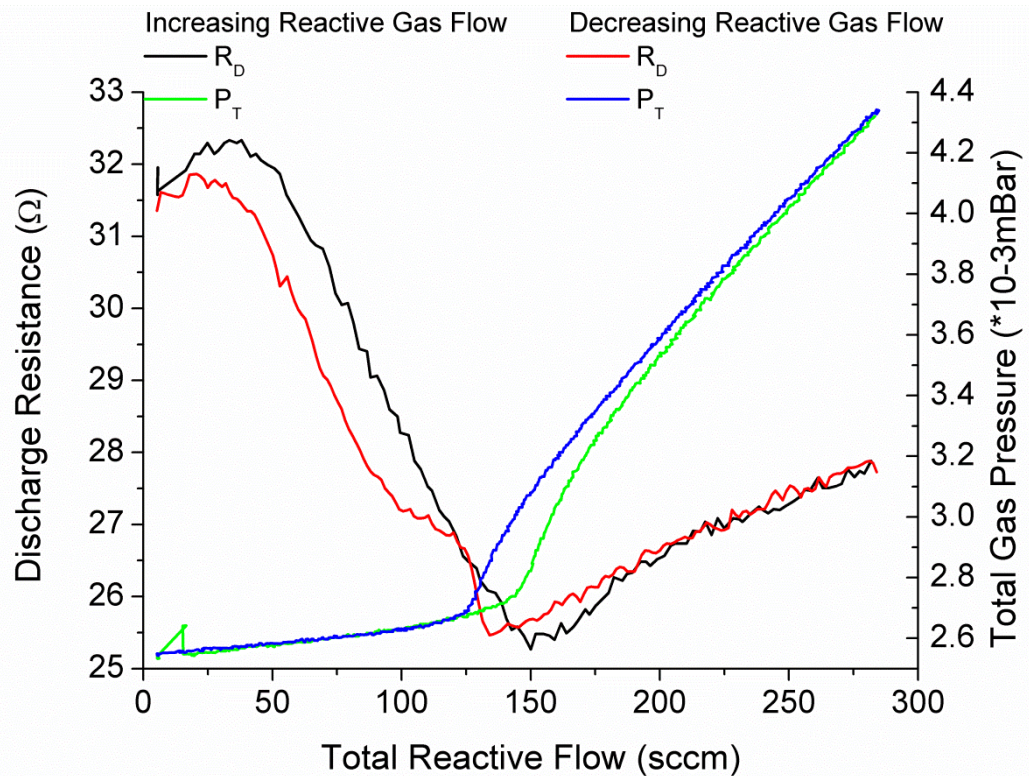


Figure 6.11 TiAl target discharge resistance and total gas pressure vs. total reactive flow rate curves: 4 targets operating in DCMS discharge; Nitrogen reactive atmosphere.

As the nitrogen flow increases, the discharge resistance initially increases by 1 Ω. After 50 sccm, the  $R_D$  decays from 32.5 to 25.5 Ω at 150 sccm. At this flow, an increase in total gas pressure rate can be observed. Beyond 150 sccm the  $R_D$  increases. At the reverse, a narrow hysteresis of 25 sccm can be observed for both the  $R_D$  and the  $P_T$ . The profile of resistance is typical for an AlN poisoning behaviour [64].

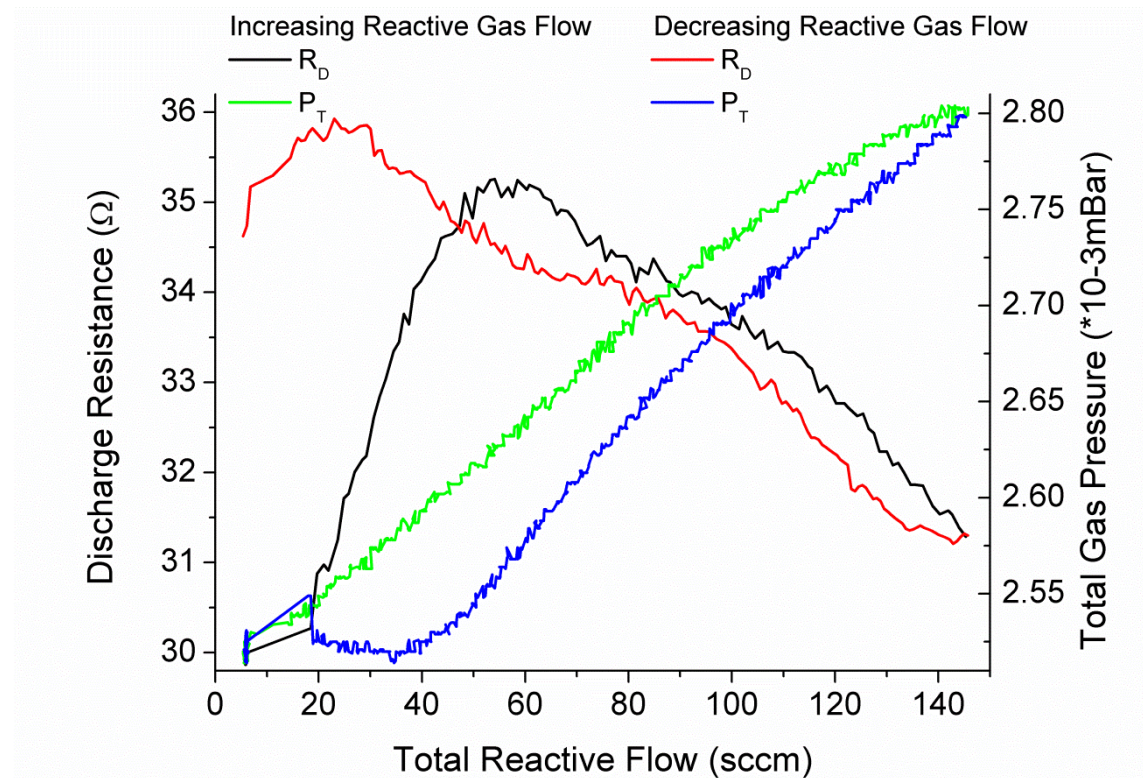
**Methane Atmosphere**

Figure 6.12 TiAl target discharge resistance and total gas pressure vs. total reactive flow rate curves: 4 targets operating in DCMS discharge; Methane reactive atmosphere

Figure 6.12 shows that for the methane atmosphere, the total gas pressure initially decreases with increasing total gas flow. Up to 18 sccm there is a minor increase in the  $R_D$ , beyond this flow, there is rapid increase and it reaches a maximum of 35  $\Omega$  at 55 sccm. After 55 sccm, the  $R_D$  drops indicating saturation of the target and release of the carbon molecules. At the 80 sccm, the decreasing rate slows down as the target becomes fully poisoned. At the reverse, the hysteresis is observed over the whole flow. However, between 50 -140 sccm it is relatively narrow; between 0-50 sccm it is very broad as the resistance does not return to its original value resulting in difference of 5  $\Omega$  between the start and end values.

**Mixed Nitrogen and Methane atmosphere**

Figure 6.13 shows the  $R_D$  and the  $P_T$  evolution for the mixed nitrogen and methane reactive atmosphere in DCMS discharge.

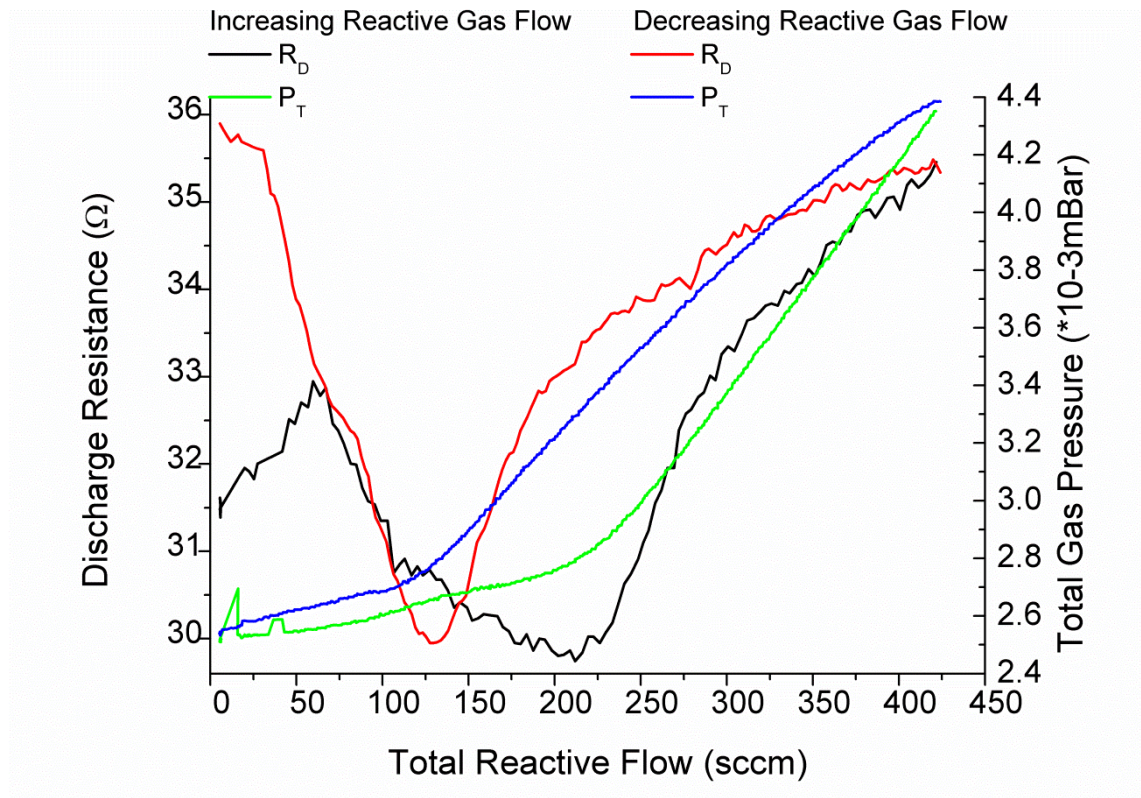


Figure 6.13 TiAl target discharge resistance and total gas pressure vs. total reactive flow rate curves: 4 targets operating in DCMS discharge; mixed nitrogen and methane reactive atmosphere

As the reactive gas flow increases, the discharge resistance increases by 1.5 Ω. At 60 sccm, the R<sub>D</sub> starts to decrease and drops by 3 Ω at 210 sccm, after which it starts to increase again. At this flow, an increase in total gas pressure rate can be observed. From 105 sccm, the decreasing rate drops down and a peak in the total gas pressure is observed. Beyond 275 sccm, the R<sub>D</sub> increase rate slows down and increase of the total gas pressure is linear. At the reverse, a broad hysteresis is observed for both R<sub>D</sub> and P<sub>T</sub>, similarly as for the V target.

### 6.3.2.2 DCMS/HIPIMS Discharge

#### Argon Atmosphere

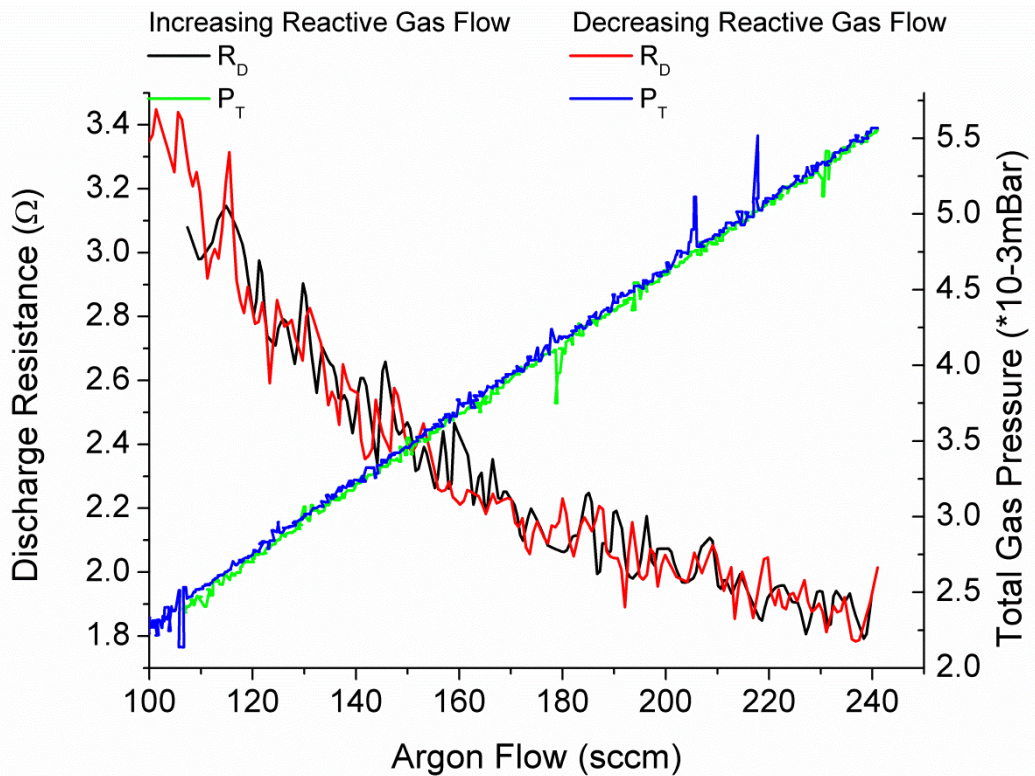


Figure 6.14 TiAl target discharge resistance and total gas pressure vs. total reactive flow rate curves: mixed DCMS/HIPIMS discharge; Argon atmosphere

Figure 6.14 shows that for the argon atmosphere, the  $R_D$  decreases exponentially with increasing argon flow, while total pressure increase. The behaviour of  $R_D$  and  $P_T$  is same as in case of DCMS. However, the drop of  $2.2 \Omega$  in HIPIMS is lower than  $6 \Omega$  in DCMS. The hysteresis is not observed on the reverse.

As for the HIPIMS discharge, the power was measured during peak. The discharge resistance is approximately 9 times lower than for the DCMS discharge; this indicates that HIPIMS influences the TiAl target to a greater extent than the V target.

**Nitrogen Atmosphere**

Figure 6.15 shows the  $R_D$  and the  $P_T$  evolution for methane reactive atmosphere in mixed DCMS/HIPIMS discharge.

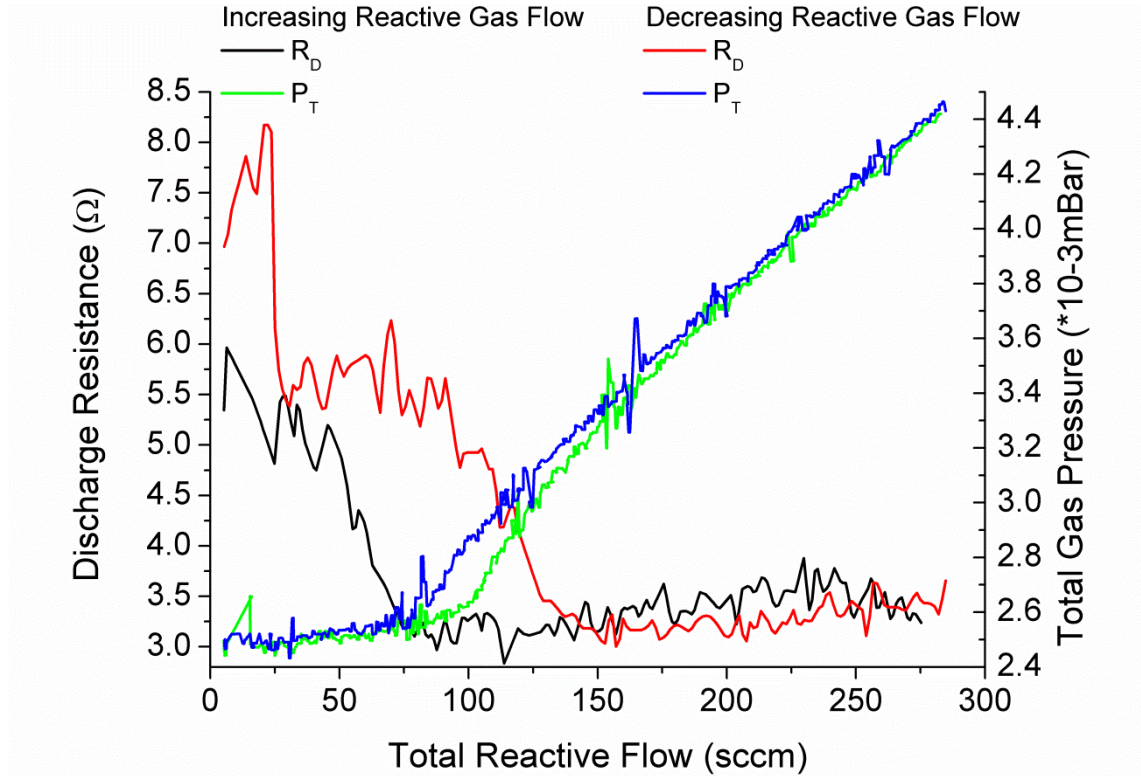


Figure 6.15 TiAl target discharge resistance and total gas pressure vs. total reactive flow rate curves: mixed DCMS/HIPIMS discharge; Nitrogen reactive atmosphere

As the nitrogen flow increases, the discharge resistance initially increases by 1  $\Omega$ . At 20 sccm, the  $R_D$  rapidly drops by 2.5  $\Omega$  as the nitrides starts to create. Between 20 and 100 sccm the drop rate is low as the target is slowly being covered with nitrides. At 100 sccm the drop rate speeds up, this is correlated with increase of the  $P_T$ . This indicates that target became poisoned and nitrogen molecules are released. From 150 sccm, the  $R_D$  begins to increase at a low rate and the total gas pressure increases linearly with the nitrogen flow.

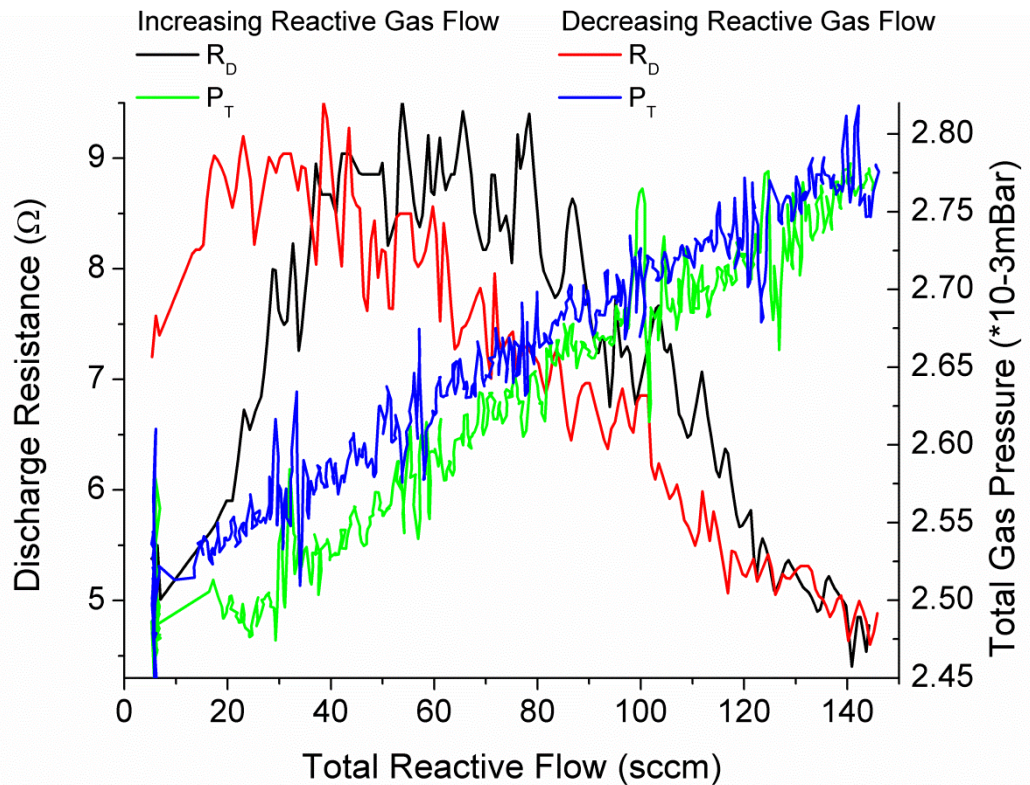
**Methane Atmosphere**

Figure 6.16 TiAl target discharge resistance and total gas pressure vs. total reactive flow rate curves: mixed DCMS/HIPIMS discharge; Methane reactive atmosphere.

Figure 6.16 shows that for the mixed nitrogen reactive atmosphere, the total gas pressure increase linearly with increasing methane flow over the whole process. The  $R_D$  initially increased by 1.5  $\Omega$  up to 60 sccm as the target becomes covered with carbides. Beyond 60 sccm the  $R_D$  drops, this indicates saturation of the target and releases the molecules. At the 120 sccm, the decreasing rate slows down as the target becomes fully poisoned. At the reverse, the hysteresis is observed between 0 and 120 sccm. There is a difference of 2  $\Omega$  between the start and the end value which is over 40% of overall change.

**Mixed Nitrogen and Methane atmosphere**

Figure 6.17 shows the  $R_D$  and the total gas pressure evolution in the mixed nitrogen and methane reactive atmosphere in the mixed DCMS/HIPIMS discharge.

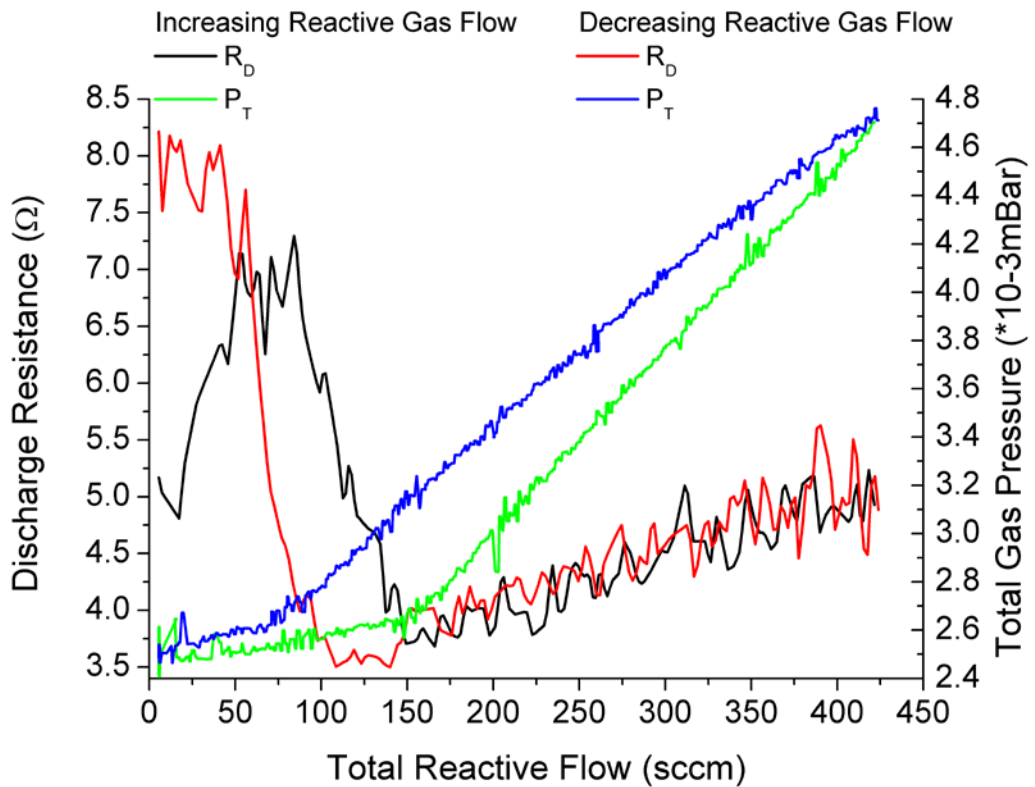


Figure 6.17 TiAl target discharge resistance and total gas pressure vs. total reactive flow rate curves: mixed DCMS/HIPIMS discharge; mixed nitrogen and methane reactive atmosphere

Initially the  $R_D$  increases, similarly as in the nitrogen, by 2  $\Omega$ . Between 50 and 85 sccm the  $R_D$  stays at the same level. At 85 sccm there is a rapid drop in the  $R_D$  from 7.2 to 3.6  $\Omega$  at 150 sccm. Beyond 150 sccm the target becomes fully poisoned and the  $R_D$  increases with low rate and the curve is similar; this is the same as for the V target (fig. 9). The hysteresis is observed between 0-150 sccm; it is relatively broad with 3  $\Omega$  of difference between the start and end values of the discharge resistance.

## 6.4 Effect of Reactive Gas Flow on the Plasma Stoichiometry

The evolution of ion flux composition with the flow of reactive gases is analysed in detail. The time resolved mass spectrometer ion signal was normalized to a maximum of the signal; the evolution of the signals was compared with evolution of the discharge resistance and the total gas pressure as well as with other measured mass species.

### 6.4.1 V Target

#### 6.4.1.1 DCMS Discharge

##### Argon Atmosphere

Figure 6.18 shows  $R_D$ ,  $P_T$ , metal and primary gases ion signals (top) and radicals ion signals (bottom) for argon flow when the experiment is performed in pure argon atmosphere with a DCMS discharge.

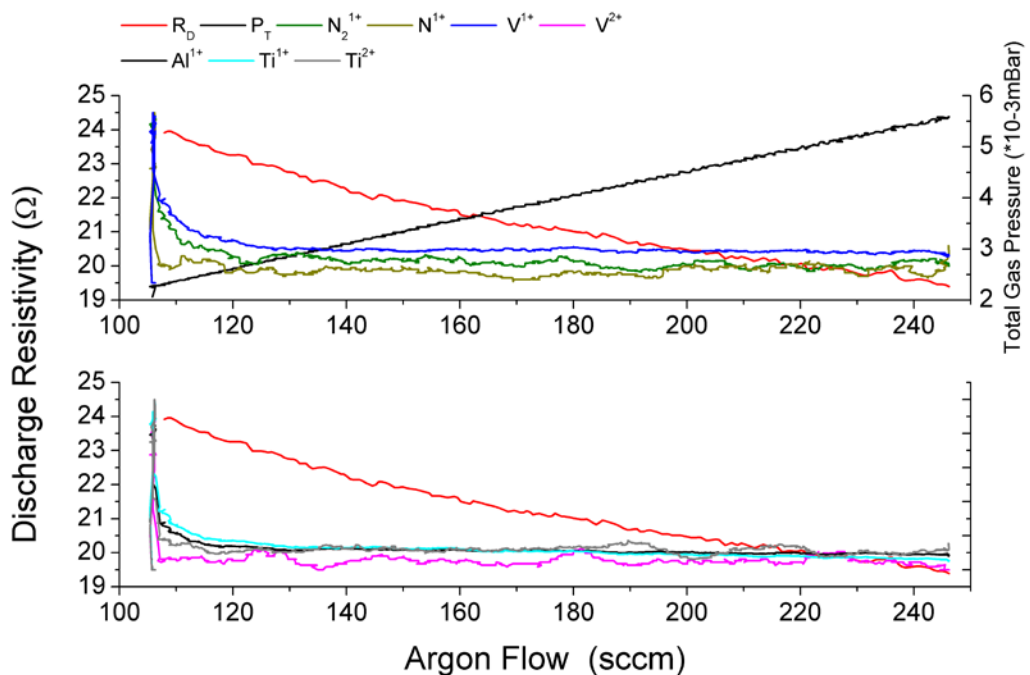


Figure 6.18 Discharge resistance, total gas pressure and mass-spectrometer data evolution in the DCMS of V discharge in an inert gas (Ar) atmosphere

As the argon flow increases, the V<sup>1+</sup>, Ti<sup>1+</sup>, V<sup>2+</sup>, Al<sup>1+</sup>, N<sub>2</sub><sup>1+</sup> and N<sup>+</sup> signals initially decrease. Beyond 125 sccm, signal levels remain at the same level. Other mass signals ions were also recorded; however they are omitted here due to their low intensity.

### Nitrogen Atmosphere

Figure 6.19 shows RD, PT, metal and primary gases ion signals (top) and radicals ion signals (bottom) for argon flow when the experiment is performed in nitrogen reactive atmosphere with a DCMS discharge.

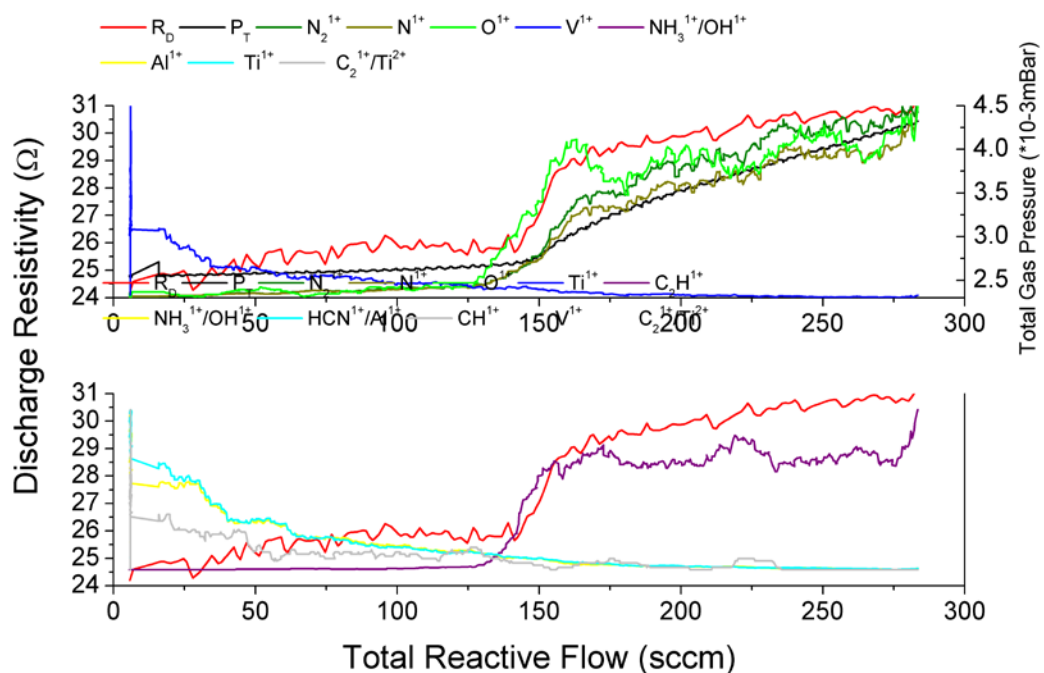


Figure 6.19 Discharge resistance, total gas pressure and mass-spectrometer data evolution in the DCMS of V discharge in a reactive gas (Ar+N<sub>2</sub>) atmosphere

As discharge resistance and total pressure increase with increasing nitrogen flow, the V<sup>1+</sup>, Ti<sup>1+</sup> and Al<sup>1+</sup> signals decrease. N<sub>2</sub><sup>1+</sup> and N<sup>1+</sup> signals increase at a low rate from 30 to 130 sccm. N<sub>2</sub> gas admitted to the chamber in this flow range will readily react and mainly get consumed at substrate surfaces and chamber walls; this will affect the target

at low level by growing nitrogen compound. This is evident from the total pressure. Beyond 130 sccm, the increase in N<sub>2</sub><sup>1+</sup> and N<sup>1+</sup> signals is observed and mass signals of 16 (O<sup>1+</sup>) and 17 (OH<sup>1+</sup>) are detected. At this stage, the system becomes saturated with nitrides and gas molecules are released into the system increasing the P<sub>T</sub> and the R<sub>D</sub> at 143 sccm. The change in the R<sub>D</sub> can be attributed to the changes in thickness, distribution and changing stoichiometry of the compound formed on the target surface. At 180 sccm, the increase rate of gas ion signals become smaller and the P<sub>T</sub> and the R<sub>D</sub> increase linearly with increasing flow. At this point, the target is fully poisoned and any change in the R<sub>D</sub> is due to a change in the plasma content and total pressure.

### Methane Atmosphere

Figure 6.20 shows R<sub>D</sub>, P<sub>T</sub> metal and primary gases ion signals (top) and radicals ion signals (bottom) for argon flow when the experiment is performed in methane reactive atmosphere in a DCMS discharge.

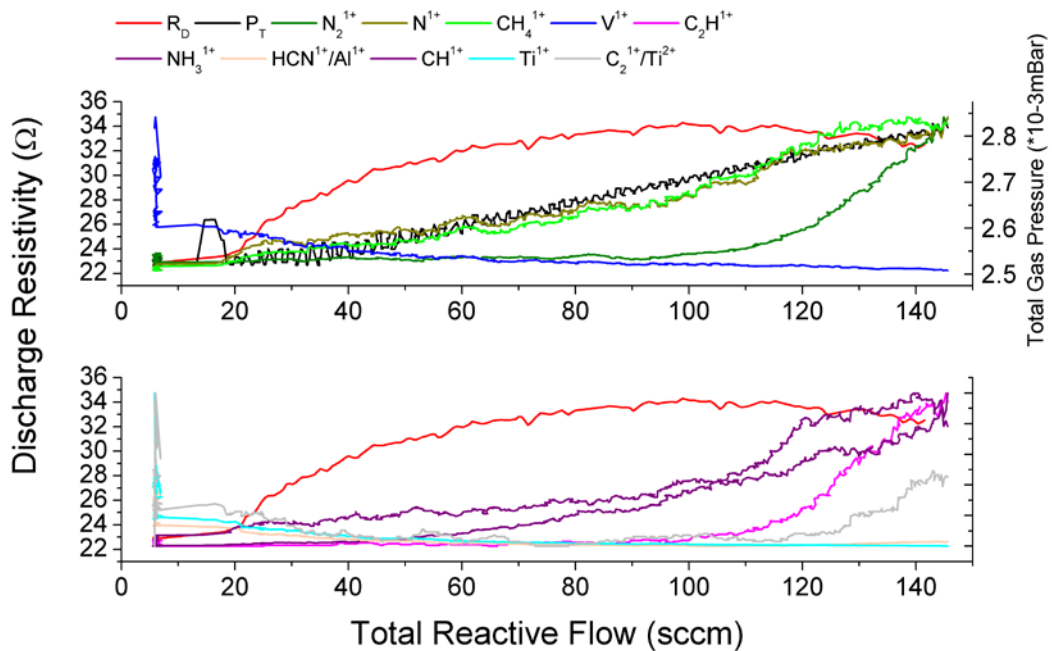


Figure 6.20 Discharge resistance, total gas pressure and mass-spectrometer data evolution in the DCMS of V discharge in a reactive gas (Ar+CH<sub>4</sub>) atmosphere

Up to 15 sccm, the  $R_D$  stays at the same level of 23  $\Omega$  and no increase of gas ions is observed. At 15 sccm, the  $CH_4^{1+}$ ,  $CH_2^{1+}$ ,  $N^{1+}$ , and  $CH^{1+}$  signal appear and a rapid increase in the  $R_D$  is observed. The increase of the in  $P_T$  is minor, indicating that changes in the  $R_D$  are mainly result of change in  $R_T$  as result of the carbide compound. From 40 sccm, the increase rate of the  $R_D$  slows down and an increase in gas signals and  $R_T$  are observed. At this flow, an increase in the decay of  $V^{1+}$  and  $Ti^{1+}$  signals is observed and appearance of  $HCN^{1+}$ ,  $N_2^{1+}$  and  $NH_3^{1+}$  is noted; this indicates saturation of the system with carbides and the release of gases. At 100 sccm, the  $C_2H^{1+}$ ,  $C_2^{1+}$  and  $HCN^{1+}$  are detected and increases in gas signals are observed. This is correlated with a decrease in the  $R_D$  which could be attributed to the rise in ionic currents; this is the result of increased ionization of the flux leading to enhanced collisions with the energetic electrons in the discharge. At 120 sccm, the increase rate of gas ions slow down and become proportional to the increase in total pressure. At this flow, the target is fully poisoned; this is 30 sccm faster than in case of nitrogen process.

### ***Mixed Nitrogen and Methane atmosphere***

Figure 6.21 shows  $R_D$ ,  $P_T$ , metal and primary gases ion signals (top) and radicals ion signals (bottom) for argon flow when the experiment is performed in mixed nitrogen and methane reactive atmosphere with a DCMS discharge.

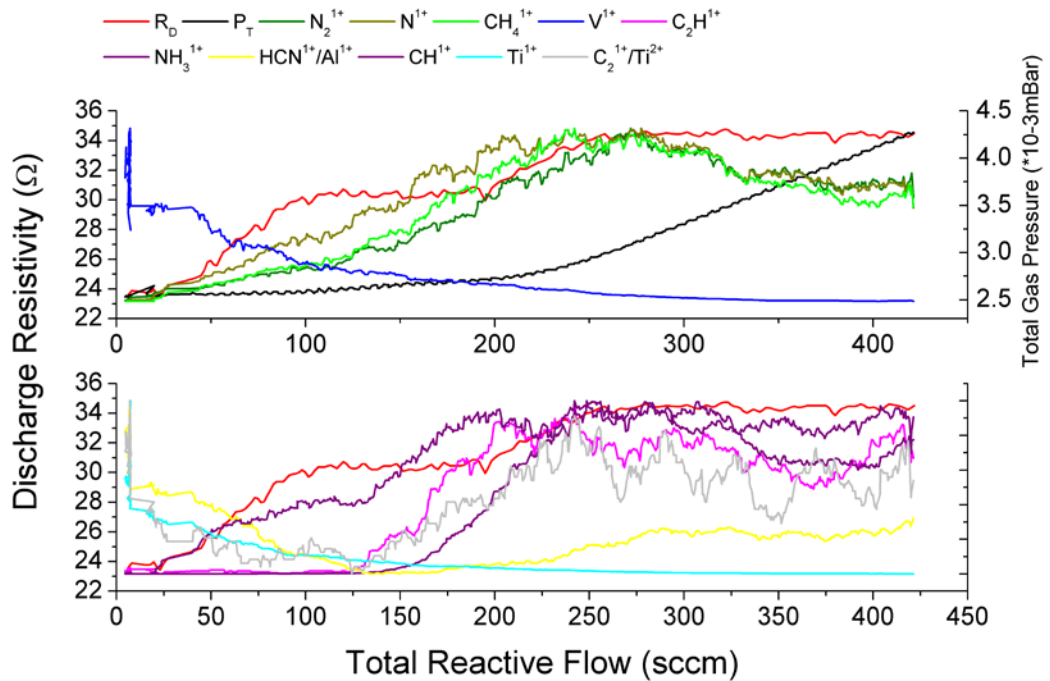


Figure 6.21 Discharge resistance, total gas pressure and mass-spectrometer data evolution in the DCMS of V discharge in a reactive gas (Ar+N<sub>2</sub>+CH<sub>4</sub>) atmosphere

The N<sub>2</sub><sup>1+</sup> and N<sup>1+</sup> are detected at 7 sccm while CH<sub>4</sub><sup>1+</sup> and CH<sup>1+</sup> at 18 sccm; this results in an increase of the discharge resistance. From 30 to 240 sccm, the dissociated N<sup>1+</sup> signal increases faster than N<sub>2</sub><sup>1+</sup>, where it reaches maximum, as well and CH<sub>4</sub><sup>1+</sup>. This is related with a sudden increase of total pressure. The V<sup>1+</sup> signal stays at the same level of 40 sccm after which signal decays and discharge resistance rate speeds up. Between 95 and 130 sccm, the CH<sup>1+</sup> remains at the same level. At this range the resistance stops increasing and stays at the level of 30 Ω. The N<sub>2</sub><sup>1+</sup> and CH<sub>4</sub><sup>1+</sup> increase is very similar ways up to 130 sccm after which the CH<sub>4</sub><sup>1+</sup> intensity increase is faster. At the same flow, the C<sub>2</sub>H<sup>1+</sup> and C<sub>2</sub><sup>1+</sup> are detected and an increase in the CH<sup>1+</sup> is observed; this indicates lower consumption of carbon. C<sub>2</sub>H<sup>1+</sup> reaches maximum at 200 sccm whereby R<sub>D</sub> starts to increase again.

The nitrogen and methane derivatives HCN<sup>1+</sup> and NH<sub>3</sub><sup>1+</sup> appear at 150 sccm, therefore indicating a delay in nitrogen saturation. They reach the maximum value at 240 sccm. After 250 sccm the N<sub>2</sub><sup>1+</sup>, N<sup>1+</sup>, CH<sub>4</sub><sup>1+</sup>, CH<sup>1+</sup> signals drop, while total pressure continues

to increase linearly and the  $R_D$  remains constant.  $C_2H^{1+}$  signal stays constant and  $HCN^{1+}$  signal slowly increases. The drop of the gas signals at high flow is caused by high pressure and a reducing electron temperature. The low electron temperature reduces methane dissociation resulting in the production of  $HCN^{1+}$  and  $C_2H_2^{1+}$  [138]. Similarly, as the  $N^{1+}$  signal, the  $N_2^{1+}$  signal reaches maximum at 270 sccm after where the  $NH_3^{1+}$  signal drops.

#### 6.4.1.2 DCMS/HIPIMS Discharge

##### Argon Atmosphere

Figure 6.22 shows  $R_D$ ,  $P_T$ , metal and primary gases ion signals (top) and radicals ion signals (bottom) for argon flow when the experiment is performed in a nitrogen reactive atmosphere with a mixed DCMS/HIPIMS discharge.

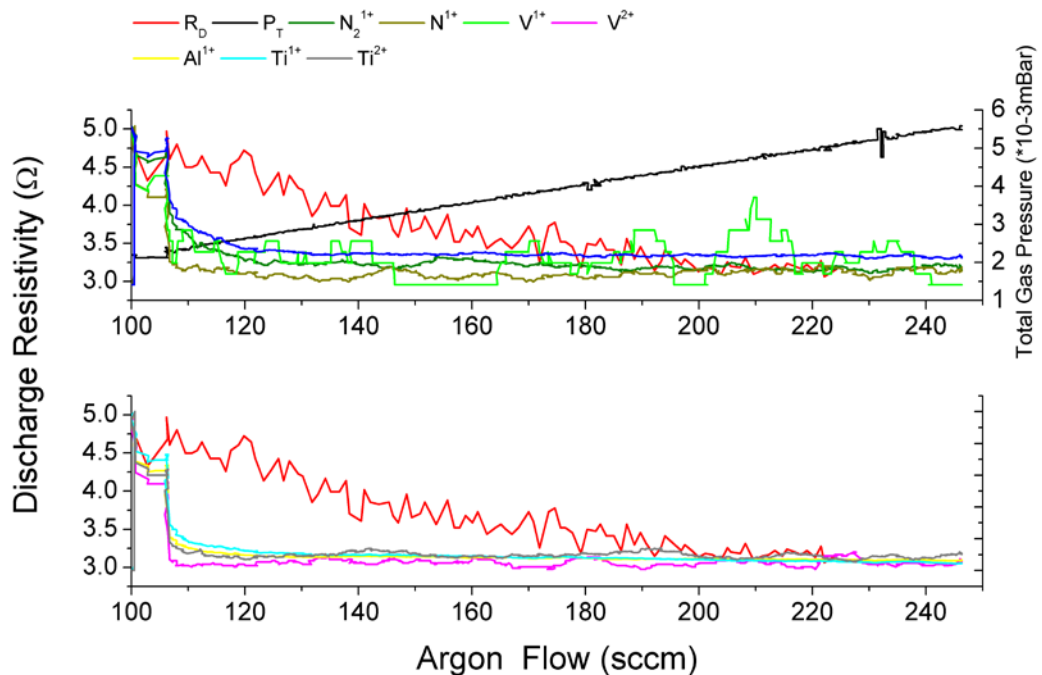


Figure 6.22 Discharge resistance, total gas pressure and mass-spectrometer data evolution in the HIPIMS of V discharge in an inert gas (Ar) atmosphere

In pure argon atmosphere, the  $R_D$  drops with increasing flow similarly as in DCMS case. The  $Ti^+$  and  $Al^{1+}$  signals increase with increasing argon flow.  $V^{1+}$  signal intensity initially increases although after 180 sccm decreases. The decrease might be caused by high ion flux from the TiAl target repulsing vanadium ions from a quadrupole probe. The  $N_2$  signal has been detected and stays on the same level for the whole process. Other signals are within the background noise level.

### Nitrogen Atmosphere

Figure 6.23 shows  $R_D$ ,  $P_T$ , metal and primary gases ion signals (top) and radicals ion signals (bottom) for argon flow when the experiment is performed in nitrogen reactive atmosphere with a mixed DCMS/HIPIMS discharge.

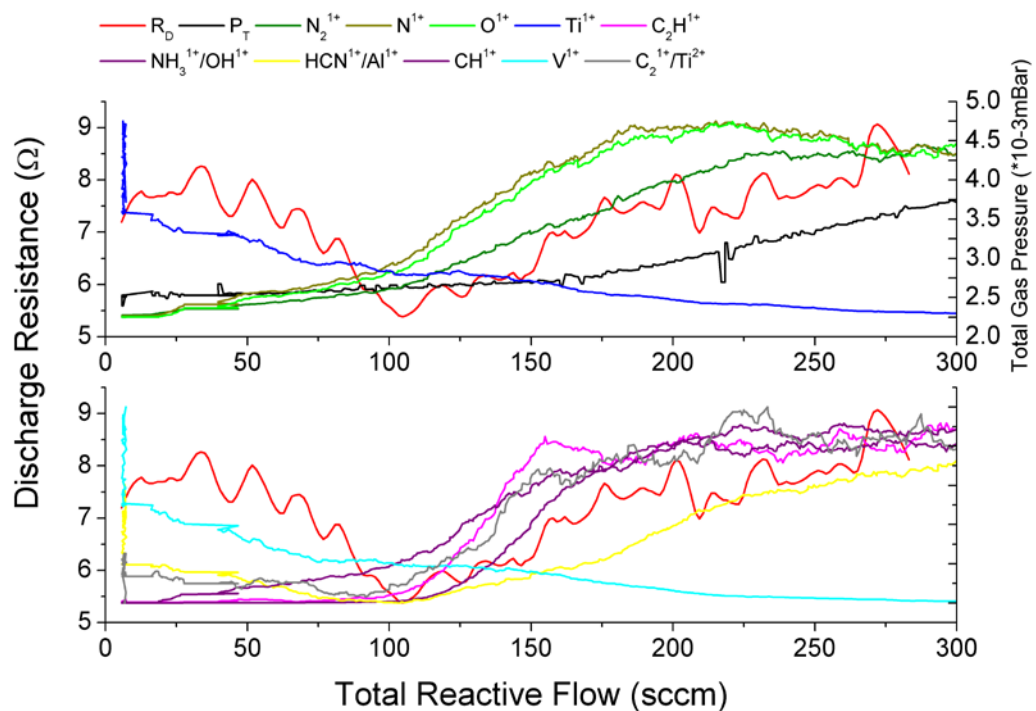


Figure 6.23 Discharge resistance, total gas pressure and mass-spectrometer data evolution in the HIPIMS of V discharge in a reactive gas (Ar+N<sub>2</sub>) atmosphere

Up to 30 sccm, the  $R_D$  stays constant and there is no increase in gas ion signal. The vanadium ion signal drops from the beginning of the process. At 30 sccm there is an

increase in N<sub>2</sub> and N ion signals and the R<sub>D</sub> decreases. At 83 sccm, the OH<sup>1+</sup> and O<sup>1+</sup> signals appear followed by a rapid increase in N<sup>1+</sup> and N<sub>2</sub><sup>1+</sup> signals with total pressure at 100 sccm. At the same flow, O<sup>1+</sup> and OH<sup>1+</sup> signals saturate and the R<sub>D</sub> increases. At 180 sccm, the nitrogen ion signals saturate and increase in total pressure and the R<sub>D</sub> becomes linear.

### Methane Atmosphere

Figure 6.24 shows R<sub>D</sub>, P<sub>T</sub>, metal and primary gases ion signals (top) and radicals ion signals (bottom) for argon flow when the experiment is performed in methane reactive atmosphere with a mixed DCMS/HIPIMS discharge.

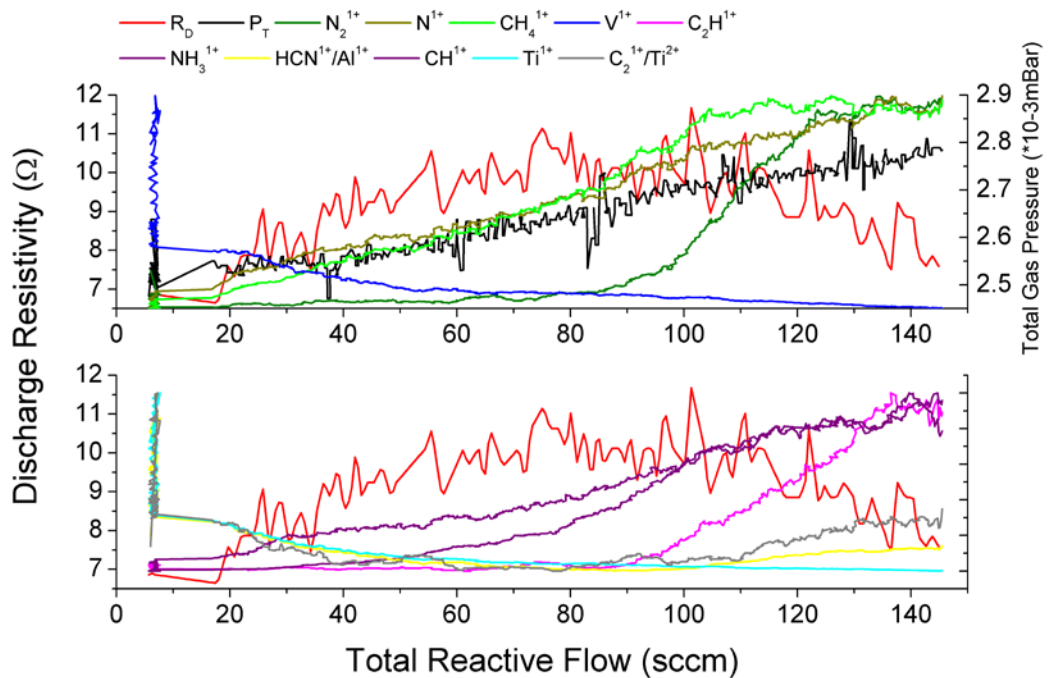


Figure 6.24 Discharge resistance, total gas pressure and mass-spectrometer data evolution in the HIPIMS of V discharge in a reactive gas (Ar+CH<sub>4</sub>) atmosphere

From 0 to 15 sccm there is no increase in CH<sub>4</sub><sup>1+</sup> and its radical ions signals. The R<sub>D</sub> increases with low gradient. At 15 sccm, the CH<sup>1+</sup>, CH<sub>2</sub><sup>1+</sup>, and CH<sub>4</sub><sup>1+</sup> signals appear and the R<sub>D</sub> increases from 6 to 11 Ω at 85 sccm. At 90 sccm, N<sub>2</sub><sup>1+</sup>, C<sub>2</sub>H<sup>1+</sup> and C<sub>2</sub><sup>1+</sup> signals

appear which is followed by the saturation of CH<sub>4</sub><sup>1+</sup> and CH<sup>1+</sup> signals. The R<sub>D</sub> decrease to 7Ω at 140 sccm.

### Mixed Nitrogen and Methane atmosphere

Figure 6.25 shows R<sub>D</sub>, P<sub>T</sub>, metal and primary gases ion signals (top) and radicals ion signals (bottom) for argon flow when the experiment is performed in mixed nitrogen and methane reactive atmosphere with a mixed DCMS/HIPIMS discharge.

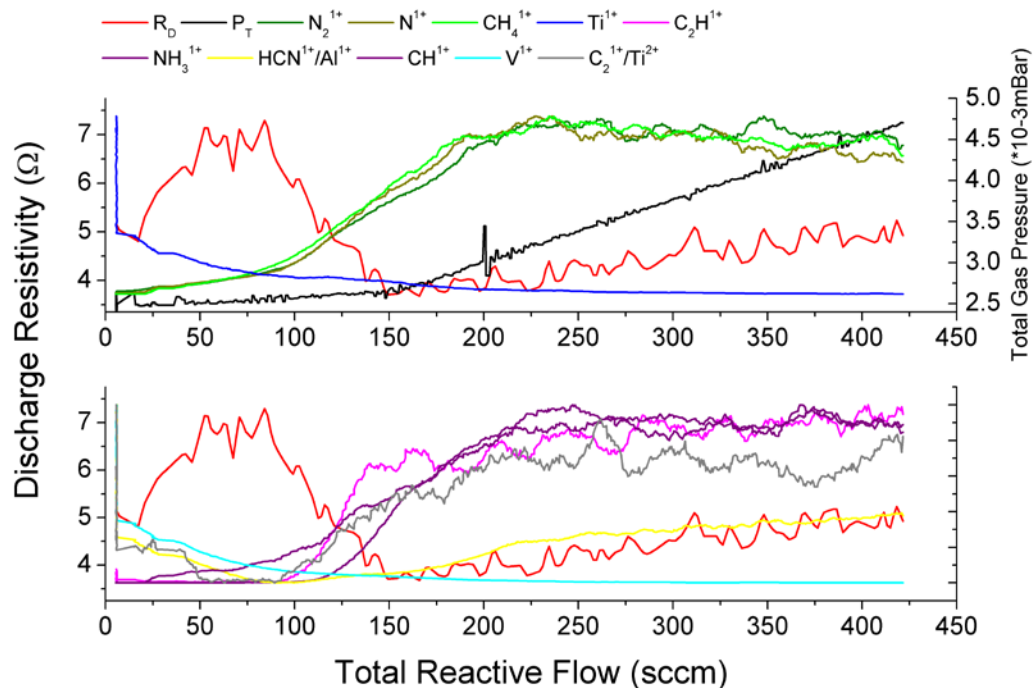


Figure 6.25 Discharge resistance, total gas pressure and mass-spectrometer data evolution in the HIPIMS of V discharge in a reactive gas (Ar+N<sub>2</sub>+CH<sub>4</sub>) atmosphere

Ion fluxes show a similar dependence as with DCMS sputtering. The vanadium signal drops with increasing R<sub>D</sub>. After 80 sccm, The R<sub>D</sub> reduces rapidly and the partial pressure of gases rapidly increases. This indicates that the target is poisoned; however, the metal content remains high. At 150 sccm, when the target is fully poisoned, the R<sub>D</sub> starts to increase. The CH<sub>4</sub><sup>1+</sup> and N<sup>1+</sup> signal drops after 200 sccm while the N<sub>2</sub><sup>1+</sup> signal increases with a lower rate.

The CH<sup>1+</sup> signal appears at the same time as primary gasses, while C<sub>2</sub>H<sup>1+</sup> appears at 70 sccm. Nitrogen containing radicals appear at 100 sccm where the R<sub>D</sub> drops.

Carbohydrates reach a maximum at 150 sccm and nitrogen containing radicals at 200 sccm.

When the reactive gas flow is reduced, primary gas radicals ion signals increase. At 200 sccm the HCN<sup>1+</sup> signal decreases; this is related to the small increase in CH<sub>4</sub><sup>1+</sup> and N<sup>1+</sup> signals. At 160 sccm the remaining gas ion signals reduce. At 75 sccm, the metal ion signal is higher than gas ion signals and the R<sub>D</sub> rapidly increases.

## 6.4.2 TiAl Target

### 6.4.2.1 DCMS Discharge

#### Argon Atmosphere

Figure 6.26 shows R<sub>D</sub>, P<sub>T</sub>, metal and primary gases ion signals (top) and radicals ion signals (bottom) for argon flow when the experiment is performed in nitrogen reactive atmosphere with a DCMS discharge.

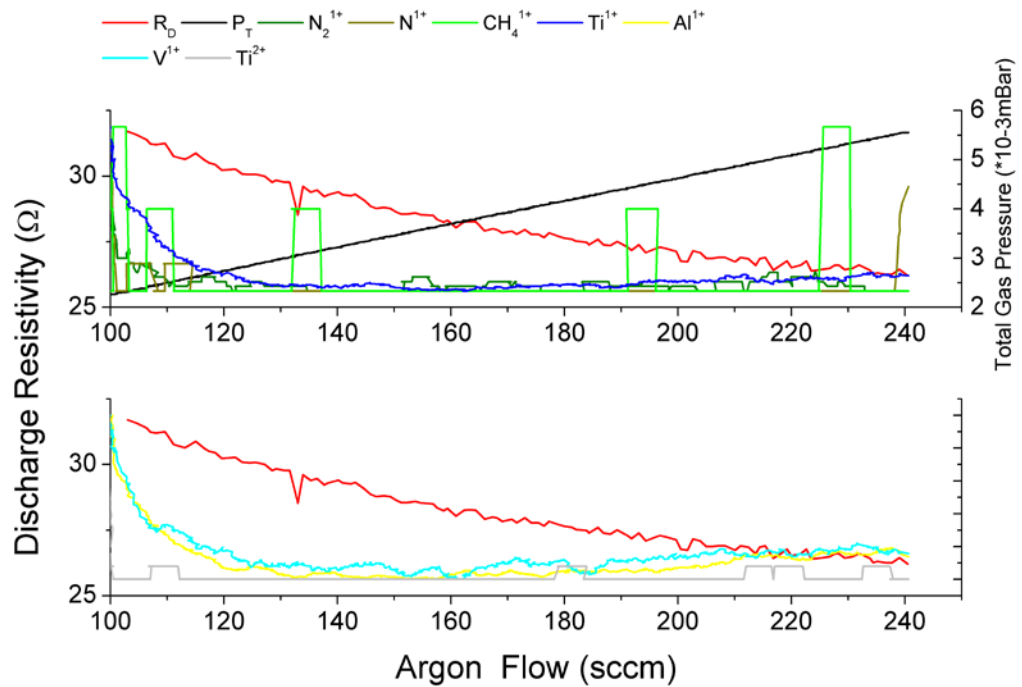


Figure 6.26 Discharge resistance, total gas pressure and mass-spectrometer data evolution in the DCMS of TiAl discharge in an inert gas (Ar) atmosphere

$R_D$  and  $P_T$  behave similarly as in the case of the vanadium target: the  $R_D$  drops with increasing argon flow, whereas the total pressure increases linearly. Metal signals of  $V^{1+}$  and  $Ti^{1+}$  drop with increasing argon flow up to 140 sccm; for higher flows they remain constant. At 180 sccm flow, the metal ion intensities increase. The  $N_2^{1+}$  signal has been detected and its intensity drops with increasing argon flow. Other primary gas and residual gas signals are hidden by the background noise level. There is no hysteresis for the  $R_D$ , the  $P_T$  or metal ions.

### ***Nitrogen Atmosphere***

Figure 6.27 shows  $R_D$ ,  $P_T$ , metal and primary gases ion signals (top) and radicals ion signals (bottom) for argon flow when the experiment is performed in nitrogen reactive atmosphere with a DCMS discharge.

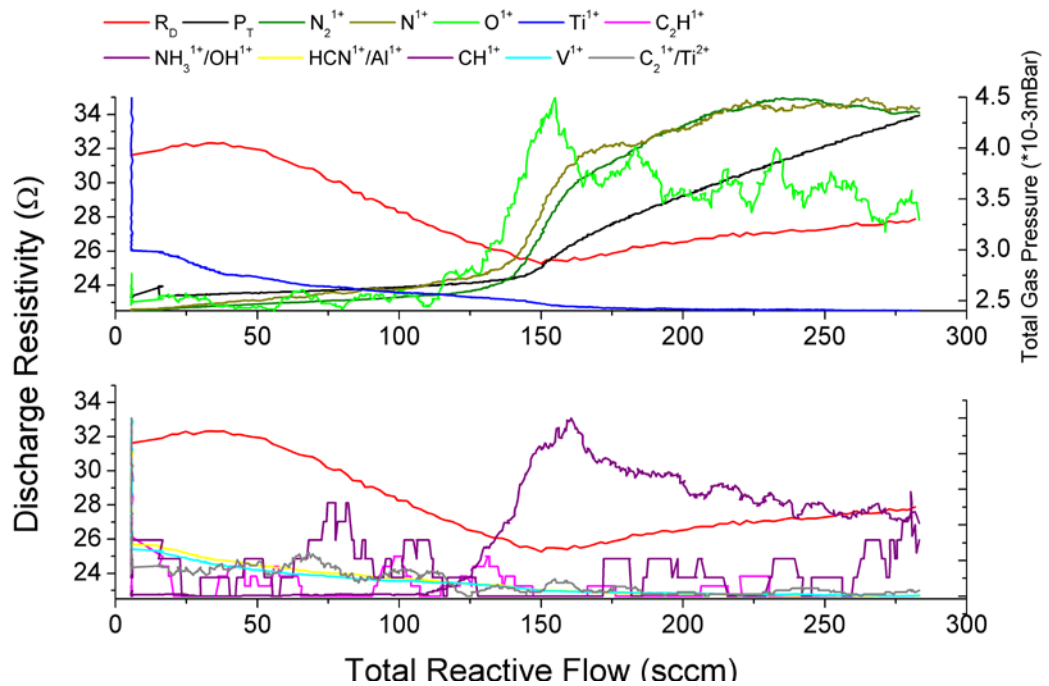


Figure 6.27 Discharge resistance, total gas pressure and mass-spectrometer data evolution in the DCMS of TiAl discharge in a reactive gas (Ar+N<sub>2</sub>+CH<sub>4</sub>) atmosphere

The Ti<sup>1+</sup> ion signal drops with increasing flow. At 50 sccm the slope of decrease becomes lower which is associated with a drop in the R<sub>D</sub>. The R<sub>D</sub> continues to drop until 150 sccm flow, following which it begins to increase. The sudden increase of total pressure, as well as in signals of N<sub>2</sub><sup>1+</sup> and N<sup>1+</sup>, are observed at this point. The TiAl target is poisoned at the same flow as the V target. At 125 sccm, the CH<sub>4</sub><sup>1+</sup> and NH<sub>3</sub><sup>1+</sup> signals appear, indicating release of gases from the chamber wall.

### ***Methane Atmosphere***

Figure 6.28 shows R<sub>D</sub>, P<sub>T</sub>, metal and primary gases ion signals (top) and radicals ion signals (bottom) for argon flow when the experiment is performed in methane reactive atmosphere with a DCMS discharge.

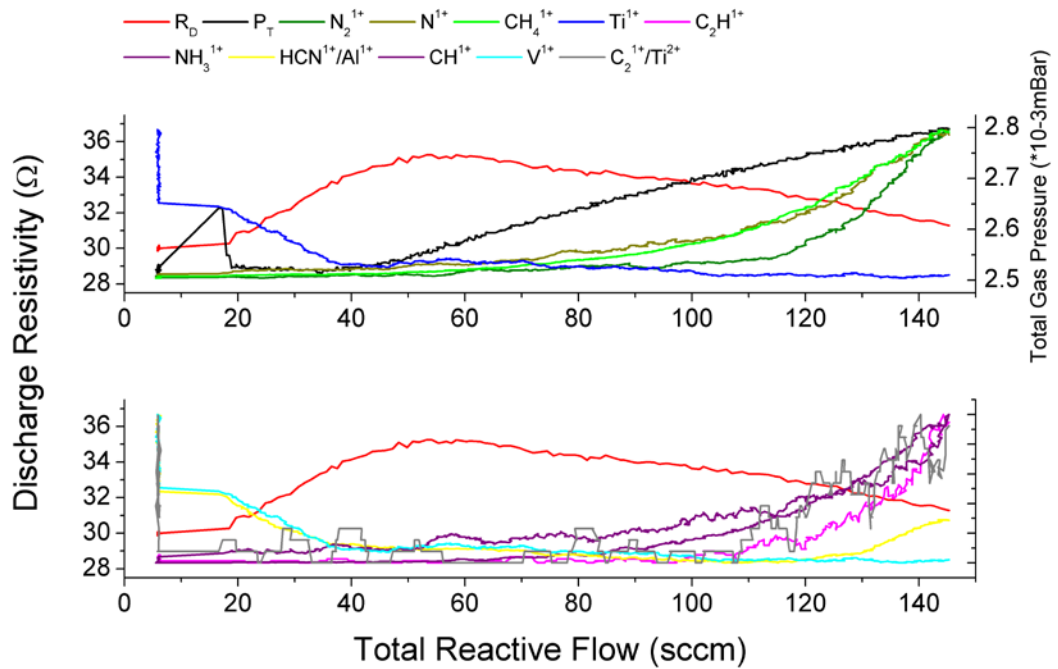


Figure 6.28 Discharge resistance, total gas pressure and mass-spectrometer data evolution in the DCMS of TiAl discharge in a reactive gas (Ar+CH<sub>4</sub>) atmosphere

Between 5-10 sccm, CH<sub>4</sub><sup>1+</sup>, N<sup>1+</sup> and CH<sup>1+</sup> signals are detected. Ti<sup>1+</sup> and Al<sup>1+</sup> signals drop linearly. At 40 sccm, the total pressure increases rapidly and the drop of metal ion intensities become very low. From this point, CH<sub>4</sub><sup>1+</sup>, N<sup>1+</sup> and CH<sup>1+</sup> signals increase logarithmically. At 60 sccm, the R<sub>D</sub> reaches its maximum; this is 40 sccm earlier than for the vanadium target. Moreover, the drop in the R<sub>D</sub> is lower than in the case of the vanadium target.

### ***Mixed Nitrogen and Methane atmosphere***

Figure 6.29 shows R<sub>D</sub>, P<sub>T</sub>, metal and primary gases ion signals (top) and radicals ion signals (bottom) for argon flow when the experiment is performed in mixed nitrogen and methane reactive atmosphere with a DCMS discharge

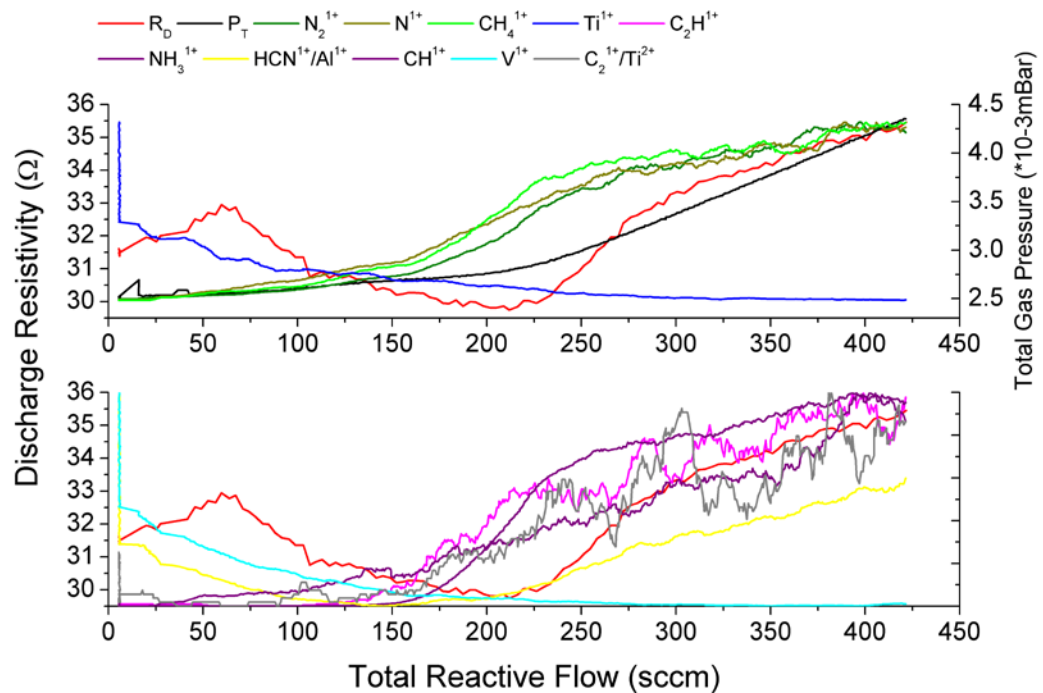


Figure 6.29 Discharge resistance, total gas pressure and mass-spectrometer data evolution in the DCMS of TiAl discharge in a reactive gas (Ar+N<sub>2</sub>+CH<sub>4</sub>) atmosphere

$R_D$  increases with the appearance of  $N_2^{1+}$ ,  $CH_4^{1+}$  and  $N^{1+}$  signals at 20 sccm. At the same flow, the  $CH^{1+}$  signal appears and a sudden drop in metal signals of  $Ti^{1+}$ ,  $Al^{1+}$  and  $V^{1+}$  are observed. The reduction in the  $R_D$  is lower than in the methane atmosphere. At 225 sccm there is a big increase in  $R_D$ ; it reaches the same level as for the vanadium target. At 60 sccm, the  $R_D$  reaches a local maximum and drops to 30  $\Omega$  at 210 sccm. At 85 sccm,  $C_2H^{1+}$  appears. At 105 sccm the signal drop rate is smallest. At 180 sccm,  $NH_3^{1+}$  and  $HCN^{1+}$  signals appear and primary gas signals increase. At 210 sccm, the  $R_D$  increases and there is an increase in the total pressure slope. From this point, the  $R_D$  follows the behaviour of gases.

### 6.4.2.2 DCMS/HIPIMS Discharge

#### Argon Atmosphere

Figure 6.30 shows  $R_D$ ,  $P_T$ , metal and primary gases ion signals (top) and radicals ion signals (bottom) for argon flow when the experiment is performed in nitrogen reactive atmosphere with a mixed DCMS/HIPIMS discharge.

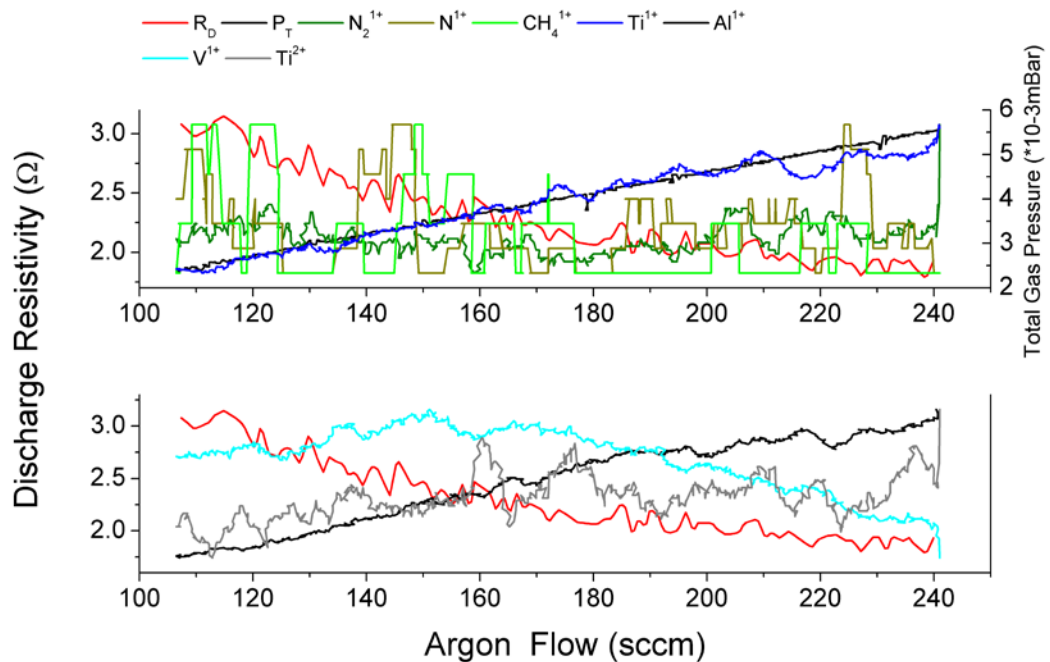


Figure 6.30 Discharge resistance, total gas pressure and mass-spectrometer data evolution in the HIPIMS of TiAl discharge in an inert (Ar) atmosphere

For argon atmosphere, the  $R_D$  behaves similarly as in the DCMS case; however, in HIPIMS, the  $R_D$  is much lower.  $Al^{1+}$ ,  $Ti^{1+}$  and  $Ti^{2+}$  signals increase with increasing argon flow indicating increasing ionisation; for DCMS, the signals initially drop and then increase.

#### Nitrogen Atmosphere

Figure 6.31 shows  $R_D$ ,  $P_T$ , metal and primary gases ion signals (top) and radicals ion signals (bottom) for argon flow when the experiment is performed in nitrogen reactive atmosphere with a mixed DCMS/HIPIMS discharge.

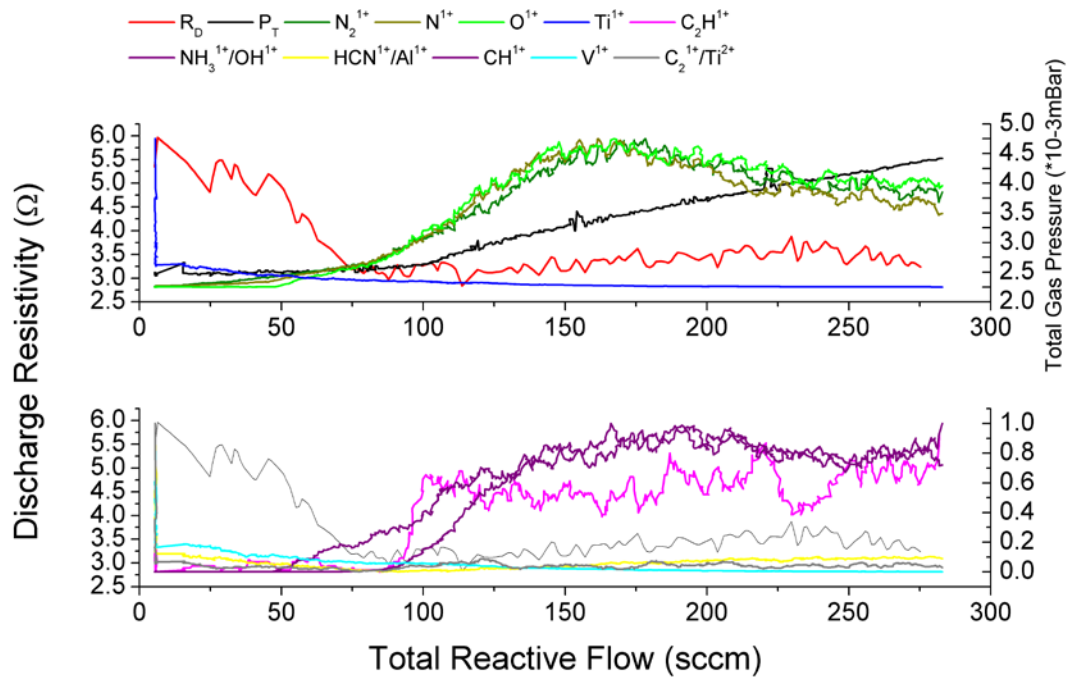


Figure 6.31 Discharge resistance, total gas pressure and mass-spectrometer data evolution in the HIPIMS of TiAl discharge in a reactive gas (Ar+N<sub>2</sub>) atmosphere

When flows increase, the Ti<sup>1+</sup>, Al<sup>1+</sup> and V<sup>1+</sup> signals decrease. At very low flow (up to 20 sccm), the gas ion signal is very low. Above 20 sccm, the N<sub>2</sub><sup>1+</sup> and N<sup>1+</sup> signals appear and the R<sub>D</sub> decreases. At 50 sccm, the O<sup>1+</sup>/CH<sup>1+</sup> signal appears whilst N<sub>2</sub><sup>1+</sup> and N<sup>1+</sup> signals increase more rapidly. At this flow, the R<sub>D</sub> drops with a greater gradient. At 80 sccm, the OH<sup>1+</sup>/NH<sub>3</sub><sup>1+</sup>, C<sub>2</sub>H<sup>1+</sup> and HCN<sup>1+</sup> signals appear and the N<sub>2</sub><sup>1+</sup> and N<sup>1+</sup> signal increases become exponential. The presence of carbon ions may be due to insufficient target cleaning. The R<sub>D</sub> reaches its minimum and starts to increase. This is followed by a rapid increase of total pressure at 100 sccm. At 160 sccm, the ion signal of gases saturates, N<sub>2</sub><sup>1+</sup> and N<sup>1+</sup> signals begin to decrease and the increase in total pressure becomes linear. At 220 sccm, the N<sub>2</sub><sup>1+</sup>, N<sup>1+</sup> and NH<sub>3</sub><sup>1+</sup> signal reductions slow down and the resistance begins to drop again with a very low gradient.

## Methane Atmosphere

Figure 6.32 shows  $R_D$ ,  $P_T$ , metal and primary gases ion signals (top) and radicals ion signals (bottom) for argon flow when the experiment is performed in methane reactive atmosphere with a mixed DCMS/HIPIMS discharge.

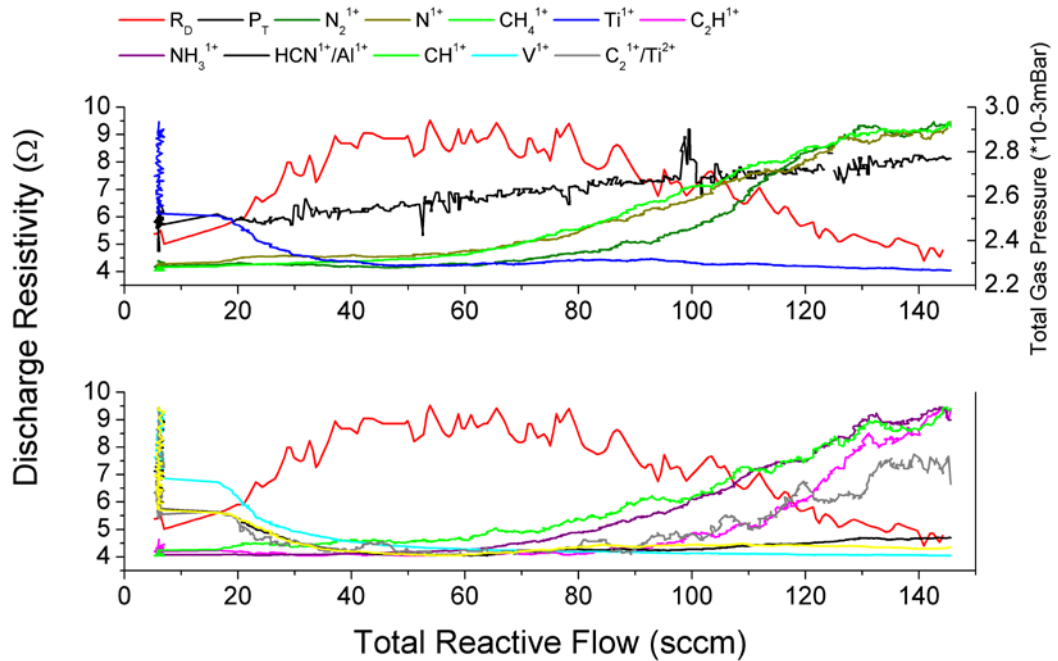


Figure 6.32 Discharge resistance, total gas pressure and mass-spectrometer data evolution in the HIPIMS of TiAl discharge in a reactive gas (Ar+CH<sub>4</sub>) atmosphere

When flows increase, the  $Ti^{1+}$ ,  $Al^{1+}$  and  $V^{1+}$  signals decrease. At very low flow, up to 18 sccm, the  $R_D$  decreases and the gas ion signals are very low. At 18 sccm, the  $CH^{1+}$ ,  $CH_2^{1+}$  and  $CH_4^{1+}$  signals appear; this results in a rapid increase of both the  $R_D$  and the  $P_T$ . At 50 sccm, the  $R_D$  reaches maximum and begins to drop whilst the  $CH^{1+}$ ,  $CH_2^{1+}$  and  $CH_4^{1+}$  signal increases become exponential. At 80 sccm, the  $N_2^{1+}$ ,  $HCN^{1+}$  and  $C_2H^{1+}$  signals appear and the  $R_D$  decreases; total pressure increase also slows down.

**Mixed Nitrogen and Methane atmosphere**

Figure 6.33 shows  $R_D$ ,  $P_T$ , metal and primary gases ion signals (top) and radicals ion signals (bottom) for argon flow when the experiment is performed in mixed nitrogen and methane reactive atmosphere with a mixed DCMS/HIPIMS discharge.

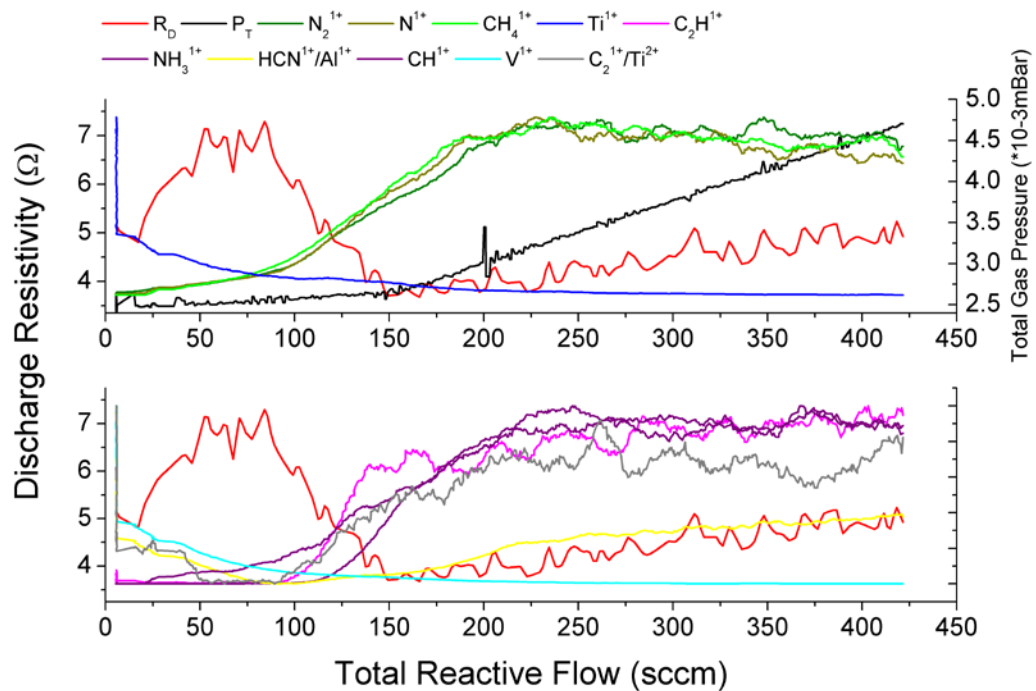


Figure 6.33 Discharge resistance, total gas pressure and mass-spectrometer data evolution in the HIPIMS of TiAl discharge in a reactive gas (Ar+CH<sub>4</sub>) atmosphere

The CH<sub>4</sub><sup>1+</sup> signal increase is observed from the beginning of the process. N<sub>2</sub><sup>1+</sup>, N<sup>1+</sup> and CH<sup>1+</sup> signals appear at 25 sccm. The Ti<sup>1+</sup> signal drops rapidly from the start of the process. Between 90 sccm, where primary gases rapidly increase and residual gases appear, and at/from 120 sccm, the vanadium signal stays constant. At this flow the  $R_D$  rapidly drops. At 120 sccm there is a small peak in the  $R_D$  which is associated with the appearance of HCN<sup>1+</sup>. At 150 sccm the C<sub>2</sub>H<sup>1+</sup> signal reaches maximum and the  $R_D$  begins to increase. At 200 sccm, the primary gases CH<sup>1+</sup>, NH<sub>3</sub><sup>1+</sup> and HCN<sup>1+</sup> signals reach their maximum. All primary gases and NH<sub>3</sub><sup>1+</sup> signals drop, while CH<sup>1+</sup>, C<sub>2</sub>H<sup>1+</sup> and HCN<sup>1+</sup> signals increases.

## 6.5. Discussion

### Effect of the Argon Atmosphere

Argon is an inert gas and does not take part in the compound growth. Thus, the total pressure increases with increasing argon flow. There is no compound creation on the target so the  $R_T$  only changes minimally due to argon atom implantation. The  $R_P$  will decrease due to the higher pressure; more volume ionisation results in an ion current increase, there at constant power there is a decrease in target voltage [45]. In pure argon atmosphere, the  $R_D$  will be dominated by the pressure and plasma ionisation degree.

### Effect of the N<sub>2</sub> Reactive Atmosphere

For the nitrogen reactive atmosphere the poisoning process can be divided into three stages.

In the first stage, the majority of the gas is gettered by metal atoms, creating a nitride compound on the target surface and chamber wall. Growth of the compound on the target causes an increase in  $R_T$ . For the V target the  $R_T$  increases as for the TiAl target the  $R_T$  decreases. At the same time, the increasing pressure increases the effective ionization of the gas resulting in a decrease of  $R_p$ .

The next stage begins with increase in partial pressure of the N<sub>2</sub> and of the N and with the increase in  $P_T$ . At this point, the target is becoming heavily covered with an insulating layer. As the  $P_T$  increases, the  $R_p$  has a higher influence on  $R_D$ .

At third stage, the increase of total pressure becomes linear; both primary and residual gas ion signals slow down. At this flow the target is fully poisoned and changes of the  $R_D$  are dominated by changes of the  $R_p$ .

For both target materials the stages occurs at the same flows as they are in the closed system.

In HIPIMS it was observed that the  $R_P$  generally has a higher influence on the  $R_D$  than on the  $R_T$ , especially at higher flows. There is no increase in  $R_T$  at the beginning of second stage. In the third stage the influence of  $R_P$  is bigger than in DCMS processes; this can be seen by the reduced increase of  $R_D$ . In HIPIMS, processes when plasma is more ionised, the drop in the  $R_D$  is much smaller than for the TiAl target. The increase in  $R_T$  might indicate a phase transition of the compound from  $V_2N$  to  $VN$ . In DCMS processes, there is a lower drop comparing to TiAl than in HIPIMS case.

### Effect of the CH<sub>4</sub> Reactive Atmosphere

For the methane reactive atmosphere there are three stages similarly as in the nitrogen atmosphere. In the first stage the  $R_D$  increases due to increase in  $R_T$  (for both targets) as the compound is created. There is a minor reduction of in the  $R_P$ , as the  $P_T$  increases. For carbon atmosphere this stage is short when compared with the nitrogen atmosphere. In the second stage the target becomes saturated and partial pressure of  $CH_4^{1+}$ ,  $CH^{1+}$ ,  $N_2^{1+}$ ,  $N^{1+}$  and  $NH_3^{1+}$  and the  $P_T$  increases. The presence of nitrides is due to nitrogen contamination of the chamber from previous experiments, as well as from atmospheric air. The metal ions reduction rate is remains very high. At this stage, the  $R_D$  is dominated by the large increase in  $R_T$  due to the lower  $R_D$  of carbide compounds.  $R_P$  is still increasing, but its effect is very small when compared to  $R_T$ .

At the third stage the target is heavily covered with the compound and there are no more changes in the stoichiometry. The  $R_T$  stays at the same level, thus the  $R_D$  drops, resulting in increasing  $P_T$  (and decreasing  $R_P$ ).

For HIPIMS, in the third region, the  $R_P$  has a higher influence which is visible as lower gradient of  $R_D$ . For the TiAl target, the third stage occurs 30 sccm earlier than in DC.

For the vanadium target, the regions are within the same flow ranges. The drop of the vanadium ion signal is less rapid than for the TiAl target; this means that the gradient in the second region is lower than for the TiAl target, but higher in third region.

In the second region, the increase of the  $R_D$  is not as steep as in same region for the TiAl target and in the third region the  $R_D$  is not increasing, like in TiAl case decrease. This change in the  $R_D$  behaviour for the vanadium target is attributed to  $R_T$  having a greater influence on  $R_D$ . The increase in  $R_T$  might indicate the phase transitions of the compound from the V<sub>2</sub>C phase to the V<sub>2</sub>C<sub>3</sub> phase transitions.

### **Effect of the Mixed N<sub>2</sub> and CH<sub>4</sub> Reactive Atmosphere**

Reactive sputtering in mixed atmosphere can be divided into four regions, regarding processes happening on the target and in the plasma.

In the first stage as the  $R_D$  increases as the compound is created. For the TiAl target, after the initial increase the  $R_D$  drops.

In the second stage an increase in the primary gases partial pressure is observed, as well as appearance of the radicals. For both targets the carbon radicals appear at lower flow than the nitrogen radicals. This indicates a change in the C:N ratio of the compound as the nitrogen is released later than the carbon. At this for the vanadium target the  $R_D$  stays constant, while for the TiAl target it decreases with lower rate than in the first stage. The partial pressure of the primary gases and the radicals increase is fast.

In the third stage a rapid increase of the PT is observed. This is associated with the increase of the  $R_D$  for both targets. At this stage the primary gases and the radicals saturates, and the increase becomes slower.

In the fourth stage the  $P_T$  increase becomes linear. The partial pressures of the primary gases and the radicals increase are very low for the TiAl target, while for the V target

they drop. At this stage, the  $R_D$  is fully dominated by the  $R_P$ ; this is controlled by the partial pressures of gases, particularly by HCN and CH.

### **Effect of the HIPIMS Discharge**

For all HIPIMS processes, the high energy pulses leads to better target cleaning; this is shown by a narrower hysteresis. However, high-energy pulses cause higher ionisation for both metal and gas atoms. Hence, the plasma is more reactive and there are more residual ions. This leads to the target being poisoned at lower flows compared with the DCMS discharge.

The mass signal profiles appear different for the DCMS and the HIPIMS discharges, as the primary gases and the radicals partial pressures are higher and the poisoning occurs earlier in HIPIMS discharge. For both discharges similar behaviour have been observed for all mass signals.

## **6.6. Conclusion**

When the total gas pressure and the resistance curves are compared with curves for the nitrogen and methane atmosphere, it can be assumed that the first increase in the  $R_D$  may be attributed to the drop of the vanadium metal. The second may be attributed to the compound creation by carbon and nitrogen. Due to the presence of carbon, the process is irreversible. The target is fully poisoned at 250 sccm.

The target poisoning studies in a various reactive atmosphere (nitrogen, methane, mixed nitrogen and methane + argon) for TiAl and V targets were successfully conducted in an industrial sized deposition chamber, operated with both DCMS and mixed DCMS/HIPIMS discharges. The following can be concluded: The target material dominates the hysteresis behaviour at the low flow. When the target becomes fully

covered with the compound, the dominating factor is plasma composition, especially radicals. When both nitrogen and methane are used, carbon shows higher reactivity and reacts with the target material faster than nitrogen.

## **7 Single Nanoscale Multilayer Coatings Deposited at Constant OES signal**

In this section an analysis of the coatings deposited at constant OES signals is performed. These coatings were deposited to get an understanding of the effect of the target poisoning level on the microstructure and mechanical properties of the films. For this purpose five Simple Nanoscale Multilayers Coatings (SNMC) were deposited at various OES signal levels between 20 - 45%. The coatings were produced using the combined DCMS / HIPIMS magnetron sputtering technique. Composition of the coatings was obtained by EDX analysis. The crystallographic orientation was analysed by X-ray diffraction. SEM imaging was used to study the surface topography and cross sectional structure of the coatings. The adhesion of the coating was determined using Rockwell indentation and the scratch tests. The scratch tests were performed on two kinds of substrates; polished HSS discs and unpolished inserts. Pin-on-disk tests were performed to determine the friction coefficient (resistance to sliding) and sliding wear resistance of TiAlCN/VCN coatings. Elemental mapping (EDX) was used to characterise wear properties and determine failures of the coating during the pin on disk test.

### **7.1 Overview of the experiments**

SNMC were deposited at different levels of target poisoning in order to cover all stages described in section 6.4, following the process sequence described in section 3.1.3 and chapter 5. The coatings differ only in the top layer, which was deposited at the last stage of the process. During this stage, the reactive gas flow was controlled with the PEM

system. The final process stage of the deposition for all SNMC is summarized in table 7.1. Coatings were deposited onto 5 different substrates: HSS disks, SS coupons, Si-wafer coupons, plain inserts and cutting inserts. Substrates are described in details in section 3.1.

Table 7.1 Deposition of the final SNMC TiAlCN/VCN coatings

Coating ID	OES signal	Deposition time	Bias voltage
45% OES	45%	4h	60V
37% OES	37%		
30% OES	30%		
25% OES	25%		
20% OES	20%		

The hardness is measured using nanohardness and microhardness tests. The adhesion to the substrate is quantified using scratch test and Rockwell hardness test (7.2-7.4).

## 7.2 Deposition Process

The total pressure and reactive flow increased as the OES signal decreased. The average reactive gas flows and average total pressure are given in table 7.2.

Table 7.2 Process parameters during deposition of SNMC

		45% OES	37% OES	30% OES	25% OES	20% OES
Average N2 flow	(sccm)	27	55.54	62.74	64.36	70.07
Average CH4 flow	(sccm)	13.66	27.84	31.52	32.22	34.95
Average PT	(Pa)	25.49	26.22	26.57	2.74	2.79

The process average total flows of the reactive gases for SNMC were overlapped with the OES signal hysteresis of the Vanadium line (figure 7.1).

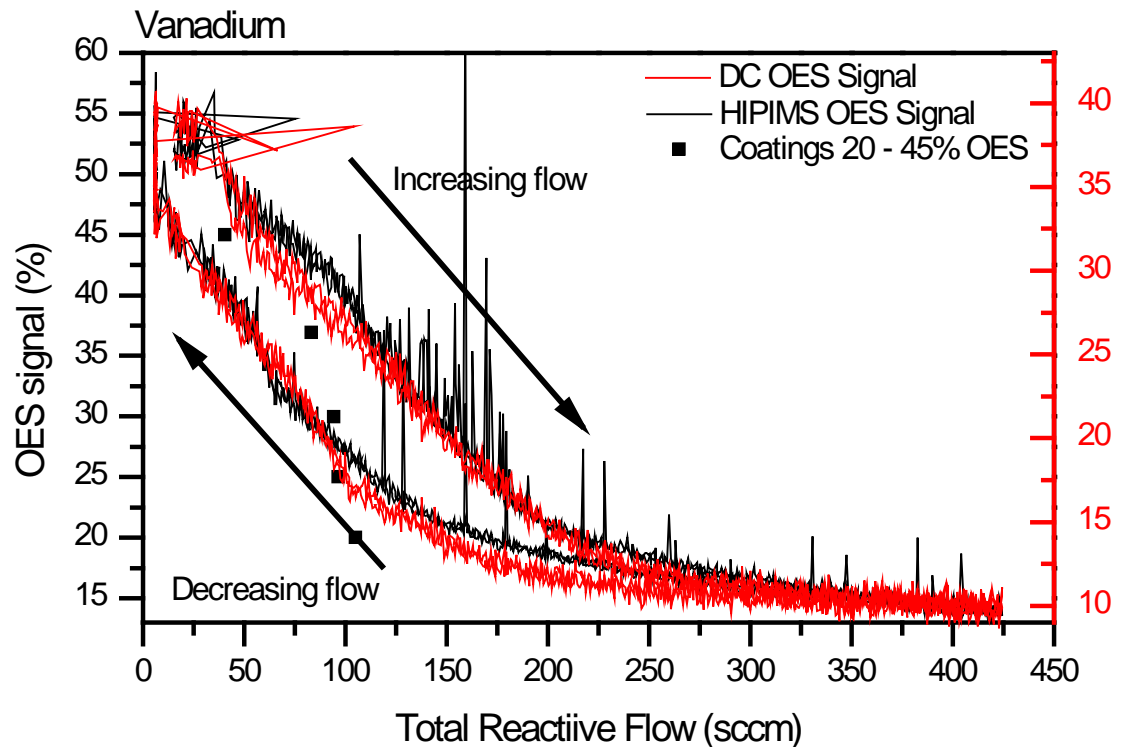


Figure 7.1 The process average total flows of the reactive gases for SNMC (black points) overlapped with the OES signal hysteresis of the Vanadium line for the DCMS (red line) and the HIPIMS (black line) discharges.

The signal used to plot hysteresis was recorded during the experiments described in section 6.4. The red line is hysteresis of the DCMS discharge, whereas black for the HIPIMS discharge, both in the mixed reactive atmosphere. Black dots represent average flow during individual SNMC coatings deposition.

It can be seen that points do not follow the hysteresis, however most of them are in between the decreasing and increasing profiles. The points do not overlap with either of the OES signal profiles. There are two reasons for this. Firstly, during the coating deposition, the OES signal was kept constant for several hours. In order to keep the OES signal constant, the gas flows were varying, while during the hysteresis analysis the reactive gas flow was controlled and the OES signal was varying. Additionally, before the TiAlCN/VCN coating deposition, a VN base layer was deposited, which

caused initial target poisoning. The second reason is the lower temperature during plasma analysis measurements.

All this changed the target condition, so that the results of both experiments can't be related directly. In order to compare the hysteresis with the average reactive flow points, the OES signal should be controlled and hysteresis analysis should be conducted after simulating the base layer deposition stage. These assumptions were tested and hysteresis experiments where only the OES signal and reactive gas flows were observed are performed. With high process temperature, simulated base layer deposition and where the process was OES controlled, the hysteresis was narrower and the fit of the deposition points with the hysteresis curves improved (not shown).

The Mechanical Properties and Chemical Composition of the SNMC is listed in table 7.3. The coating thickness and thus the deposition rate of the SNMC decreases logarithmically with decreasing OES signal. This is caused by a drop in sputter rate when the target is being poisoned [42].

The general trend shows that coating hardness increases with increasing reactive gas flow. The exception is the coating deposited at 37% OES signal, which combines a dense structure and high thickness of 4.63  $\mu\text{m}$ . This will be discussed in detail in section 7.4. Both microhardness and nanohardness test results also follow the general trend.

The elastic modulus of coatings 30%, 25% and 20% OES is in the same range of about 330 GPa. The elastic modulus of coatings deposited at 37% OES signal is highest with 377 GPa. The lowest elastic modulus is observed for coatings deposited at 45% OES signal where  $E=114$  GPa.

Table 7.3 The Mechanical Properties and Chemical Composition of the SNMC

		45% OES	37% OES	30% OES	25% OES	20% OES
Average N2 flow	(sccm)	27	55.54	62.74	64.36	70.07
Average CH4 flow	(sccm)	13.66	27.84	31.52	32.22	34.95
Average PT	(Pa)	25.49	26.22	26.57	2.74	2.79
Atomic content (%)	C	3.6	11.7	13.6	8.5	9.3
	N	1.9	24.4	29.7	32.1	35.8
	O	6.5	3.5	3.0	9.7	5.1
	Al	19,6	15,0	17,0	15,2	14,6
	Ti	27,0	17,3	14,5	12,8	12,2
	V	41,5	28,2	22,2	21,6	23,0
Thickness	( $\mu\text{m}$ )	5,1	4,63	3,98	2,36	2,24
Microhardness	(HK)	780	3721	3209	3479	3699
Nanohardness	(MPa)	3792	29341	18009	29233	27713
Young's Modulus	(GPa)	114	377	323	337	331

### 7.3 Composition of Single Nanoscale Multilayer Coatings

Semi-quantitative EDX analysis of the coatings showed that all TiAlCN/VCN coatings were under-stoichiometric. Figure 7.2a shows that the gas to metal ratio increases linearly as the gas flow increases reaching almost stoichiometric level for coating 20% OES.

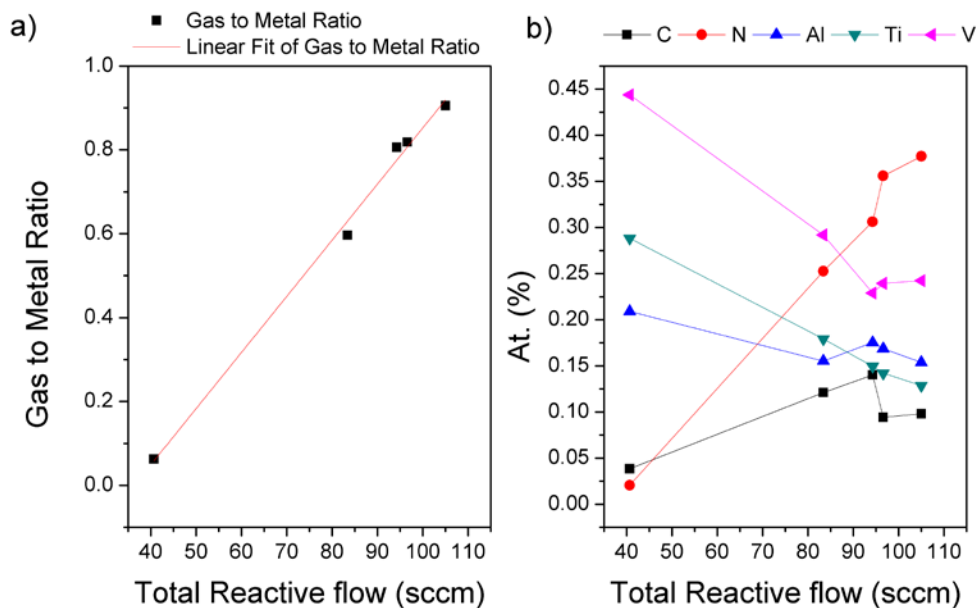


Figure 7.2 Composition of SNMC: a) metal to gas content ratio, b) atomic % of elements.

An increase of nitrogen and carbon contents is observed as the total reactive flow increased (Fig. 7.2b). Up to a flow of 94 sccm both the carbon and nitrogen increased linearly, where for the nitrogen the increase is faster than for the carbon. At flows higher than 95 sccm, the carbon content drops, while the nitrogen increases.

Metal elements generally decrease with increasing reactive gas flow. There is an increase in Al content at the 94 sccm, after where it continues to drop. As the gas flow increases beyond 95 sccm the vanadium content increases. As the characteristic X-ray line energies for the L- series for carbon and vanadium are in the same range, it can be assumed that increasing carbon content is actually detected as increasing vanadium content. This explains the reduction in carbon content with increasing methane flow.

## 7.4 Crystallographic structure of SNMC investigated by XRD analysis and SEM

### Coating 45% OES signal

Both Bragg-Brentano (BB) and glancing angle (GA) XRD analysis (fig. 7.3) show an amorphous structure with a very broad peak near  $40^\circ$ . This peak is a result of overlapping of different phases in Al-C-N clusters observed in the coatings.

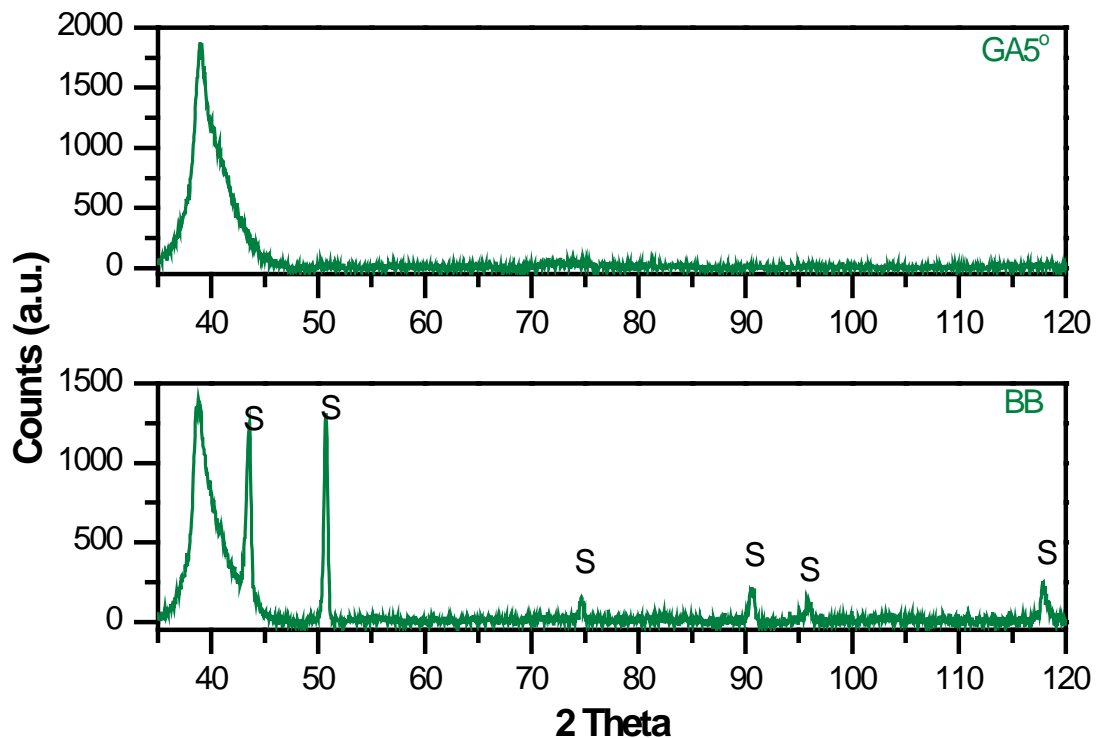
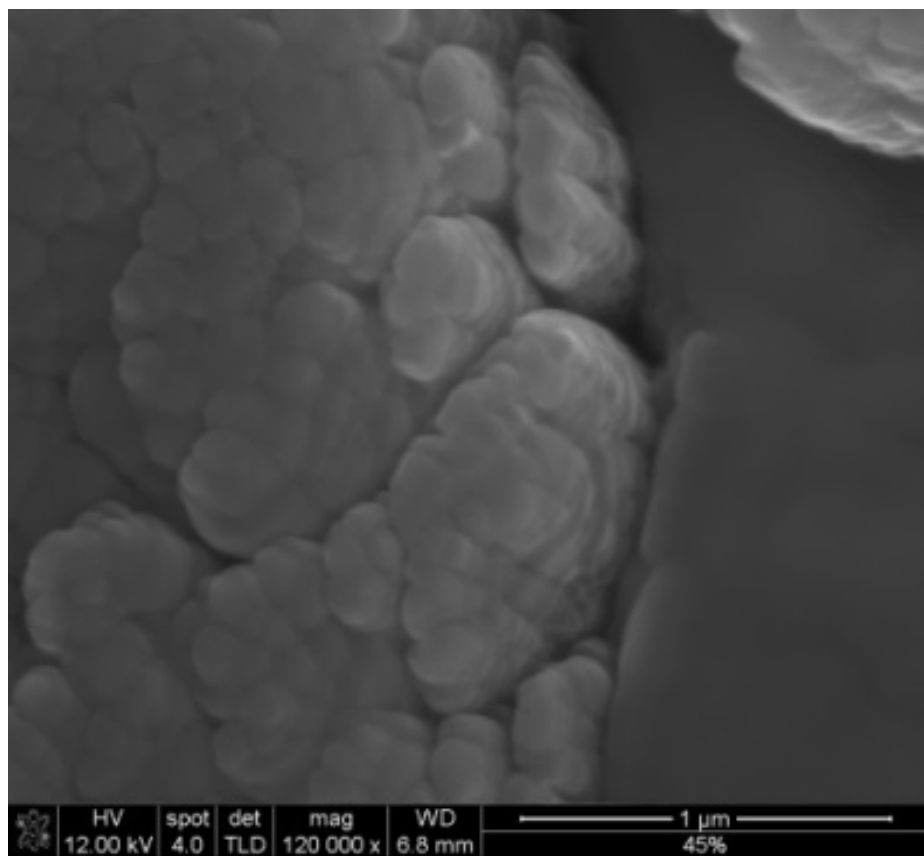


Figure 7.3 The Bragg-Brentano and Glancing Angle XRD patterns of the 45% OES coating

Figure 7.4 shows a high magnification image of the surface morphology. The coating has a complex structure. From the bottom to about  $2\ \mu\text{m}$  the coating is glassy, almost amorphous. From a thickness of  $2\ \mu\text{m}$  the formation of porous clusters can be observed. They are spread over the whole coating. Optical microscopy of the coating deposited on

the HSS disc revealed that these clusters are more densely spaced in the centre of the disc and become sparsely near the edge of the disc. EDX spectroscopy (fig. 7.5) shows that porous clusters mainly consist of aluminium, carbon and nitrogen, where the carbon content is 200% higher and the nitrogen content 60% more than in the glassy area.



*Figure 7.10 SEM image of the surface structure for coating 45% OES. The coating consists of glassy amorphous structure and porous islands with globular structure.*

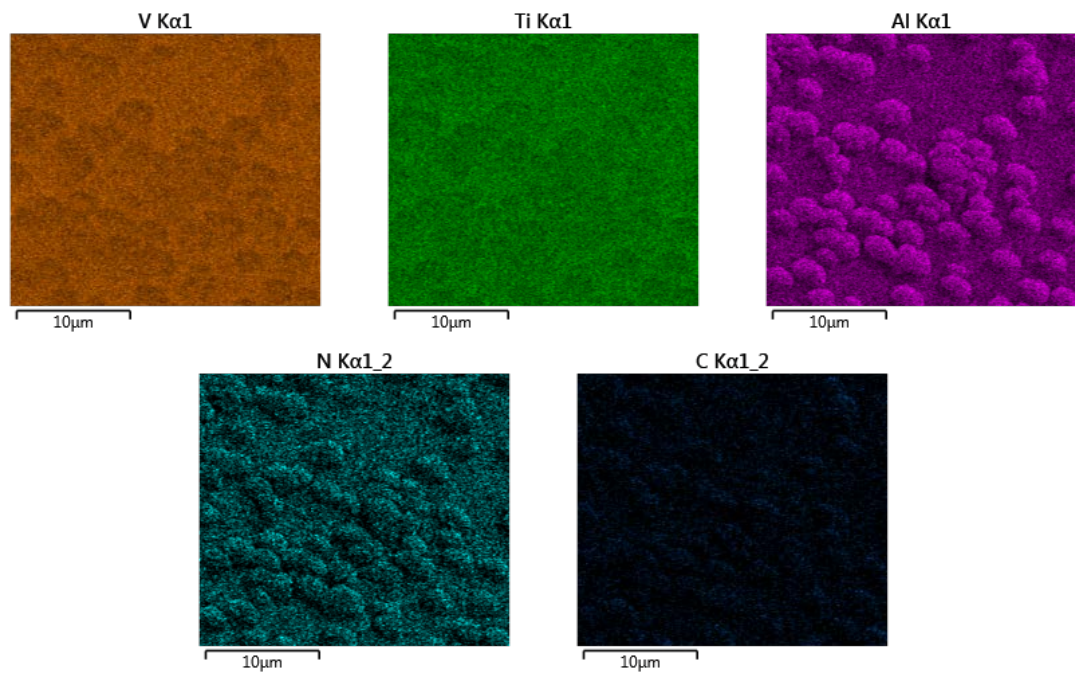


Figure 7.5 The EDX analysis of V, Ti, Al, N and C elements for coating 45% OES. The glassy structure have uniform distribution of all metal elements, whereas porous island consists mainly of Al, C and N.

The cross sectional image (fig 7.6) reveals that these porous clusters have a wedged shape. They start to form from approximately 2.5  $\mu\text{m}$  thickness and grow to 630 nm above the glossy structure. The VN base layer is 160 nm thick can be easily distinguished from coating as it has a columnar structure.

The Raman spectrum of carbon peaks is presented in fig 7.7. The calculated  $I_D/I_G$  ratio is 0.74 and showing mixed carbon phases with a predominating graphitic phase

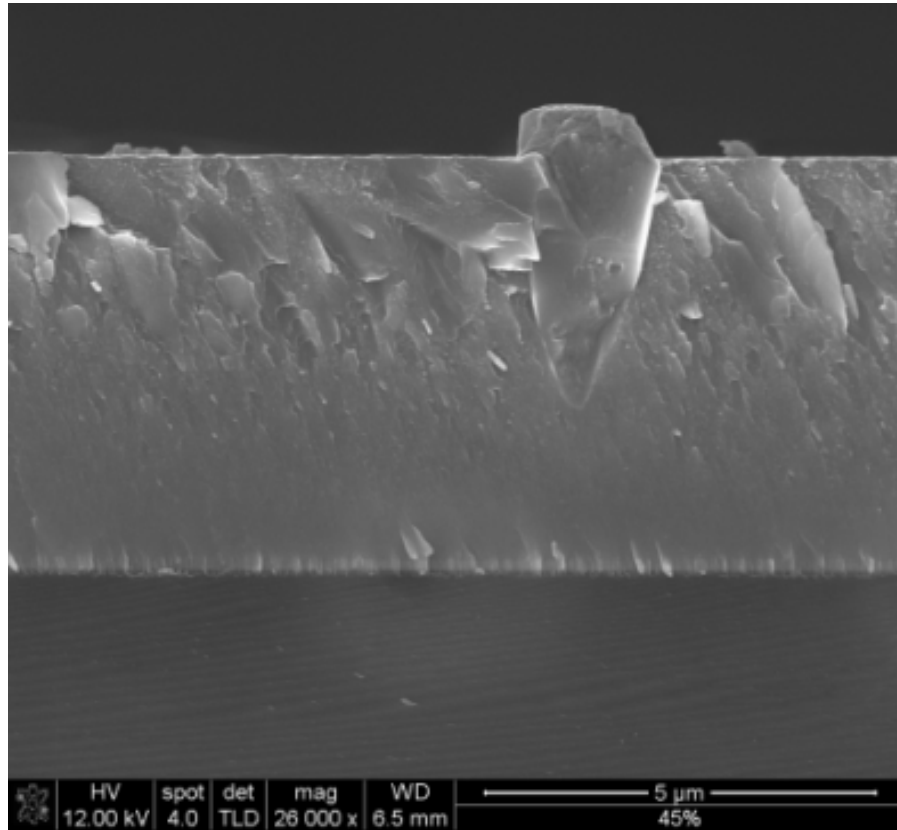


Figure 7.6 SEM cross-section of the 45% OES coating. The glassy structure is up to about 2 μm, then coating become structured and porous structures become to growth over the whole coating.

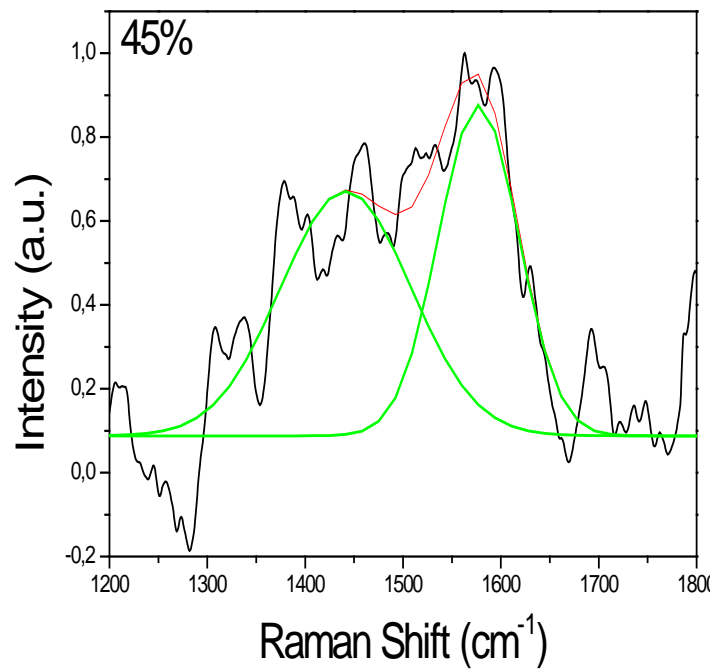


Figure 7.7 RAMAN Spectra of carbon peaks of the coating 45% OES.

### Coating 37% OES signal

The XRD trace of the coating deposited at 37% OES signal shows a mix of (111), (200), (220), (311) and (222) phases (fig. 7.8).

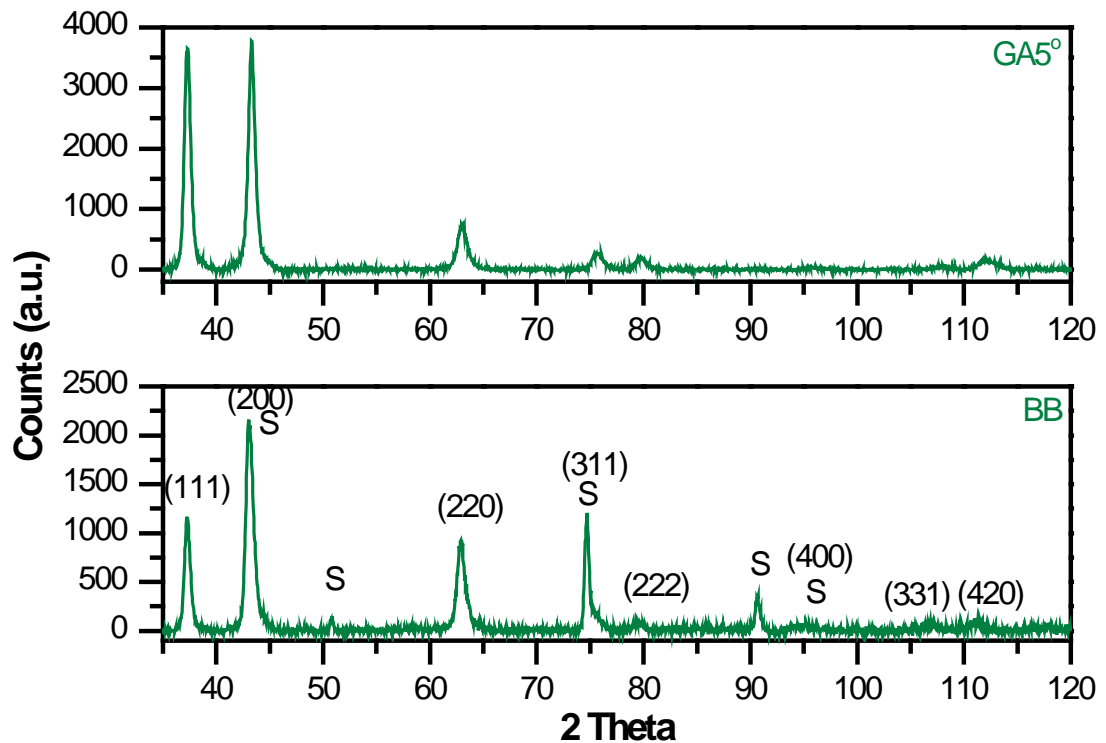


Figure 7.8 The Bragg-Brentano and Glancing Angle XRD patterns of the 37% OES coating

The high magnification SEM image (fig. 7.9) shows that coating 37% OES has a dense globular structure. The cross section (fig 7.10) shows uniform and columnar like structure with a very smooth top surface. As columns grow parallel to each other from the bottom to the top, no competitive growth is observed. The base layer is 160 nm thick and columnar. There is a gradual transformation from the base layer to the coating.

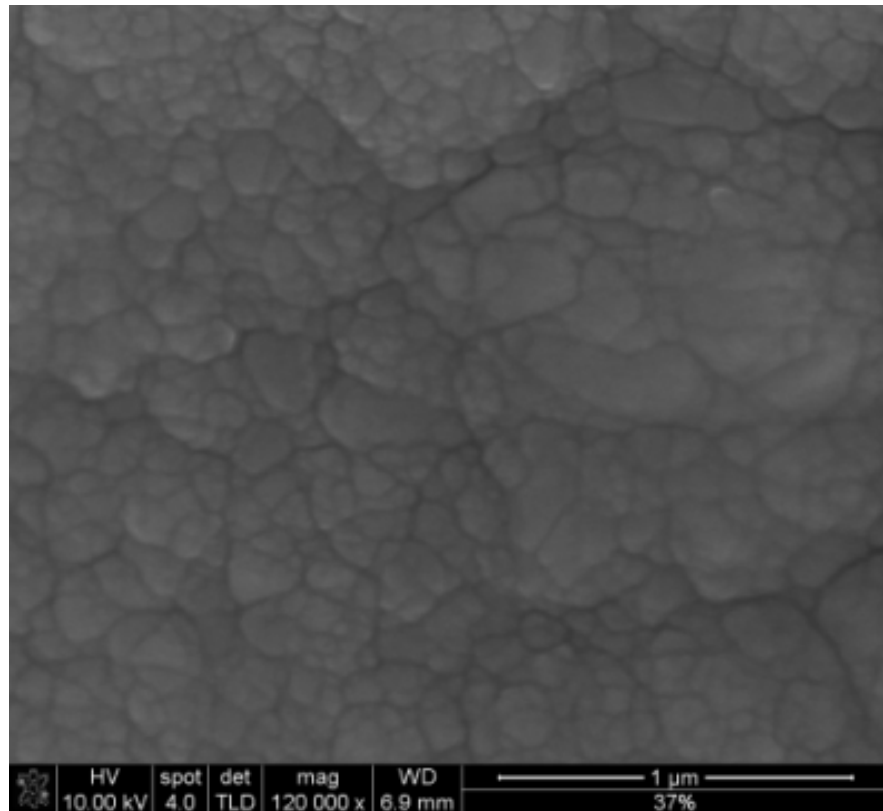


Figure 7.9 SEM image of the surface structure for coating 37% OES

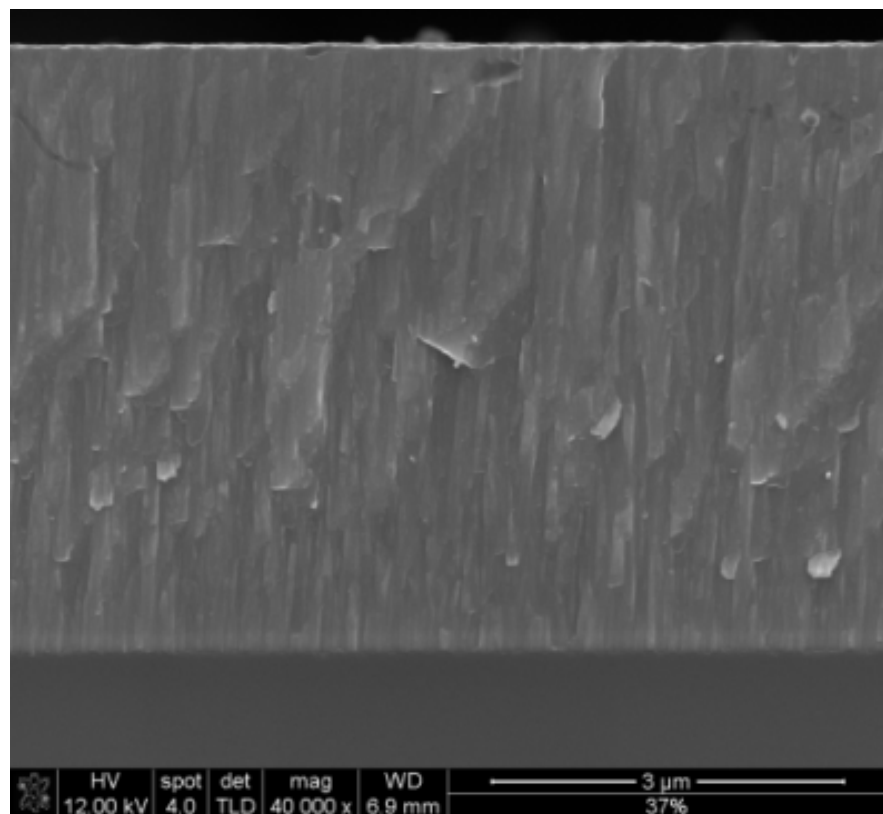


Figure 7.10 SEM cross-section of the 37% OES coating.

The Raman spectrum of carbon peaks is presented in fig 7.11. The calculated  $I_D/I_G$  ratio is 0.48 with no separation between peaks.

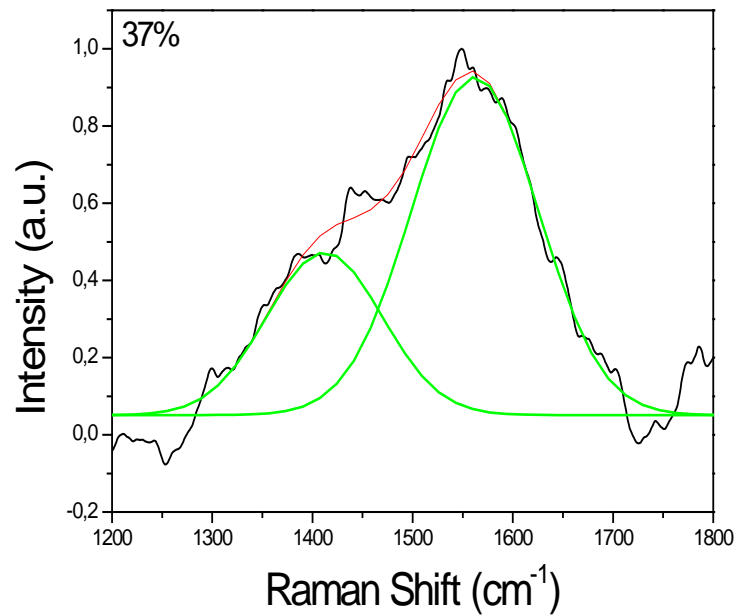


Figure 7.11 RAMAN Spectra of carbon peaks of the coating 37% OES

### Coating 30% OES signal

The SNMC deposited at 30% OES signal has shown a single-phase B1-NaCl structure, with weak (111) texture, strong (111) and (200) reflections as well as weak (220), (311) and (222) reflections (fig. 7.12).

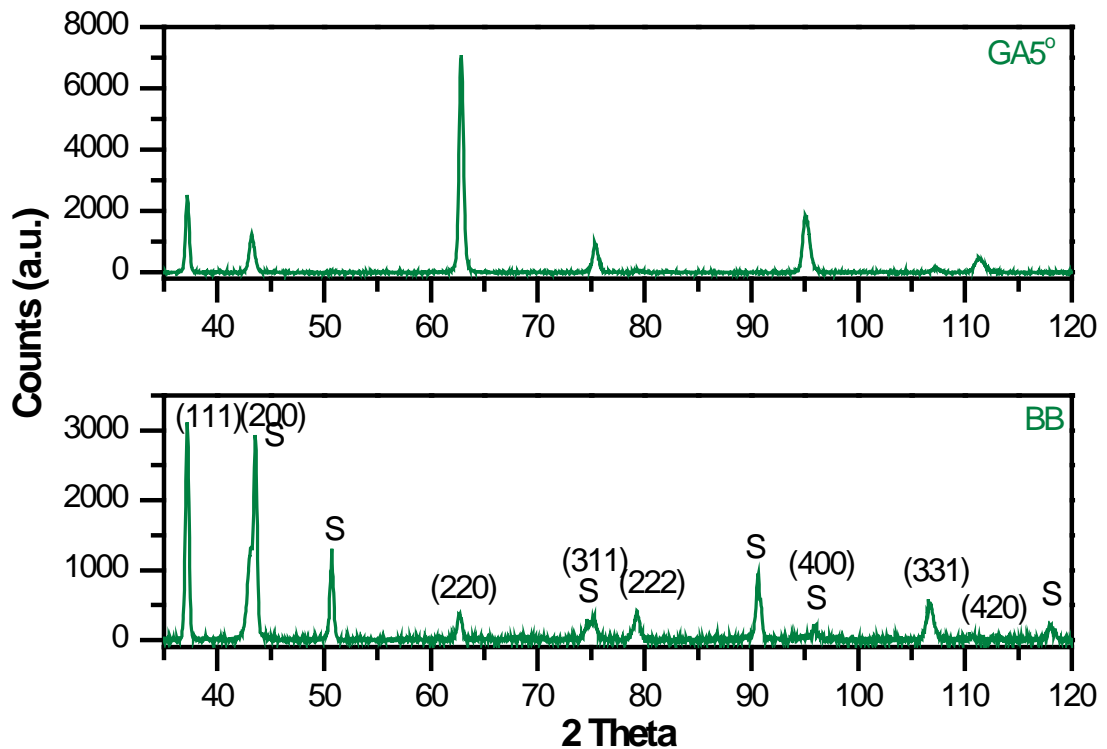


Figure 7.11 The Bragg-Brentano and Glancing Angle XRD patterns of the 45% OES coating

Figure 7.13 shows the architecture evolution of the coating. The base layer is 310 nm thick with a sharp interference with the multilayered coating. Columns are smaller at the bottom of the coating and become broader with increasing thickness reaching diameter of ~160 -300 nm. This indicates competitive growth. Columns are large, well defined, terminated with sharp triangular tops, resulting in a faceted topology (fig. 7.14).

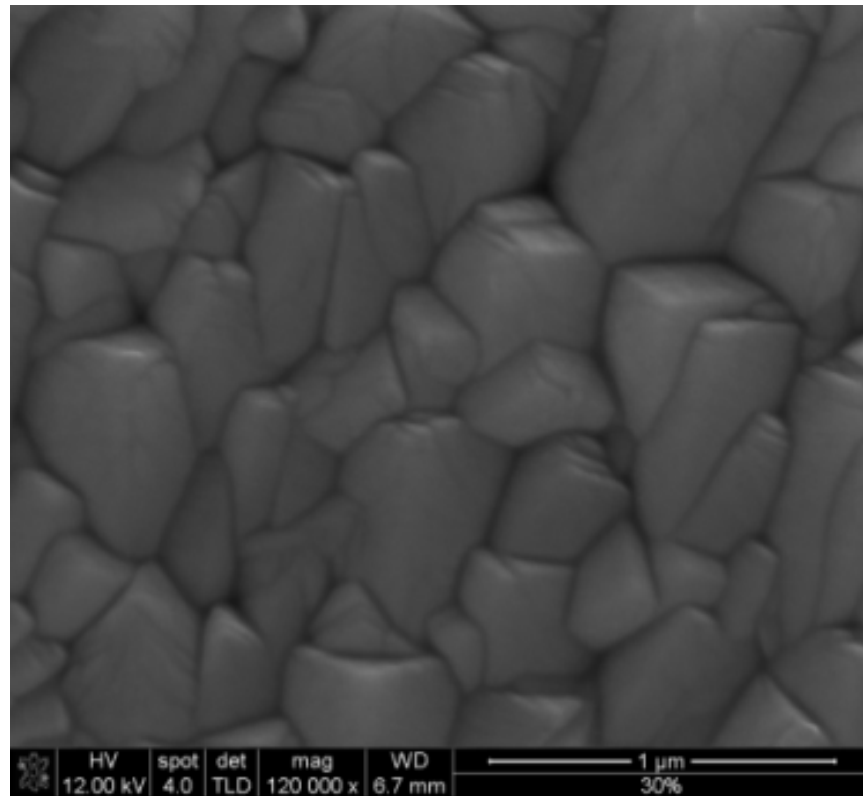


Figure 7.13 SEM image of the surface structure for coating 30% OES

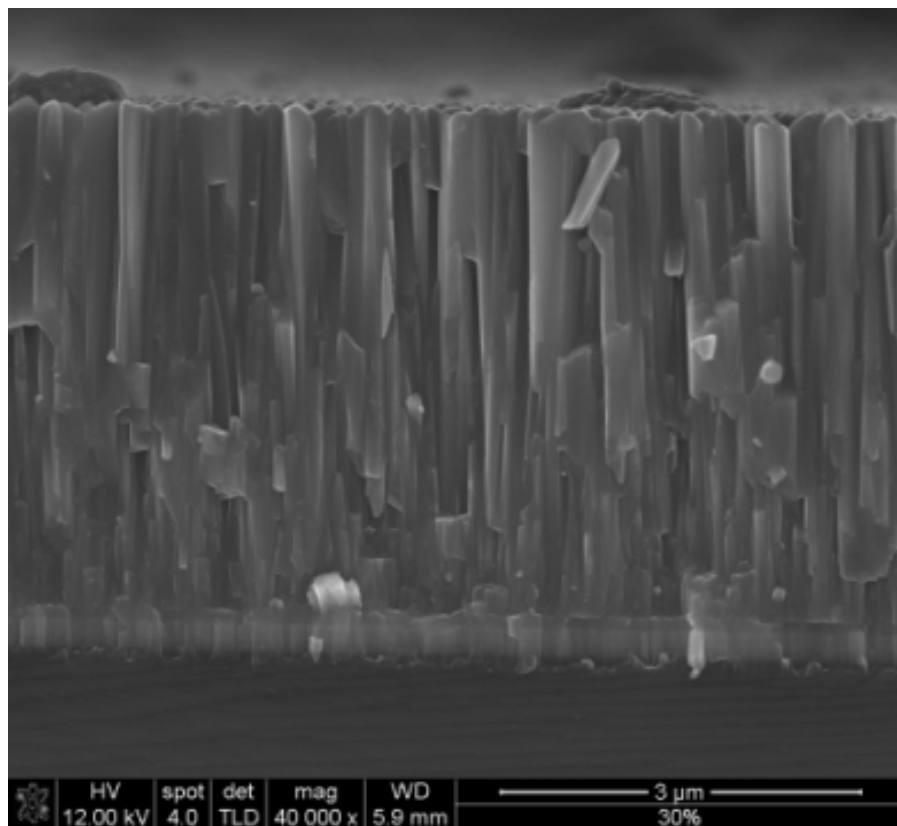


Figure 7.12 SEM cross-section of the 30% OES coating

The Raman spectrum of carbon peaks is presented in fig 7.15. The calculated  $I_D/I_G$  ratio is 0.9 with well-defined peaks.

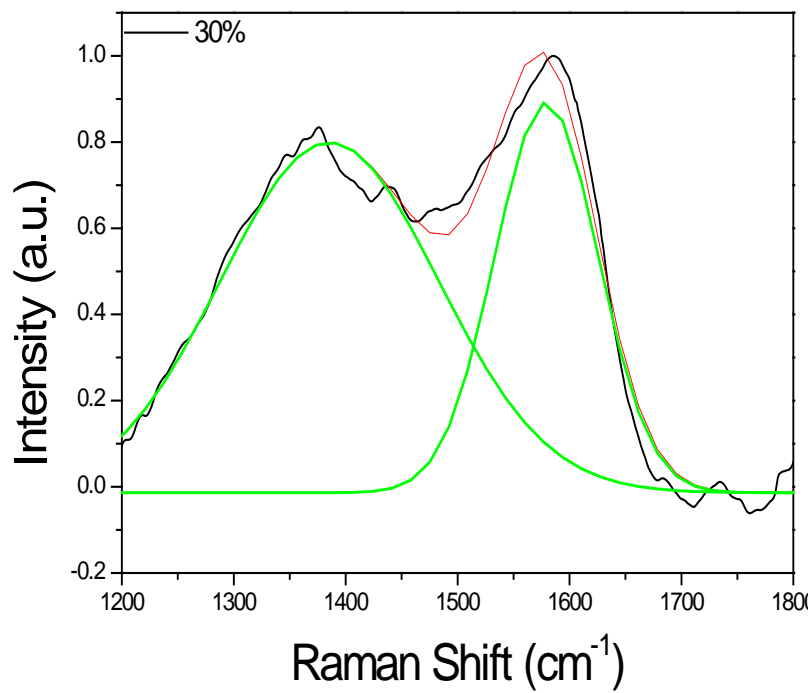


Figure 7.13 RAMAN Spectra of carbon peaks of the coating 30% OES

### Coating 25% OES signal

The coating deposited at 25% OES signal has shown a single-phase B1-NaCl structure, with preferred (220) texture (fig 7.16). Peaks are low intensity and broad.

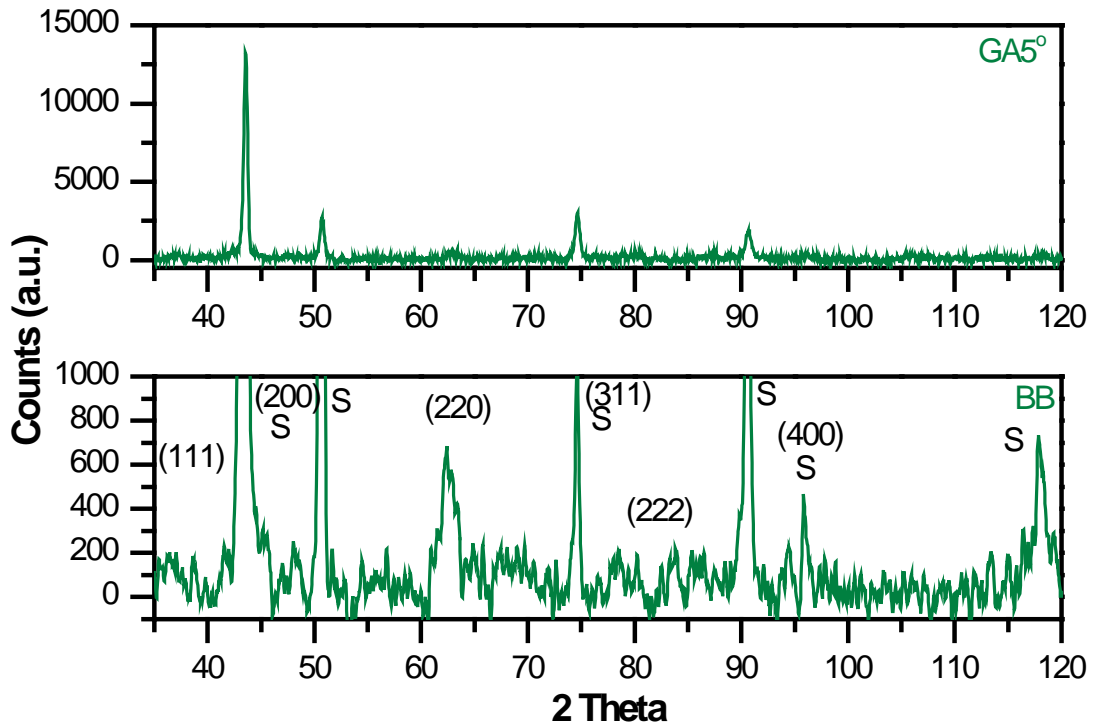


Figure 7.16 The Bragg-Brentano and Glancing Angle XRD patterns of the 25% OES coating

Figure 7.18 shows that the coating has dense, columnar structure with columns of 170-250 nm broad width, terminated with rounded tops, resulting in a cauliflower-like topology (fig. 7.17). The base layer is 250 nm thick with a smooth transition to the coating. No competitive grow is observed, however the column size appears to be smaller in the early stages of film growth. This may be influenced by the base layer structure.

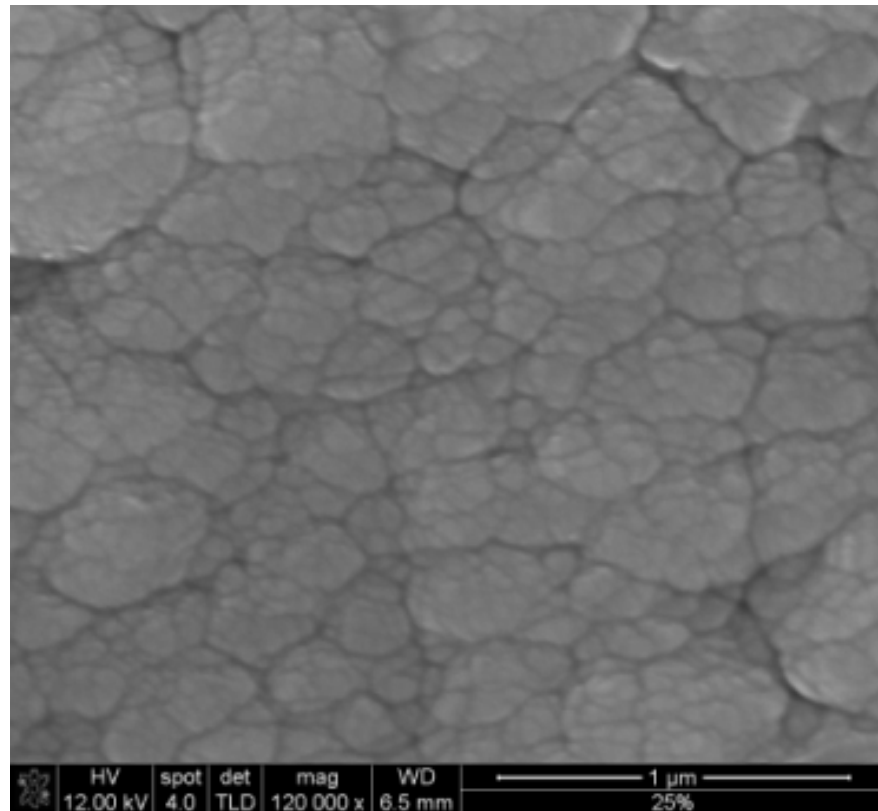


Figure 7.14 SEM image of the surface structure for coating 25% OES

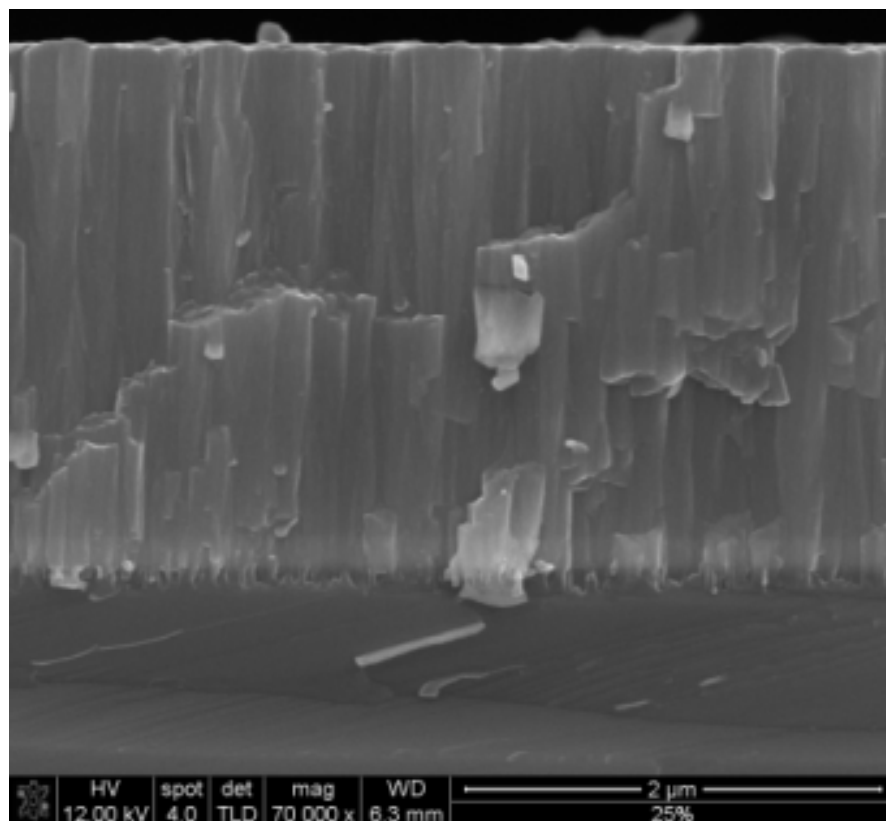


Figure 7.15: SEM cross-section of the 25% OES coating.

The Raman spectrum of carbon peaks is presented in fig. 7.19. The calculated ID/IG ratio is 0.86 with a clear separation of the peaks.

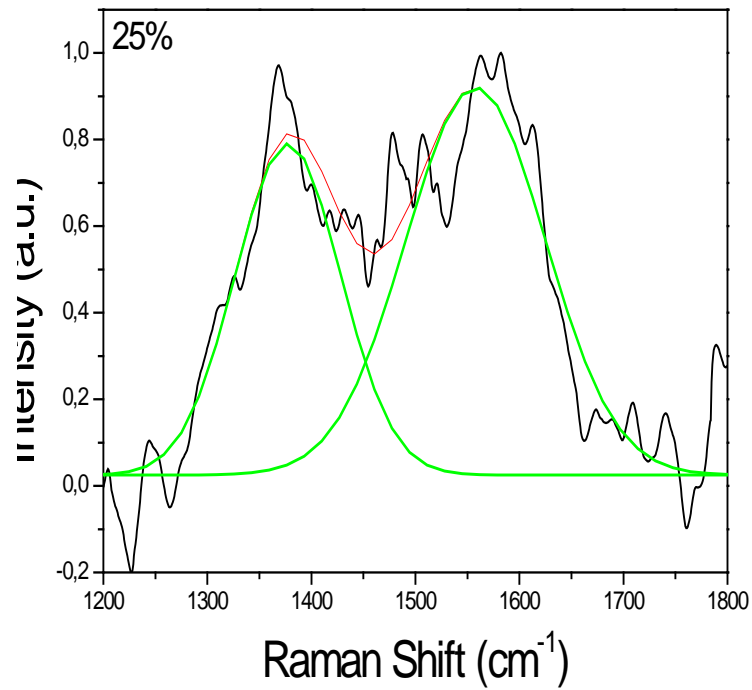


Figure 7.16 RAMAN Spectra of carbon peaks of the coating 25% OES

## Coating 20% OES signal

Similarly to the coating deposited at 25% OES, the 20% OES coating has a (220) preferred orientation of fcc structure, with broad and of low intensity peaks (fig.7.20).

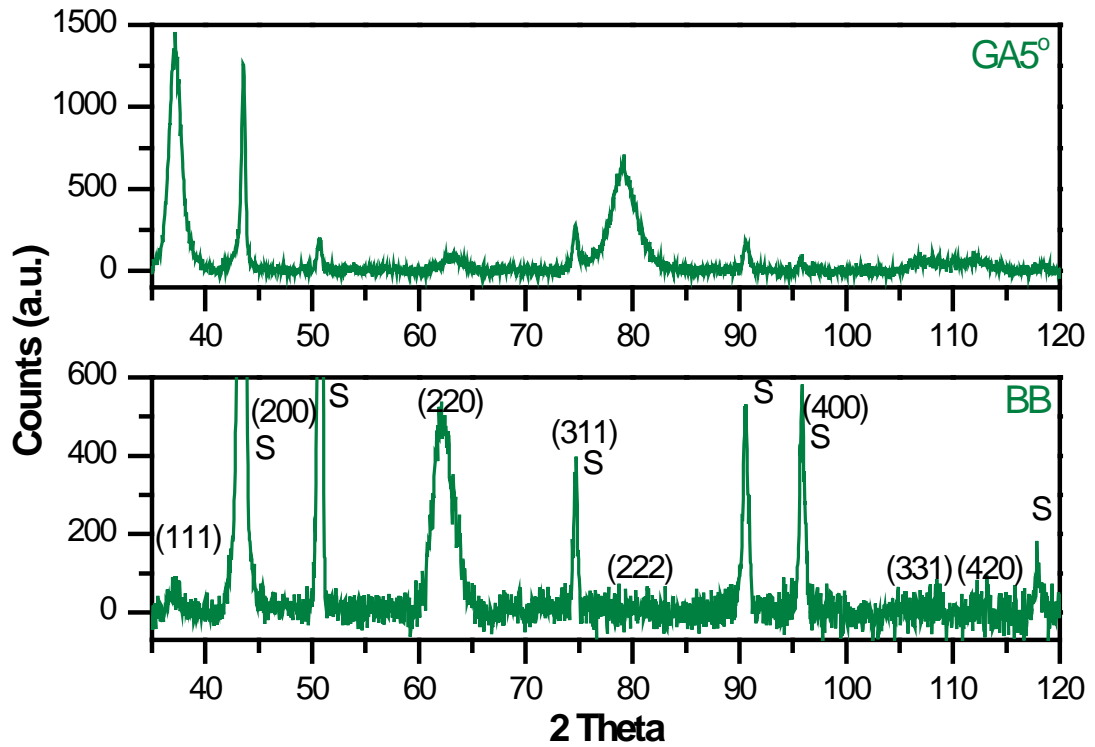


Figure 7.17 The Bragg-Brentano and Glancing Angle XRD patterns of the 20% OES coating

The coating consists of (~100-200 nm) columns terminated with rounded tops (fig. 7.22), resulting in a cauliflower-like topology (fig. 7.22). The base layer is 150 nm thick with a smooth transition to the coating. No competitive grow is observed.

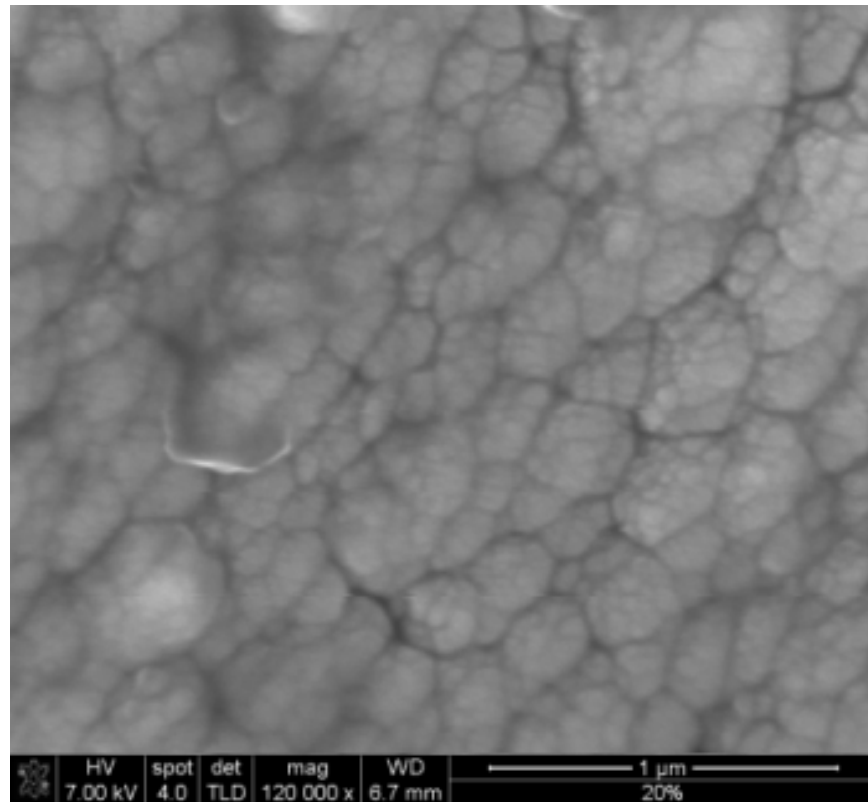


Figure 7.18 SEM image of the surface structure for coating 20% OES

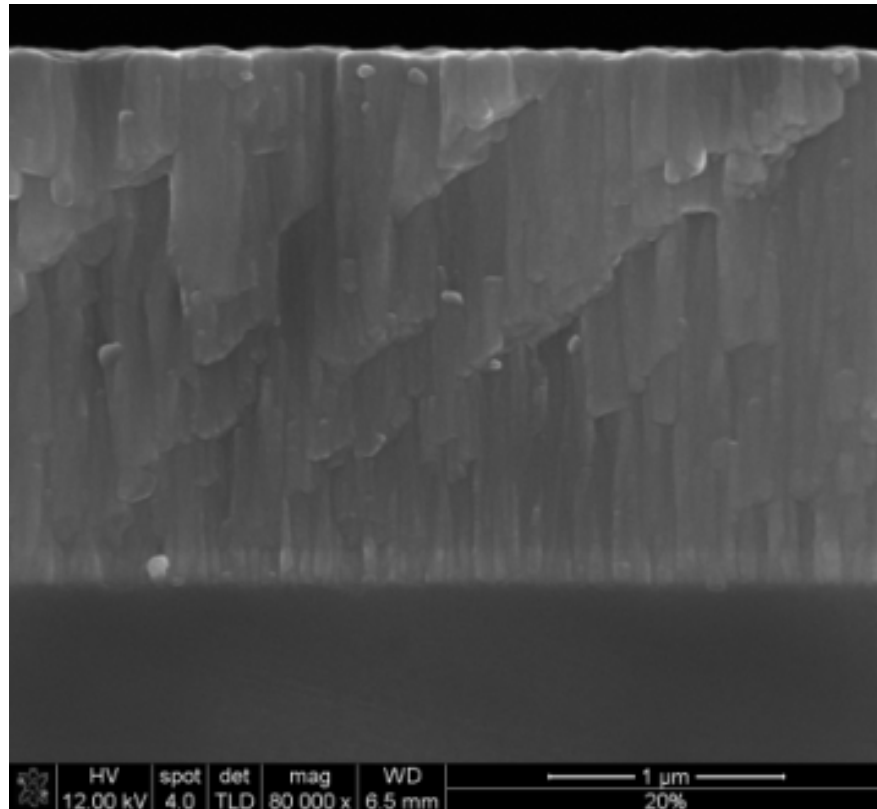
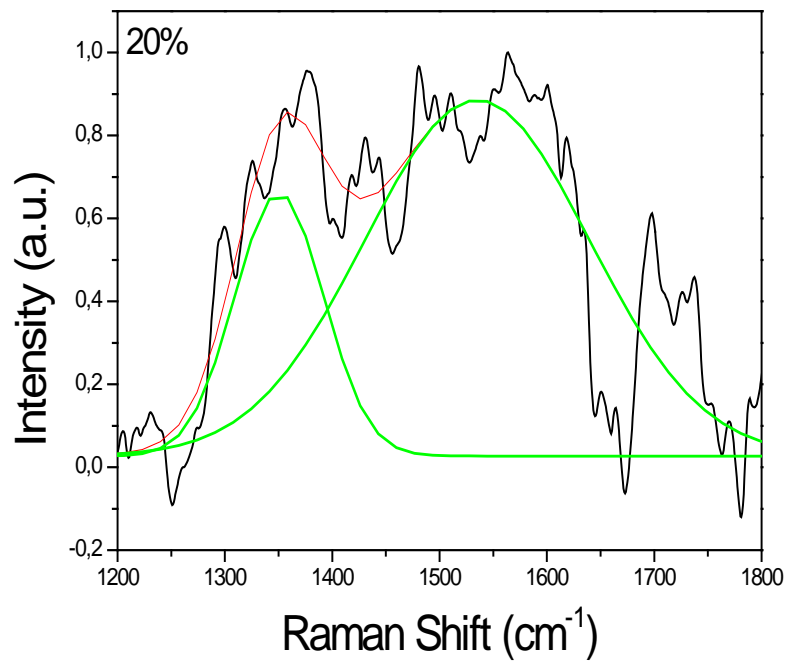


Figure 7.22 SEM cross-section of the 25% OES coating

The Raman spectrum of carbon peaks is presented in fig 7.23. The calculated  $I_D/I_G$  ratio is 0.74 with a subtle separation of the peaks.



7.23 RAMAN Spectra of carbon peaks of the coating 20% OES

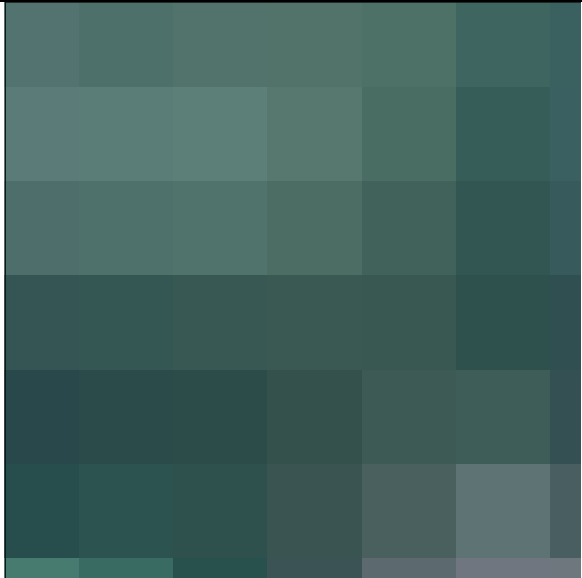
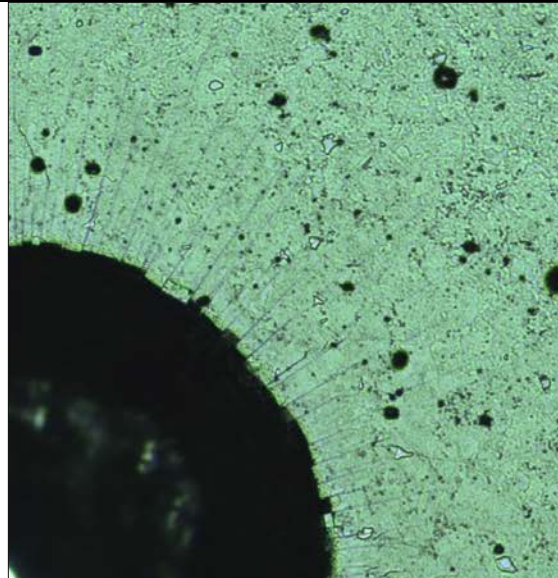
## 7.5 Adhesion

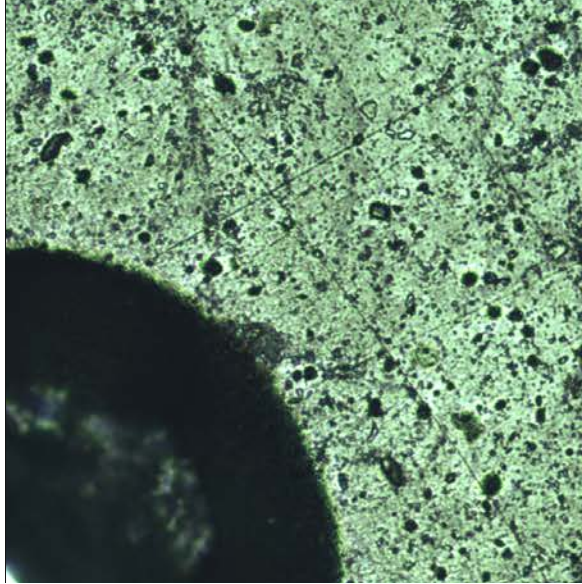
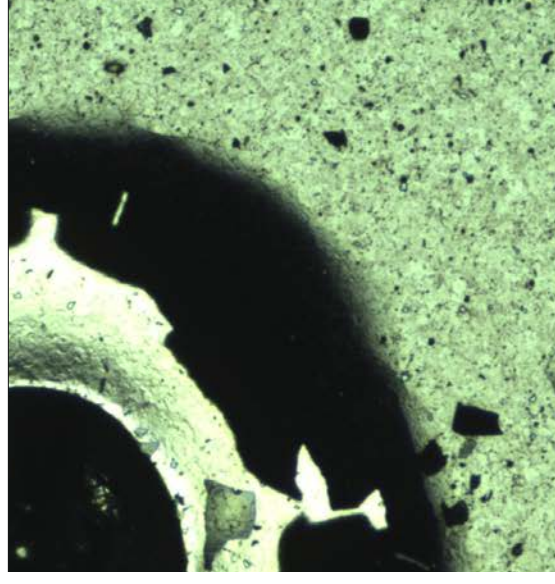
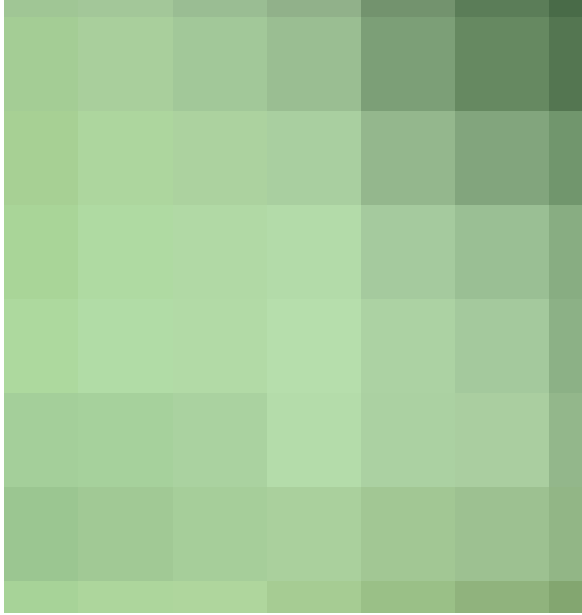
### Rockwell C test

The Rockwell indentation test shows a decline in adhesion as the coatings become more ceramic. Table 7.4 exhibits optical microscope images of all samples.

The coating 45% OES can be classified as grade O. There is no delaminating nor cracking. Coatings 37% OES and 30% OES have micro-cracks without delamination of the coating. The coating at 25% OES has fallen below grade 3. The coating is completely delaminated in the crater vicinity and the substrate was clearly exposed. The ratio of the adhesive delamination to the radius of the indent is 1.67. The coating 20% OES shows microcracks and micro-delamination, thus it is classified as grade 2. Coatings 45% OES, 37% OES and 30% OES are within acceptable standards of grading, whereas both coatings deposited at 25% OES and 20% OES show insufficient adhesion.

Table 7.4: Rockwell indentation marks of SNMC

45% OES	37% OES
	

30% OES	25% OES
	
20% OES	
	

### Scratch Test

Table 7.5 shows maximum load during the scratch test before coating fails.

Table 7.5 Results of the scratch test on HSS and plain inserts

Coating ID	Maximum load $L_c$ (N)				
	45% OES	37% OES	30% OES	25% OES	20% OES
Inserts	3 N	48 N	40 N	80 N	>100 N
HSS	11 N	35 N	45 N	20 N	20 N

Despite good result in the Rockwell indentation test, the coating 45% OES shows the lowest adhesion. It failed at a critical load between 3-11 N. Such inconsistency of these two tests is result of a very low hardness, causing "smearing off" of coating by the scrubbing tip of the scratch test. Coatings 37% OES and 30% OES have similar critical load limit range of 35-48 N. Both coatings 25% OES and 20% OES have a very low adhesion to the HSS substrate with a load limit of 20 N. The adhesion to the insert is extremely high, 80 N and over 100 N for coatings 25% OES and 20% OES respectively. Analysis by EDX revealed that for low metal content coatings the adhesion failure on HSS substrates occurred between the VN base layer and the TIAICN/VCN coating.

## 7.6 Wear Resistance – Pin on Disk

Room temperature wear behaviour of the coatings is shown in fig. 7.24.

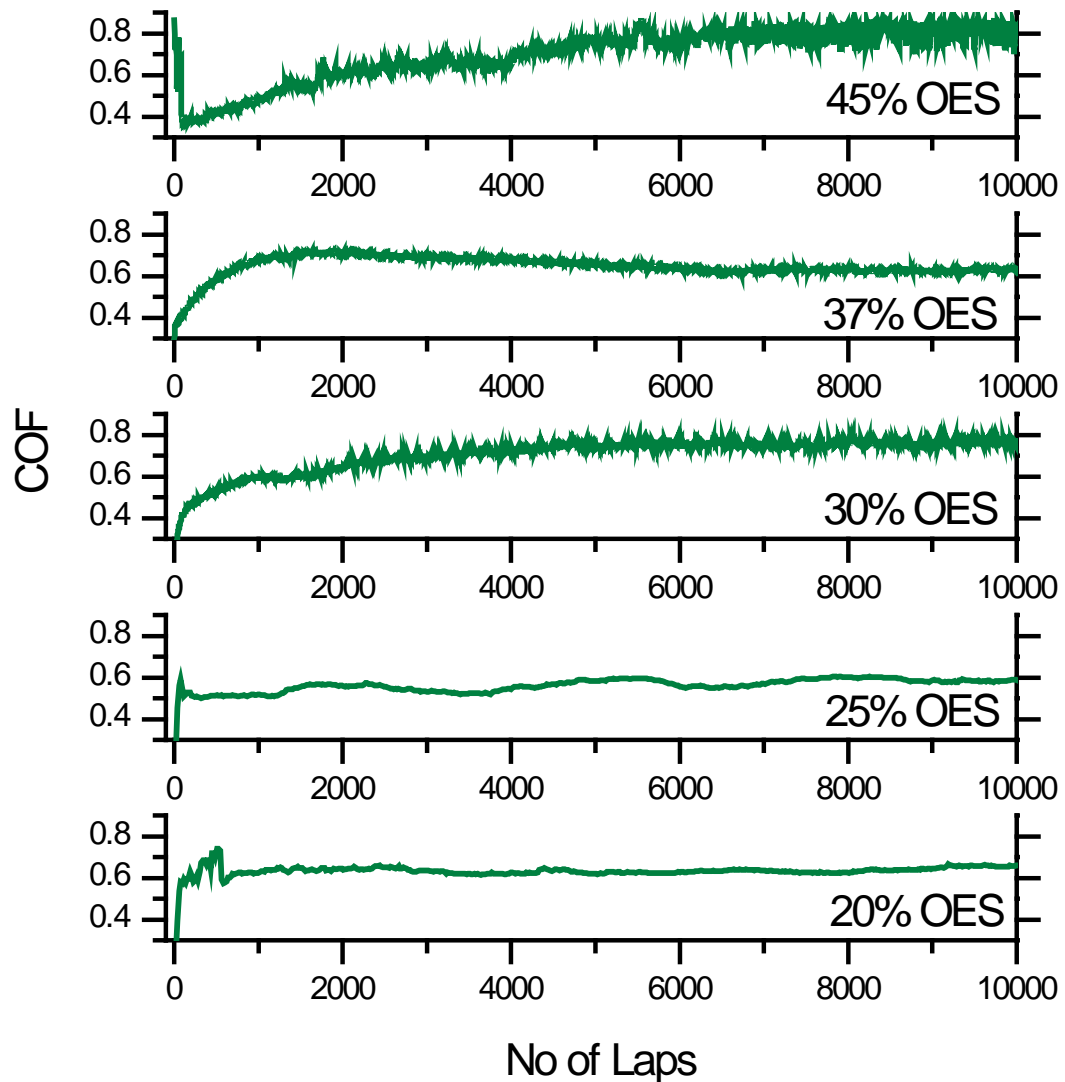


Figure 7.24 Coefficient of friction as a function of number of laps for room temperature of SNMC

The coating 45% OES has a very high peak in the run-in period which is due to Al-C-N islands along the coating. Once they are worn flat the COF rapidly drops, and then increases again. After 6000 laps the COF settled at 0.81 and oscillations with increasing

amplitude appear. It is highly possible that at this point the coating is removed and the substrate is revealed.

The profile of the coating 37% OES increases during the run-in time to 0.70 at 800 laps and then drops to 0.65 at 7000 laps. The COF stays at the same level of 0.65 for the remainder of the test duration. The profile is very smooth and stable.

For the coating 30% OES, the COF increases in two steps: first up to 0.60 at 1000 laps then the COF slightly decreases and increases again up to 0.65 at 4000 laps and remains constant until the end of the test. The amplitude of the oscillations remains constant leading to reduced friction value.

Coatings 25% and 20% OES have a peak at the beginning of test, which is caused by coating spallation. The coating 25% OES delaminated in some few tens of laps and the coating 20% OES failed after 530 laps, which can be seen as a sudden drop in COF. The SEM images (fig. 7.31 and 7.33) together with elemental mapping analysis (fig. 7.32 and 7.34) show that both coatings peeled off and ball was sliding against the base layer. This results in a low COF of 0.56 and 0.63 for the coatings 25% OES and 20% OES respectively.

The wear tracks generated after the pin-on-disk test were investigated using SEM microscopy and EDX mapping. Results are presented in the following paragraphs.

## Coating 45% OES

The SEM of and EDX mapping of the wear track are presented in fig. 7.25 and 7.26 respectively.

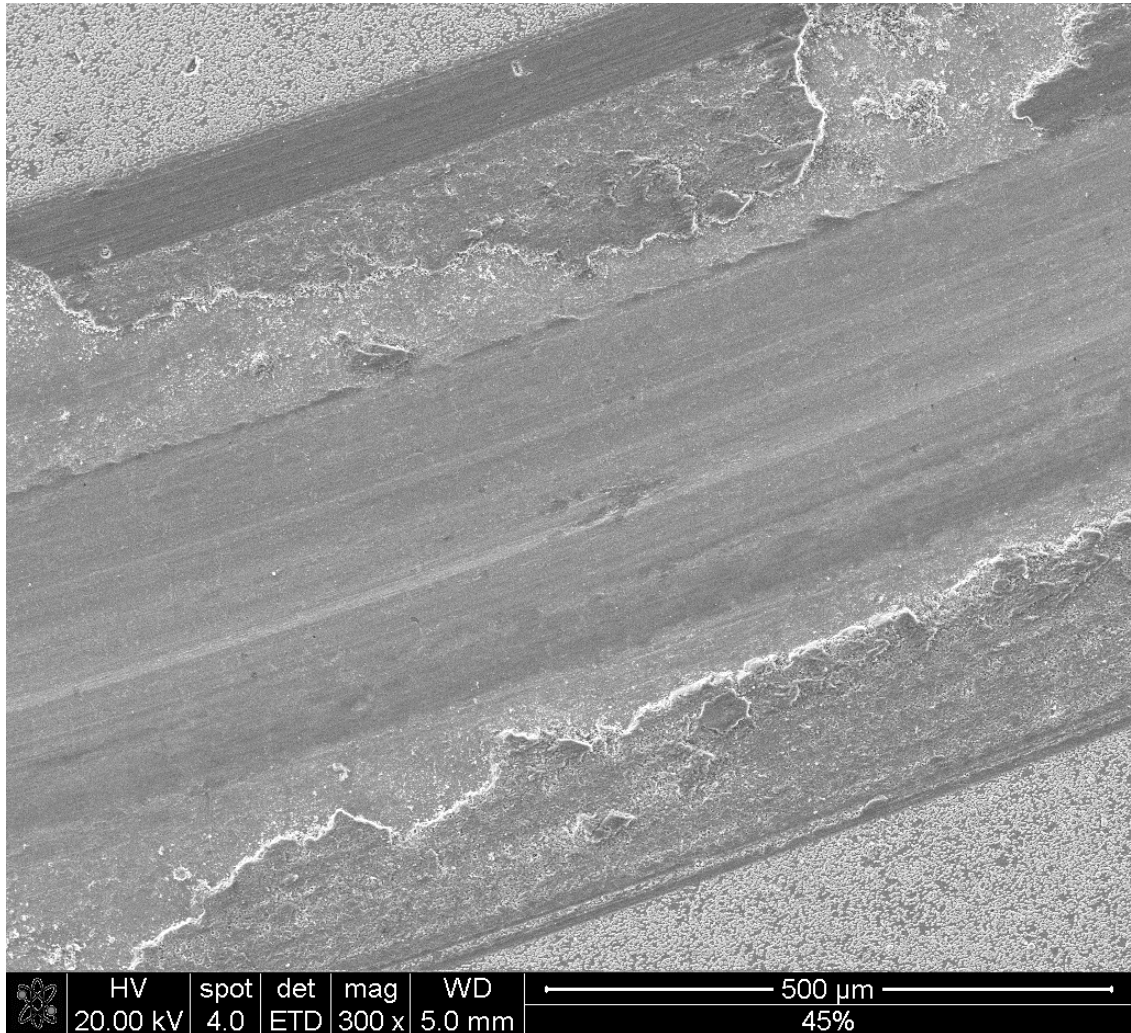


Figure 7.25 SEM image of the wear track created by room temperature pin on disk testing.

The wear track is very wide and deep. The coating was totally removed and the ball was sliding against the substrate, which results in a very high COF. Coating failures can be observed both between the coating and base layer, as well as between base layer and substrate. Oxides can be observed at the substrate and in the coating region, suggesting that some oxides have been created.

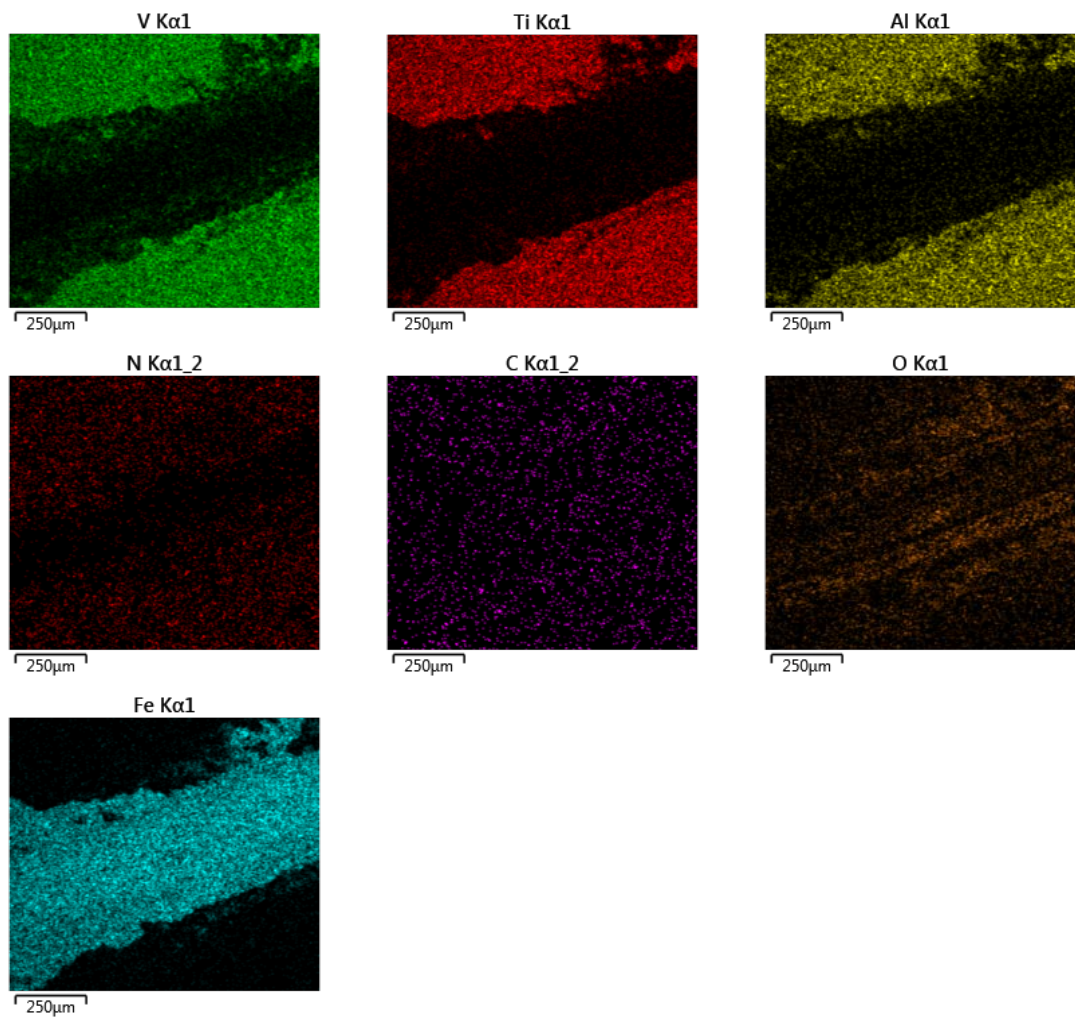
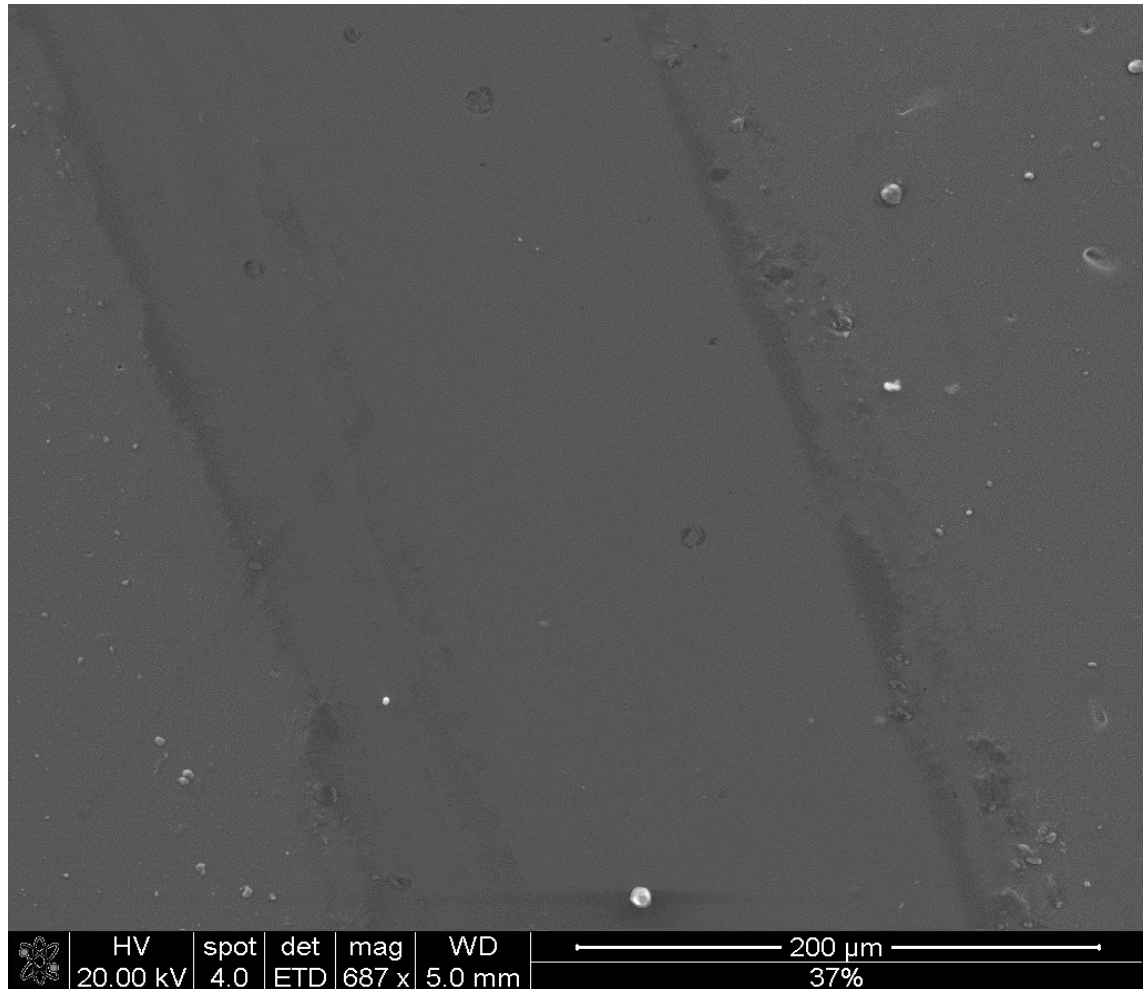


Figure 7.26 The EDX analysis of V, Ti, Al, N, C, Fe, and O elements within the wear track created by room temperature pin on disk testing

## Coating 37% OES

The SEM of and EDX mapping of the wear track are presented in fig. 7.27 and 7.28 respectively.



*Figure 7.27 SEM image of the wear track created by room temperature pin on disk testing*

Coating 37% OES clearly shows an excellent wear resistant behaviour. The wear track is smooth and shallow. The oxide debris is created at the edge of the wear track. The low wear rate can be attributed to the dense microstructure, strong interfacial adhesion and high hardness.

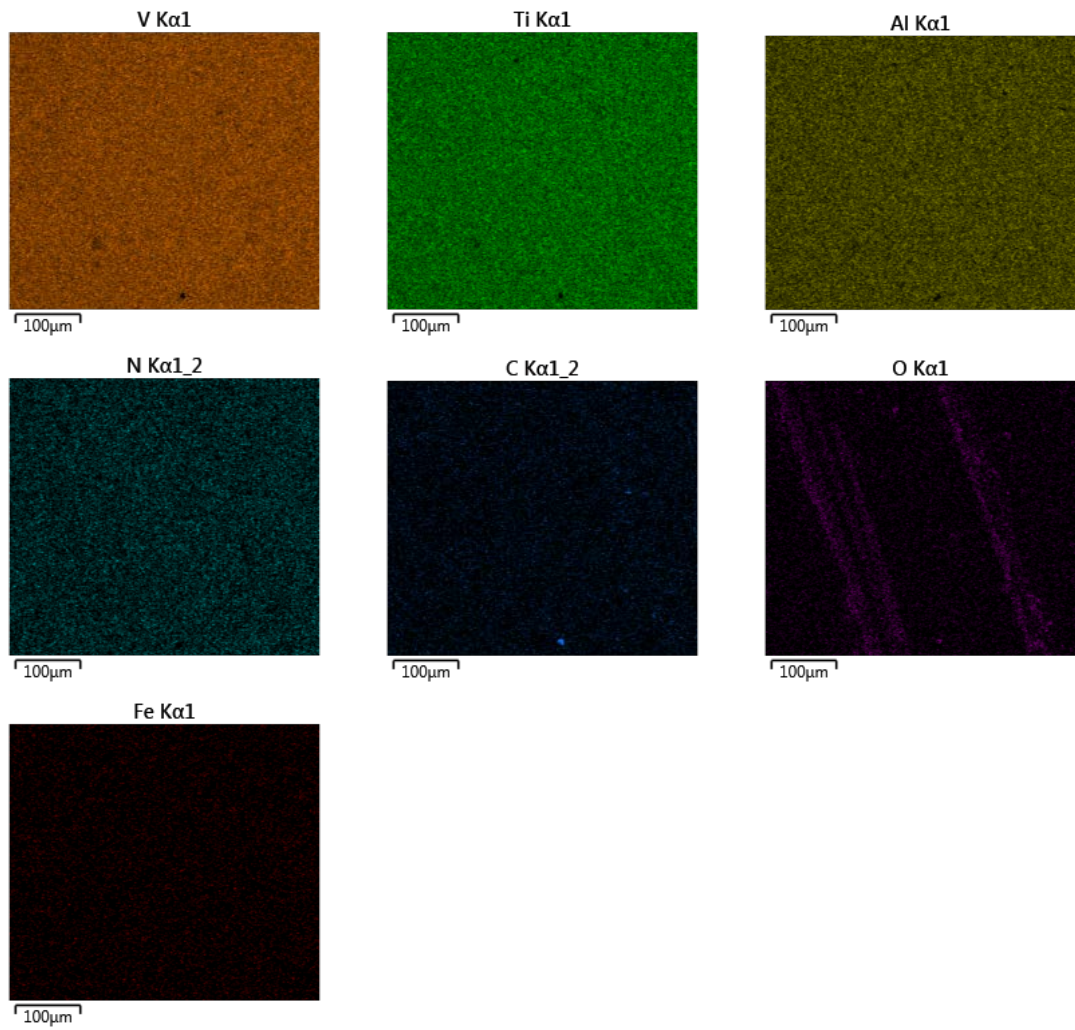


Figure 7.28 The EDX analysis of V, Ti, Al, N, C, Fe, and O elements within the wear track created by room temperature pin on disk testing

## Coating 30% OES

The SEM of and EDX mapping of the wear track are presented in fig. 7.29 and 7.30 respectively.

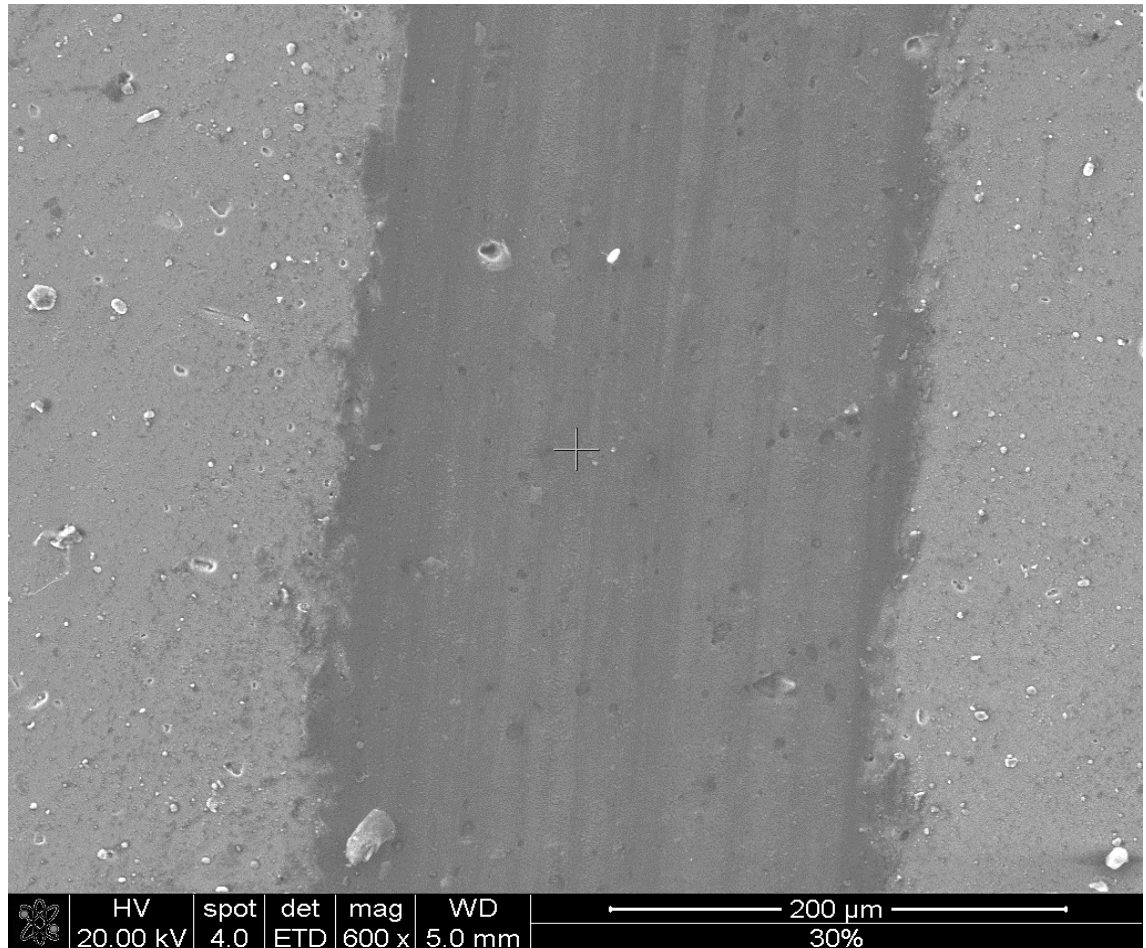


Figure 7.29 SEM image of the wear track created by room temperature pin on disk testing

The wear track is very smooth and narrow. The depth measurement shows that the wear track is  $0.3 \mu\text{m}$  deeper than in the case of the coating deposited at 37% OES signal.

However, there is a wide and high oxide layer produced within the wear track, which is higher than surface level. The oxide layer of approximately 40-50% oxygen content is evenly distributed along the wear track. This indicates an efficient performance of the coating as a solid lubricant.

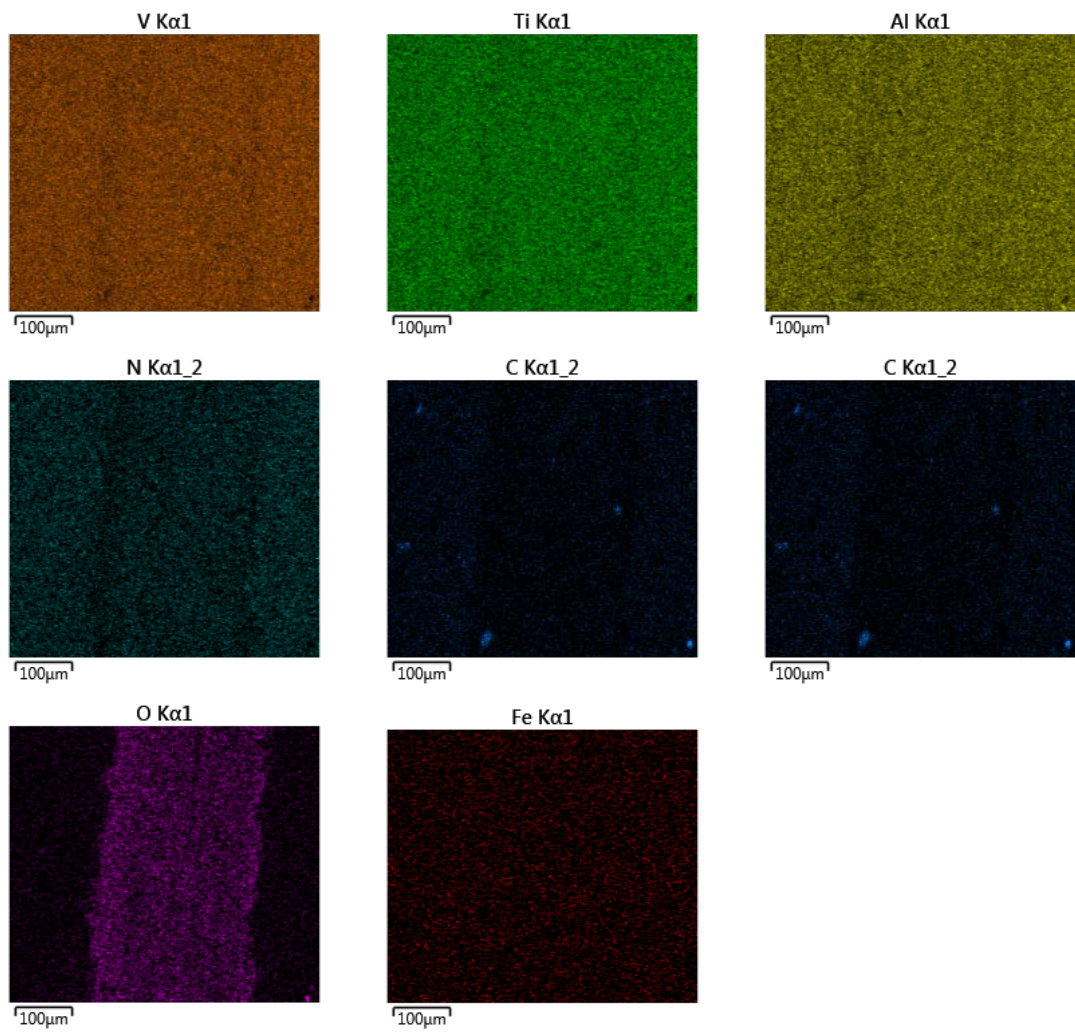


Figure 7.30 The EDX analysis of V, Ti, Al, N, C, Fe, and O elements within the wear track created by room temperature pin on disk testing

## Coating 25% OES

The SEM of and EDX mapping of the wear track are presented in fig. 7.31 and 7.32 respectively.

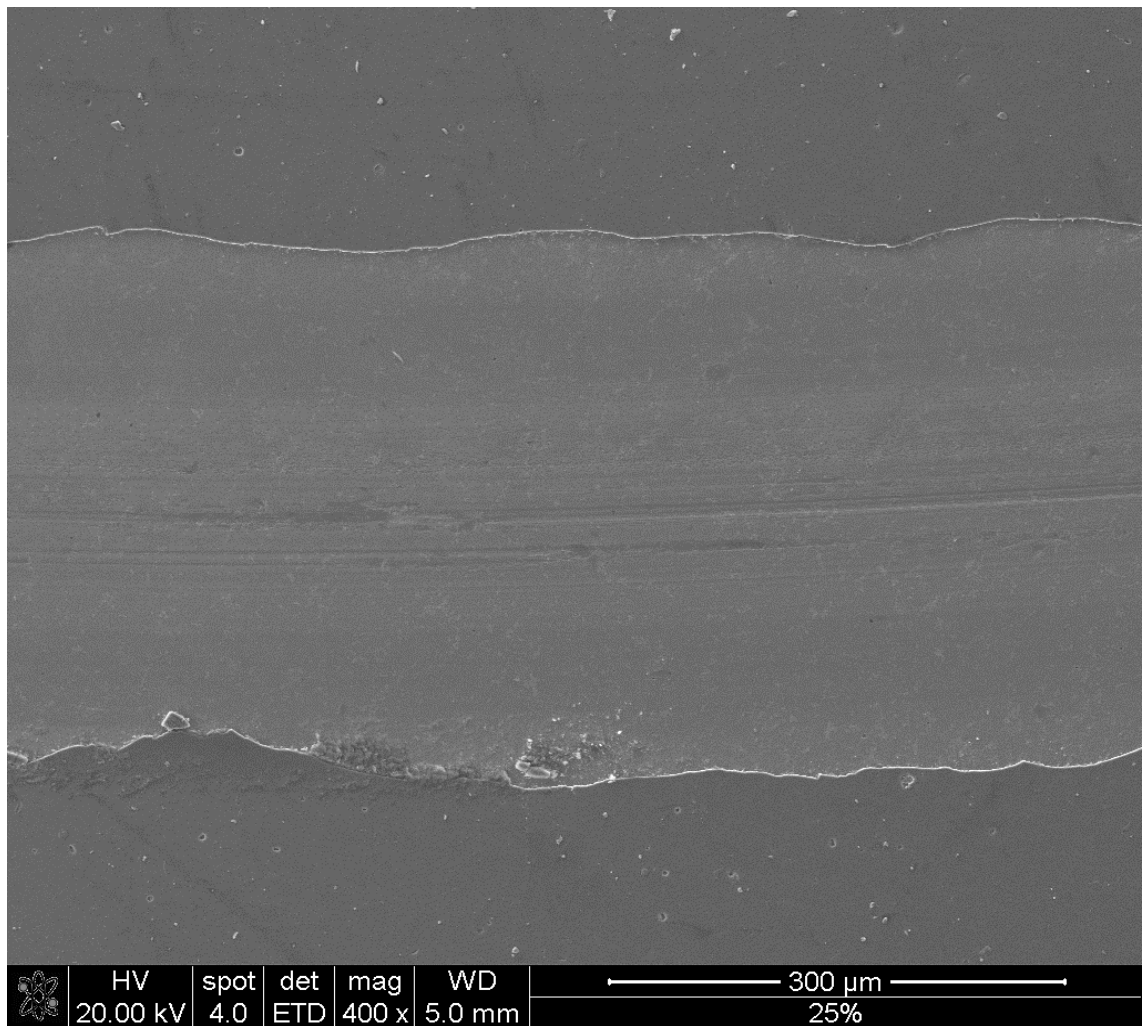


Figure 7.31 SEM image of the wear track created by room temperature pin on disk testing

Comparing to the coating 30% OES the coating 25% OES has a wider wear track. The coating is obviously worn away as the substrate has been exposed. The VN base layer can be seen at the edges of wear track (fig. 7.32 - V and N element), which suggests that coating 25% OES failed at the coating - base layer level. The  $\text{Al}_2\text{O}_3$  ball was sliding

against the very thin base layer. Oxygen can be observed all along the wear track and wide oxide debris is observed at one of the base layer edges.

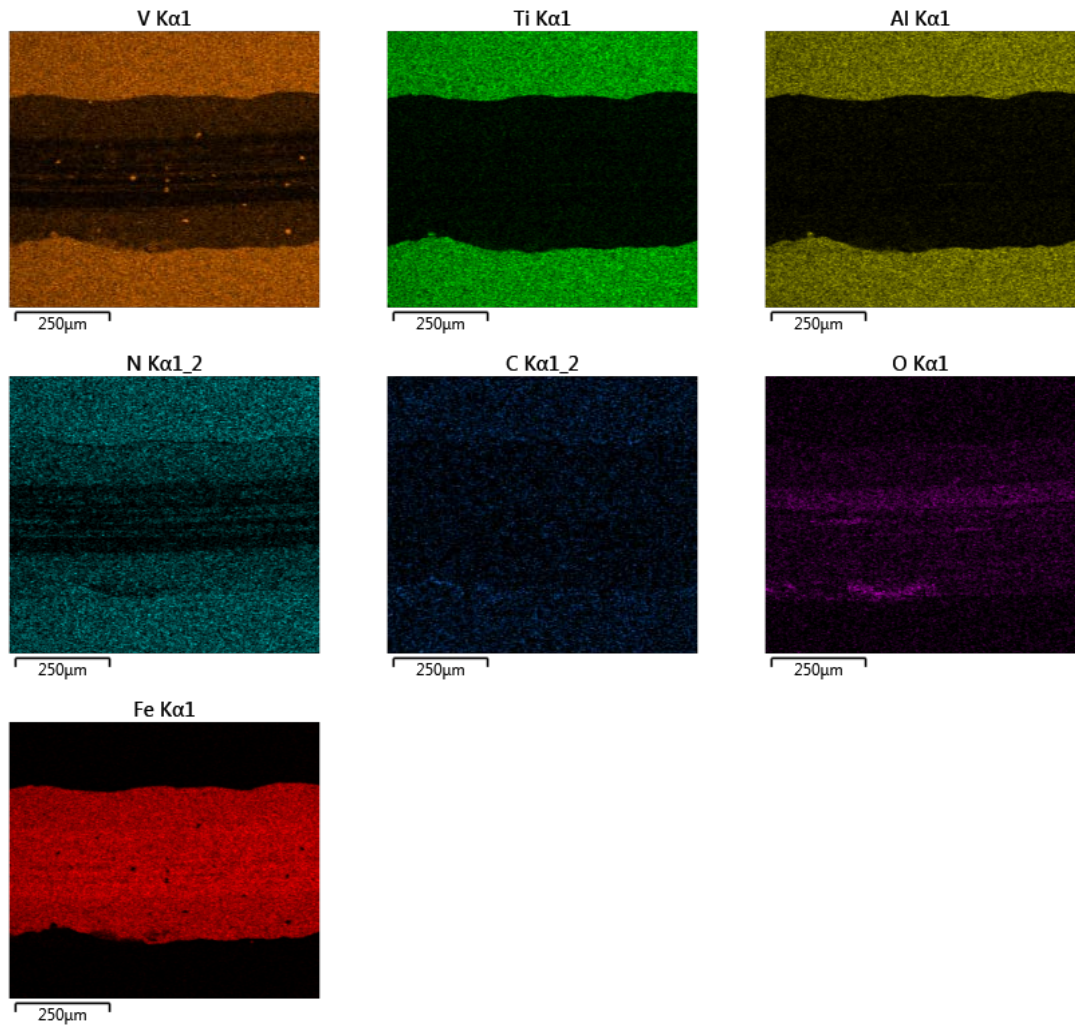


Figure 7.32 The EDX analysis of V, Ti, Al, N, C, Fe, and O elements within the wear track created by room temperature pin on disk testing

## Coating 20% OES

The SEM of and EDX mapping of the wear track are presented in fig. 7.33 and 7.34 respectively.

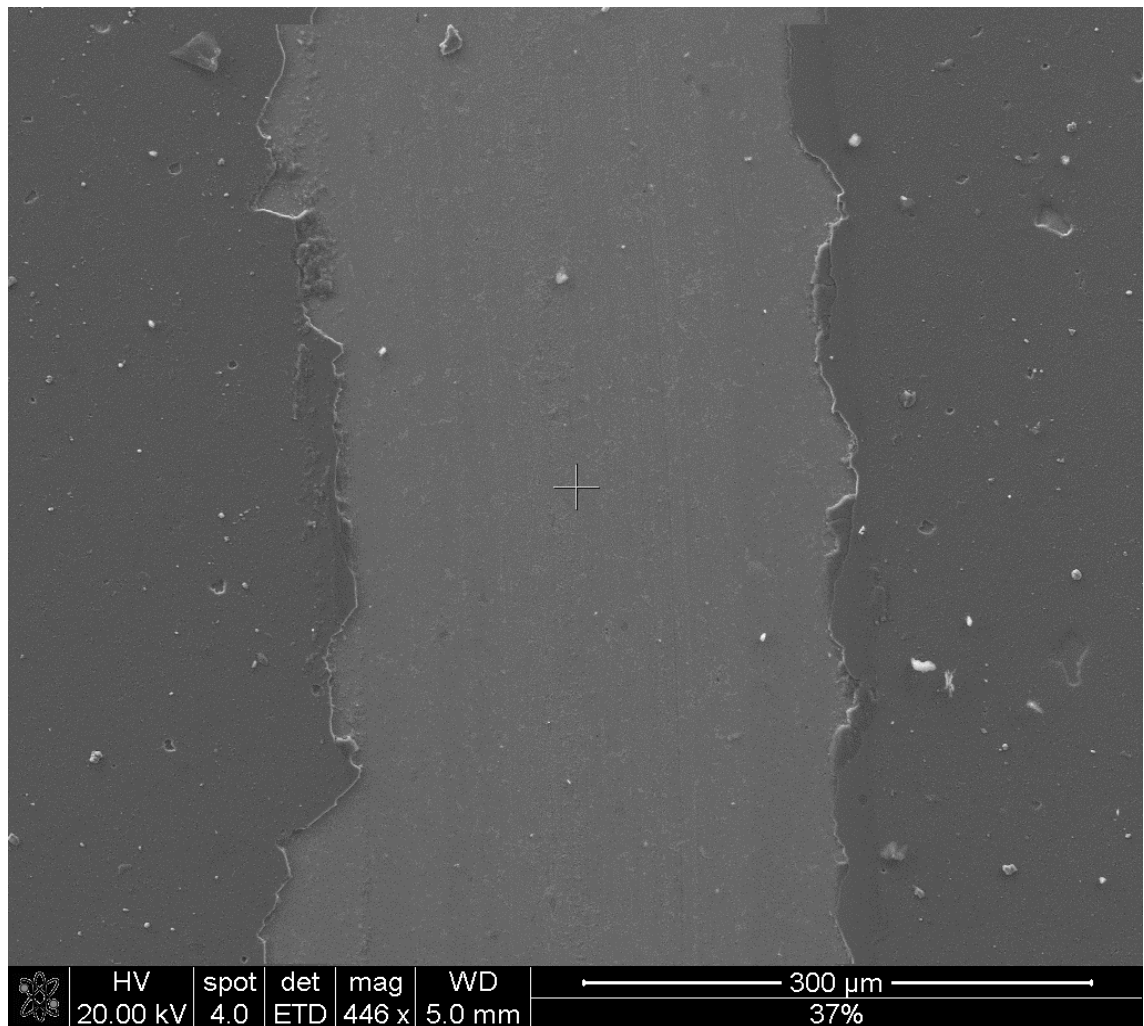


Figure 7.33 SEM image of the wear track created by room temperature pin on disk testing

The coating deposited at 20% OES signal exhibits a similar wear mechanism as the coating which failed at the coating - base layer level and substrate was exposed. Oxygen can be observed all along the wear track with small oxygen containing debris in the middle of wear track.

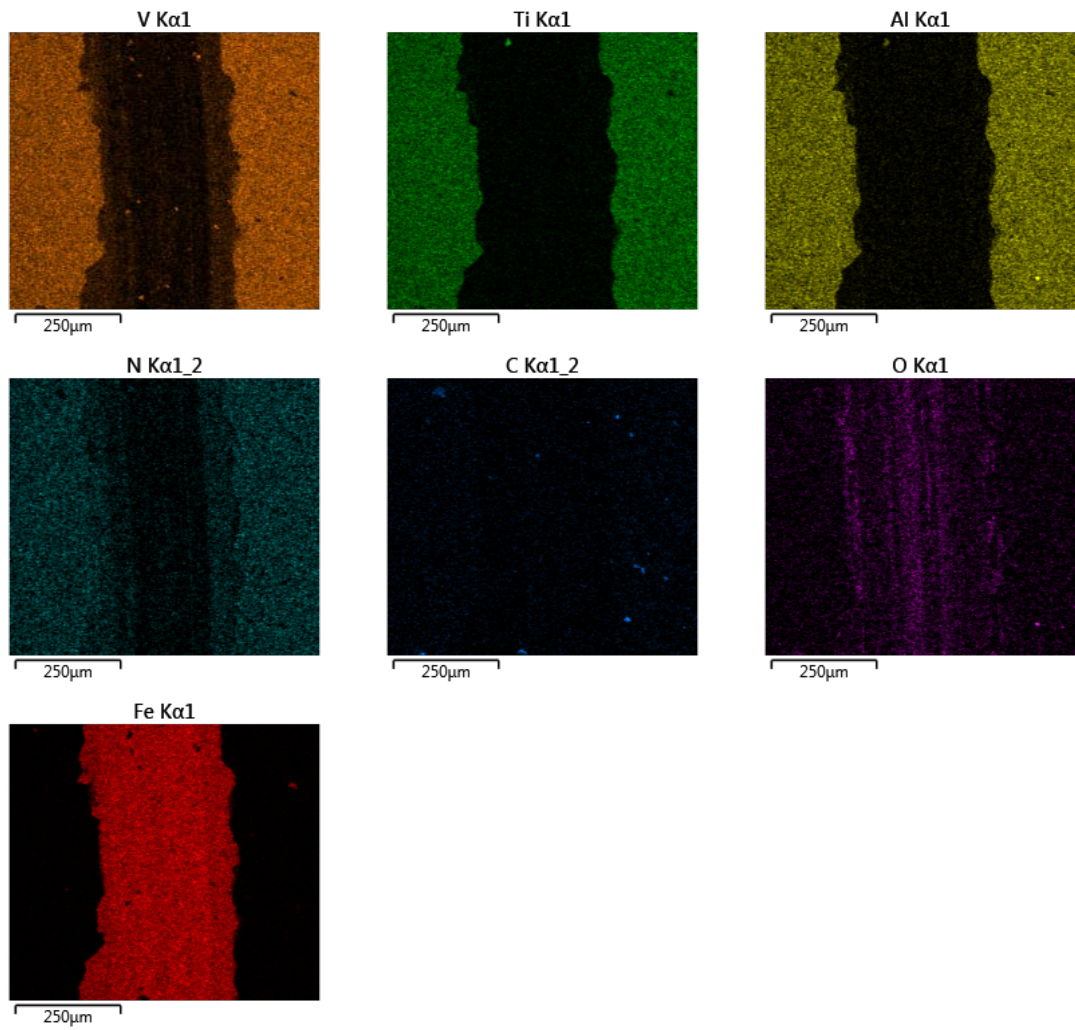


Figure 7.34 The EDX analysis of V, Ti, Al, N, C, Fe, and O elements within the wear track created by room temperature pin on disk testing

Table 7.6 summarises the tribological properties of SNMC. The COF is highest for coating 45% OES. Then it rapidly decreases to 0.65 for coating 37% OES, and increases again up to 0.75 for coating 30% OES. For the rest of the SNMC, the COF decreases with decreasing metal content.

The wear rate of the coatings 30% OES is almost one magnitude lower than that of the coating 37% OES. The wear rate results are opposite to the COF and contradicting to the general tribological trend. The low wear rate of coating 30% OES is caused by the oxide tribofilm growth within the wear track, reducing the removed volume. Due to spallation of coatings 20% OES, 25% OES and 45% OES the wear rate could not be calculated.

Table 7.6 of the Tribiological properties of TiAlCN/VCN deposited at different OES levels

	CoF ( $\text{mm}^3\text{N}^{-1}\text{m}^{-1}$ )	Wear rate	Wear track size ( $\mu\text{m}$ )	Maximum depth ( $\mu\text{m}$ )	Coating thickness ( $\mu\text{m}$ )
45% OES	$0.81 \pm 0.01$		$565 \pm 54$	7.32	5,1
37% OES	$0.65 \pm 0.03$	3.3E-15	$210 \pm 22$	0.21	4,63
30% OES	$0.75 \pm 0.02$	5.8E-16	$240 \pm 10$	0.51	3,98
25% OES	$0.56 \pm 0.02$		$347 \pm 39$	2.54	2,36
20% OES	$0.63 \pm 0.01$		$311 \pm 16$	2.46	2,24

## 7.7 Discussion

The XRD ( $\Theta/2\Theta$ ) XRD measurements revealed that TiAlCN/VCN coatings exhibit significantly different textures depending on the reactive gas flow and composition of the coatings. The coatings contain various textures, resulting in broad peaks. Thus, it is difficult to identify unambiguously the exact phases.

The coatings exhibit a single-phase B1-NaCl structure, which is composed of crystal structure (111) (200) and (220) planes.

The presence of the (111) plane can be associated with columnar growth and faceted surfaces [139].

With increasing reactive gas flow, the (220) peak becomes broader and shifts towards lower  $2\Theta$  values as shown in fig 7.35. Peak broadening indicates smaller grain size. This is due to carbon acting as a grain refiner, hindering grain growth [140, 141]. The shift to lower  $2\Theta$  values has been observed for TiC [140] and VCN [142] lattices. This can be associated with lattice strain indicating a residual stress in the plane parallel to the coating surface [143], as well as nitrogen atoms being replaced by carbon in the VCN lattice [142].

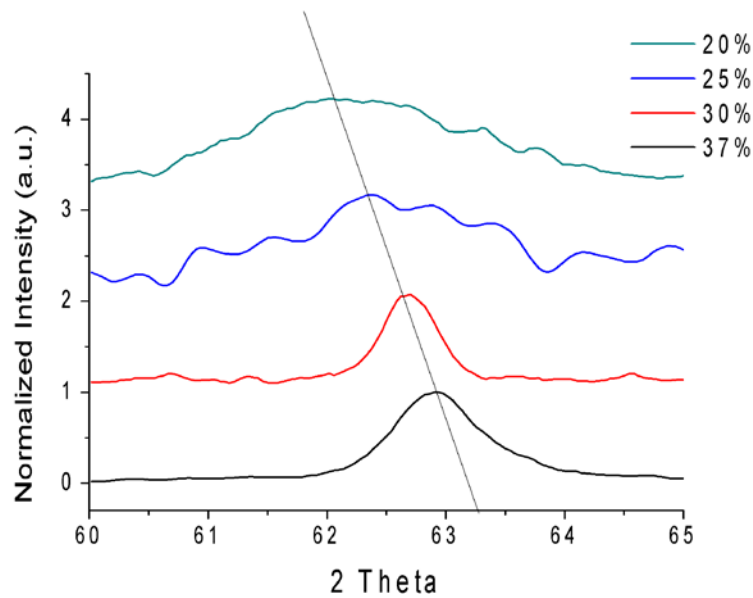


Figure 7.35 A shift to lower  $2\theta$  values has been observed

Cross sectional SEM micrographs show a transformation from non-columnar to columnar morphology, as the coatings become more ceramic. The difference in crystal structure and grain size can be attributed to the highly ionized flux of metal atoms for the more metallic coatings. Large grains are the result of columnar growth with large numbers of voids. Smaller grains in the coating 37% OES are the result of larger nucleation site densities and increased adatom mobility which leads to denser and well defined films [143–145]. As described earlier, the high carbon presence is responsible for the dense structure and low grain size of coatings 25% OES and 20% OES.

The analysis of inserts at the cutting edge by Raman spectroscopy shows that all SNMC coatings have mixed disorder and graphitic carbon phases with a dominant graphitic phase. For ceramic coatings, increasing the reactive flow increases the content of the graphitic phase. As the  $I_D/I_G$  ratio increases, the cauliflower shaped morphology changes to a dome shape indicating increased carbon segregation phases

growing between individual columns. Ferrari *et al.* [147] shows that the  $I_D/I_G$  ratio for nanocrystalline graphite increases when cluster size decreases. Highly graphitized carbon can lead to good tribological properties.

The coating 45% OES has sub-stoichiometric composition that leads to low hardness. It has a dense, amorphous structure with a secondary phase embedded in an amorphous matrix. The local accumulation of carbon and nitrogen causes high roughness of the surface. Low hardness of the coating is a reason of the contradicting adhesion test results. Soft surfaces have low stresses and exhibit no microcracks or delamination around the Rockwell indentation, but the low hardness causes smearing of the coating with progressing load during the scratch test. High roughness and softness disqualifies this coating for cutting purpose.

The coating 37 % OES has a very dense structure with randomly orientated crystal grains which leads to high hardness. The high graphitic peak suggests low friction and high hardness indicating that this coating may have a good wear resistance.

The coating 30% OES has lower hardness compared to the other ceramic coatings. This can be an effect of the open columnar structure compared with coating 37% OES.

For low metal content coatings 25% and 20% OES the texture shifts towards a (220) preferred orientation. This results in porous, cauliflower-like surface structure with grain size of 50-200 nm. It has been observed, that with increasing  $N_2$  flow the coating texture will shift from (111) to (220) preferred orientation [148], this has also been observed in the experiments of this study.

Coatings 25% OES and 20% OES have a similar crystal structure and morphology. The reduced microstructure density of the 25% OES coating leads to lower hardness and higher oxygen content.

Scratch test analysis revealed that for a low metal content, coatings perform better on the inserts than on HSS disks (table 7.5). The reason for this may be different thermal expansion of the substrate and the coating. During the heating step HSS expands to a higher extent than the ceramic inserts. When a high metal content coating is deposited on a metal substrate after deposition process and substrate cooling, both substrate and coating will contract in the same range. In case of the low metal content coating, the substrate will shrink more than the coating, which will result in residual stresses. Accordingly high stresses will be created in the case of depositing high metal content on the ceramic coating. Additionally to thermal expansion, the adhesion on inserts may be improved due to the high surface roughness, causing more nucleation sites and thus denser, more adhesive coatings. Additionally, for low metal content coatings, there is a big difference in OES signal levels during the base layer deposition and nanoscale multilayer coating deposition, where during base layer deposition the OES signal is much higher. In order to quickly reduce the OES signal, a high reactive flow is introduced into the chamber. This results in high carbon and nitrogen content in the lowest part of the nanoscale multilayer coating and can be a reason for the low adhesion to the base layer. The good adhesion of the VN base layer is attributed to metal ion ( $V^+$ ) etching by HIPIMS. Because metal ions are heavier than gas ions, they have a higher kinetic energy and are accelerating toward the substrate with higher momentum and thus metal atoms are implanted in the substrate surface. In effect, the coating starts to grow within the substrate. Due to

this implantation the adhesion of the coating will be enhanced considerably. The base layer adheres well to the high metal content coatings; however there is a need to improve the adhesion for low metal coatings. This can be achieved by a gradual change of the metal to gas ratio between the deposition steps.

EDX detection of oxygen in the tribofilm, as well as in the wear debris, indicates tribo-oxidation as a major wear mechanism for coatings 30% OES and 37% OES. The 45% OES coating failed the PIN on Disk test due to low hardness of the coating. The low adhesion between coating and TiAlCN/VCN coating was the reason for the failure of coatings 25% OES and 20% OES.

## 7.8 Conclusions

Target poisoning effect can be utilized to control the composition and morphology of the coatings. This can be done in a very complex system consisting of different target materials and while using multiple reactive gases. Simple Nanoscale Multilayers coatings were deposited successfully at various OES signal levels.  $\Theta$ - $2\Theta$  XRD measurements revealed that TiAlCN/VCN coatings can exhibit different phase structures and different preferred orientation depending on reactive gas flows. As the OES signal decreases, the coating microstructure becomes more columnar and carbon segregation can be observed.

At low OES signal levels there is a big difference between the OES signal during base layer deposition and nano-multilayer coating which leads to a rapid increase in reactive gas flow in the initial stages of growth. This further leads to low adhesion as shown in section 7.5 resulting in poor wear properties of the coatings.

The low adhesion of low metal content coatings and a rapid increase of reactive gas flows is solved in the next section (Advanced Nanoscale Multilayer Coatings) by introducing OES signal ramping.

## 8 Advanced Nanoscale Multilayer Coatings Deposited at Gradient Pressure

In this section, an analysis of the Advanced Nanoscale Multilayer Coatings (ANMC) deposited at gradient pressure is performed. These coatings were deposited to utilize target poisoning monitoring system to control the microstructure, mechanical properties of the films and coating architecture development; it was also intended to improve the mechanical and tribological properties of Simple Nanoscale Multilayer Coatings SNMC. The microstructure, crystallography and mechanical properties are analysed and compared with SNMC. The cross-section of the coatings is analysed in order to determine the influence of gradient pressure on the architecture development.

### 8.1 Overview of the experiments

ANMC consists of various SNMC layers. During the following stages of the deposition, the amount of nitrogen and methane were varied in steps. The process sequence was described in section 3.1 and 5. The ANMC deposition processes are summarized in table 8.1.

Firstly, two samples were deposited to improve adhesion of the low metal content coatings. For this purpose, a reactive gas ramping was introduced between individual layers of ANMCs; this was in order to eliminate a rapid increase in gas partial pressures. For coating 25% OES (B), the bias voltage was reduced to 50 V in order to reduce stresses in the coating. Coating 37/25% OES consists of two SMNC layers. The VN base layer initially transitions to a thin metal rich layer deposited at 37% OES; this is then gradually changed to a thick, low metal content layer deposited at 25% OES. The last coating consists of 5 SNMC coatings where each layer is deposited for the same amount of time. The VN base layer transition to a metal rich layer deposited at

45% OES; the following layers were deposited at 37%, 30%, 25% and 20% OES. This coating has been labelled as 45:20% OES.

Table 8.1 Deposition of the ANMC TiAlCN/VCN coatings

Advanced Nanoscale Multilayer Coatings			
Coating ID	Deposition Step	Deposition time (min)	Bias Voltage (V)
25% OES (B)	Signal Ramping from Base Layer signal level	10	50
	25%	240	
37/25% OES	Signal Ramping from Base Layer signal level	10	60
	37%	30	
	Signal Ramping	10	
	25%	200	
45:20% OES	45%	60	60
	Signal Ramping	10 min	
	37%	60	
	Signal Ramping	10 min	
	30%	60	
	Signal Ramping	10 min	
	25%	60	
	Signal Ramping	10 min	
20%	60		

Composition of the coatings is obtained by EDX analysis. The texture is identified with X-Ray diffraction. SEM imaging is used to obtain surface topography and cross sectional structure of the coatings. The adhesion of the coating was determined using Rockwell indentations and scratch tests.

## 8.2 Deposition Process

The process parameters and mechanical properties of the ANMC are summarised in tables 8.2 and 8.3. The total pressure and reactive gas flows of individual layers of

ANMC differ from those in SNMC. This difference is the result of changing target conditions whilst depositing prior layers.

For coating 45:20% OES, whilst deposition of the first layer with OES signal level of 45% and half time of the second layer with OES signal level of 37%, the reactive gas ratio was set to 1:1. Thus bottom layers of the coating are carbon rich.

Table 8.2 Process parameters during deposition of ANMC

ANMC		Average N <sub>2</sub> flow (sccm)	Average CH <sub>4</sub> flow (sccm)	Average P <sub>T</sub> (mBar ×10 <sup>-3</sup> )
25% OES (B)		59.56	29.82	2.66
37/25% OES	Layer ID			
	37%	50.85	25.47	2.604
	25%	63.88	31.99	2.656
45:20% OES	Layer ID			
	45%	15.33	15.39	2.539
	37%	39.23	25.17	2.584
	30%	65.83	33.02	2.653
	25%	67.56	33.89	2.652
	20%	70.85	35.53	2.730

ANMC are thick when compared with low metal content SNMC. Hardness is lower than SNMC deposited at high reactive flows with lowest 2055 HK for 25% OES (B), 3208 and 3389 for 37/25 and 45:20% OES respectively.

Table 8.3 Mechanical properties of ANMC

ANMC	Thickness (um)	Micro-Hardness (HK)	Nano-hardness (MPa)	Young's Modulus (GPa)
25% OES (B)	3,25	2055	14837	308
37/25% OES	3,54	3208	21709	361
45:20% OES	5,53	3389	21866	338

The Young's Modulus of the coating 25% OES (B) is low when compared with SNMC with a value of 308 GPa. Coating 45:20% OES is in the same range as low metal content SNMC with Young Modulus of 338 GPa, coating 37/25% OES has Young's Modulus of 361 GPa which is higher than all SNMCs.

### 8.3 Composition of ANMC

Semi-quantitative EDX analysis of the coatings is shown in table 8.4. Similar to SNMC, coatings are under-stoichiometric. The highest gas to metal ratio is found in coating 37/25% OES with a value of 0.82. Coatings 45:20% OES and 25% OES (B) have a gas to metal ratio of 0.5 and 0.79 respectively. Coating 25% OES (B) has a very low gas to metal ratio when compared with SMNC 20% and 25% OES. Also, it was deposited at the highest average reactive gas flow when compared with other ANMC.

Table 8.4 Composition of ANMC

Atomic content (%)						
	C	N	O	Al	Ti	V
25% OES (B)	9.7	21.3	15.9	16.6	13.8	22.7
37/25% OES	12.0	31.1	4.4	17.1	13.7	21.7
45:20% OES	9.1	31.6	8.3	16.0	14.1	21.3

The content of metals for coatings 37/25% OES and 45:20% OES is on the same level, while the N and C contents change. Coating 45:20% OES has the highest nitrogen content while coating 37/25% OES has the highest carbon content. Coating 25% OES (B) has a lower gas to metal ratio and the highest C/N ratio when compared with other ANMCs.

## 8.4 Crystallographic structure of ANMC investigated by XRD analysis and SEM

### Coating 25% OES (B)

Coating 25% OES (B) has shown a single-phase B1-NaCl structure with a strong [200] and weak [220] [111] [222] peaks as in fig.8.1.

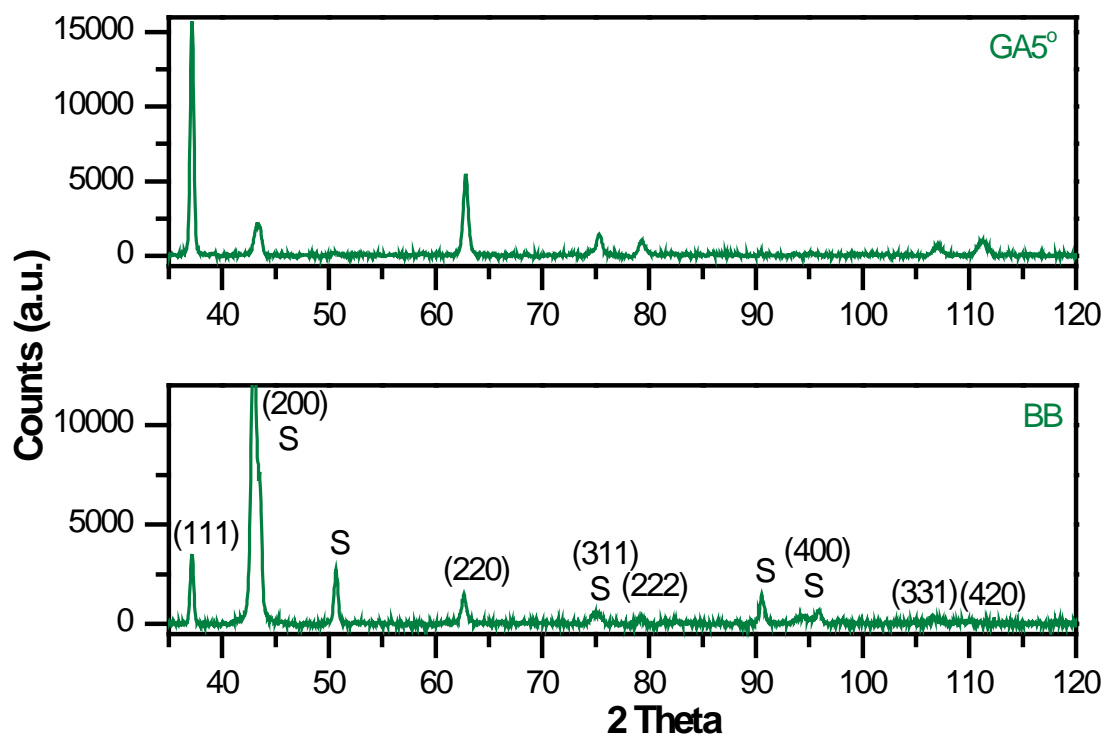


Figure 8.1 The Bragg-Brentano and Glancing Angle XRD patterns of the 25% OES (B) coating.

The cross section (fig. 8.2) shows that the coating consists of well-defined columns with large diameters ( $\sim 180$  -300 nm); they terminate with sharp triangular tops which results in a faceted topology (fig. 8.3). The base layer is 220 nm thick with a gradual transition to the coating. The coating has typical zone T structure of Thornton Model.

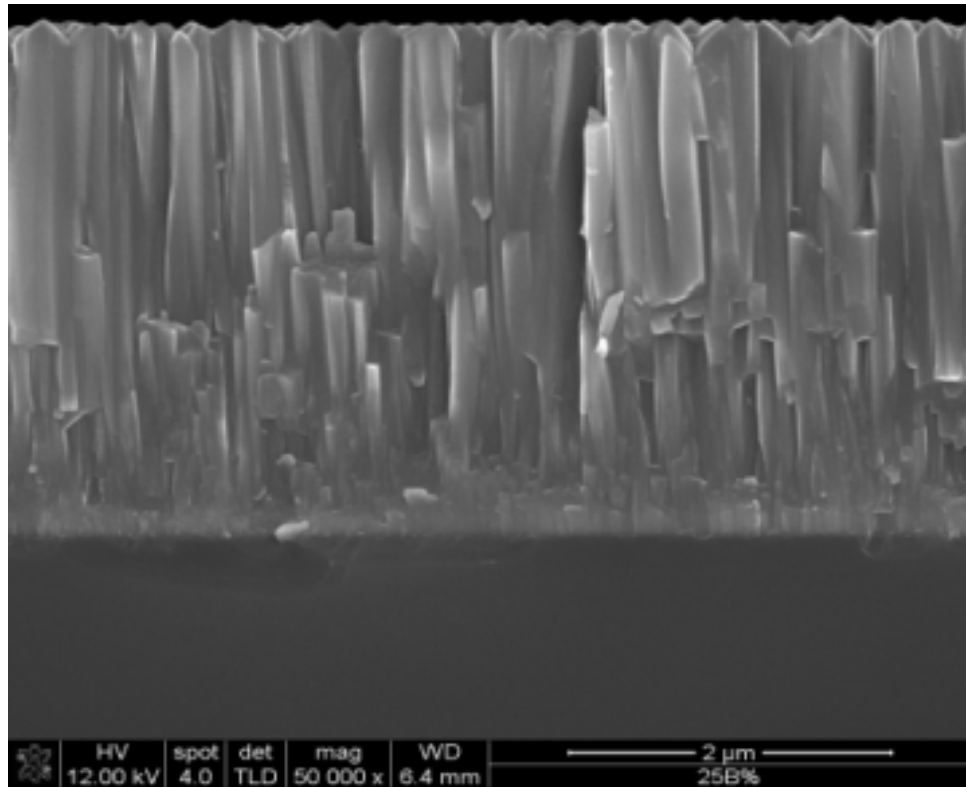


Figure 8.2 SEM cross-section of the 25% OES (B) coating

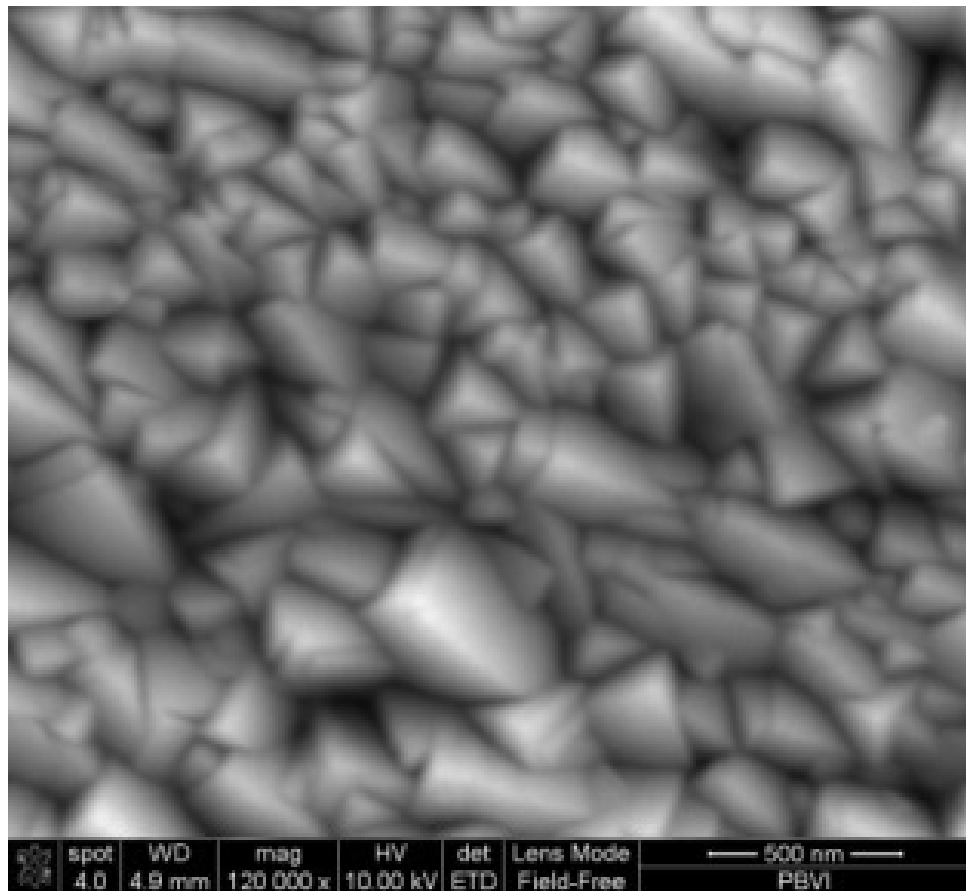


Figure 8.3 SEM image of the surface structure for coating 25% OES (B).

The Raman Spectrum is presented in fig. 8.4. The  $I_D/I_G$  ratio is 1.26 with a clear peak separation.

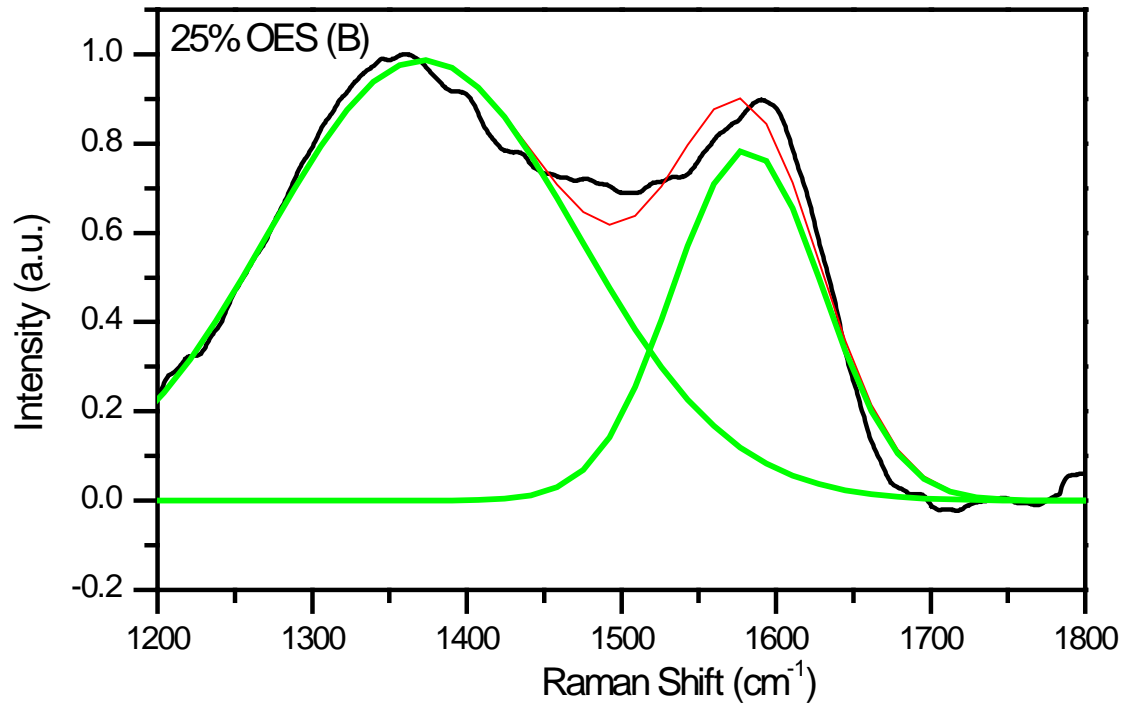


Figure 8.4 RAMAN Spectra of carbon peaks of the coating 25% OES (B).

## Coating 37/25% OES

Coating 37/25% OES shows [200] preferred oriented planes with low [220, 111, 222] and [400] peaks with a single-phase B1-NaCl structure.

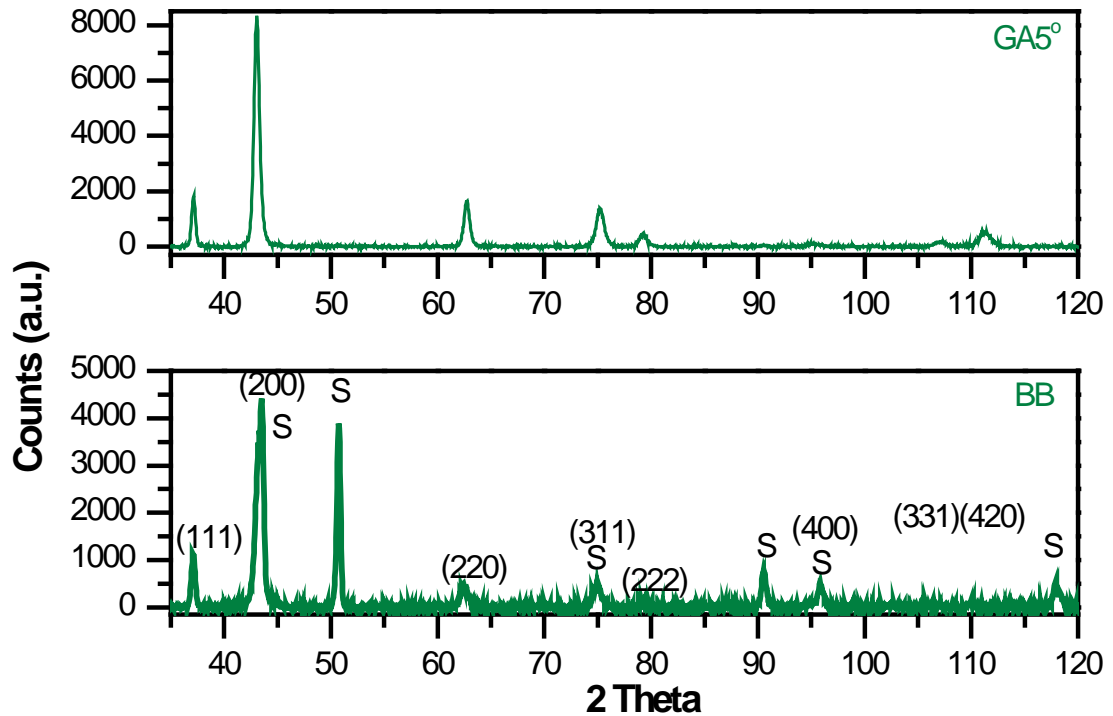


Figure 8.5. The Bragg-Brentano and Glancing Angle XRD patterns of the 45:20% OES coating

The cross section SEM in fig. 8.6 imaging shows that the structure changes from dense, fine grained columns to large diameter (~160 -300 nm) columns, terminated with sharp triangular tops, resulting in a faceted topology (fig. 8.7). The architecture evolution of the coating is analysed in detail in section 8.5.1. The  $I_D/I_G$  ratio is 1.4 with clear peak separation

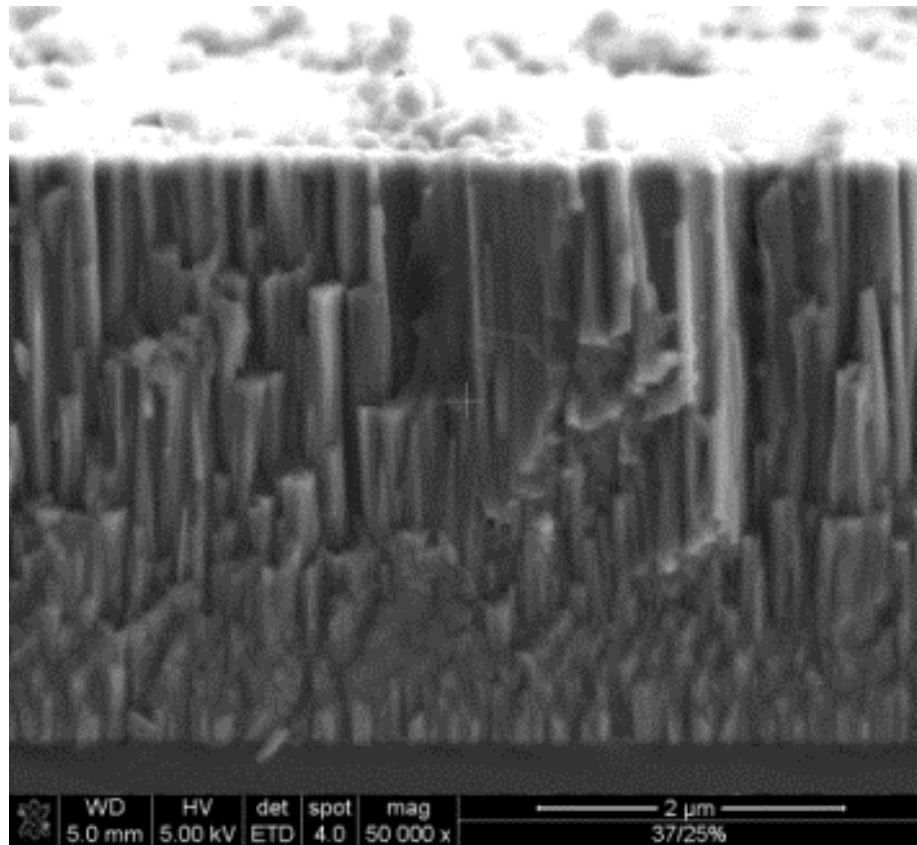


Figure 8.6 SEM cross-section of the 37/25% OES coating

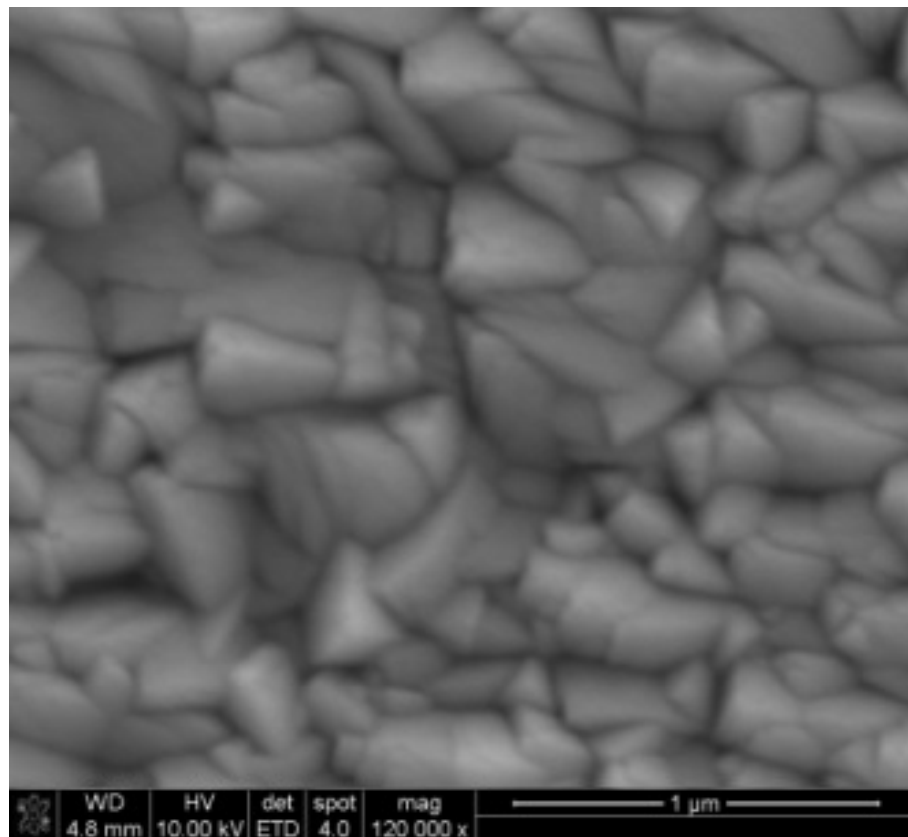


Figure 8.7 SEM image of the surface structure for coating 37/25% OES.

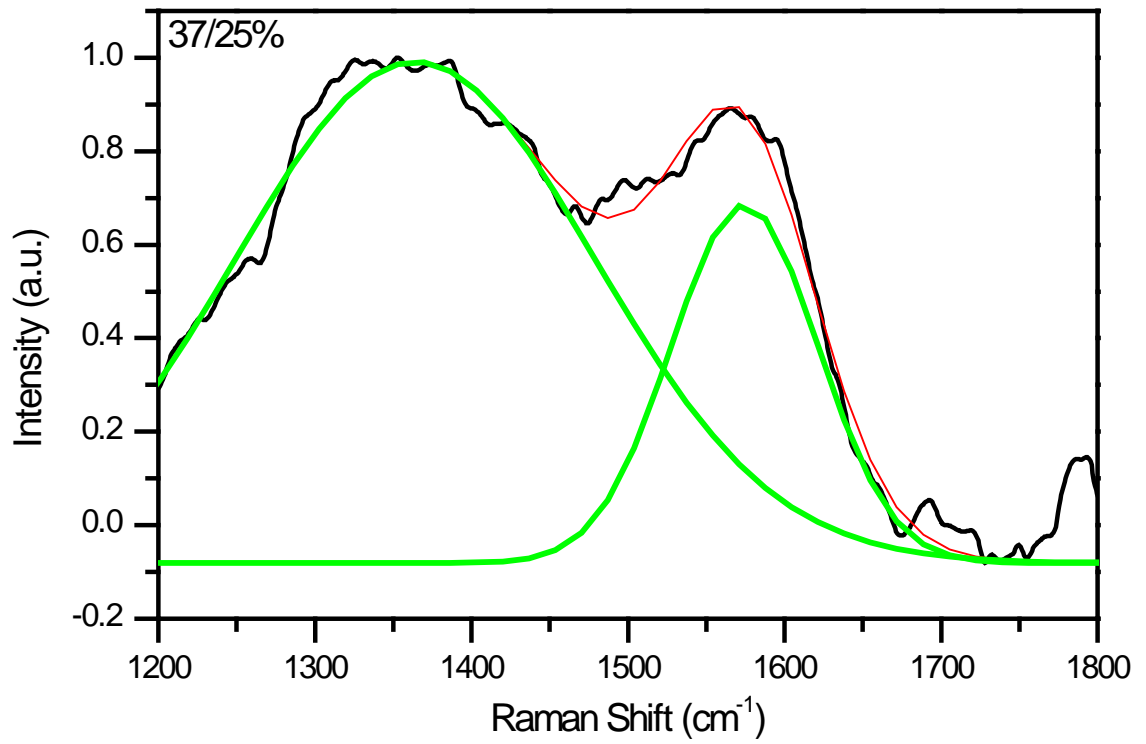


Figure 8.8 RAMAN Spectra of carbon peaks of the coating 37/25% OES

## Coating 45:20% OES

Coating 45:20% OES shows random orientation with a mix of [111, 200, 222] and [311] planes. GAXRD analysis reveals a single-phase B1-NaCl structure (fig.8.9).

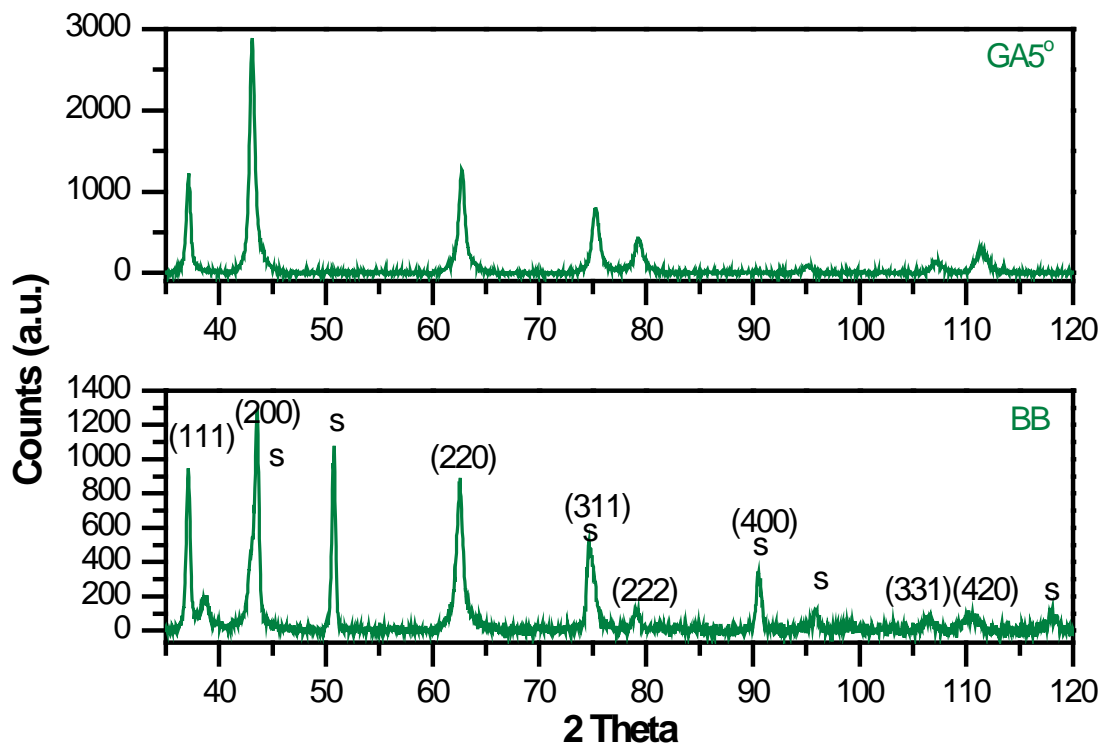


Figure 8.9 The Bragg-Brentano and Glancing Angle XRD patterns of the 45:20% OES coating

The top view shows large 200-400 nm, various shaped grains consisting of smaller (a few nanometres) globular grains (fig. 8.10). The groove networks are likely the origin of the columnar boundaries coated with a cauliflower-like layer. The structure of the coating changes from a dense and glossy structure to large diameter (~160 -300 nm), well-defined columns, terminated with round tops. The transition between dense and columnar structure is rapid. The coating architecture is analysed in section 8.5.2. The  $I_D/I_G$  ratio is 1.39 with a subtle separation of the peaks.

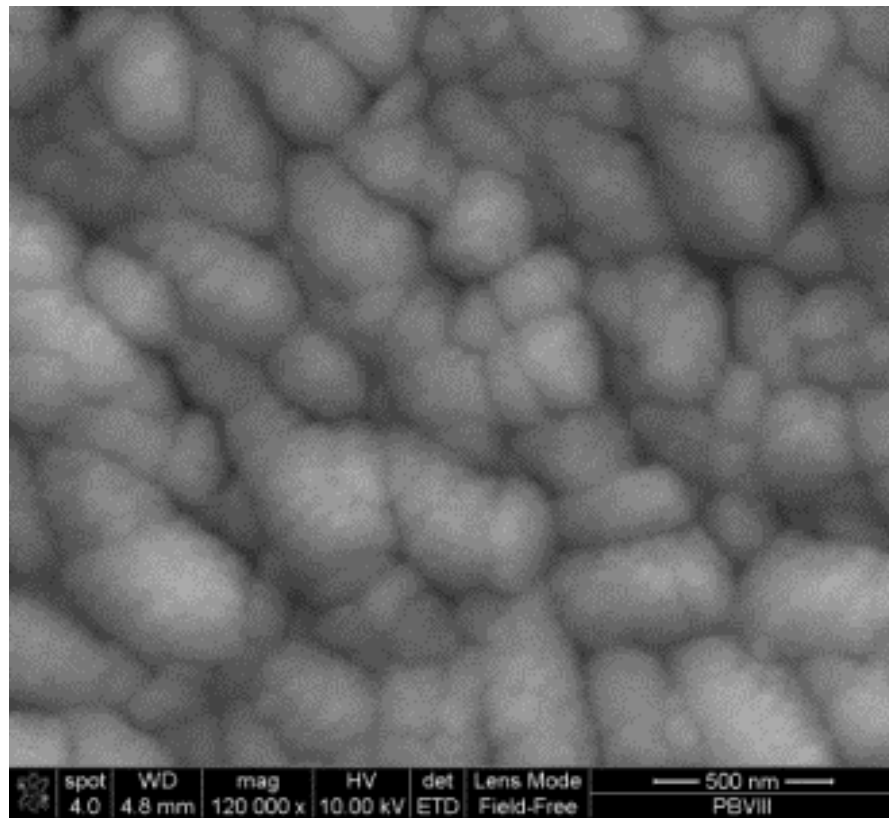


Figure 8.10 SEM of the surface structure for coating 45:20% OES

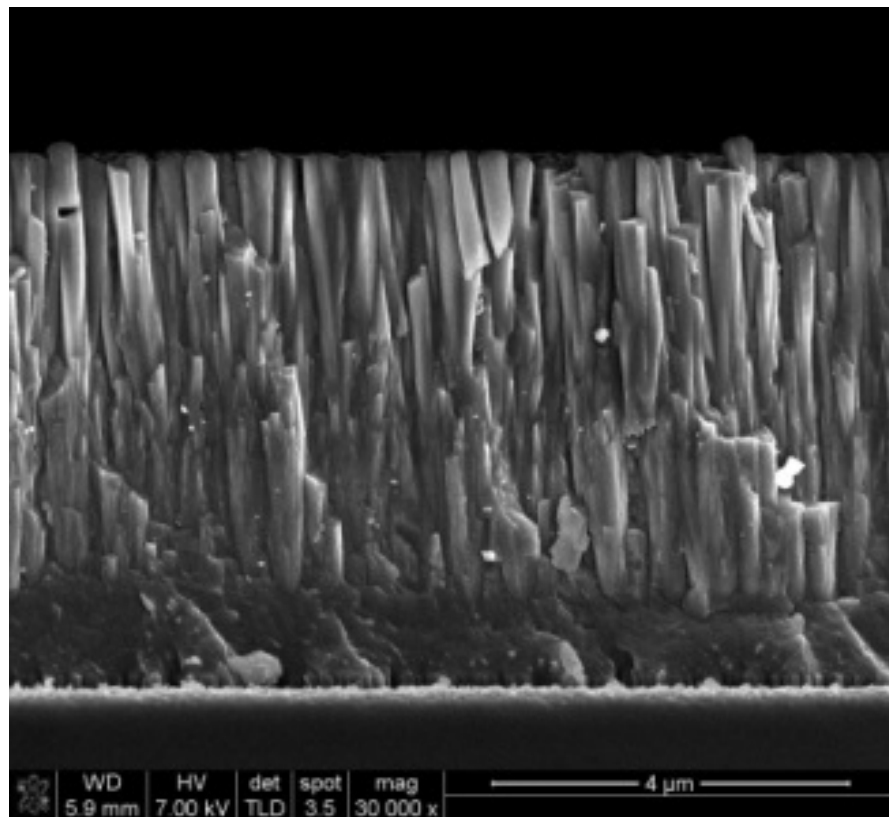


Figure 8.11 cross-section of the 45:20% OES coating

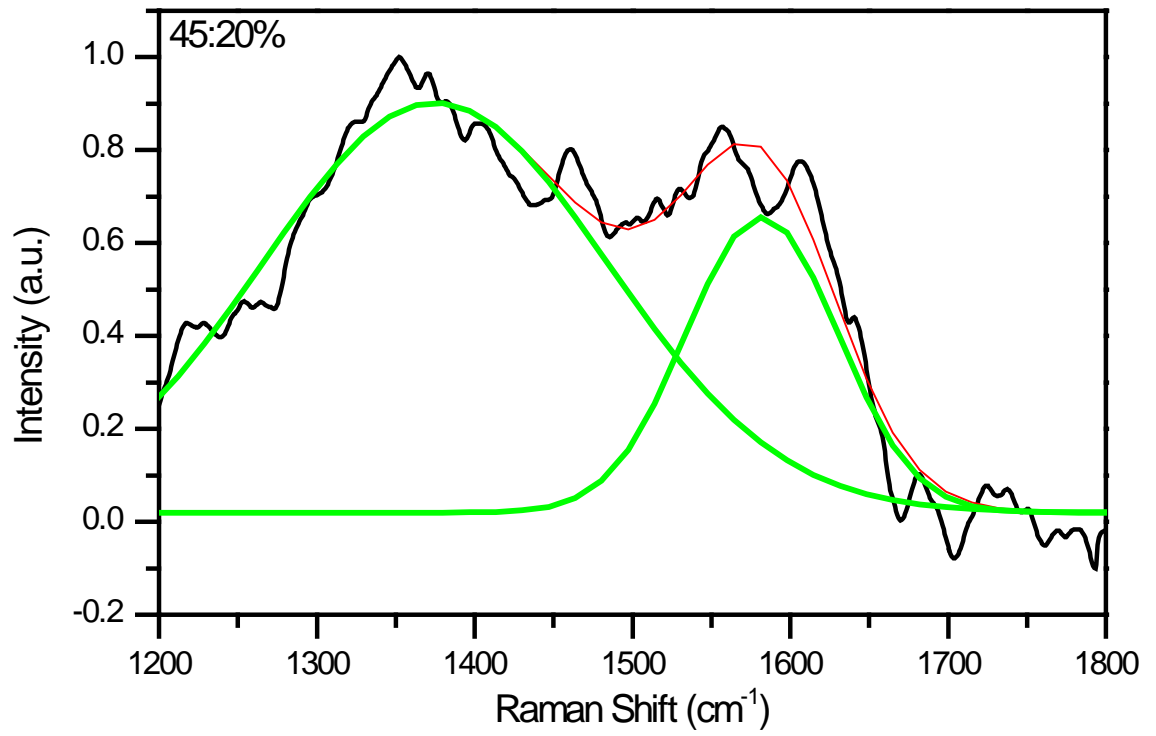


Figure 8.12 RAMAN Spectra of carbon peaks of the coating 45:20% OES (B).

## 8.5 Structure Evolution of Advanced TiAlCN/VCN Nanoscale Coating

The architecture evolution of coatings 37/25% and 45:20% OES was studied with SEM images of the fractional cross section of coatings deposited on silicon substrate. Results are confirmed using Focused Ion Beam (FIB) cross section on inserts. The elemental distribution of elements across the coating thickness was carried out with X-ray mapping.

### 8.5.1 Coating 37/25% OES

The cross section SEM analysis (fig. 8.13) shows that the coating 37/25% OES consists of the VN base layer (average thickness ~180nm), gradually transitioning to a thick and dense TiAlCN/VCN metallic layer (~920 nm); this is followed by a thick, dense and columnar TiAlCN/VCN ceramic top layer (~2620 nm).

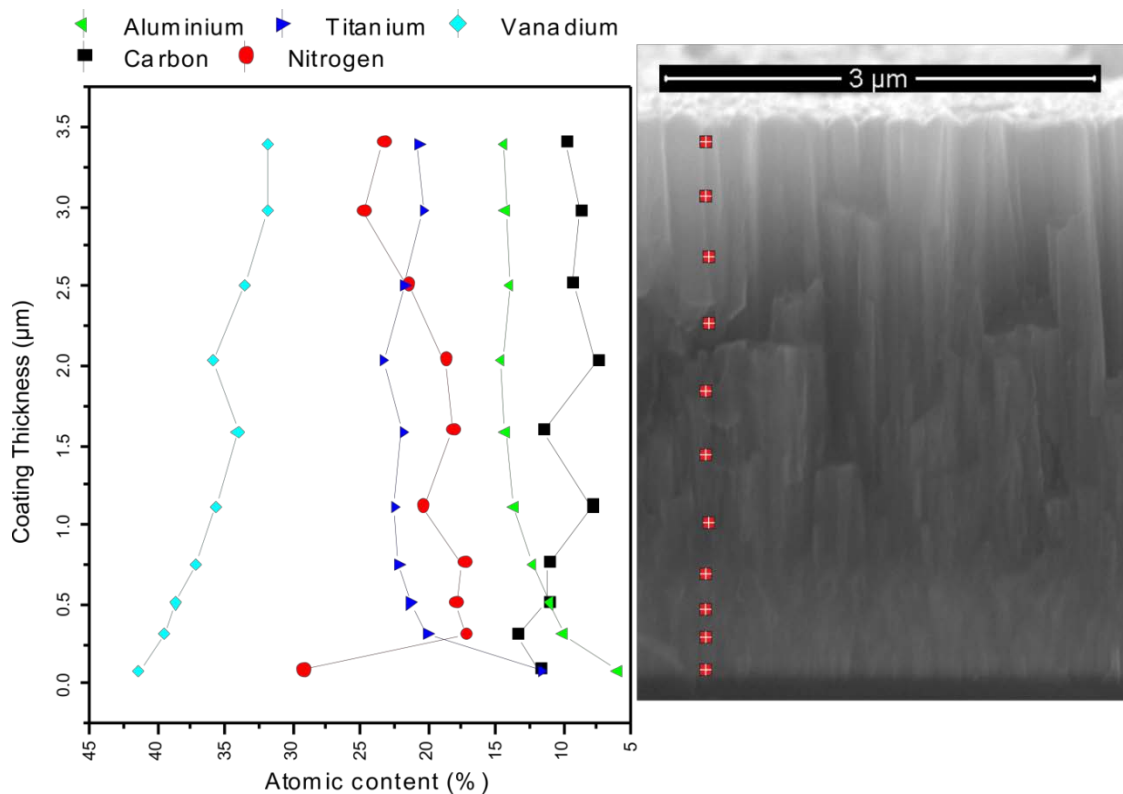


Figure 8.13 The evolution of coating stoichiometric along the coating thickness.

The EDX analysis across the cross-section is presented in fig. 13. At the base layer, the coating is V and N rich; however, traces of other elements are also measured. This may be due to contamination during sample preparation; it could also be due to implantation of metal ion and diffusion of carbon. At the metallic layer, the nitrogen content drops and the titanium content increases rapidly; however, aluminium increases at higher thickness. After 1.6  $\mu\text{m}$ , aluminium reaches a maximum content and stays at a constant level; titanium and vanadium behave in the same manner. Nitrogen and carbon contents fluctuate over the coating thickness but an increased content of N in the ceramic layer can be observed. Carbon incorporation remains constant with increasing methane flow. At the very surface of the coating, a decrease in nitrogen and an increase of carbon is observed.

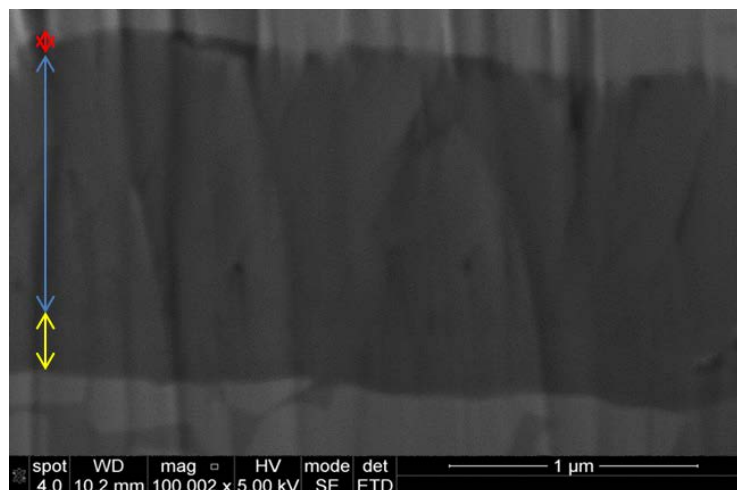


Figure 8.14 The BS SEM analysis of the FIB cross section on the insert. Colours indicates various regions of the coating: yellow – the high metal content region; blue – the low metal content region; red – the low nitrogen and high carbon content region.

The FIB analysis on the insert confirms the Si-wafer analysis. In fig. 8.14, the yellow area has high metal content: blue is a low metal content region and red is a low nitrogen content layer.

### 8.5.2 Coating 45:20% OES

The 45:20% OES coating consists of a VN base layer (~200nm) transitioning to a dense and glossy TiAlCN/VCN metallic layer; this is followed by a thick, dense and columnar TiAlCN/VCN ceramic layer. The columns transition from very dense and low diameter to very broad and well defined columns. Using the deposition rate from SNMC experiments, the thickness of the individual layer has been calculated and is given in table 8.5.

Table 8.5 Thickness of the individual layer calculated using deposition rate of the SNMC

	45% OES	37% OES	30% OES	25% OES	20% OES
% of Coating	16	30	25	15	14
Thickness ( $\mu\text{m}$ )	0.91	1.65	1.41	0.8	0.76

Fig. 8.15 shows high magnification images of the chosen area of the cross section. The VN base layer is well bonded with the substrate; this can be seen via the crystal growth from the silicon substrate (fig. 8.15 a). However, there is a rapid transformation from the columnar base layer to the TiAlCN/VCN metal-rich layer 45% OES (fig. 8.15 b). The transformation between glossy 45% OES layer and dense columnar structure is also well-defined (fig. 8.15 c). Columns gradually transform from narrow to broad in smooth steps. The 37% OES layer is comprised of small and densely packed columns. In 30% OES layer the columns become coarser with distinct boundaries. As more reactive gas is added in layers 25% OES and 20% OES, columns become coarser. Widening of the columns indicates competitive growth. However, the columns are terminated in a dome shape (fig. 8.15d).

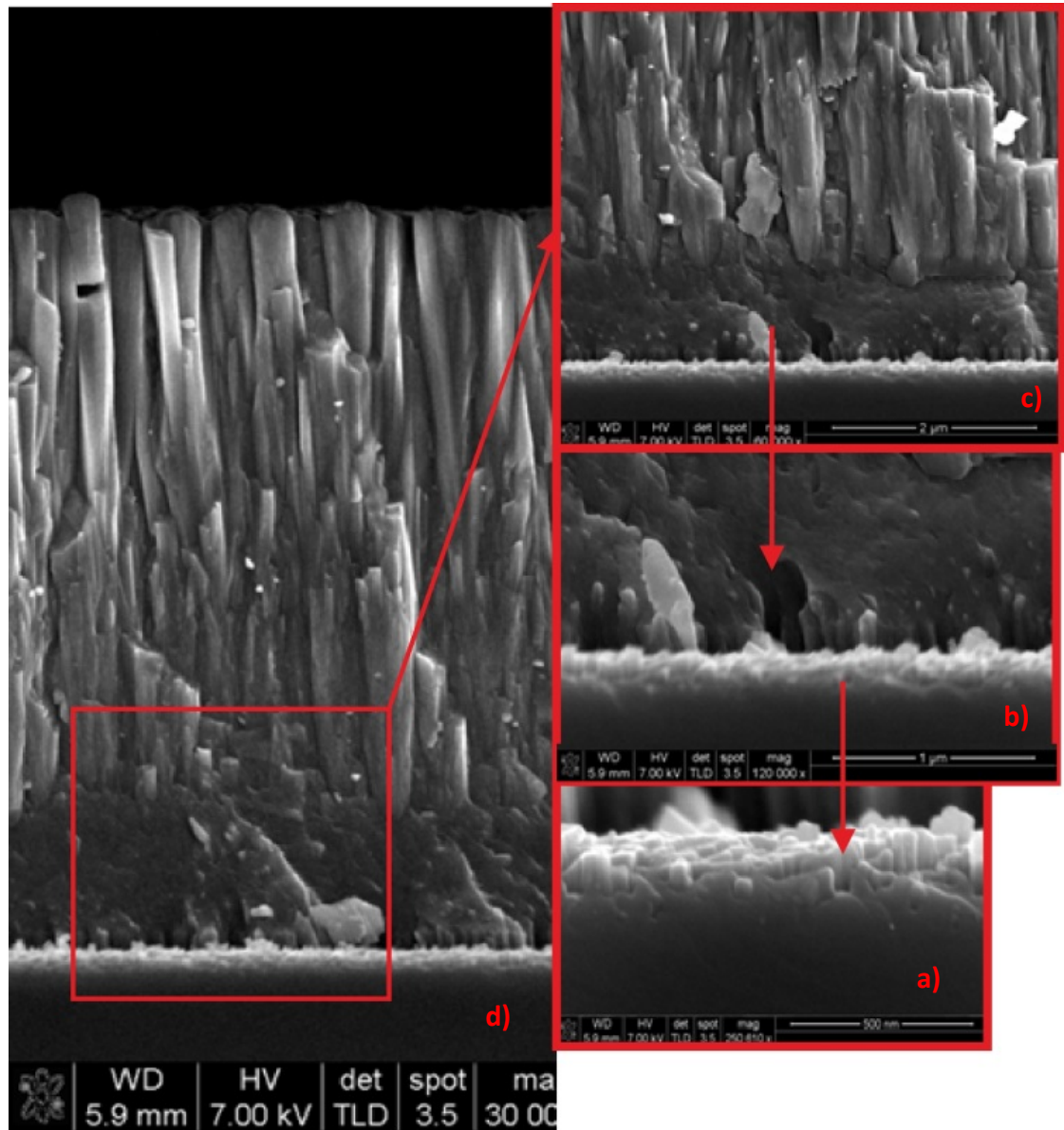


Figure 8.15 The high magnification cross section SEM image of the 45:20% OES coating. Borders between the VN base layer and 45% layer of the TiAlCN/VCN coating and between 45% and 37% layers are rapid and easily distinguished.

The EDX analysis across the cross-section is presented in fig. 8.16. Similarly, as in the case of coating 37/25% OES, the base layer consists of V and N. Traces of other elements are detected. Due to high carbon flow, during the deposition of the 45% OES layer, high carbon content can also be observed in the base layer. At the metallic layer, the nitrogen content drops and the vanadium, titanium, aluminium and carbon content increase rapidly. Over the coating thickness, the carbon content fluctuates but a general decreasing trend can be observed. The nitrogen content increases with the coating thickness and reaches almost 45% near the surface. With increasing coating thickness, the metal content drops in four steps; these steps represent the different OES layers.

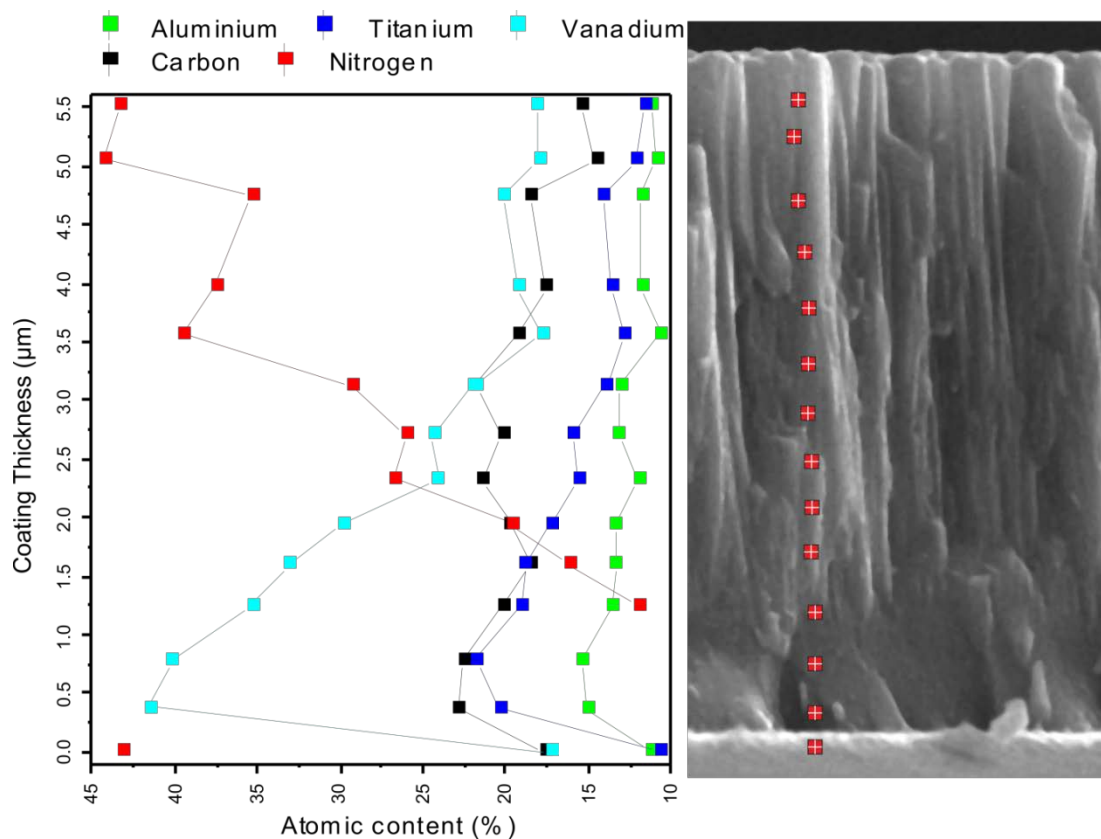
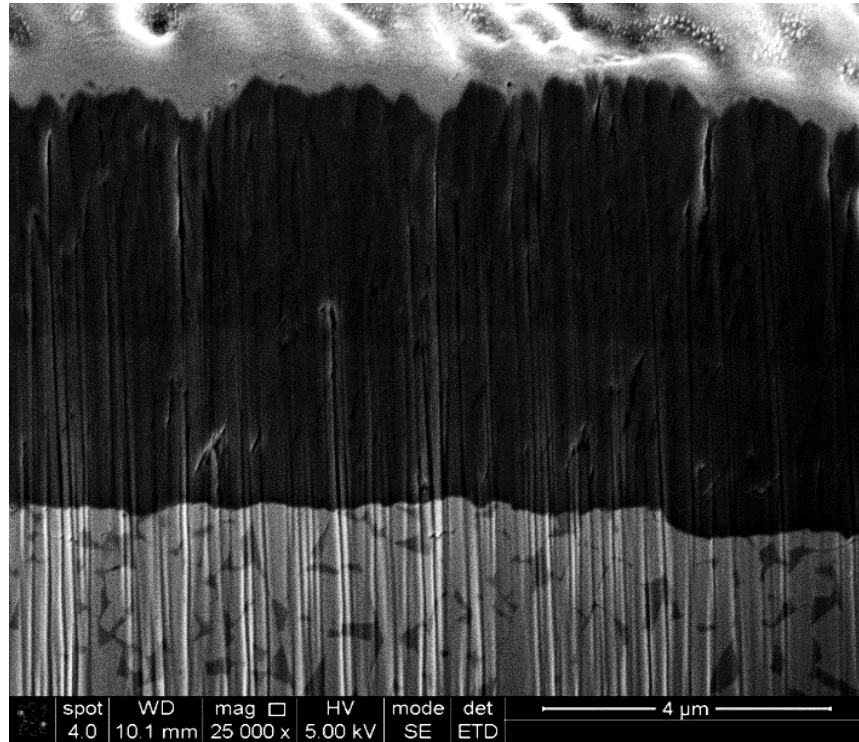


Figure 8.16 The evolution of coating stoichiometric along the coating thickness.

The FIB cross-section on a insert presented in fig. 8.17 shows a small contrast difference between layers deposited 45% and 37% OES metal; there is a clear border between layers deposited at 37% and 30% OES. The individual layers of 30%, 25% and 20% OES cannot be determined as a change to a darker colour.



*Figure 8.17 The BS SEM analysis of the FIB cross section on the insert. Two regions can be observed – bright at the bottom of the coating is metal rich and dark, where metal content is reduced.*

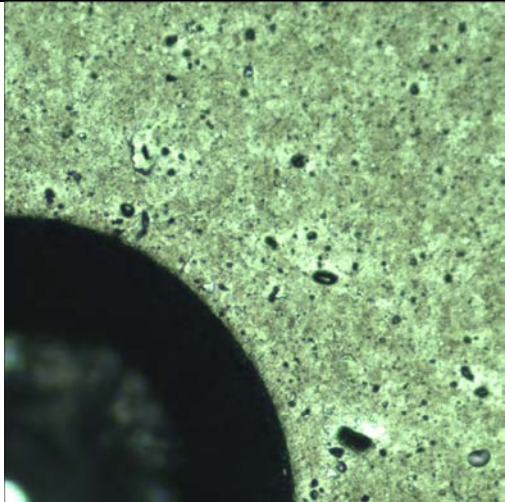
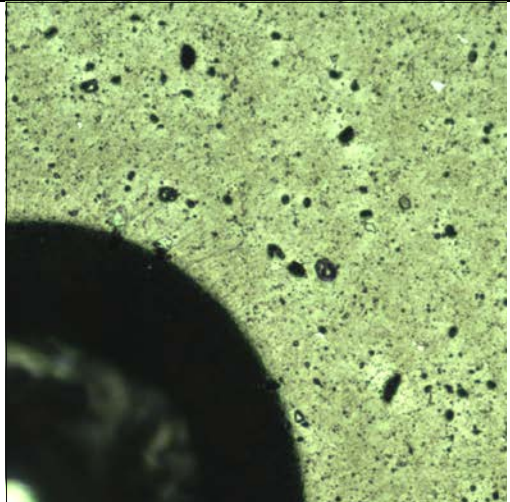
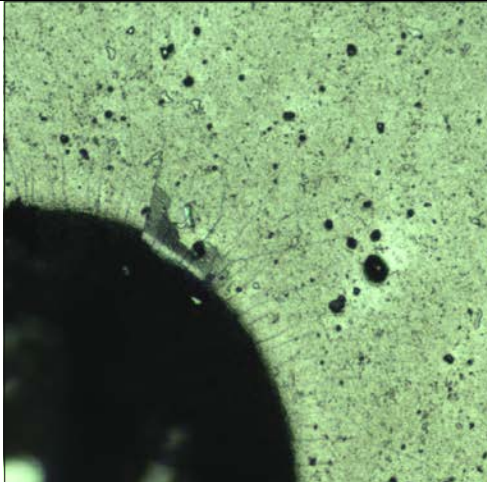
## 8.6 Adhesion

### Rockwell B test

Table 8.6 contains optical microscopy images of HSS samples.

In all ANMC the adhesion has been improved. Coatings 25% OES (B) and 37/25% OES are classified as Class 0. Microcracks and slight delamination have been observed around the edge of the indent of the coating 45:20% OES. Failures are classified as class 1.

Table 8.6 Rockwell indentation marks of ANMC

25% OES (B)	37/25% OES
	
45:20% OES	
	

## Scratch Test

All ANMC performed better on the inserts than on HSS disks (table 8.7), similarly as in case of SNMC. The critical load for the coating 45:20% OES is similar for both substrates: 41 N for HSS and 52 N for insert.

25% OES B coating has a relatively low load limit for both substrates of 28 N for HSS and 42 N for insert. Coating 37/25% OES has low adhesion to HSS substrate of 25 N and very high adhesion to insert exceeding 100 N. For coating 45:20% OES, the load limit for both substrates is in the same range of 41-52 N.

*Table 8.7 Maximum load during the scratch test on HSS and plain inserts*

Coating ID	25% OES B	37/25% OES	45:20% OES
Inserts	42 N	>100 N	52 N
HSS	28 N	27 N	41 N

## 8.7 Wear Resistance – Pin on Disk

The wear behaviour of TiAlCN/VCN ANMC against the number of laps is plotted in fig. 8.18. The wear properties are summarised in table 8.8. The run-in period was observed between 0 and 1000 laps for all ANMC. Coating 25% OES (B) has very low coefficient of friction (COF) of 0.56 with smooth wear behaviour. Very low amplitude oscillations can be observed.

Coating 37/25% OES has an average COF of 0.73. The friction coefficient curve shows high oscillations that increase after 3500 laps. Oscillation indicates presence of debris and a three-body rolling contact mechanism. The COF increased slightly towards the end of the test.

Coating 45:20% OES has a smooth friction coefficient curve with an average CoF of 0.69. The CoF diverges from the maximum after passing 5500 laps. This can indicate changing in the layer composition due to wearing through to another layer.

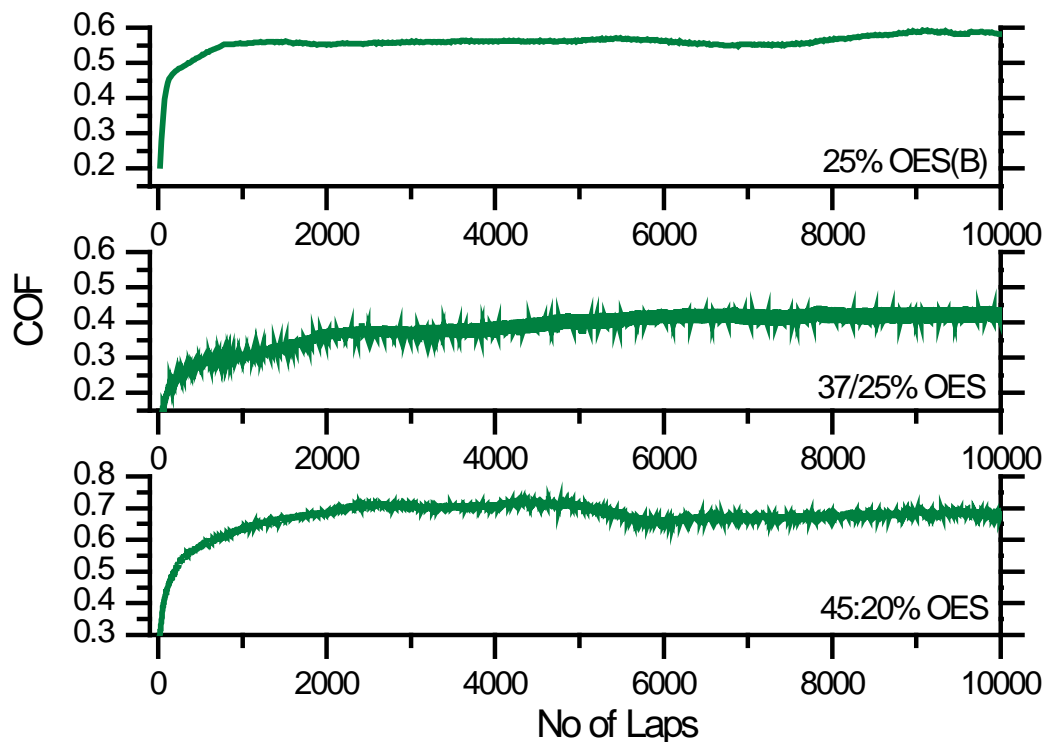
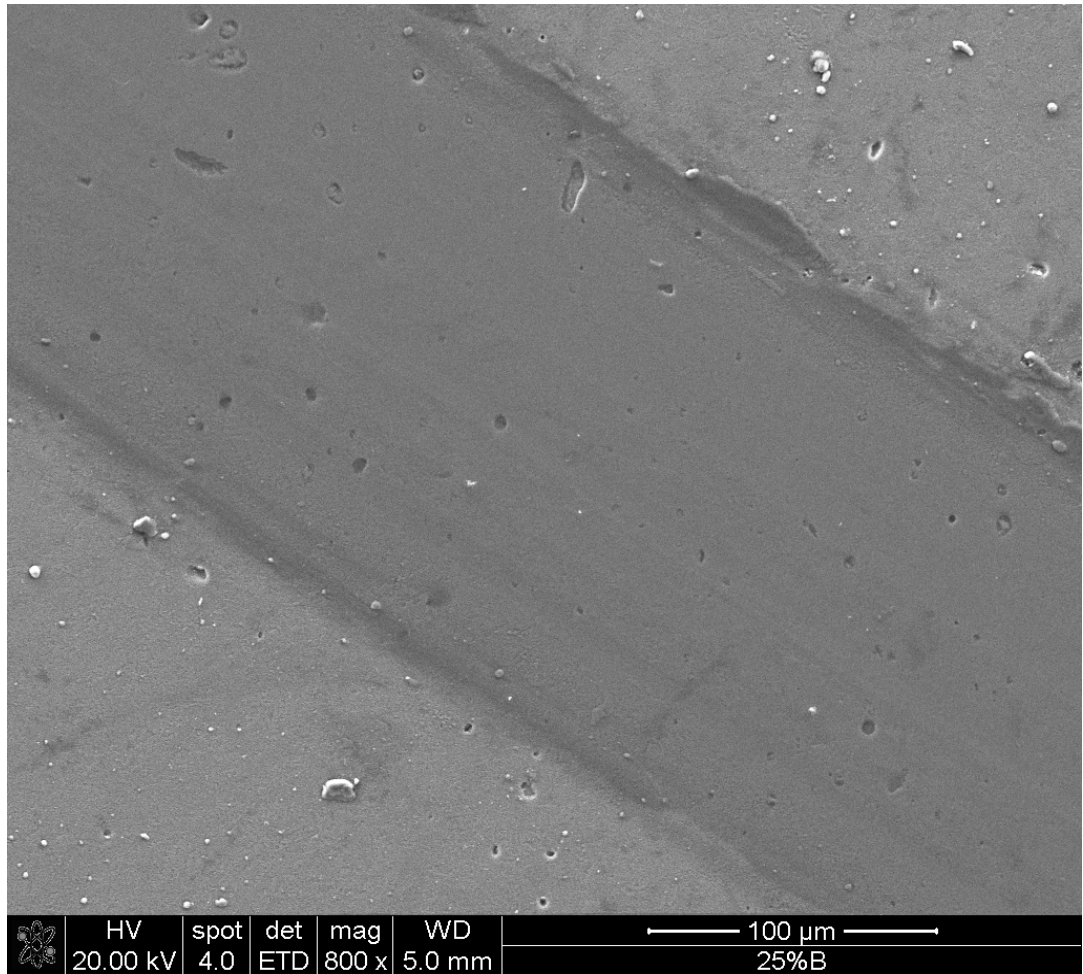


Figure 8.18 Coefficient of friction as a function of number of laps for room temperature of ANMC

Table 8.8 Wear behaviour of ANMC

	COF	Wear rate ( $\text{mm}^3\text{N}^{-1}\text{m}^{-1}$ )	Wear track size ( $\mu\text{m}$ )	Maximum depth ( $\mu\text{m}$ )
<b>25%B</b>	$0.56 \pm 0.01$	1.2E-15	$179 \pm 15$	0.23
<b>37/25%</b>	$0.73 \pm 0.01$	3.4E-16	$209 \pm 4$	0.32
<b>45:20%</b>	$0.69 \pm 0.02$	5.6E-17	$184 \pm 39$	0.32

**25% OES B**

*Figure 8.19 SEM image of the wear track created by room temperature pin on disk testing.*

Coating 25% OESB has a very smooth wear track. Oxides can be observed along the centre and at the edges of the wear track.

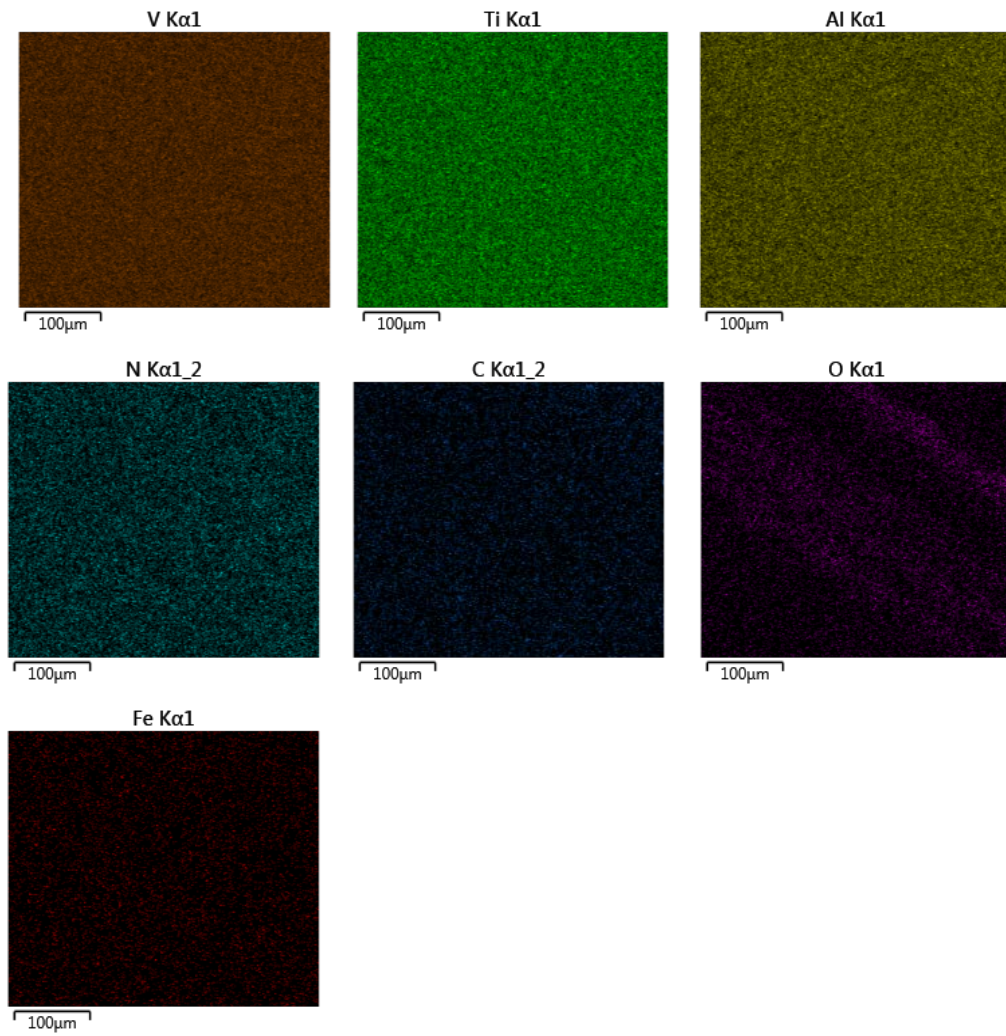
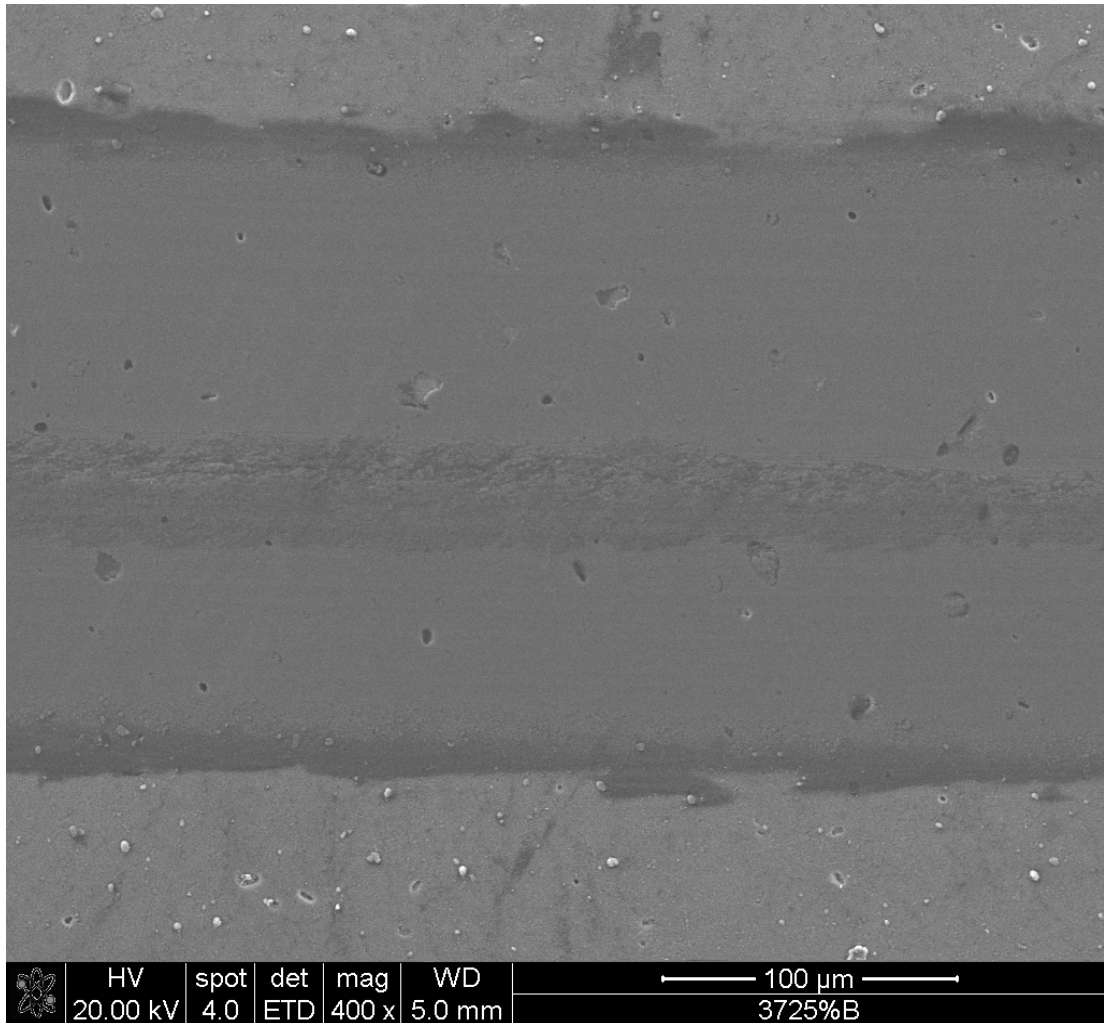


Figure 8.20 The EDX analysis of V, Ti, Al, N, C, Fe, and O elements within the wear track created by room temperature pin on disk testing

**37/25% OES**

*Figure 8.21 SEM image of the wear track created by room temperature pin on disk testing.*

Coating 37/25% OES has a very smooth wear track. Oxide debris can be observed in the middle and at the edges of the wear track.

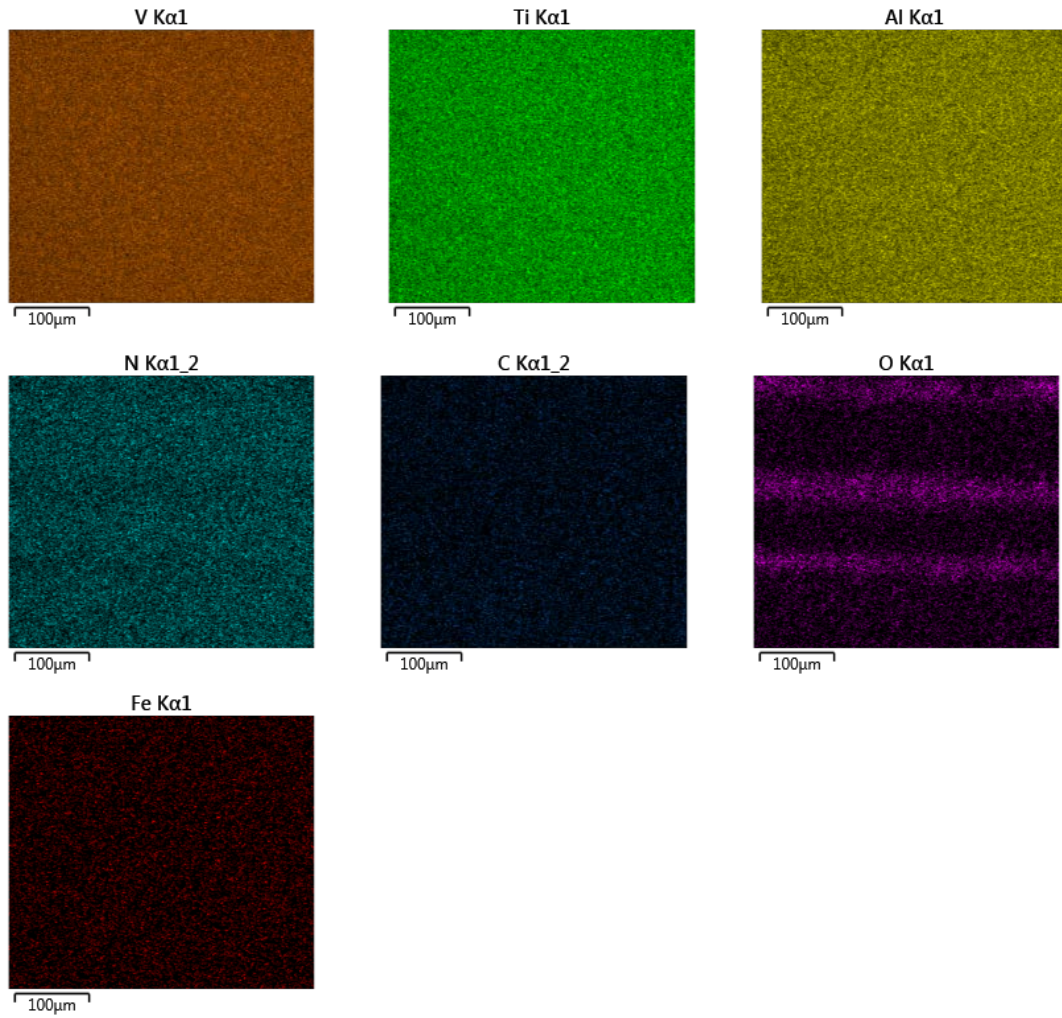
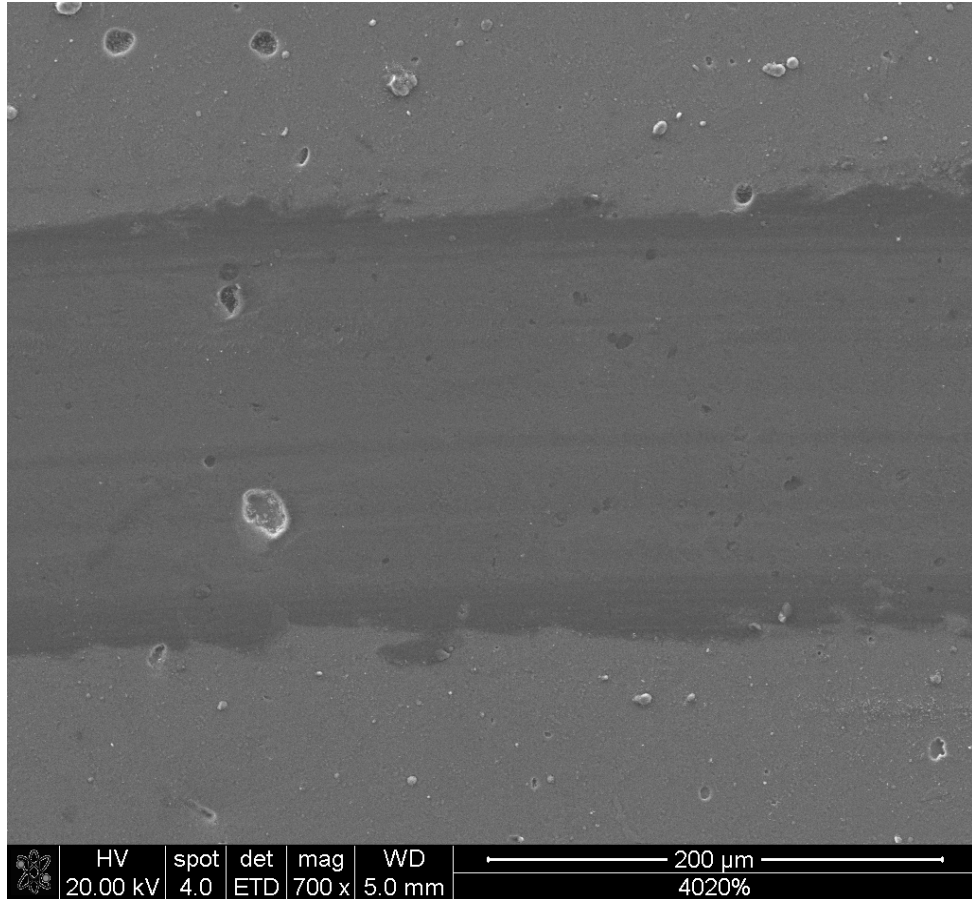


Figure 8.22 The EDX analysis of V, Ti, Al, N, C, Fe, and O elements within the wear track created by room temperature pin on disk testing

**45:20% OES**

Coating 45:20% OES shows excellent lubricant behaviour. The wear track is smooth and similarly, as in 30% OES coatings, a high amount of oxides is observed.



*Figure 8.23 SEM image of the wear track created by room temperature pin on disk testing.*

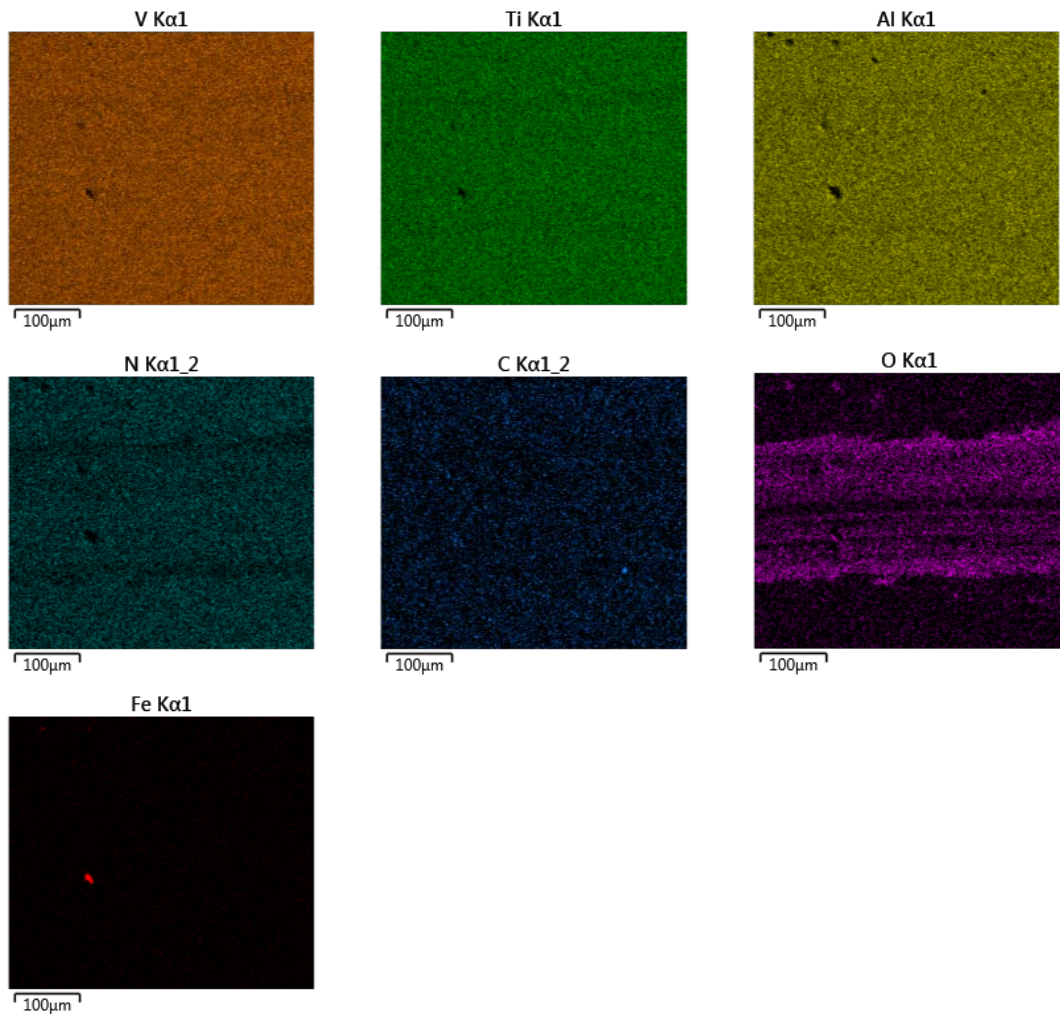


Figure 8.24 The EDX analysis of V, Ti, Al, N, C, Fe, and O elements within the wear track created by room temperature pin on disk testing

## 8.8 Discussion

Lowering the bias voltage in coating 25% OES (B) compared to 25% OES coating causes the columnar structure to change from a [220] orientation to a [200] orientation. This is caused by lowering the kinetic energy of the incoming ions. Low energetic ions lead to loose packing of atoms, causing increased thickness of the coating as well as reduced hardness. The ramping layer introduced between the base layer and the coating provided a gradient change in structure. Lower bias and gradient change of architecture, lead to a better adhesion in both tests when compared with low metal content SNMC. However, adhesion during scratch testing of this coating is relatively low. The pin on

disk test of the 25% OES (B) coating shows excellent performance with low COF and wear rate.

The structure of coating 37/25% OES transitions from a very dense columnar structure to large, loosely packed columns resulting in a faceted surface. Dense structure has a high metal content where columns are more ceramic. Such structure results in a drop of hardness when compared with SNMC deposited at 37% and 25% OES (B). Despite the lower hardness, this coating shows very good tribological behaviour.

Coating 45:20% OES consist of five SNMC layers, transforming from very dense glossy structure to broad, well-defined columns terminating with round tops. However, as can be seen at image 8.15, the transition between 45% OES and 37% OES is very rapid; this may be a reason for low cohesive strength. Additionally, the coating is very thick (over 5  $\mu\text{m}$ ) which may explain the high residual stresses in the coating. Microhardness of the coating is average for ceramic SNMCs. The coating shows good wear properties and good behaviour.

Generally, the friction behaviour is dominated by an oxide tribofilm formation.

The  $I_D/I_G$  ratio has been found in the range of 1.26-1.4 indicating a graphitic nature. The increase in the  $I_D/I_G$  ratio indicates an increase in disorder of the carbon-carbon bonds.

The X-ray diffraction analysis of both SNMC and ANMC suggest that appearance of [111] texture is associated with a faced structure, and [220] with globular. [111] texture is associated with high carbon content in the coating.

The amorphous carbon matrix and hard metal carbide phases results in high hardness and elastic modulus.

The crossectional SEM images revealed structure evolution of ANMC; this changed from a dense, glossy columnar structure to a well-defined facet terminated columns for

coatings 25% OES B, and 37/25% OES and dome terminated columns for coating 45:20 OES.

The cross-sectional SEM images of the coating 25% OES B and 37/25% OES show a columnar structure with voids along the column boundaries. This type of microstructure is attributed to low adatom mobility leading to the shadowing effect. This kind of microstructure is also observed for layers deposited at a low OES signal in coating 45:20 OES.

For coating 37/25%, the columnar structure is relatively dense without any voids along the column boundaries. For coating 25% OES B deposited at -50V bias voltage, a columnar structure with voids along the columnar boundaries is observed.

As the applied substrate bias decreases, the coating structure changes from dense to open columnar microstructure (zone-T in Thornton's Structure Model).

The Raman spectroscopy analysis reveals that contrary to SNMCs, AMSCs are predominated with a disordered carbon structure. The  $I_D/I_G$  ratio of ANMC is  $>1$  indicating higher predominant disorder structure of the carbon phases. The peaks are well distinguished. Raman spectroscopy, together with architecture of the coating, indicates segregation of carbon inbetween columns.

## 8.9 Conclusion

Various poisoning levels, together with the ramping of the signal, were used to deposit ANMCs. The adhesion of the coatings deposited with high reactive gas flow has been improved.  $\Theta$ -2 $\Theta$  XRD measurements revealed that TiAlCN/VCN coatings can exhibit [200] preferred orientation for coatings 25% OES (B) and 37/25% OES coatings. Mixed [111, 200, 222] and [311] texture was observed for the 45:20% OES coating. In ANMC, as OES signal decreases in following layers, a change in stoichiometry can be observed. Near

the base layer, coatings are more metallic and the contents of N and C increase with thickness. In coating 45:20% OES, all individual layers, except layers 25% OES and 20% OES, can be distinct. The change in stoichiometry influences the structure of the coatings. It changes from a dense, glossy coating for 45:20% OES and dense columnar for coating 37/25% OES to broad, distinct columns.

Improvement in adhesion, and the gradual change of the structure, results in very good wear properties of all coatings.

## **9 Effect of Target Poisoning Level on the Tribiological Properties**

In this section, the cutting performance of SNMC and ANMC are tested using high-speed milling. EDX mapping is used to determine the flank wear and the BUE. TiAlCN/VCN coating performance is compared with the standard coating Ti35Al65N.

### **9.1 Overview of the experiments**

Milling tests we performed on a P20 steel bar with a hardness of 48 RC using a high-speed milling machine (MAZAK FJV-25). The cutting performance of the coated inserts was tested in comparison with a cemented carbide insert; this was coated with a standard coating (Ti35Al65N). The cutting conditions were as described in section 3.5.10.

After the cutting test, a post mortem analysis of each insert was performed. Both rake and flank sides of the inserts were analysed after the maximum number of passes. The failures of the coatings were investigated with EDX spectroscopy and SEM microscopy using BS and SE modes. The EDX spectroscopy was used for elemental mapping of coating and substrate chemical composition. Iron and oxygen were also mapped in order to determinate BUE. With this method, the borders between exposed substrates, coatings and BUE can easily be distinguished.

## 9.2 Flank Wear of Inserts

The cutting tests were performed on all coatings except the coating deposited at 45% OES; this was due to its low adhesion and very poor tribological behaviour as discussed in section 7.6 Wear Resistance – Pin on Disk. The failure of the coating was established when substrate was revealed and/or wear reached pre-defined criteria of 0.13 mm. The results of cutting tests for several inserts are shown in Fig. 9.1 as flank wear against the number of passes. Each pass is equal to a cutting distance of 33 mm. Some of the tests were performed in the same year of the deposition whilst some were performed after approximately one year. It can be noticed that tests are not repeatable. This can be an effect of variation in the batch.

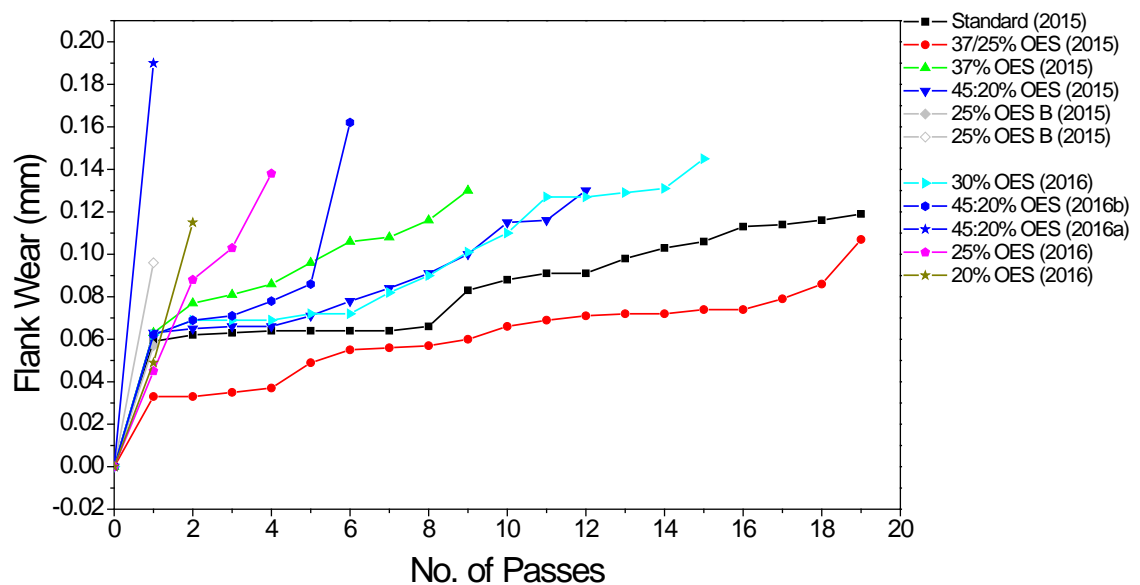


Figure 9.1 Flank wear of coated inserts plotted against number of passes (1 pas = 33 mm) in milling P20 steel.

The tool life of the insert coated with standard coating was 19 passes. The flank wear stays constant up to 8 passes at 0.06 mm; following this, the wear rapidly increases and continues to increase to 0.12 mm. The insert coated with 25% OES (B), despite good performance during pin on disk test, failed after only one pass. In order to eliminate insert failure, this coating was tested twice. Inserts coated with low metal SNMC

survived only 2 and 4 passes for 20 and 25% OES respectively. The insert coated with coating 37% OES failed after 12 passes. The flank wear increase was high and increased linearly from the first pass to 0.13 mm. The best of SNMC coated insert was insert coated with 30% OES which survived 15 passes. The flank wear stays relatively constant up to 7 passes at 0.082 mm. After 7 passes, the flank wear increases up to 0.127 mm after 13 passes; following this, the flank wear increase slows down.

The advanced architecture coatings were 12 passes for 45:20% OES coated insert and 19 passes for 37/25% OES coated insert. After 4 passes, the flank wear of insert coated with 45:20% OES was at the same level as the insert coated with the standard coating. The flank wear increased up to 0.13 mm after 12 passes. For coating 45:20% OES, tests were repeated 1 year after the deposition and coating showed worse performance with only 1 and 6 passes. Coating 37/25% OES shows the lowest flank wear. For 4 passes it stayed constant at 0.03 mm; after this it slowly increased to 0.08 mm. The last two passes increased flank rate to 0.11 mm after leading to coating failure.

## 9.3 Post Mortem analysis

### Standard Coating

The standard coating survived 19 passes. The SEM and EDX images of flank and rake of the insert coated with standard coating are given in Fig 9.2 and 9.3

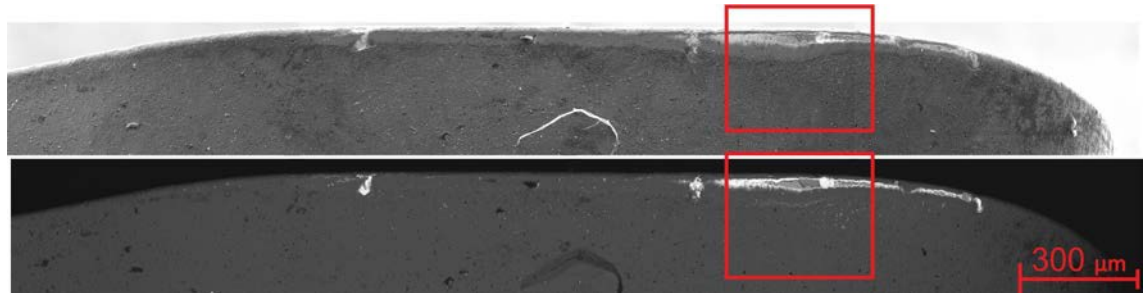
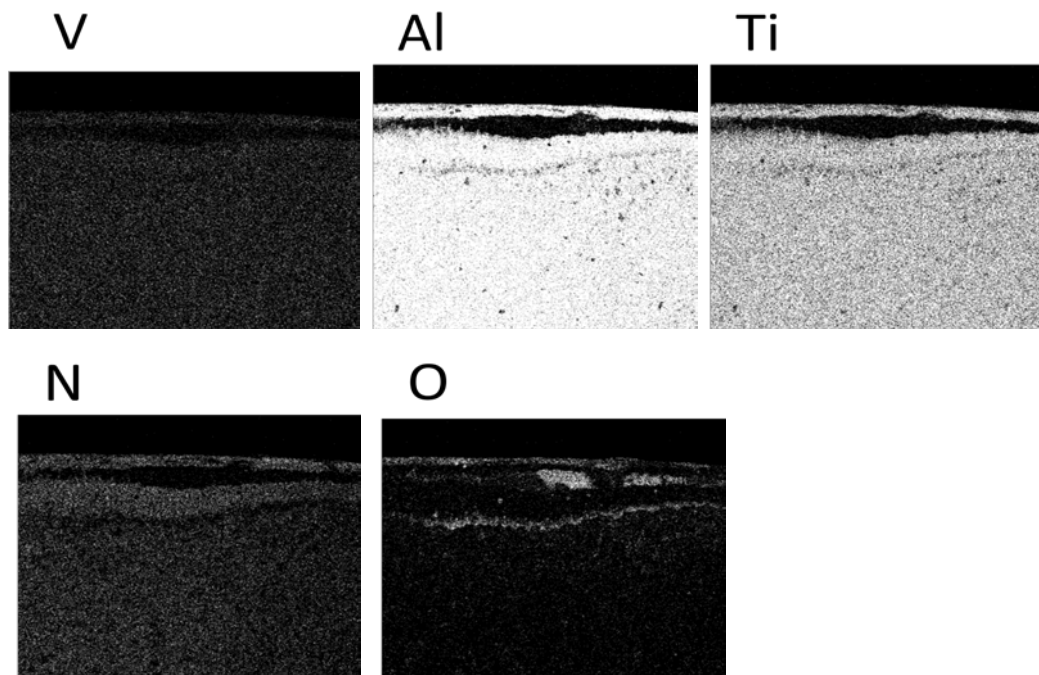


Figure 9.2 SE (top) and BS (bottom) SEM image of insert flank coated with the standard coating after 19 passes on the P20 steel bar



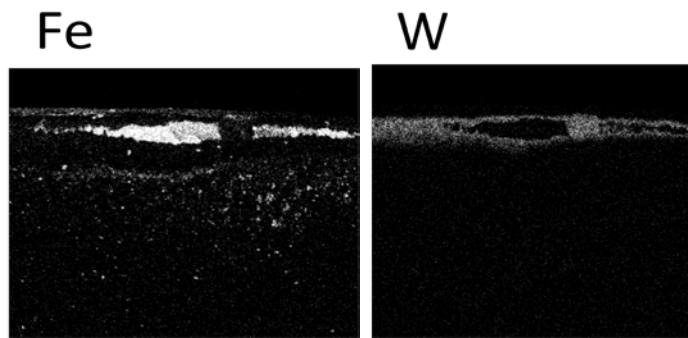


Figure 9.3 The EDX analysis of V, Ti, Al, N, C, O, Fe, and W elements within the wear Scar created by milling in P20 steel bar. The presence of the FE indicates BUE creation; presence of the W – exposure of the substrate.

The dominant failure, at the flank is the abrasive wear. The coating has been worn off and the substrate has been exposed. The abrasive scar is 120  $\mu\text{m}$  wide and substrate exposure is 50  $\mu\text{m}$  wide. A small chipped off area can be observed (a, b) which indicates adhesive failure. The EDX analysis revealed presence of BUE inside the abrasive scar as well on top of the coating. BUE inside the scar is continuous and dense, while at the coating there are separated spots, distributed over 200  $\mu\text{m}$ . The high oxygen area is overlapping with BUE, indicating the creation of Iron oxides.

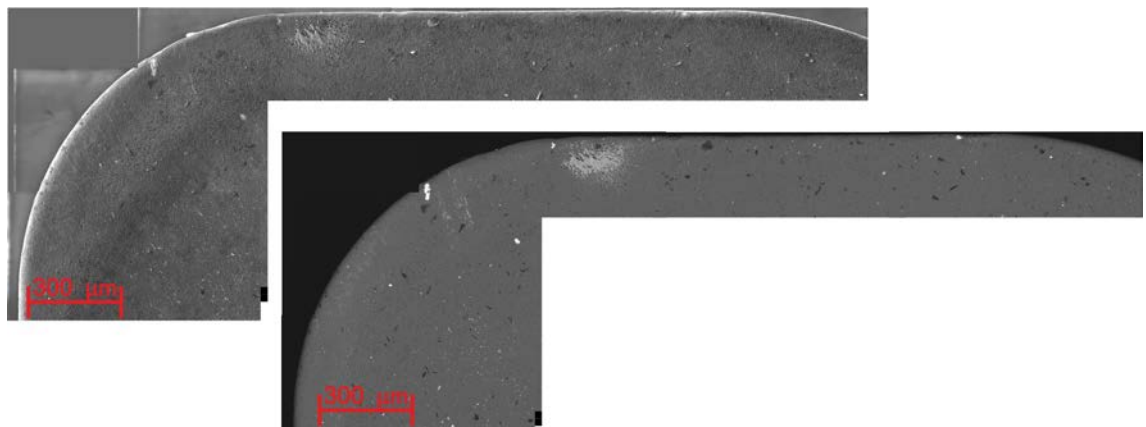


Figure 9.4 SE (top) and BS (bottom) SEM image of insert rake coated with the standard coating after 19 passes on the P20 steel bar

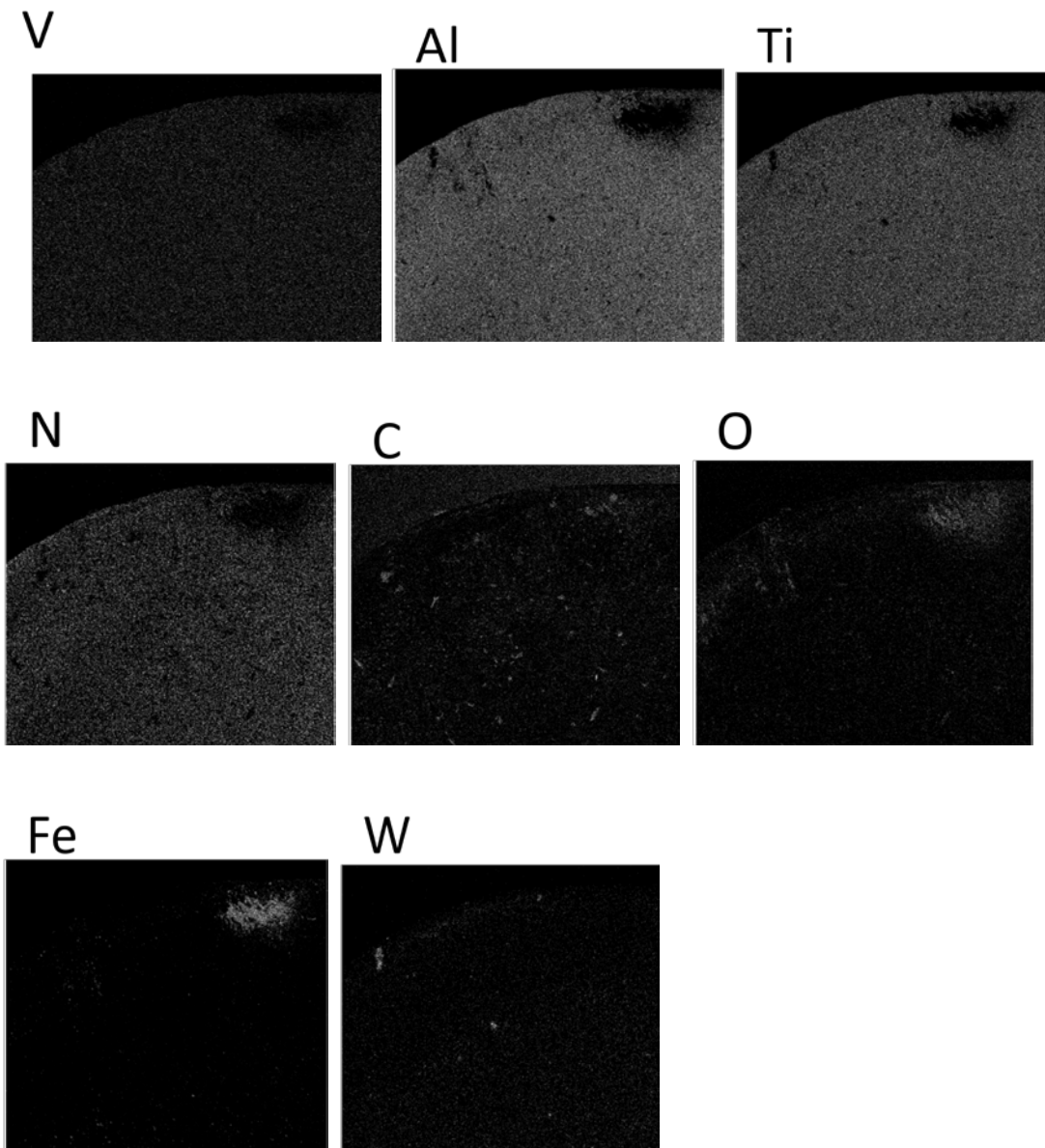


Figure 9.5 The EDX analysis of V, Ti, Al, N, C, O, Fe, and W elements within the wear Scar created by milling in P20 steel bar. The presence of the FE indicates BUE creation; presence of the W – exposure of the substrate.

At the rake the dominant failure is BUE. The BUE is accumulated in one part of the rake for all inserts. This must be caused by the geometry of the insert. There is also some chipping due to adhesive failure.

### Coating 25% OES B

Coating 25% OES B failed after one pass. There was a big adhesive failure both on flank and rake which is shown in fig. 9.6 and fig.9.7. The coating on the flank was

peeled off in two chips c.a. 70  $\mu\text{m}$  radius. They resulted in a large chip on the rake exposure the insert up to 300  $\mu\text{m}$  from the edge.

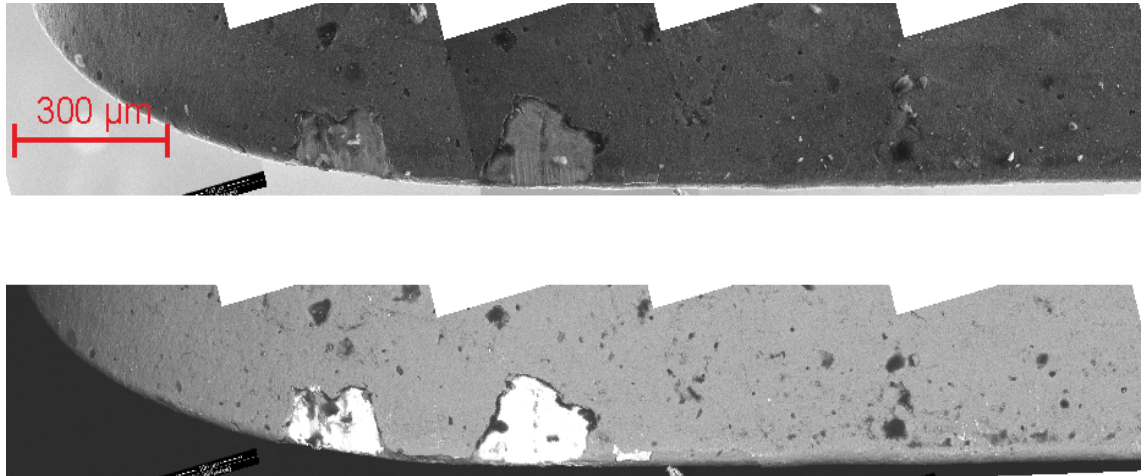


Figure 9.6 SE (top) and BS (bottom) SEM image of insert flank coated with the 25% OES (B) coating after 1 pass on the P20 steel bar

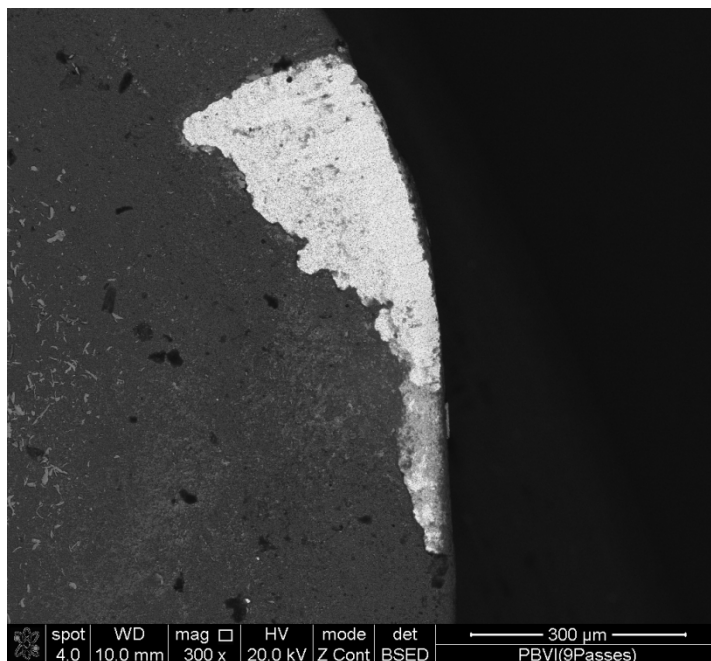


Figure 9.7 SE (top) and BS (bottom) SEM image of insert rake coated with the 25% OES (B) coating after 1 pass on the P20 steel bar

## Coating 25% OES

Coating 25% OES failed after two passes. The SEM imaging shows that adhesive failure at the flank that the main failure occurs between the base layer and the TiAlCN/VCN multilayer coating. The thin VN base layer is also worn trough. At the rake the substrate is exposed the edge, which is related to the flank failure. The BUE is observed in two areas.

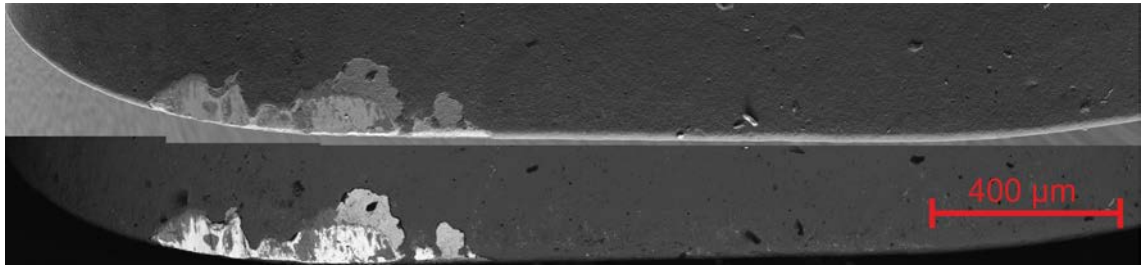


Figure 9.8 SE (top) and BS (bottom) SEM image of insert flank coated with the 25% OES coating after 2 passes on the P20 steel bar

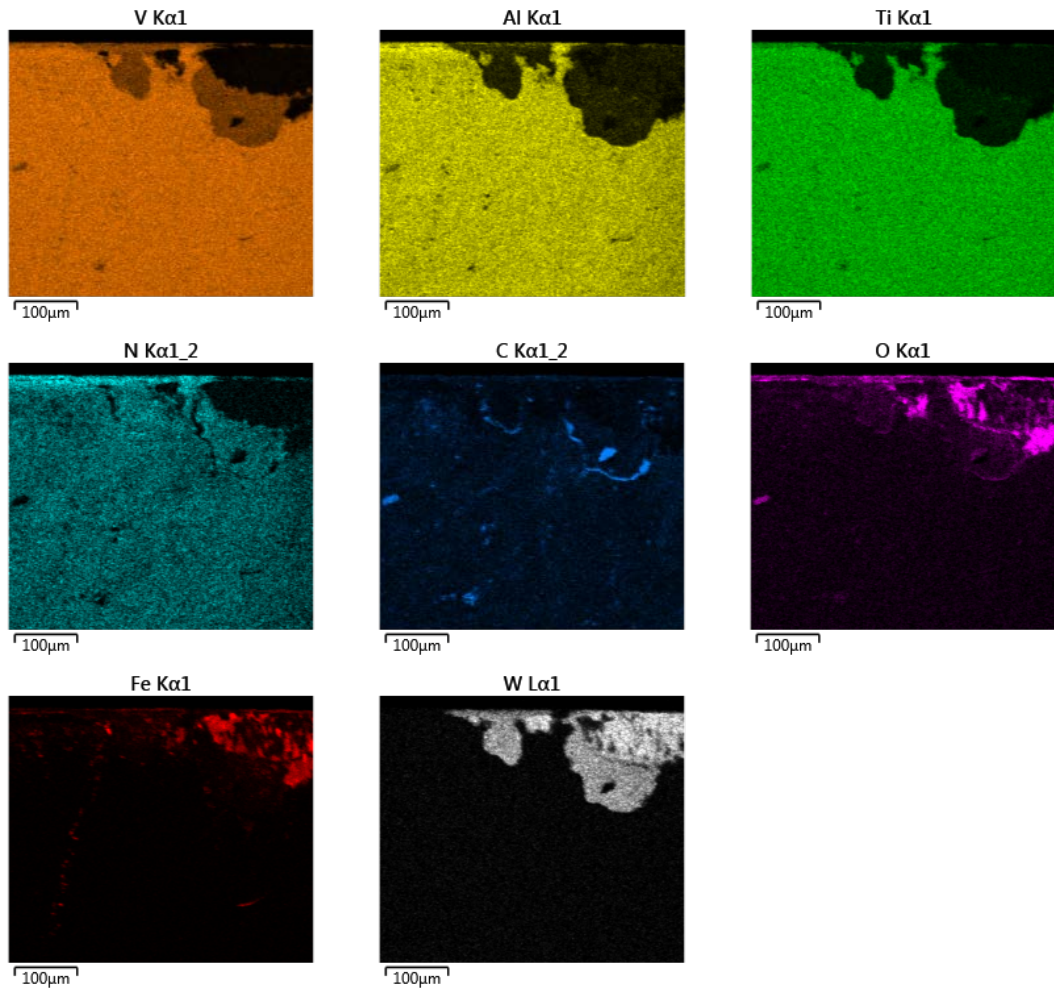
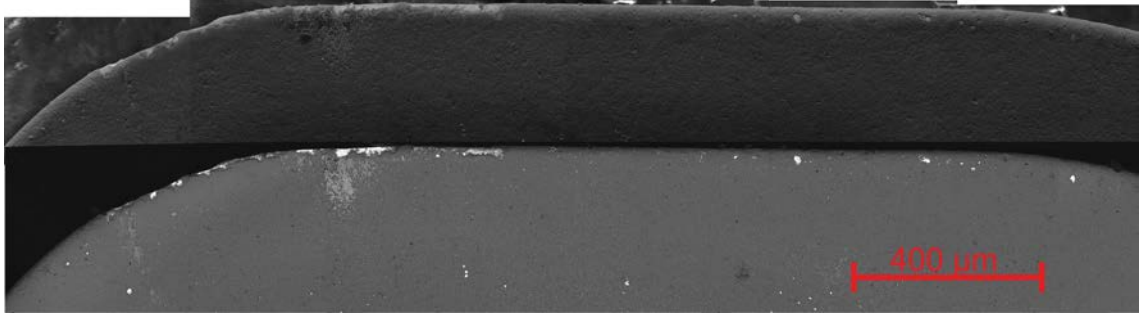


Figure 9.9 The EDX analysis of V, Ti, Al, N, C, O, Fe, and W elements within the wear Scar created by milling in P20 steel bar. The presence of the FE indicates BUE creation; presence of the W – exposure of the substrate.



*Figure 9.10 SE (top) and BS (bottom) SEM image of insert rake coated with the 25% OES coating after 2 passes on the P20 steel bar*

## Coating 20% OES

Coating 20% OES failed after 4 passes. Similarly as for the coating 25% OES, an adhesive failure occurred between the base layer and the TiAlCN/VCN multilayer coating. There is no visible failure on the rake. Also no BUE has been observed.

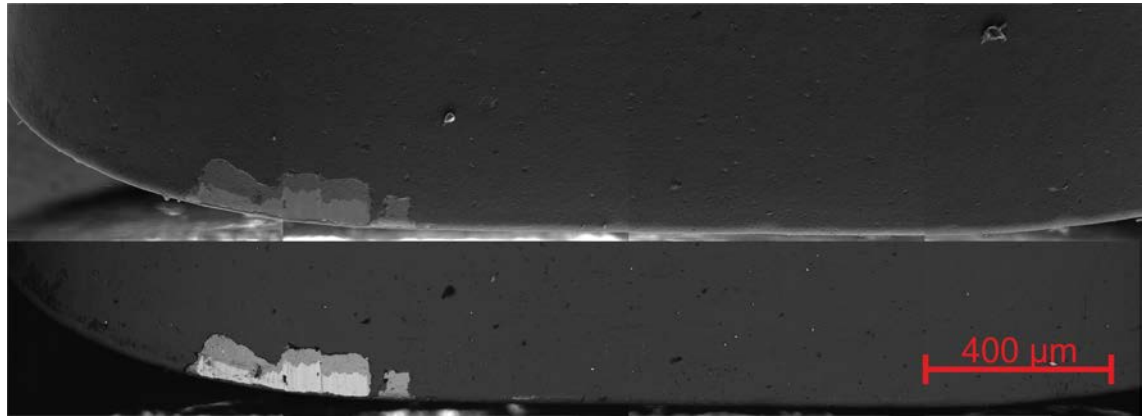
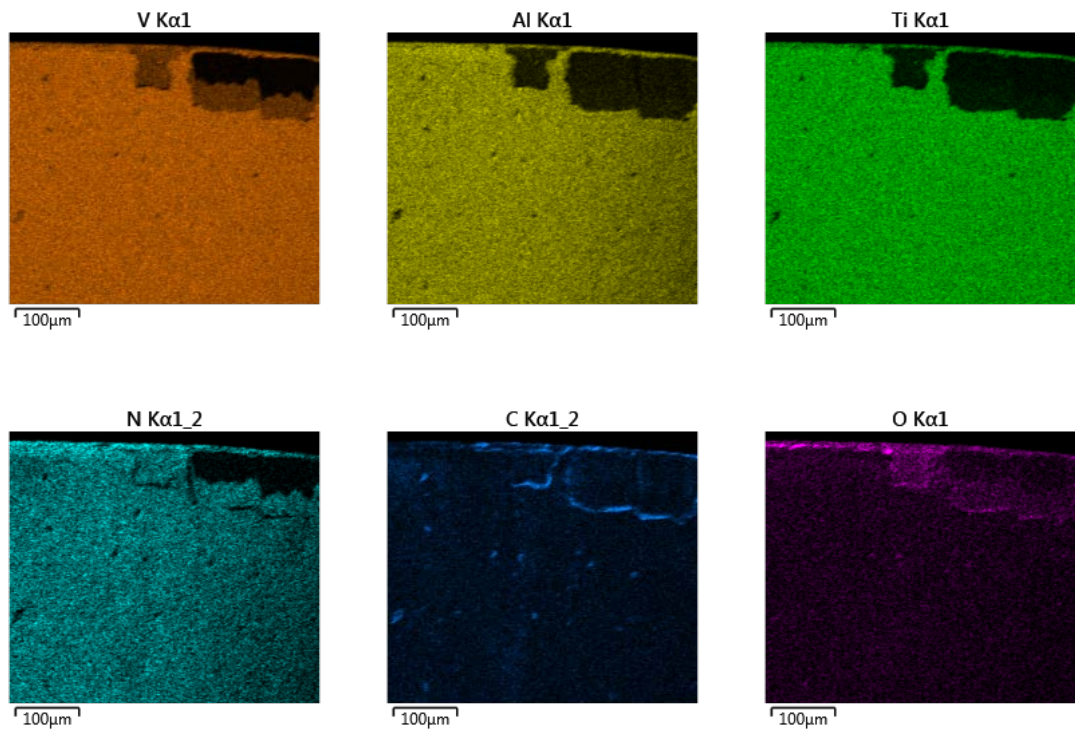


Figure 9.11 SE (top) and BS (bottom) SEM image of insert flank coated with the 20% OES coating after 4 passes on the P20 steel bar



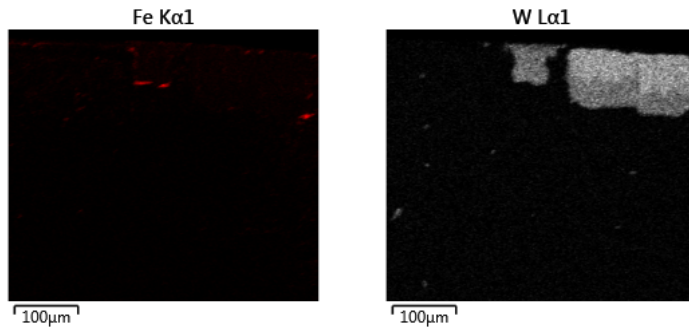


Figure 9.12 The EDX analysis of V, Ti, Al, N, C, O, Fe, and W elements within the wear Scar created by milling in P20 steel bar. The presence of the FE indicates BUE creation; presence of the W – exposure of the substrate.

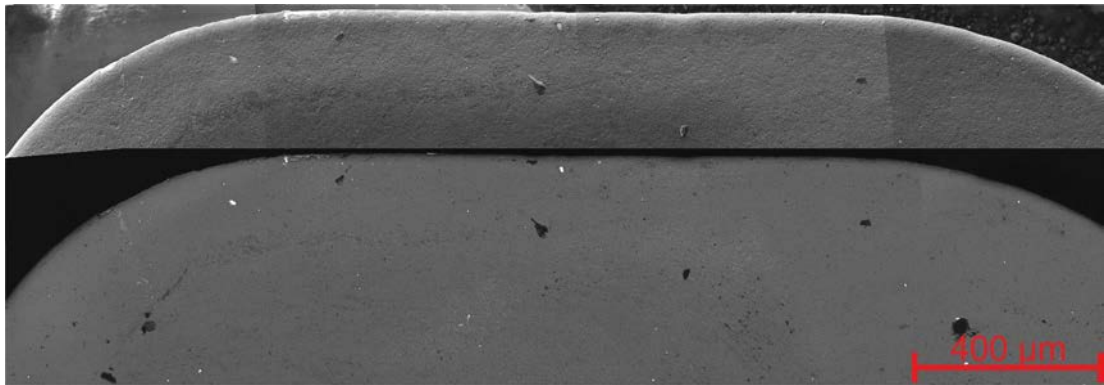
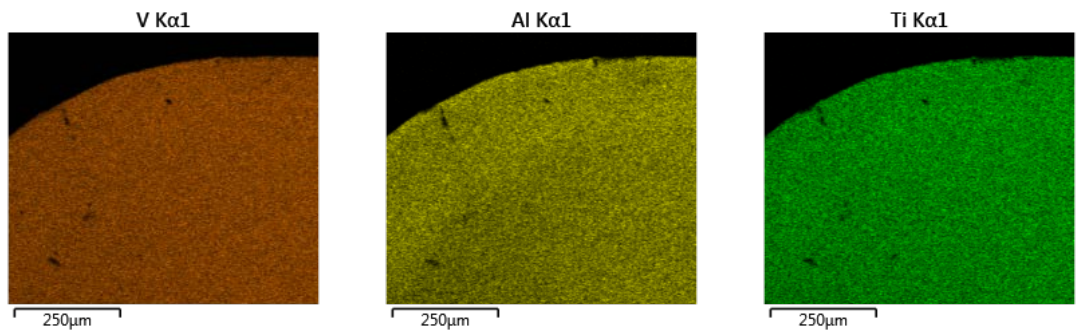


Figure 9.13 SE (top) and BS (bottom) SEM image of insert rake coated with the 20% OES coating after 4 passes on the P20 steel bar



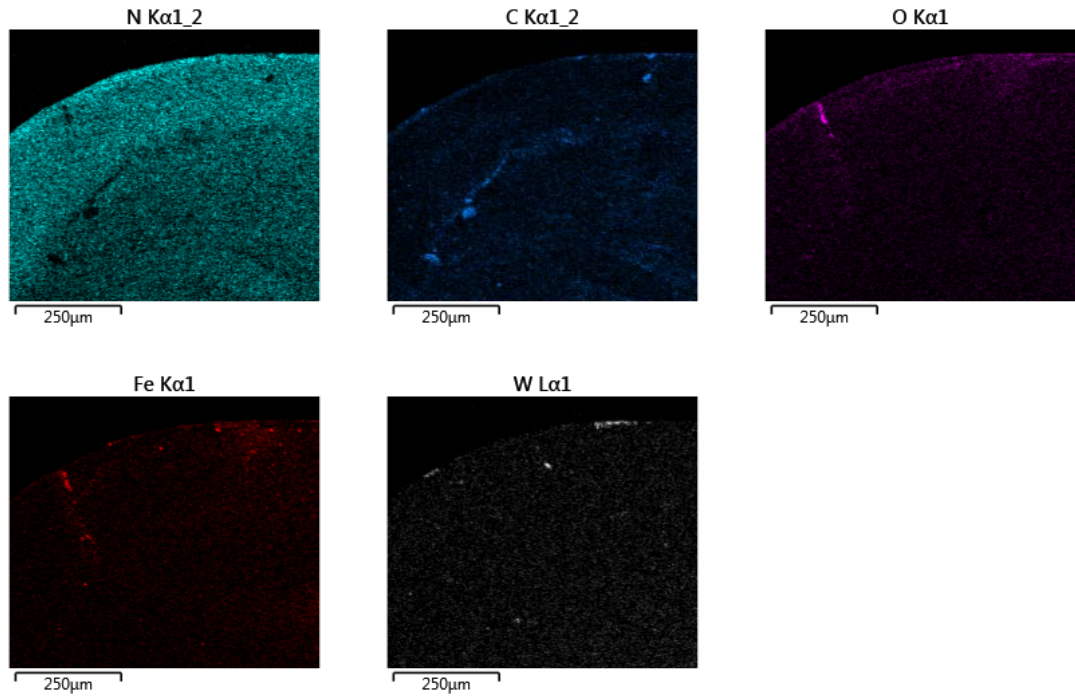


Figure 9.14 The EDX analysis of V, Ti, Al, N, C, O, Fe, and W elements within the wear Scar created by milling in P20 steel bar. The presence of the FE indicates BUE creation; presence of the W – exposure of the substrate.

## Coating 37% OES

Coating 37% OES failed after 9 passes. As shown in fig. 9.19 and fig. 9.20, the main wear mechanism was abrasive wear that left the scar as ca 0.25 mm wide. However, substrate is only exposed at the cutting edge. There is also some chipping due to adhesive failure. The EDX analysis shows that there is low BUE in the form of small, separated spots. The high amount of oxygen indicates creation of oxides. It can be noticed all over the coating and accumulated at the edge of the coating scar as well as at the cutting edge.

At the rake the BUE is dense and accumulated in one place. No abrasive wear is noticed. The EDX shows a small area where the coating was chipped off. There is high carbon contamination around BUE. Oxides are created all over the coating. However, there is higher accumulation near to BUE area; this may indicate higher rubbing against the work piece around this area.

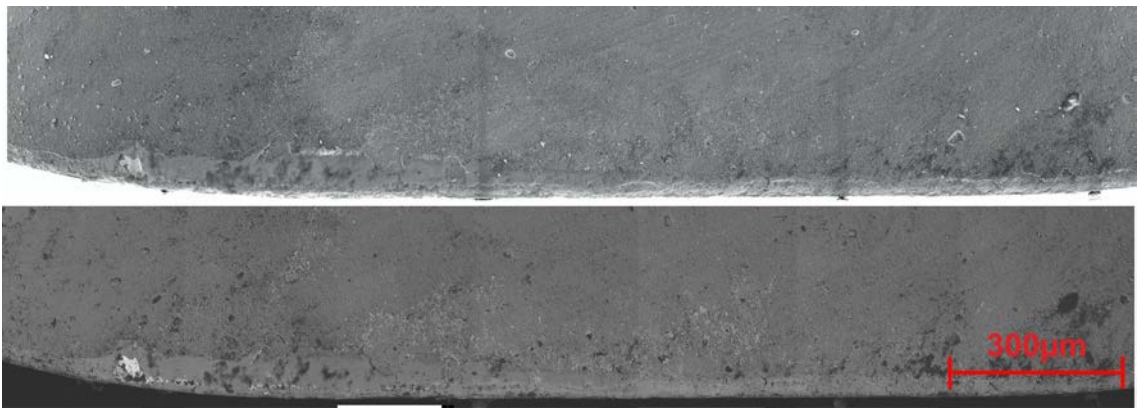


Figure 9.19 SE (top) and BS (bottom) SEM image of insert flank coated with the 37% OES coating after 9 passes on the P20 steel bar

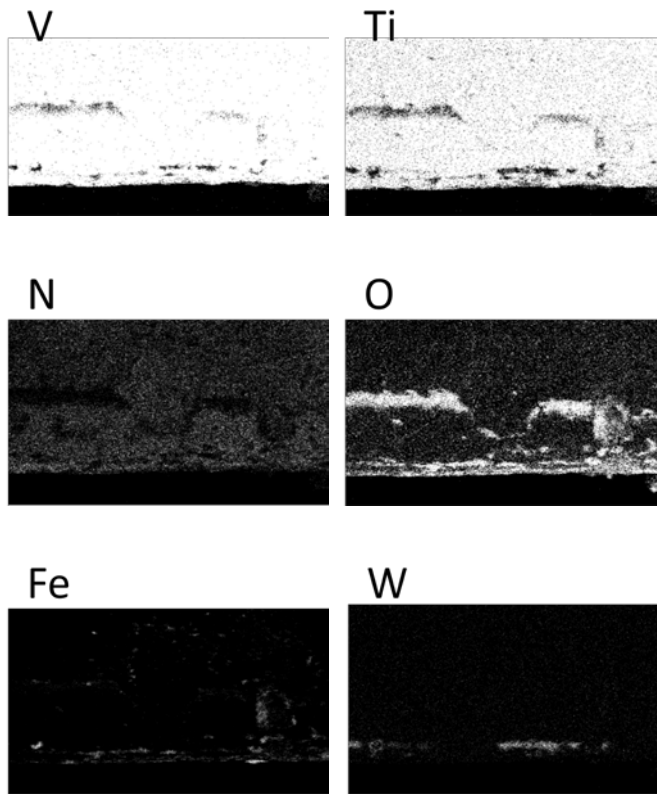


Figure 9.20 The EDX analysis of V, Ti, Al, N, C, O, Fe, and W elements within the wear Scar created by milling in P20 steel bar. The presence of the FE indicates BUE creation; presence of the W – exposure of the substrate.

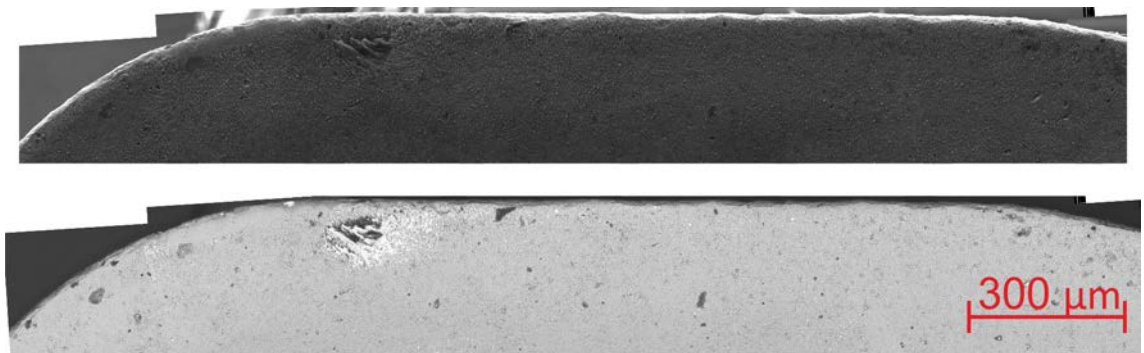


Figure 9.21 SE (top) and BS (bottom) SEM image of insert rake coated with the 37% OES coating after 9 passes on the P20 steel bar

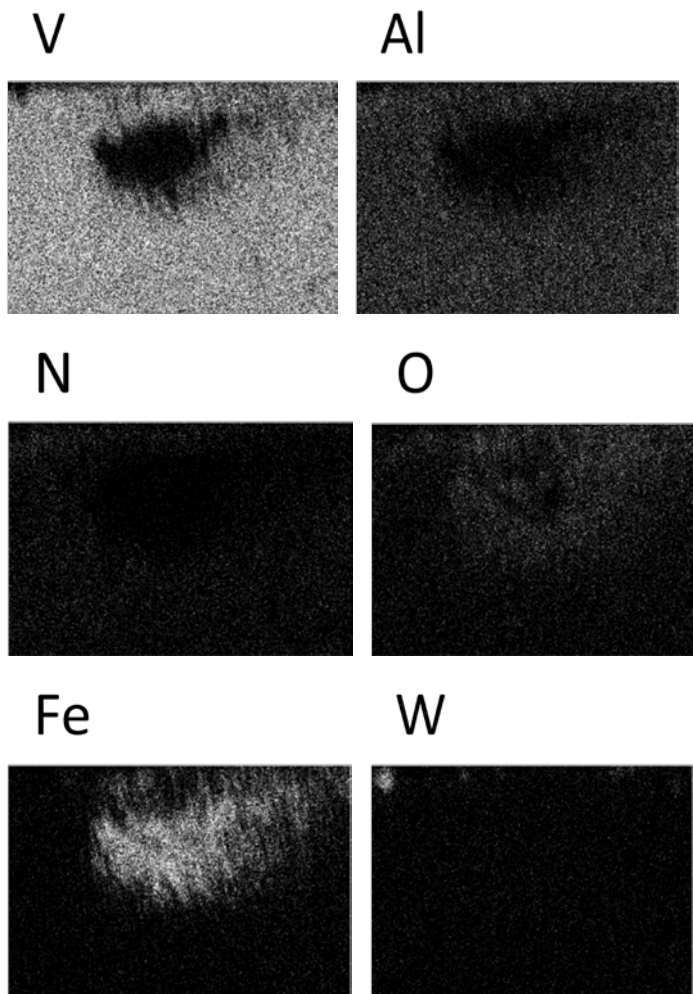


Figure 9.22 SE (top) and BS (bottom) SEM image of insert rake coated with the 37% OES coating after 9 passes on the P20 steel bar

### Coating 45:20% OES

Coating 45:20% OES failed after 12 passes. There is low abrasive wear and low BUE formation. Two craters can be observed; failure in these areas is adhesive and cohesive chipping of the coating. The craters are a consequence of adhesive failure at the rake. As figure 9.23 and fig. 9.24 show the failure progressive within the crater, increasing the crater depth. However, new craters didn't form. The BUE forms in small disconnected regions. The EDX shows oxides created at the cutting edge and a layer of about 100  $\mu\text{m}$ ; this is 100  $\mu\text{m}$  away from the cutting edge. Within this layer, a small amount of Al and Ti is observed.

On the rake, a large chipped area is observed; this caused the adhesion failure. A small amount of BUE is visible.

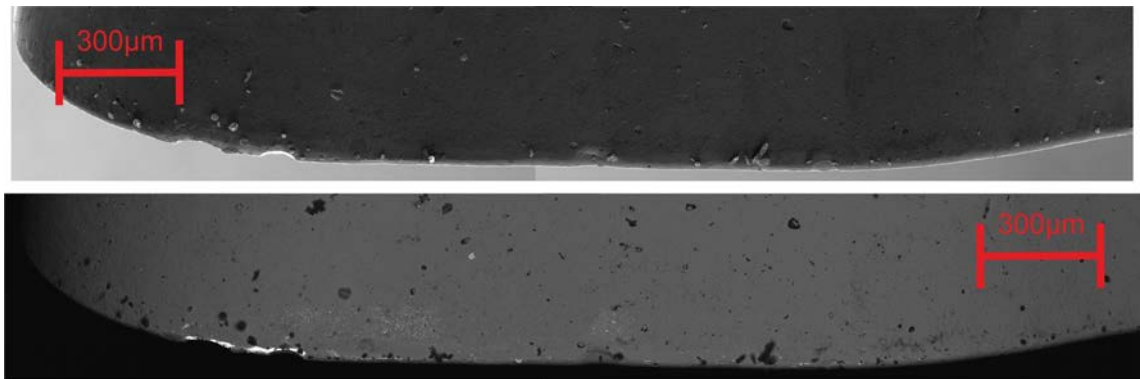
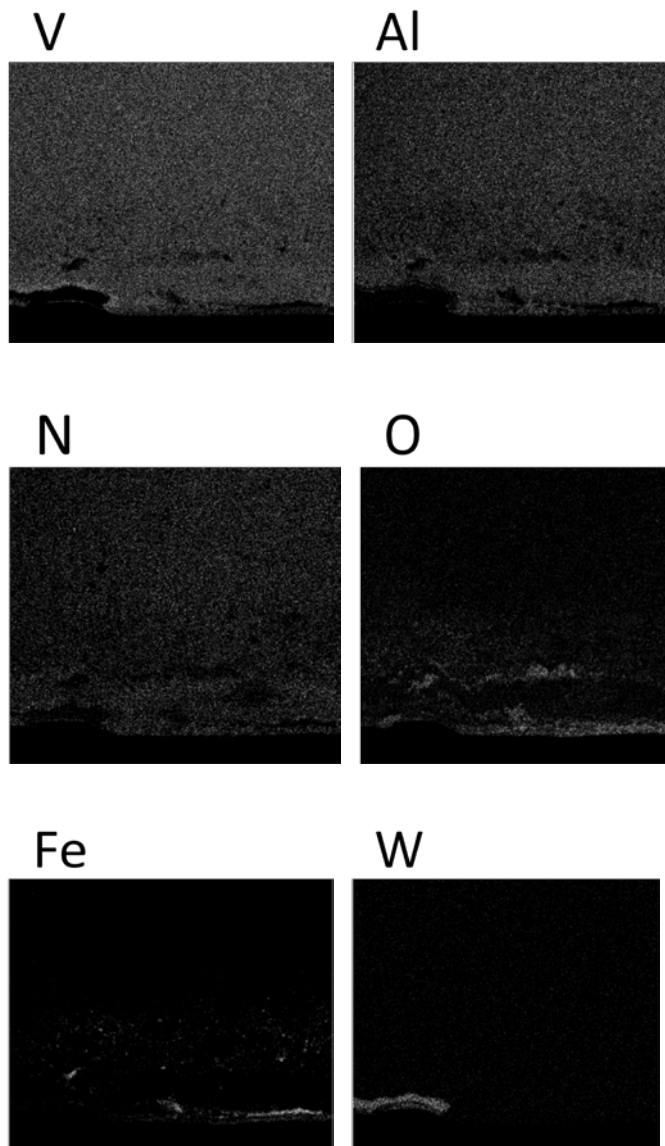


Figure 9.23 SE (top) and BS (bottom) SEM image of insert flank coated with the 45:20% OES coating after 12 passes on the P20 steel bar



*Figure 9.24 The EDX analysis of V, Ti, Al, N, C, O, Fe, and W elements within the wear Scar created by milling in P20 steel bar. The presence of the FE indicates BUE creation; presence of the W – exposure of the substrate.*

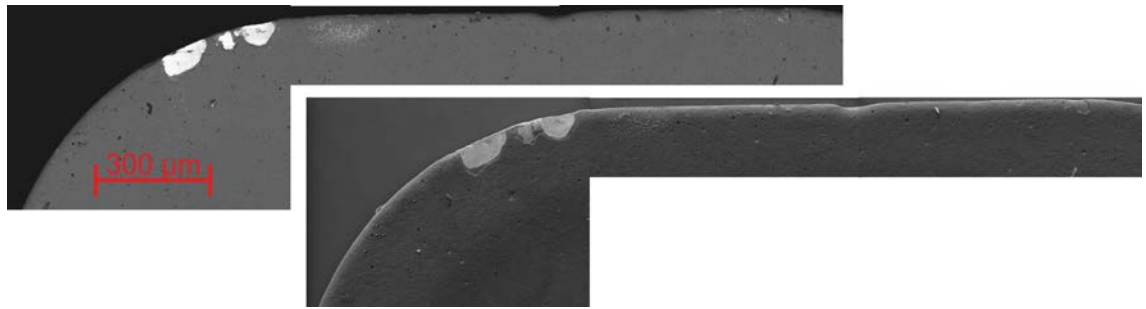


Figure 9.25 SE (top) and BS (bottom) SEM image of insert rake coated with the 45:20% OES coating after 12 passes on the P20 steel bar

### Coating 30% OES

Coating 30% OES failed after 15 passes due to exposure of the substrate. The main failure is abrasive wear. There is no BUE observed at the flank. The substrate has been exposed.

On the rake a small BUE is observed and a small abrasive wear at the edge

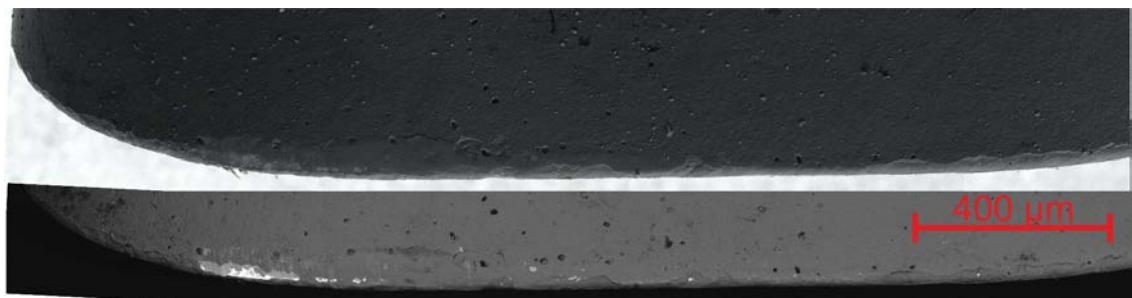
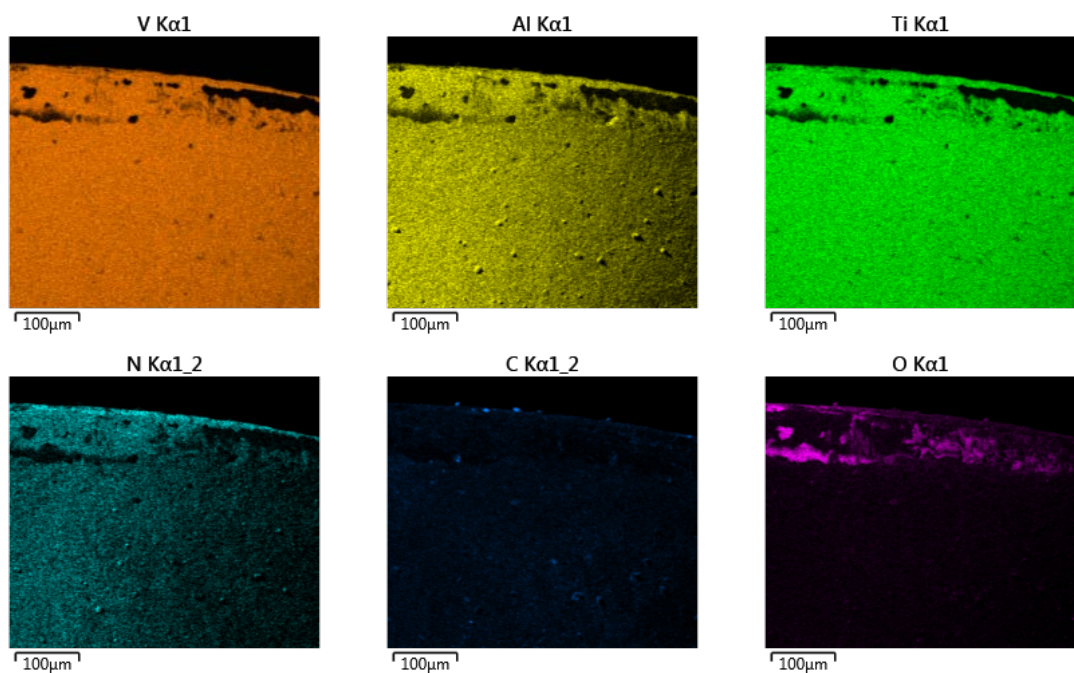


Figure 9.15 SE (top) and BS (bottom) SEM image of insert flank coated with the 30% OES coating after 15 passes on the P20 steel bar



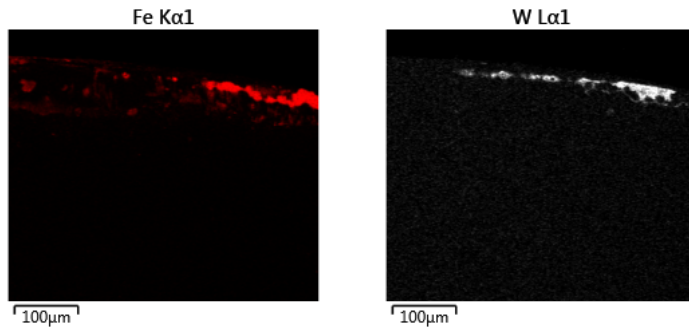


Figure 9.16 The EDX analysis of V, Ti, Al, N, C, O, Fe, and W elements within the wear Scar created by milling in P20 steel bar. The presence of the FE indicates BUE creation; presence of the W – exposure of the substrate.

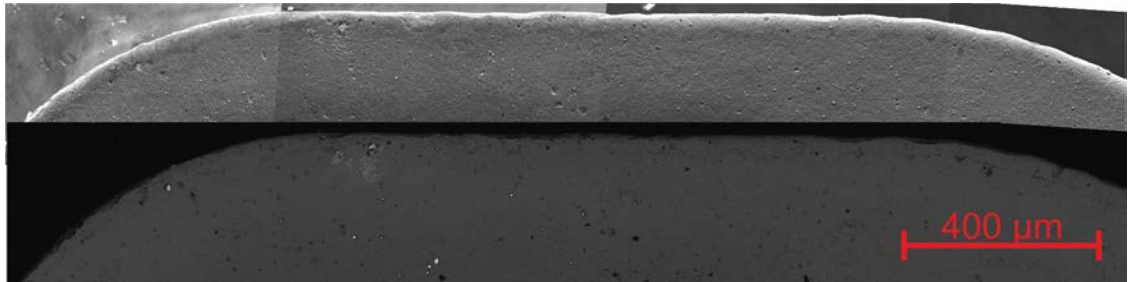


Figure 9.17 SE (top) and BS (bottom) SEM image of insert rake coated with the 30% OES coating after 15 passes on the P20 steel bar

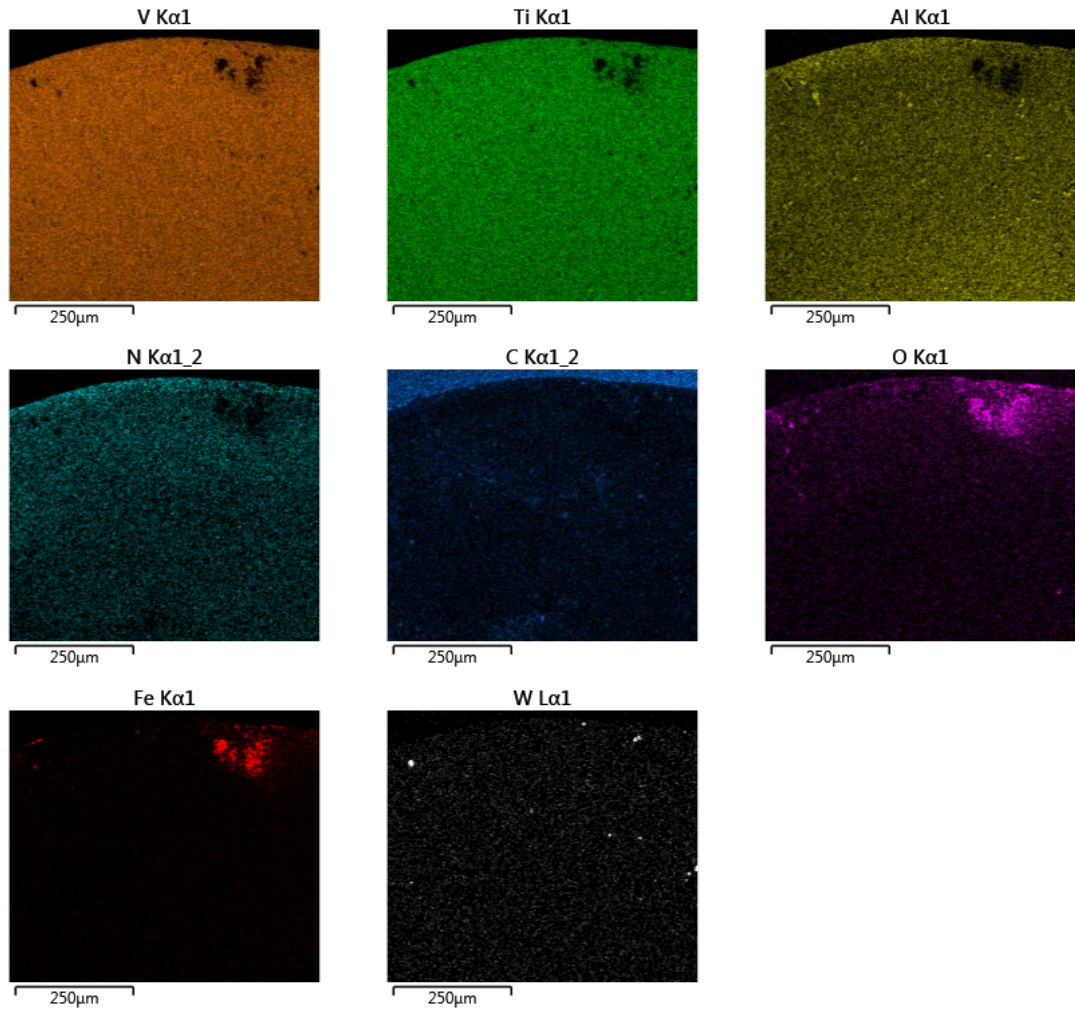


Figure 9.18 The EDX analysis of V, Ti, Al, N, C, O, Fe, and W elements within the wear Scar created by milling in P20 steel bar. The presence of the FE indicates BUE creation; presence of the W – exposure of the substrate.

### Coating 37/25% OES

The dominant failure at the flank is the abrasive wear. Also, adhesive failure can be observed as the coating chipped off. The abrasive scar is c.a. 75  $\mu\text{m}$  wide and substrate exposure is 10  $\mu\text{m}$  wide. The EDX analysis revealed trace presence of BUE at the cutting edge and inside at the exposed substrate coating. The high oxygen area is overlapping with BUE, indicating the creation of iron oxides.

At the rake, the dominant failure is adhesive and no abrasive wear is noticed. BUE is accumulated in one place. It is dense but small when compared with coating 37% OES and Standard. The oxides cover the whole area of the coating.

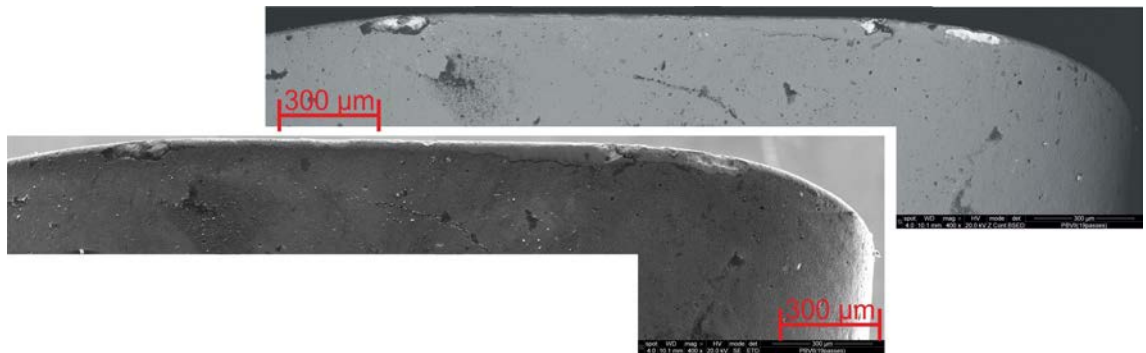
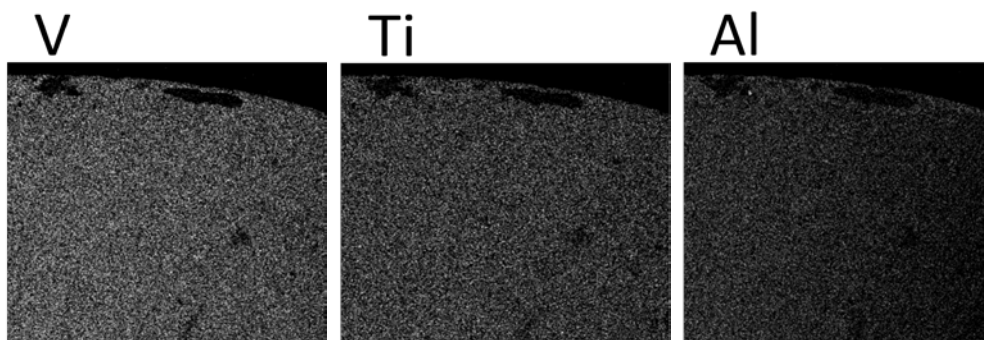


Figure 9.26 SE (top) and BS (bottom) SEM image of insert flank coated with the 37/25% OES coating after 19 passes on the P20 steel bar



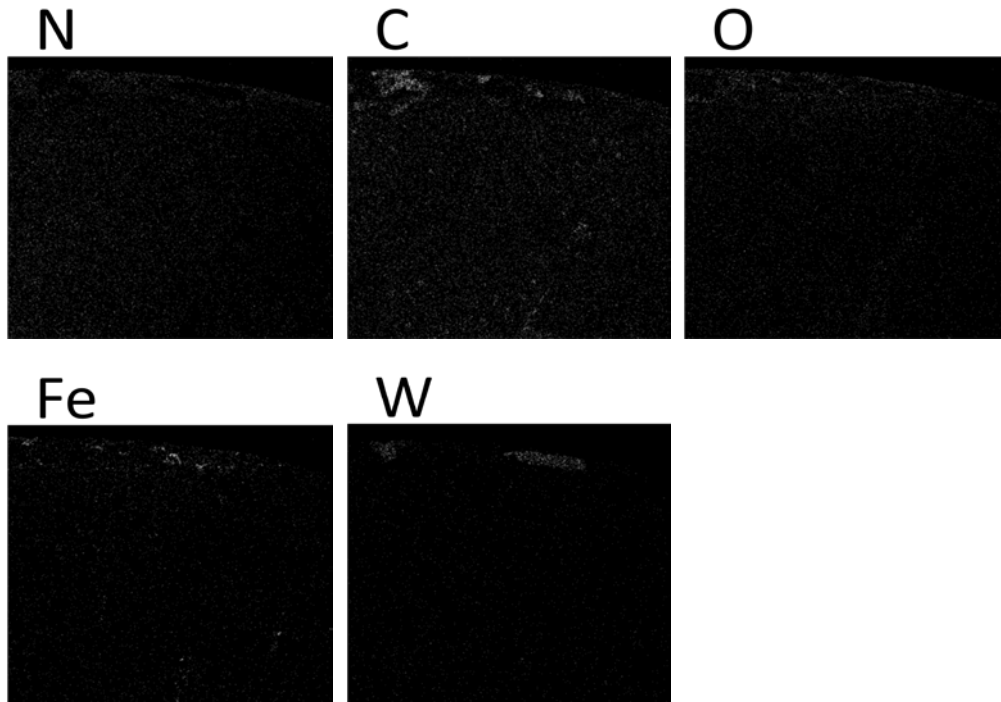


Figure 9.27 The EDX analysis of V, Ti, Al, N, C, O, Fe, and W elements within the wear Scar created by milling in P20 steel bar. The presence of the FE indicates BUE creation; presence of the W – exposure of the substrate.

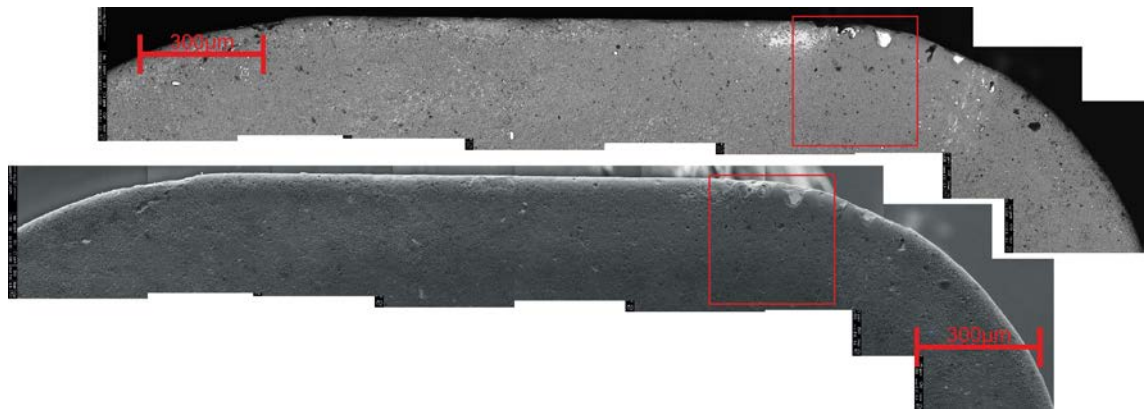


Figure 9.28 SE (top) and BS (bottom) SEM image of insert rake coated with the 37/25% OES coating after 19 passes on the P20 steel bar

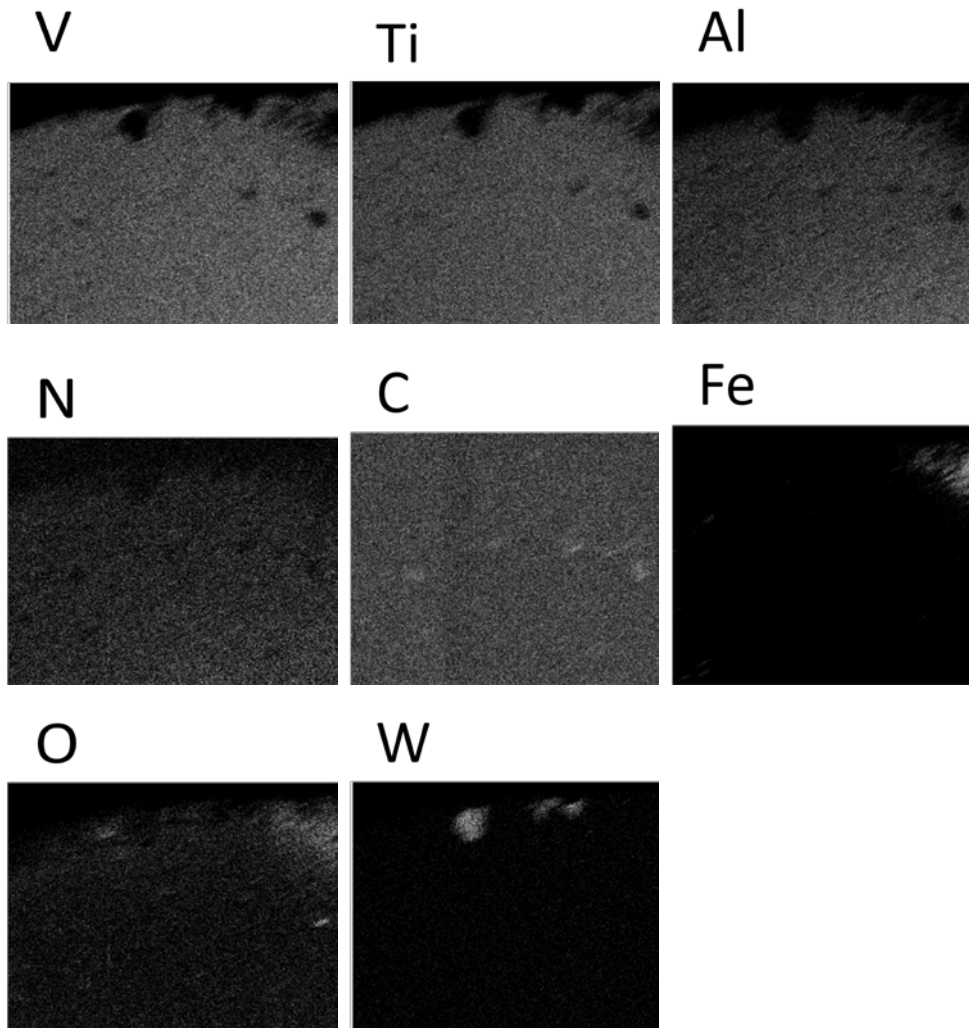
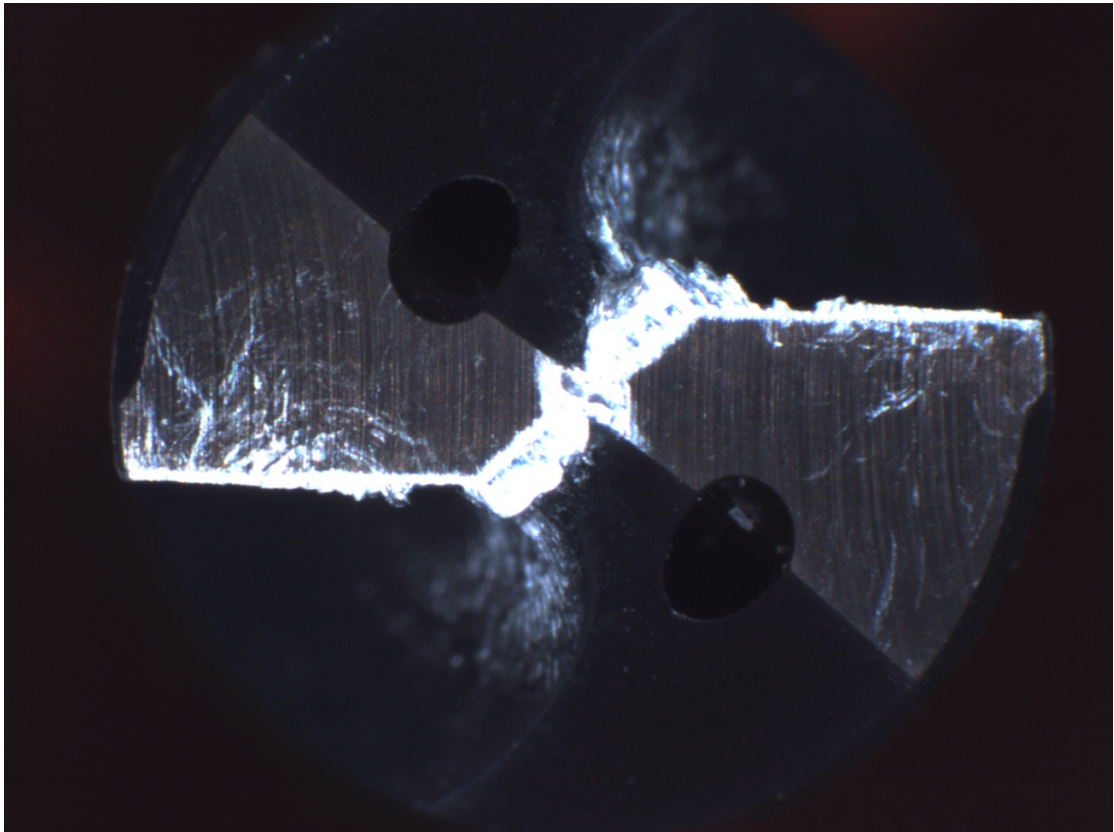


Figure 9.29 The EDX analysis of V, Ti, Al, N, C, O, Fe, and W elements within the wear Scar created by milling in P20 steel bar. The presence of the FE indicates BUE creation; presence of the W – exposure of the substrate.

## 9.4 Drilling Test of coating deposited at 45:20%

To study the coating - work piece material interaction of TiAlCN/VCN coating deposited at 45:20% OES drilling experiment was conducted at Sandvik Coromant, Sheffield. The test was performed on 2024 grade aluminium which proved to be challenging for machining. Testing was stopped after 290 holes were drilled due to a considerable build-up of aluminium; this can be seen in figure 8.30. The tool life is considered to be similar in standard to titanium diboride coatings, however, through the combination of an optimised geometry and coating chemistry, it is possible to improve the lifetime of the tool fourfold.



*Figure 8.30 Top view of coated drill after drilling 290 holes in aluminium. The BUE is visible at the cutting edges.*

## 9.5 Discussion

Contrary to laboratory tests, coating 25% OES B failed the milling tests. This might be a result of the impact during approaching the insert to the metal bar.

Coating 45:20% OES shows very good properties to prevent BUE creation. The BUE is located only at the rake of the tool and on the exposed substrate. After 12 passes no abrasive wear is observed, this shows very good wear/shear properties, this can be attributed to high levels of lubricious oxides which can be observed both at the Insert as well as in the wear track. Tests had to be stopped due to adhesive failures which were also identified during scratch testing. Following improvement of the coating, the adhesion should be tested on the aluminium alloys.

The coating deposited at 37/25% OES failed after the same number of passes as a standard coating. However, the abrasive scar is narrower and less substrate has been exposed. The BUE is very small when compared with the Standard coating with considerable high BUE creation. This will result in an improved surface finish. Since the coating shows good wear behaviour and low BUE creation, it can be tested on the aluminium alloys.

## 9.5 Conclusion

SNMC and ANMC coatings have been tested in the dry milling. Table 9.1 shows summary of the tests.

*Table 9.1 Summary of failure mechanisms of the SNMC and ANMC TiAlCN/VCN coating, during cutting tests in P20 steel bar*

Coating ID	Max. No. of Passes	Flank failure	Rake failure
Standard	19	Abrasive, Adhesive, BUE	BUE Small adhesive
20% OES	4	Adhesive to base layer	
25% OES	2	adhesive to base layer	BUE
30% OES	15	Abrasive	Small BUE
37% OES	9	Abrasive, Adhesive	Abrasive, BUE
25% OES (B)	1	Adhesive	Adhesive
37/25% OES	19	Adhesive, BUE	Adhesive BUE
45:20% OES	12	Abrasive, Adhesive	Abrasive Adhesive

## Summary

This thesis consists of broad spectrum development of TiAlCN/VCN coatings. The investigation can be divided in three main fields: Effect of plasma etching, Effect of the Target Poisoning, and Utilization of the target poisoning for deposition of various TiAlCN/VCN coatings.

Firstly the in chapter 4, the plasma etching with  $V^+$  ions and its influence on the substrate surface, cutting edge and the material removal were investigated. The main finding was:

- With increasing energy applied to the HIPIMS cathode both the metal ion/gas ion and the metal ion/metal neutral ratio increased;
- The removal of the material was mainly determined by the holding time;

- Etching removes loosely bound surface debris increasing the surface roughness. This leads to increased adhesion to the coating.
- For higher charge, vanadium implantation is more effective by approximately 10 at. % . The argon content in the coating is reduced as plasma becomes more metal-ion rich. During etching the carbon is removed more easily than tungsten.

In chapter 6 the target poisoning studies in a various reactive atmospheres (Ar, N<sub>2</sub>, CH<sub>4</sub>) for various pure DCMS and combined HIPIMS+DCMS discharges were successfully conducted. The following can be concluded:

- The target material dominates the hysteresis behaviour at the low flow. When the target becomes fully covered with the compound, the dominating factor is plasma composition, especially radicals.
- When both nitrogen and methane are used, carbon shows higher reactivity and reacts with the target material faster than nitrogen
- When HIPIMS discharge is applied, the total pressure and the discharge resistivity hystereses are narrower. However the poisoning has greater influence, as plasma is more reactive.

SNMC and ANMC coatings were successfully deposited on various substrates. In chapters 7 and 8 coatings were analysed in the lab environment. Table 10 shows summary of mechanical and tribological properties of the TiAlCN/VCN coatings investigated in this research as well as previously investigated TiAlCN/VCN, TiAlN, and V/C/N coatings.

The TiAlCN/VCN coating family deposited for this research generally shows higher hardness than TiAlCN/VCN coating deposited by Kamath et al. However coatings show lower wear resistance and higher CoF, which can be related to lower C/N content in

coatings. The microstructure analysis shows that microstructure of high metal content TiAlCN/VCN coatings differ from coatings deposited by Kamath et al. while coatings 25% OES and 20% OES have similar microstructure consisting dense columns with dome finished tops [6, 149]. The reason is that during deposition of Kamath’s coating there was no target poisoning control, and coatings were deposited at the high nitrogen and methane flow, similarly as coatings 25% OES and 20% OES. Those coatings show similar properties to VC containing coatings with high hardness and low CoF. TiAlN coatings have much lower CoF than V containing coatings.

Table 10 Summary of the mechanical and tribological properties

	CoF	Wear rate (mm <sup>3</sup> N <sup>-1</sup> m <sup>-1</sup> )	Thickness (μm)	Microhardness (HK)	Nanohardness (MPa)	Young's Modulus (GPa)	Cutting test Passes
45% OES	0.81	--	5.1	780	3792	114	--
37% OES	0.65	3.30E-15	4.63	3721	29341	377	9
30% OES	0.75	5.80E-16	3.98	3209	18009	323	15
25% OES	0.56	--	2.36	3479	29233	337	2
20% OES	0.63	--	2.24	3699	27713	331	4
25% OES B	0.56	1.20E-15	3.25	2055	14837	308	1
37/25% OES	0.73	3.40E-16	3.54	3208	21709	361	19
45:20% OES	0.69	5.60E-17	5.53	3389	21866	338	12
TiAlCN/VCN [5]	0.5	1.40E-17	--	3000	--	--	--
TiAlN/VN [150]	0.4	2.30E-17	--	--	31700	--	--
Ti55Al45N [151]	0.3	1.00E-16	1.9	--	32500	--	--
Ti35Al65N [151]	0.25	1.00E-16	1.8	--	31400	--	19
VN [152]	0.62	8.90E-17	8.5	2970	--	--	--
VN/VC [152]	0.56	5.20E-18	6.1	3762	--	--	--
VN/VC/VC [152]	0.5	2.03E-16	9	3362	--	--	--
VC [152]	0.55	1.73E-14	11.1	3720	--	--	--

From chapters 7 and 8 following can be concluded:

- TiAlCN/VCN coatings exhibit a single-phase B1-NaCl structure with different preferred orientation depending on reactive gas flows. As the OES signal decreases, the coating microstructure becomes more columnar and carbon segregation can be observed.

- At low OES signal levels there is a big difference between the OES signal during base layer deposition and nano-multilayer coating which leads to a rapid increase in reactive gas flow in the initial stages of growth. This further leads to low adhesion resulting in poor wear properties of the coatings. The adhesion of the coatings deposited at the high poisoning level can be improved by introducing ramping of the signal between the base layer and the TiAlCN/VCN multilayer coatings. This was observed both in lab test as in the cutting tests.
- Lowering the bias from -60 to -50V for the coating deposited at high poisoning level, changes structure from dense, dome terminated columns to a well-defined columns resulting in faced structure. Coating deposited at lower bias shows good wear behaviour for lab test, however in fails in real cutting environment.
- By controlling the poisoning it is possible to deposit coating with advanced architecture, where structure change from amorphous or dense columnar structure with a high metal content to a low metal, high carbon and nitrogen content regions. The thickness of the regions can be controlled.

The cutting tests in chapter 9, together with the mechanical and tribological tests of the coatings brings following conclusions:

- Low metal content coatings (25% OES, 20% OES) show low friction coefficient when compared with other TiAlCN/VCN coatings. Coating shows also high hardness and low elasticity. Despite it, coatings shows poor wear resistance due to the coating delamination between base layer and the TiAlCN/VCN layer. The poor wear resistance causes that coating fails in the cutting tests.

- The coating 30% OES is hard and elastic. The tribotest show low wear resistance with a high CoF. High CoF can be caused by the columnar structure with the faced top.
- Coating 30% OES coated insert performs well in cutting tests. It survives 15 passes which is only 4 passes less than the standard coating with almost no BUE created. However, a high abrasive wear is observed which is related to high CoF. Due to very low BUE creation, good mechanical and tribological properties this coating should be test in cutting aluminium alloys, which are softer and causes less abrasive wear.
- The highest hardness has coating 37% OES with the denser microstructure. It also has low wear resistance and CoF of 0.65 which is in typical range of TiAlCN/VCN coatings (table 10). Despite excellent mechanical and good tribological properties this coating survived only 9 passes, which is less than half of the standard coatings. The main reason was very high abrasive wear.
- The coating 45% OES shows the worst mechanical properties. It is soft, very rough which cause high CoF and very low wear resistance. This coating can't be used as a tool protective coating and it was not tested in the cutting tests.
- Reducing bias for the coating 25% OES B improved the tribological properties when compared with coatings 25% OES and 20% OES. It shows the lowest CoF of 0.56 (same as 20% OES coating). However, it still has high wear coefficient. Moreover, reducing bias resulted in columnar structure and lowest hardness. For this reason, coating failed the cutting test.

- The coating 37/25% combined the hardness and low wear resistance. Similarly, as coating 30% OES the columnar structure with the faced top results in high CoF resulting in abrasive wear. However, high C/N content layer leads to excellent cutting test results. The coating 37/25% OES coated insert survived 19 passes, which is the same lifetime as the insert coated with the standard coating. Moreover, the coating 37/25 OES coated inserts exhibit significantly reduced BUE tendency and the lower wear damages.
- Coating 45:20 OES shows the lowest wear rate and high hardness. However, coating is very thick, which can lead to internal stresses of the coatings. This result in local chipping of the coating, disqualifying it for using it for the industry purpose. Chipping of the coating will lead to short lifetime of tool and low finishing quantity of the coating. However, on the insert that survived 12 passes significantly reduced BUE is observed, showing good performance of the top layer. The good mechanical properties and low BUE creation indicates that cutting performance of the coating could be improved by reducing the thickness, especially of the first metallic layer (45% OES).

- [1] P. E. Hovsepian, G. Kamath, a P. Ehiasarian, R. Haasch, and I. Petrov, "Microstructure, Oxidation and Tribological Properties of TiAlCN/VCN Coatings Deposited by Reactive HIPIMS," *IOP Conf. Ser. Mater. Sci. Eng.*, vol. 39, p. 12011, Sep. 2012.
- [2] *Handbook of Deposition Technologies for Films and Coatings - Science, Technology and Applications*, 2nd ed. 1994.
- [3] P. E. Hovsepian, "Nanoscale Multilayer PVD Coatings Deposited by the Combined HIPIMS / UBM Technology for Applications in Aerospace , Automotive and Biomedical Industries ."
- [4] P. E. Hovsepian, A. P. Ehiasarian, A. Deeming, and C. Schimpf, "VmeCN based nanoscale multilayer PVD coatings deposited by the combined high power impulse magnetron sputtering/unbalanced magnetron sputtering technology," *Plasma Process. Polym.*, vol. 4, no. SUPPL.1, pp. 897–901, 2007.
- [5] G. Kamath, a P. Ehiasarian, Y. Purandare, and P. E. Hovsepian, "Tribological and oxidation behaviour of TiAlCN/VCN nanoscale multilayer coating deposited by the combined HIPIMS/(HIPIMS-UBM) technique," *Surf. Coatings Technol.*, vol. 205, no. 8–9, pp. 2823–2829, Jan. 2011.
- [6] P. E. Hovsepian, A. P. Ehiasarian, and I. Petrov, "Structure evolution and properties of TiAlCN/VCN coatings deposited by reactive HIPIMS," *Surf. Coatings Technol.*, vol. 257, pp. 38–47, 2014.
- [7] Peter Sigmund, "Theory of Sputtering. I. Sputtering Yield of Amorphous and Polycrystalline Targets," *Phys. Rev.*, vol. 184, no. August, pp. 383–416, 1969.
- [8] A. Rockett, *The Materials Science of Semiconductors*. Springer US, 2007.
- [9] M. A. M. Palazon, "Carbon Nitride Deposition by Magnetron Sputtering: Structural , Mechanical , Electrical and Optical Properties," Dublin City University, 2000.
- [10] R. . A. P.J Kelly, "Magnetron sputtering: a review of recent developments and applications," *Vacuum*, vol. 56, no. 3, pp. 159–172, 2000.
- [11] R. P. Jeffrey A. Hopwood, *Ionized Physical Vapor Deposition*. Elsevier Science, 1999.
- [12] B. Chapman, *Glow Discharge Processes, Sputtering and Plasma Etching*. Wiley, 1980.
- [13] B. Window and N. Savvides, "Charged particle fluxes from planar magnetron sputtering sources," *J. Vac. Sci. Technol. A*, vol. 4, pp. 196–202, 1986.
- [14] B. Window, "Recent advances in sputter deposition," *Surf. Coatings Technol.*, vol. 71, no. 2, pp. 93–97, 1995.
- [15] A. Matthews, *Advanced Surface Coatings: a Handbook of Surface Engineering*, Softcover. Springer, 2012.
- [16] D. M. Mattox, "Handbook of physical vapor deposition (PVD) processing." William Andrew ; Elsevier Science [distributor], Norwich, N.Y.; Oxford, 2010.
- [17] J. W. Bradley and T. Welzel, "Physics and phenomena in pulsed magnetrons: an overview," *J. Phys. D. Appl. Phys.*, vol. 42, no. 9, p. 93001, 2009.
- [18] S. M. M. Komath G. Mohan Rao, M. Komath, G. Mohan Rao, and S. Mohan, "Studies on the optimisation of unbalanced magnetron sputtering cathodes," *Vacuum*, vol. 52, no. 3, pp. 307–311, Mar. 1999.
- [19] A. P. P. Ehiasarian, R. New, W.-D. Münz, L. Hultman, U. Helmersson, V. Kouznetsov, W.-D. Muenz, L. Hultman, U. Helmersson, and V. Kouznetsov, "Influence of high power densities on the composition of pulsed magnetron plasmas," *Vacuum*, vol. 65, no. 2, pp. 147–154, 2002.
- [20] J. Bohlmark, "Fundamentals of High Power Impulse Magnetron Sputtering," Linköping University Institute of Technology, 2006.
- [21] U. H. and I. P. Karol Macák, Vladimir Kouznetsov, Jochen Schneider, "Ionized sputter deposition using an extremely high plasma density pulsed magnetron discharge," *J. Vac. Sci. Technol. A*, vol. 18, no. 4, pp. 1533–1537, 2000.
- [22] I. P. Vladimir Kouznetsova, Karol Macáka, Jochen M. Schneidera, Ulf Helmerssona, "A novel pulsed magnetron sputter technique utilizing very high target power densities," *Surf. Coatings Technol.*, vol. 122, no. 2–3, pp. 290–293, 1999.
- [23] L. T.-G. and M. T. Ludovic de Poucques, Jean-Christophe Imbert, Caroline Boisse-

- Laporte, Jean Bretagne, Mihai Ganciu, "Study of the transport of titanium neutrals and ions in the post-discharge of a high power pulsed magnetron sputtering device," *Plasma Sources Sci. Technol.*, vol. 15, no. 4, p. 661, Nov. 2006.
- [24] V. Stranak, M. Quaas, R. Bogdanowicz, H. Steffen, H. Wulff, Z. Hubicka, M. Tichy, and R. Hippler, "Effect of nitrogen doping on  $TiO_x N_y$  thin film formation at reactive high-power pulsed magnetron sputtering," *J. Phys. D. Appl. Phys.*, vol. 43, no. 28, p. 285203, Jul. 2010.
- [25] A. P. Ehasarian and W. D. Münz, "High power pulsed magnetron sputtered CrN x films," *Surf. coatings ...*, vol. 164, pp. 267–272, 2003.
- [26] H.-E. W. Jurgen Meichsner, Martin Schmidt, Ralf Schneider, *Discharge physics of high power impulse magnetron sputtering*, vol. 205. 2011.
- [27] W. D. Münz, D. Schulze, and F. J. M. Hauzer, "A new method for hard coatings: ABS," *Surf. Coatings Technol.*, vol. 50, pp. 169–178, 1992.
- [28] U. H. J.T. Gudmundsson, J. Alamib, "Spatial and temporal behavior of the plasma parameters in a pulsed magnetron discharge," *Surf. Coatings Technol.*, vol. 161, no. 2–3, pp. 249–256, Dec. 2002.
- [29] R. Machunze, a. P. Ehasarian, F. D. Tichelaar, and G. C. a M. Janssen, "Stress and texture in HIPIMS TiN thin films," *Thin Solid Films*, vol. 518, no. 5, pp. 1561–1565, 2009.
- [30] W.-D. Münz, M. Schenkel, S. Kunkel, J. Paulitsch, K. Bewilogua, and W.-D. M. et al., "Industrial applications of HIPIMS," *J. Phys. Conf. Ser.*, vol. 100, pp. 1–6, 2008.
- [31] G. Greczynski, J. Jensen, J. Böhlmark, L. Hultman, J. Böhlmark, and L. Hultman, "Microstructure control of CrN<sub>x</sub> films during high power impulse magnetron sputtering," *Surf. Coatings Technol.*, vol. 205, no. 1, pp. 118–130, 2010.
- [32] W.-D. Münz, "HIPIMS: The New PVD Technology," *Vak. Forsch. und Prax. Suppl. Vacuum's Best*, vol. 20 (Suplem, pp. 27–32, 2008.
- [33] A. P. Ehasarian, J. G. Wen, and I. Petrov, "Interface microstructure engineering by high power impulse magnetron sputtering for the enhancement of adhesion," *J. Appl. Phys.*, vol. 101, no. 5, pp. 1–10, 2007.
- [34] E. Broitman and L. Hultman, "Adhesion improvement of carbon-based coatings through a high ionization deposition technique," *J. Phys. Conf. Ser.*, vol. 370, p. 12009, Jun. 2012.
- [35] I. Safi, "Recent aspects concerning DC reactive magnetron sputtering of thin films: a review," *Surf. Coatings Technol.*, vol. 127, no. 2–3, pp. 203–218, May 2000.
- [36] S. Berg, T. Nyberg, and T. N. S. Berg, "Fundamental understanding and modeling of reactive sputtering processes," *Thin Solid Films*, vol. 476, pp. 215–230, 2005.
- [37] W. D. S. J. M. Schneider S. Rohde, A. Matthews, J. M. Schneider, S. Rohde, W. D. Sproul, and A. Matthews, "Recent developments in plasma assisted physical vapour deposition," *J. Phys. D. Appl. Phys.*, vol. 33, pp. R173–R186, 2000.
- [38] D. Rosén, I. Katardjiev, S. Berg, W. Möller, and H.-E. W. Jurgen Meichsner, Martin Schmidt, Ralf Schneider, *TRIDYN simulation of target poisoning in reactive sputtering*, vol. 228, no. 1–4 SPEC. ISS. 2005.
- [39] D. Depla and R. De Gryse, "Target poisoning during reactive magnetron sputtering: Part III: the prediction of the critical reactive gas mole fraction," *Surf. Coatings Technol.*, vol. 183, no. 2–3, pp. 196–203, May 2004.
- [40] D. Depla, R. De Gryse, and R. De Gryse, "Target poisoning during reactive magnetron sputtering: Part II: the influence of chemisorption and gettering," *Surf. Coatings Technol.*, vol. 183, no. 2–3, pp. 190–195, May 2004.
- [41] J. Musil, P. Baroch, J. Vlček, K. H. Nam, and J. G. Han, "Reactive magnetron sputtering of thin films: present status and trends," *Thin Solid Films*, vol. 475, no. 1–2, pp. 208–218, Mar. 2005.
- [42] W. D. Sproul, D. J. Christie, D. C. Carter, and D. C. C. W.D. Sproul D.J. Christie, "Control of reactive sputtering processes," *Thin Solid Films*, vol. 491, pp. 1–17, 2005.
- [43] D. D. and S. H. and S. M. and R. De Gryse, "Towards a more complete model for reactive magnetron sputtering," *J. Phys. D. Appl. Phys.*, vol. 40, no. 7, p. 1957, 2007.

- [44] S. B. T. Kubart O. Kappertz T. Nyberg, T. Kubart, O. Kappertz, T. Nyberg, and S. Berg, "Dynamic behaviour of the reactive sputtering process," *Thin Solid Films*, vol. 515, pp. 421–424, 2006.
- [45] D. Depla and R. De Gryse, "Target voltage measurements during DC sputtering of silver in a nitrogen/argon plasma," *User Model. User-adapt. Interact.*, vol. 69, pp. 529–536, 2003.
- [46] H.-E. W. Jurgen Meichsner, Martin Schmidt, Ralf Schneider, *Reactive Sputter Deposition*, vol. 109. 2008.
- [47] Z. Ahmad and B. Abdallah, "Controllability analysis of reactive magnetron sputtering process," *Acta Phys. Pol. A*, vol. 123, no. 1, pp. 3–6, 2013.
- [48] and J. N. A. Pflug, B. Szyszka, V. Sittinger, "Process Simulation for Advanced Large Area Optical Coatings," in *Proceedings of 46th Annual SVC Technical Conference, Society of Vacuum Coaters, San Francisco, CA, 2003*, p. 241.
- [49] D. Depla, S. Mahieu, and R. De Gryse, "Magnetron sputter deposition: Linking discharge voltage with target properties," *Thin Solid Films*, vol. 517, no. 9, pp. 2825–2839, 2009.
- [50] J. Meichsner, S. Martin, R. Schneider, and H.-E. Wagner, "Nonthermal Plasma Chemistry and Physics." 2012.
- [51] S. I. S. O.A. Fouad Abdul K Rumaiz, O. a. a. Fouad, A. K. Rumaiz, S. I. Shah, H.-E. W. Jurgen Meichsner, Martin Schmidt, Ralf Schneider, O. a. a. Fouad, A. K. Rumaiz, and S. I. Shah, "Reactive sputtering of titanium in Ar/CH<sub>4</sub> gas mixture: Target poisoning and film characteristics," *Thin Solid Films*, vol. 517, no. 19, pp. 5689–5694, Aug. 2009.
- [52] and A. von K. J. B. \* A. C. M. Schulze, "Time-Resolved Molecular Beam Mass Spectrometry of the Initial Stage of Particle Formation in an Ar/He/C<sub>2</sub>H<sub>2</sub> Plasma," *J. Phys. Chem. A*, vol. 111 (42), pp. 10453–10459, 2007.
- [53] and M. C. M. van de S. J. B. D. C. Schram, "Detailed TIMS Study of Ar/C<sub>2</sub>H<sub>2</sub> Expanding Thermal Plasma: Identification of a-C:H Film Growth Precursors," *J. Phys. Chem. A*, vol. 109 (44), pp. 10153–10167, 2005.
- [54] H.-E. W. Jurgen Meichsner, Martin Schmidt, Ralf Schneider, *Hysteresis, structural and composition characteristics of deposited thin films by reactively sputtered titanium target in Ar/CH<sub>4</sub>/N<sub>2</sub> gas mixture*, vol. 29, no. 8. 2013.
- [55] M. Aiempanakit, T. Kubart, P. Larsson, K. Sarakinos, J. Jensen, and U. Helmersson, "Hysteresis and process stability in reactive high power impulse magnetron sputtering of metal oxides," *Thin Solid Films*, vol. 519, pp. 7779–7784, 2011.
- [56] K. S. J. Alami S. Bolz, J. Alami, S. Bolz, and K. Sarakinos, "High power pulsed magnetron sputtering: Fundamentals and applications," *J. Alloys Compd.*, vol. 483, no. 1–2, pp. 530–534, Aug. 2009.
- [57] M. Audronis, V. Bellido-Gonzalez, and B. Daniel, "Control of reactive high power impulse magnetron sputtering processes," *Surf. Coatings Technol.*, vol. 204, no. 14, pp. 2159–2164, 2010.
- [58] W. D. S. and B. E. Sylvia, "Multi-Level Control for Reactive Sputtering," in *45th Annual Technical Conference Proceedings of the Society of Vacuum Coaters, Orlando, FL, 2002*, p. 11.
- [59] and L. C. M. R. Visokay, J. J. Chambers, A. L. P. Rotondaro, R. Kuan, L. Tsung, M. Douglas, H. Bu, A. Shanware, "Properties of Hf-Based Oxide and Oxynitride Thin Films," in *Proceedings of the 2002 AVS 3rd International Conference on Microelectronics and Interfaces, Santa Clara, CA, 2002*, p. 127.
- [60] W. D. Sproul, D. J. Christie, D. C. Carter, A. E. Industries, F. Collins, S. Berg, and T. Nyberg, "Control of the Reactive Sputtering Process Using Two Reactive Gases," *46th Annu. Tech. Conf. Proc. Soc. Vac. Coaters*, pp. 98–102, 2003.
- [61] J. Schulte and G. Sobe, "Magnetron sputtering of aluminium using oxygen or nitrogen as reactive gas," *Thin Solid Films*, vol. 324, no. 1–2, pp. 19–24, 1998.
- [62] W. R. Thompson, T. J. Henry, J. M. Schwartz, B. N. Khare, and C. Sagan, "Plasma discharge in N<sub>2</sub> + CH<sub>4</sub> at low pressures: Experimental results and applications to Titan," *Icarus*, vol. 90, no. 1, pp. 57–73, 1991.

- [63] T. Solidfilms, A. Okamoto, and T. Serikawa, "REACTIVE SPUTTERING Ar-N, MIXTURE," vol. 137, pp. 143–151, 1986.
- [64] J. Affinito and R. Parsons, "Mechanisms of voltage controlled, reactive, planar magnetron sputtering of Al in Ar/N<sub>2</sub> and Ar/O<sub>2</sub> atmospheres," *J. Vac. Sci. ...*, vol. 2, no. 3, p. 1275, 1984.
- [65] S. Schiller, U. Heisig, K. Steinfelder, J. Strümpfel, R. Voigt, R. Fendler, and G. Teschner, "On the investigation of d.c. plasmatron discharges by optical emission spectrometry," *Thin Solid Films*, vol. 96, no. 3, pp. 235–240, 1982.
- [66] W. D. Sproul and J. R. Tomashek, "Rapid rate reactive sputtering of a group IVb metal." Google Patents, 1984.
- [67] K. Miyoshi, Ed., *Solid Lubrication Fundamentals and Applications (Materials Engineering)*, 1st ed. CRC Press, 2001.
- [68] B. Bhushan, *Modern Tribology Handbook, Two Volume Set*, 1st ed. CRC Press, 2000.
- [69] A. Cavaleiro and J. T. de Hosson, Eds., *Nanostructured Coatings (Nanostructure Science and Technology)*, 2006th ed. Springer, 2006.
- [70] M. L. U Wiklund, "Low friction PVD titanium-carbon coatings," *Wear*, vol. 241, pp. 230–234, 2000.
- [71] R. Saito, M. S. Dresselhaus, and G. Dresselhaus, Eds., *Physical Properties of Carbon Nanotubes*. World Scientific Publishing Company, 1998.
- [72] A. Krüger, *Carbon Materials and Nanotechnology*, 1st ed. Wiley-VCH, 2010.
- [73] M. S. D. et al., *Science of Fullerenes and Carbon Nanotubes*. Academic Press, 1996.
- [74] N. Savvides and T. J. J. Bell, "Hardness and elastic modulus of diamond and diamond-like carbon films," *Thin Solid Films*, vol. 28, pp. 289–292, 1993.
- [75] R. W. G. Wyckoff, *Crystal Structures*. Interscience Publishers, 1958.
- [76] R. W. G. Wyckoff, *In Crystal Structures*. Interscience Publishers, 1965.
- [77] R. H. Savage, "Graphite Lubrication," *J. Appl. Phys.*, vol. 19,1, pp. 1–10, 1948.
- [78] B. M. O. A Magneli, "Studies of the Vanadium Pentoxide-Molybdenum Trioxide System: I. The Relation between the Crystal Structures of the Two Oxides," *Acta Chem. Scand*, vol. 5, pp. 581–584, 1951.
- [79] E. Lugscheider, O. Knotek, K. Bobzin, S. Bärwulf, K. B. S. B. E. Lugscheider O. Knotek, and L. et al., "Tribological properties, phase generation and high temperature phase stability of tungsten- and vanadium-oxides deposited by reactive MSIP-PVD process for innovative lubrication applications," *Surf. Coatings Technol.*, vol. 133–134, pp. 362–368, 2000.
- [80] S. Nagata, "Susceptibilities of the vanadium Magneli phases V<sub>18</sub>O<sub>32</sub>, t at low temperature," *Phys. Rev. B*, vol. 20, no. 7, 1979.
- [81] F. Reidenbach, *ASM Handbook: Volume 5: Surface Engineering (Asm Handbook) (Asm Handbook)*, 10th ed. ASM International, 1994.
- [82] P. Balog, D. Orosel, Z. Cancarevic, C. Schön, M. Jansen, and P. B. et al., "V<sub>2</sub>O<sub>5</sub> phase diagram revisited at high pressures and high temperatures," *J. Alloys Compd.*, vol. 429, no. 1–2, pp. 87–98, Feb. 2007.
- [83] A. Erdemir, "A crystal-chemical approach to lubrication by solid oxides," *Tribol. Lett.*, vol. 8, pp. 97–102, 2000.
- [84] L. Yate, L. Martínez-de-Olcoz, J. Esteve, and A. Lousa, "Control of the bias voltage in d.c. PVD processes on insulator substrates," *Vacuum*, vol. 83, no. 10, pp. 1287–1290, 2009.
- [85] J. Thornton, "The Microstructure of Sputter-deposited Coating," *J. Vac. Sci. Technol. A* 4, vol. 6, pp. 3059–3065, 1986.
- [86] K. J. Robbie and M. J. Brett, "Method of depositing shadow sculpted thin films." Google Patents, 1999.
- [87] J. ~A. Thornton, "Influence of apparatus geometry and deposition conditions on the structure and topography of thick sputtered coatings," *J. Vac. Sci. Technol.*, vol. 11, p. 666, Jul. 1974.
- [88] R. Messier, A. P. Giri, and R. A. Roy, "Revised structure zone model for thin film physical structure," *J. Vac. Sci. Technol. A*, vol. 2, no. 2, pp. 500–503, 1984.

- [89] P. J. Kelly and R. D. Arnell, "Development of a novel structure zone model relating to the closed-field unbalanced magnetron sputtering system," *J. Vac. Sci. Technol. A*, vol. 16, no. 5, pp. 2858–2869, 1998.
- [90] A. Barnett S.; Madan, "Superhard superlattices," *Met. Powder Rep.*, vol. 53, p. 36–36(1), 1998.
- [91] P. C. Yashar, W. D. Sproul, and W. D. S. P. C. Yashar, "Nanometer scale multilayered hard coatings," *Vacuum*, vol. 55, no. 3–4, pp. 179–190, Dec. 1999.
- [92] H. Holleck and V. Schier, "Multilayer PVD coatings for wear protection," *Surf. Coatings Technol.*, vol. 76–77, no. 1995, pp. 328–336, Nov. 1995.
- [93] M. S. et al., M. Stueber, H. Holleck, H. Leiste, K. Seemann, S. Ulrich, and C. Ziebert, "Concepts for the design of advanced nanoscale PVD multilayer protective thin films," *J. Alloys Compd.*, vol. 483, no. 1–2, pp. 321–333, Aug. 2009.
- [94] U. H. et al., "Growth of single crystal TiN/VN strained-layer superlattices with extremely high mechanical hardness," *J. Appl. Phys.*, vol. 62, no. 2, p. 481, 1987.
- [95] Y. N. Kok, "Nanoscale Multilayer Me-Graphite Coatings Grown by Combined Steered Cathodic Arc/Umbalance Magnetron Sputtering," Sheffield Hallam University, 2005.
- [96] H. C. Barshilia, A. Jain, and K. S. Rajam, "Structure, hardness and thermal stability of nanolayered TiN/CrN multilayer coatings," *Vacuum*, vol. 72, no. 3, pp. 241–248, 2003.
- [97] W. Mu, L. A. Donohue, P. E. Hovsepian, and W. D. M. et al., "Properties of various large-scale fabricated TiAlN- and CrN-based superlattice coatings grown by combined cathodic arc unbalanced magnetron sputter deposition," *Surf. Coatings Technol.*, vol. 125, pp. 269–277, 2000.
- [98] Q. Luo, G. Robinson, M. Pittman, M. Howarth, W.-M. Sim, M. R. Stalley, H. Leitner, R. Ebner, D. Caliskanoglu, P. E. Hovsepian, and Q. L. et al., "Performance of nano-structured multilayer PVD coating TiAlN/VN in dry high speed milling of aerospace aluminium 7010-T7651," *Surf. Coatings Technol.*, vol. 200, no. 1–4, pp. 123–127, Oct. 2005.
- [99] M. G. Hocking, *Metallic and ceramic coatings: Production, high temperature properties, and applications*. J. Wiley, 1989.
- [100] Hugh O. Pierson, *Handbook of Refractory Carbides and Nitrides*. Elsevier, 1996.
- [101] P. D. Desai, H. M. James, and C. Y. Ho, "Electrical Resistivity of Aluminum and Manganese," *Journal of Physical and Chemical Reference Data*, vol. 13, no. 4. pp. 1131–1172, 1984.
- [102] T. Marr, J. Freudenberger, A. Kauffmann, J. Romberg, I. Okulov, R. Petters, J. Scharnweber, A. Eschke, C.-G. Oertel, U. Kühn, J. Eckert, W. Skrotzki, and L. Schultz, "Processing of Intermetallic Titanium Aluminide Wires," *Metals (Basel)*, vol. 3, no. 2, pp. 188–201, 2013.
- [103] H.-E. W. Jurgen Meichsner, Martin Schmidt, Ralf Schneider, *TiAlNTiAlON Si3 N4 tandem absorber for high temperature solar selective applications*, vol. 89, no. 19. 2006.
- [104] J. Koo, J.-W. Lee, T. Doh, Y. Kim, Y.-D. Kim, and H. Jeon, "Study on the characteristics of TiAlN thin film deposited by atomic layer deposition method," *J. Vac. Sci. Technol. A*, vol. 19, no. 6, 2001.
- [105] E. de Hoffmann and V. Stroobant, *Mass Spectrometry: Principles and Applications*. Wiley, 2007.
- [106] E. De Hoffmann and V. Stroobant, *Mass Spectrometry - Principles and Applications.*, vol. 29, no. 6. 2007.
- [107] D. W. Ball, *The Basics of Spectroscopy*. SPIE- The International Society for Optical Engineering, 2001.
- [108] K. a Marx, "Quartz crystal microbalance: a useful tool for studying thin polymer films and complex biomolecular systems at the solution-surface interface.," *Biomacromolecules*, vol. 4, no. 5, pp. 1099–120, 2003.
- [109] R. Hippler, H. Kersten, M. Schmidt, and K. H. Schoenbach, Eds., *Low Temperature Plasmas: Fundamentals, Technologies and Techniques (2 volume set)*, 2nd ed. Wiley-VCH, 2008.
- [110] D. N. Ruzic, *Electric probes for low temperature plasmas (AVS monograph series)*, 1st

- ed. American Vacuum Society, 1994.
- [111] D. Brandon and W. D. Kaplan, *Microstructural Characterization of Materials*, 2nd ed. Wiley, 2008.
- [112] Y. Leng, *Materials Characterization Introduction to Microscopic and Spectroscopic Methods*, 1st ed. Wiley, 2013.
- [113] F. C. Campbell, *Phase Diagrams: Understanding the Basics*. United State of America: ASM International, 2012.
- [114] “XPert PRO MPD X-Ray Diffraction System.” .
- [115] S. Logothetidis, N. Kalfagiannis, K. Sarakinos, P. Patsalas, and S. L. et al., “Investigation of bilayer period and individual layer thickness of CrN/TiN superlattices by ellipsometry and X-ray techniques,” *Surf. Coatings Technol.*, vol. 200, no. 22–23, pp. 6176–6180, Jun. 2006.
- [116] M. Birkholz, *Thin Film Analysis by X-Ray Scattering*. Weinheim, FRG: Wiley-VCH Verlag GmbH & Co. KGaA, 2005.
- [117] R. L. McCreery, *Raman Spectroscopy for Chemical Analysis*. Wiley, 2005.
- [118] T. V. Vorburger and J. Raja, “Surface finish metrology tutorial.” Jun-1990.
- [119] R. Chattopadhyay, *Surface Wear: Analysis, Treatment, and Prevention*. ASM International, 2001.
- [120] Hutchins and I. Hutchings, *Tribology, Friction and Wear of Engineering Materials*. Elsevier Limited, 1992.
- [121] M. H. A. Wachal, *Tribologia*. Wydawnictwa Naukowo-Techniczne, 1980.
- [122] S. J. J. Bull, “Failure modes in scratch adhesion testing,” *Surf. Coatings Technol.*, vol. 50, no. 1, pp. 25–31, Jan. 1991.
- [123] A. S. M. International, *Hardness Testing*, 2nd ed. ASM International, 1999.
- [124] “Fine Ceramics(advances ceramics, advanced technical ceramics) - Roskwell indentation test foe evaluation of adhesion of ceramic coatings,” *Br. Stand.*
- [125] S. J. Bull and E. G. Berasetegui, “An overview of the potential of quantitative coating adhesion measurement by scratch testing,” *Tribol. Int.*, vol. 39, no. 2, pp. 99–114, 2006.
- [126] “Standard Test Method for Adhesion Strength and Mechanical Failure Modes of Ceramic Coatings by Quantitative Single Point Scratch Testing.” .
- [127] W. C. Oliver, G. M. Pharr, and G. M. P. W.C. Oliver, “Measurement of hardness and elastic modulus by instrumented indentation: Advances in understanding and refinements to methodology,” *J. Mater. Res.*, vol. 19, no. 1, pp. 3–20, Mar. 2004.
- [128] J. S. B.-G. P.K. Datta, Ed., *Advances in surface engineering Volume III Engineering Applications*. The Royal Society of Chemistry, 1997.
- [129] A. P. Ehiasarian, “Development of PVD Coating Processes Informed By Plasma Diagnostics,” Sheffield Hallam University, 2002.
- [130] W. Yan, C. L. Pun, and G. P. Simon, “Conditions of applying Oliver–Pharr method to the nanoindentation of particles in composites,” *Compos. Sci. Technol.*, vol. 72, no. 10, pp. 1147–1152, Jun. 2012.
- [131] J. R. Conrad, J. L. Radtke, R. a. Dodd, F. J. Worzala, N. C. Tran, and J. R. C. et al., “Plasma source ion-implantation technique for surface modification of materials,” *J. Appl. Phys.*, vol. 62, no. 11, p. 4591, 1987.
- [132] R. Communication and T. E. Sheridan, “Sheath expansion at a corner,” *J. Phys. D Appl. Phys.*, vol. 29, pp. 2725–2728, 1996.
- [133] S. Qi, W. Zhiwei, G. Changxin, H. Zhongyi, G. C. S. Qi W. Zhiwei, and H. Zhongyi, “Study on the treatment capability of a plasma-based ion implanting trench-shaped target,” *Model. Simul. Mater. Sci. Eng.*, vol. 13, no. 6, pp. 829–839, Sep. 2005.
- [134] N. I. for Standard Technology, “NIST Atomic Spectra Database Lines Form.” .
- [135] K. L. S. S.M. Rossnagel, “Optical emission in magnetrons: Nonlinear aspects,” *J. Vac. Sci. Technol. A.*, vol. 7, no. 3, pp. 968–971, 1989.
- [136] A. P. E. G. Kamath, P. E. Hovsepian, G. Kamath, a. P. Ehiasarian, and P. E. Hovsepian, “Properties of TiAlCN/VCN Nanoscale Multilayer Coatings Deposited by Mixed High-Power Impulse Magnetron Sputtering (HiPIMS) and Unbalanced Magnetron Sputtering Processes—Impact of HiPIMS During Coating,” *IEEE Trans. Plasma Sci.*, vol. 38, no.

- 11, pp. 3062–3070, Nov. 2010.
- [137] A. J. L. Michael A. Lieberman, “Atomic Collisions,” in *Principles of Plasma Discharges and Materials Processing, Second Edition*, John Wiley & Sons, Inc., 2005, pp. 43–85.
- [138] B. R. BRONFIN, “Hydrogen Cyanide Synthesis in a Thermal Radiofrequency Induction Plasma,” in *Chemical Reactions in Electrical Discharges*, pp. 423–440.
- [139] L. Hultman, G. Håkansson, U. Wahlström, J.-E. Sundgren, I. Petrov, F. Adibi, and J. E. Greene, “Transmission electron microscopy studies of microstructural evolution, defect structure, and phase transitions in polycrystalline and epitaxial Ti<sub>1-x</sub>Al<sub>x</sub>N and TiN films grown by reactive magnetron sputter deposition,” *Thin Solid Films*, vol. 205, no. 2, pp. 153–164, Dec. 1991.
- [140] M. Samuelsson, K. Sarakinos, H. Högborg, E. Lewin, U. Jansson, B. Wälivaara, H. Ljungcrantz, and U. Helmersson, “Growth of Ti-C nanocomposite films by reactive high power impulse magnetron sputtering under industrial conditions,” *Surf. Coatings Technol.*, vol. 206, no. 8–9, pp. 2396–2402, 2012.
- [141] T. Zehnder and J. Patscheider, “Nanocomposite TiC/a-C:H hard coatings deposited by reactive PVD,” *Surf. Coatings Technol.*, vol. 133–134, pp. 138–144, 2000.
- [142] C. Mitterer, N. Fateh, and F. Munnik, “Microstructure-property relations of reactively magnetron sputtered VC<sub>x</sub>Ny films,” *Surf. Coatings Technol.*, vol. 205, no. 13–14, pp. 3805–3809, 2011.
- [143] T. Savişalo, D. B. Lewis, P. E. Hovsepian, and W.-D. Münz, “Influence of ion bombardment on the properties and microstructure of unbalanced magnetron deposited niobium coatings,” *Thin Solid Films*, vol. 460, no. 1–2, pp. 94–100, Jul. 2004.
- [144] S. M. Rossnagel and J. J. Cuomo, “Film modification by low energy ion bombardment during deposition,” *Thin Solid Films*, vol. 171, no. 1, pp. 143–156, 1989.
- [145] M. Samuelsson, D. Lundin, J. Jensen, M. A. Raadu, J. T. Gudmundsson, and U. Helmersson, “On the film density using high power impulse magnetron sputtering,” *Surf. Coatings Technol.*, vol. 205, no. 2, pp. 591–596, 2010.
- [146] a. N. Reed, M. a. Lange, C. Muratore, J. E. Bultman, J. G. Jones, and a. a. Voevodin, “Pressure effects on HiPIMS deposition of hafnium films,” *Surf. Coatings Technol.*, vol. 206, no. 18, pp. 3795–3802, 2012.
- [147] A. C. Ferrari and J. Robertson, “Interpretation of Raman spectra of disordered and amorphous carbon,” *Phys. Rev. B*, vol. 61, no. 20, pp. 14095–14107, May 2000.
- [148] B. Shew and J. Huang, “The effects of nitrogen flow on reactively sputtered Ti-Al-N films,” *Surf. Coatings Technol.*, vol. 71, pp. 30–36, 1995.
- [149] Q. Luo, C. Schimpf, A. P. Ehasarian, L. Chen, and P. E. Hovsepian, “Structure and Wear Mechanisms of Nanostructured TiAlCN/VCN Multilayer Coatings,” *Plasma Process. Polym.*, vol. 4, no. S1, pp. S916–S920, Apr. 2007.
- [150] Q. Luo, “Temperature dependent friction and wear of magnetron sputtered coating TiAlN/VN,” *Wear*, vol. 271, no. 9–10, pp. 2058–2066, Jul. 2011.
- [151] D. Jianxin and L. Aihua, “Dry sliding wear behavior of PVD TiN, Ti<sub>55</sub>Al<sub>45</sub>N, and Ti<sub>35</sub>Al<sub>65</sub>N coatings at temperatures up to 600°C,” *Int. J. Refract. Met. Hard Mater.*, vol. 41, pp. 241–249, Nov. 2013.
- [152] E. Grigore, C. Ruset, and C. Luculescu, “The structure and properties of VN-VCN-VC coatings deposited by a high energy ion assisted magnetron sputtering method,” *Surf. Coatings Technol.*, vol. 205, no. SUPPL. 2, pp. S29–S32, 2011.